IN-VIVO MAGNETIC RESONANCE IMAGING BIOMARKERS OF NEUROINFLAMMATORY DEMYELINATING DISEASE

By

Ian J. Tagge

A DISSERTATION

Presented to the Department of Biomedical Engineering
and the
Oregon Health & Science University School of Medicine
in partial fulfillment of
the requirements for the degree of

Doctor of Philosophy

January 2016

School of Medicine
Oregon Health & Science University

CERTIFICATE OF APPROVAL

This is to certify that the PhD dissertation of

Ian J Tagge

IN-VIVO MAGNETIC RESONANCE IMAGING BIOMARKERS OF NEUROINFLAMMATORY DEMYELINATING DISEASE

has been approved

Mentor/Advisor – William Rooney, Ph.D.

Committee Chair – Monica Hinds, Ph.D.

Committee Member – Charles Springer, Jr., Ph.D.

Committee Member – Steven Kohama, Ph.D.

Committee Member – Dennis Bourdette, M.D.

Committee Member – Randall Woltjer, M.D., Ph.D.

TABLE OF CONTENTS

Abbreviations

ADEM	acute disseminated encephalomyelitis
AGEA	Allen Gene Expression Atlas
B_0	Static magnetic field
BBB	blood brain barrier
BET	Brain Extraction Tool
CA	contrast agent
CBLL	cerebellum
CC	corpus callosum
CSF	cerebral spinal fluid
CWM	cerebral white matter
Cz	cuprizone
DCE-MRI	dynamic-contrast-enhanced MRI
EC	external capsule
FeO	ferumoxytol (ferumoxtran)
FLAIR	fluid attenuated inversion recovery
FLASH	fast low angle shot
FLIRT	FMRIB's Linear Image Registration Tool
FNIRT	FMRIB's Nonlinear Image Registration Tool
FSL	Functional Magnetic Resonance Imaging of the BRAIN (FMRIB) Software Library
GBCA	gadolinium-based contrast agent
gCC	genu of the corpus callosum
GM	gray matter
GRE	gradient recalled echo
HC	healthy control
IC	internal capsule
iCC	isthmus of the corpus callosum
JM	Japanese macaque
JME	Japanese macaque encephalomyelitis
JMRV	Japanese macaque radinovirus
K^{trans}	the plasma volume fraction CR rate constant product
MBP	myelin basic protein
MPRAGE	magnetization prepared rapid acquisition gradient echo
MR	magnetic resonance
MRI	magnetic resonance imaging
mRNA	messenger ribonucleic acid
MS	multiple sclerosis
MT	magnetization transfer
MTR	magnetization transfer ratio
NAGM	normal-appearing gray matter
NAWM	normal-appearing white matter
NMO	neuromyelitis optica
NPC	neural progenitor cell

OPC …… oligodendrocyte precursor cell
PVWM …….. periventricular white matter
R_1 …… longitudinal relaxation rate (≡1/T_1)
RF …… radio frequency
SC …… spinal cord
sCC …… splenium of the corpus callosum
SSM …… Shutter-Speed Model
SVZ …… subventricular zone
T …….. Tesla
T_1 …… longitudinal relaxation time constant
T_2 …… transverse relaxation time constant
T_1-w …… T_1-weighted image
T_2-w …… T_2-weighted image
TE ……. echo time
TR ……. repetition time
TSE …….. turbo spin echo
WM …… white matter
WMSH …….. white matter signal hyperintensity
ω …….. Larmor frequency
γ …… gyromagnetic ratio

Index of Figures

Index of Tables

Acknowledgements

This work would not have been possible without tremendous support and input from my mentors and collaborators. I would like to acknowledge and thank the following people and groups:

First, I would like to thank my PhD mentor, Dr. William Rooney, for always challenging me and providing mentorship, guidance, and encouragement throughout my graduate training. He has consistently pushed me to grow and expand both my knowledge and my skills, and has taught me the importance of developing and pursuing new ideas and new directions for my research. I would like to thank Dr. Charles Springer and Dr. Xin Li for introducing me to magnetic resonance imaging and for being my first mentors in the Advanced Imaging Research Center. Dr. Charles Springer has also served as a valuable member of my committee who never let me get away with anything. I would like to thank Dr. Steve Kohama for his time and contributions to my research and training both before and during my graduate training, and for serving on my committee. I would like to thank Dr. Monica Hinds for her guidance and service as the chair of my committee. Thanks to Dr. Dennis Bourdette for serving on my committee and acting as a co-mentor on my training grant. I am grateful for Dr. Randy Woltjer's willingness to serve on my oral examination committee and for his indispensable contributions to the cuprizone project on extremely short notice.

Thanks to additional contributors to the cuprizone project: Jim Pollaro, Audrey O'Connor, Dr. Yosef Berlow, Megan Chalupsky, Dr.Priya Chaudhary, Dr. Mac Johnson, Evan Calkins, and Danielle Galipeau.

Thanks to the additional collaborators from the Japanese Macaque Encephalomyelitis group: Dr. Scott Wong, Dr. Robert Zweig, Vince Warren, Minsha Manoharan, Dr. Larry Sherman, and the ONPRC DCM staff.

I would also like to acknowledge additional past and present members of the AIRC who have had an impact on my training and my work: Dr. Manoj Sammi, Brendan Moloney, Eric Earl, Bill Woodward, Jingang Xu, Laura McMahon, Katherine Powers, Dr. Mark Woods, Erin Taber, Dr. Valerie Anderson, Dr. Tom Barbara, Dr. John Grinstead, Daniel Schwartz, Dr. Cory Wyatt, Mara Bahri, Dr. Wei Huang, Dr. Jack Simon, Paul Raab, Dr. Merryl Lobo, Dr. Jeff Njus, and Dr. Mohan Jayatilake. Additional thanks goes to Andy Rekito, Dr. Meredith Hartley and Dr. Owen McCarty.

I am grateful for the following funding sources that have supported my graduate training: The National MS Society, The Nancy Davis Foundation, Vertex/OHSU SRA-05-07-4, W.M. Keck Foundation, NIH S10 OD018224 01, Oregon Opportunity Fund, National Center for Research Sources 3UL1RR024140-04S1, National Institute of Neurological Disorders and Stroke 1F31NS089260-01A1, the International Society for Magnetic Resonance in Medicine, and ARCS Foundation, Portland Chapter.

Finally I would like to thank my parents, Frank and Mary Tagge, and my partner, Brittany Krake, for all of their love and support.

Abstract

Introduction

Multiple sclerosis (MS) is an inflammatory disease of the central nervous system (CNS) and a leading cause of non-traumatic neurological disability in young and middle aged adults.[1] Diagnosis, monitoring, and the study of MS all rely heavily on magnetic resonance imaging (MRI) thanks to its ability to non-invasively observe brain tissue pathology in-vivo. A variety of advanced imaging techniques have been proposed to evaluate tissue and vascular properties including water content, myelin content (to assess demyelination and remyelination), vascular permeability (BBB breakdown in the case of neuroinflammatory diseases), and vascular density in-vivo. In vivo magnetic resonance imaging biomarkers of disease were developed in two separate animal models of MS and subsequently extended to human studies.

Methods

The cuprizone model of demyelination in mice was used to investigate the utility of magnetization transfer imaging (MTI) in assessing myelin content in-vivo in healthy controls, immediately after acute demyelination, and after a period of spontaneous remyelination. MRI data were acquired using an 11.75T horizontal bore instrument (Bruker Biospin, Billerica, MA) and custom built radio frequency (RF) receive coils. Myelin content and other tissue changes were evaluated post-mortem with histological and immunohistochemical analyses.

A multicenter study subsequently endeavored to create a reproducible, standardized protocol for quantitative imaging in MS. One male subject with clinically-definite MS traveled to seven participating North American sites and underwent and underwent two distinct 3T MRI sessions at each site. Magnetization transfer ratio (MTR) and quantitative T_1 imaging sequences were developed, standardized, and acquired at all sites. Image quality and biomarker reproducibility were evaluated within and across sites.

Japanese macaque encephalomyelitis (JME), a novel spontaneous demyelinating disease in non-human primates was investigated as a potential model of MS. JME Lesion distribution was characterized and compared to MS and MS-like human demyelinating diseases. Quantitative dynamic-contrast-enhanced (DCE) MRI experiments provided estimates of BBB permeability; a subset of animals were observed in a short-term longitudinal study to evaluate (1) lesion evolution, and (2) corticosteroid treatment efficacy. MRI data were acquired on a 3T human instrument (Siemens, Erlangen, Germany) at the Oregon National Primate Research Center.

Human DCE-MRI data were collected at 3T with either an 8-channel (n=4 healthy control (HC), 3 MS) or 24-channel (n = 3 HC, 14 MS) radiofrequency head coil. Rapidly-sampled single-slice DCE-MRI data acquired during injection of contrast agent capture the first-pass dynamics of contrast agent before extravasation becomes appreciable. Estimates of water molecule lifetime in brain capillaries (related to brain metabolism) and blood volume were obtained and compared between HC and MS white matter and cortical gray matter.

Results

In the absence of significant inflammation or axonal loss, as in the cuprizone mouse model of demyelination, magnetization transfer ratio (MTR) is a useful, semi-quantitative biomarker of myelin content in-vivo. MTR correlated well with histological measurements of myelin content. Whole-brain coverage obtained in MR images revealed a complex spatial pattern of demyelination in the mouse corpus callosum that was previously not described. Additionally, even after recovery, MTR values in treated animals did not return to levels comparable to age matched controls.

Careful protocol standardization yielded highly reproducible MTR maps in an MS subject imaged at seven North American imaging sites. One site demonstrated unusually low session 1 gray matter MTR; all other sites showed good agreement between sessions and values were consistent across sites in normal-appearing brain tissue and in lesion areas. Quantitative T_1 maps obtained using a variable flip angle (progressive saturation) approach demonstrated a high degree of variability; this technique requires more work to ensure reproducibility.

Lesion distribution in JME shares many characteristics with not only MS, but also its mimics. Cerebellar white matter is preferentially affected, followed by spinal cord and brainstem. Lesion evolution is rapid, and disease progression is aggressive. Treatment with anti-inflammatory doses of corticosteroids is ineffective, but higher doses similar to what is used in to treat acute demyelinated events in human disease shows promise as a method of slowing, if not stopping

or even reversing disease progression. BBB permeability in JME is similar to what has been reported in MS.

Blood volume and brain capillary water molecule lifetimes in normal-appearing brain tissue were elevated in MS compared to controls. Parametric maps demonstrate both focal and diffuse disease-related changes in microvasculature and metabolic activity consistent with previous reports. Importantly, these results demonstrate the feasibility of measuring disease activity in the cortical gray matter. Segmentation of single-slice data is possible, which allows cortical gray matter to be analyzed separately from white matter.

Discussion

Developing imaging biomarkers of disease using animal models, where access to post-mortem tissue allows careful validation, is important in studying and treating human disease. Non-invasive biomarkers, such that those presented in this work, are perfectly suited for longitudinal investigations of progression and treatment of disease. Standardization of quantitative and semi-quantitative imaging protocols is essential for multi-site studies, and accurate comparison of results across studies. Application of these biomarkers in larger human studies will advance patient care and improve patient outcomes.

Introduction to Multiple Sclerosis

Multiple Sclerosis (MS) is an inflammatory demyelinating disease of the central nervous system (CNS), affecting an estimated 400,000 people in the U.S. and 2 million people worldwide.[2] It is the leading cause of non-traumatic neurological disability in young and middle-aged adults. Clinically, MS patients present with highly varied neurological symptoms that may include sensations of numbness, vision impairment, fatigue, failing coordination, and bladder dysfunction. Cognitive decline, including memory impairment, attention deficits, and reduced mental processing, is observed in 40%-65% of patients.[3–8] MS-related cognitive and physical disability frequently lead to unemployment, and thus MS is a major health concern with considerable economic consequences.[9]

Diagnosing Multiple Sclerosis

Diagnosis of MS is generally achieved by a combination of clinical assessments of cognitive[10] and physical impairment (measured commonly with the Expanded Disability Status Scale[11]) followed by magnetic resonance imaging (MRI) of the brain; years may elapse between initial symptoms and final diagnosis of MS. Patients who experience an initial acute attack followed by a period (often years) of remission before the next attack (relapse), and also present with MRI-visible lesions, are classified as having relapsing-remitting MS (RRMS). Approximately 50% of MS patients are diagnosed with RRMS after 2 years, 80% after 20 years. Over time, recovery from relapse is incomplete, and

persistent symptoms accumulate. The disease eventually becomes progressive in 65% of RRMS patients, indicating the transition from RRMS into secondary progressive MS (SPMS).[3] Primary progressive MS (PPMS), in which disease is progressive from onset with no periods of remission, is diagnosed in nearly 20% of MS patients.[3]

Inflammation, demyelination, blood brain barrier (BBB) compromise, and impaired microvascular function are common in multiple sclerosis (MS).[12,13] Other demyelinating diseases and syndromes such as acute disseminated encephalomyelitis (ADEM), and neuromyelitis optica (NMO) present with clinical symptoms that mimic MS, complicating differential diagnosis in these patients.[14,15] Clinically similar, each of these diseases has a unique pathogenesis, and misdiagnosis can lead to use of inappropriate therapies that may exacerbate symptoms and pathology The International Panel on Diagnosis of MS have created the McDonald Criteria describing important clinical and MRI features of MS.[16] Dissemination in time (DIT) and dissemination in space (DIS) are key characteristics of MS, demonstrated by new clinical presentation, new lesions on MRI, or both.[16] . Thus, MRI is an important diagnostic tool as it not only demonstrates lesion distribution and morphology, but also is sensitive to clinically silent lesions.[17,18] Descriptions of lesion characteristics, including morphology and spatial distribution, are included in diagnostic criteria for MS, ADEM, and NMO to assist differential diagnosis and expedite treatment.[16,19–21]

Acute white matter lesions in MS are identified using contrast-enhanced MRI.[22] The typical MR contrast agents are FDA approved low molecular weight

gadolinium (Gd) chelates (gadolinium based contrast agents, GBCA). The combination of contrast agent administration and time series acquisition of T_1-weighted MR images is known as dynamic contrast enhanced MRI. Active acute lesions with a compromised BBB appear bright on T_1-weighted (T_1-w) MRI images after GBCA injection, and are thus termed GBCA-enhancing lesions. Recent revisions to the McDonald Criteria emphasize that presence of GBCA-enhancing lesions coincident with non-enhancing lesions (assumed to be inactive chronic lesions) during a single MRI examination reliably demonstrates DIS and DIT, thus reducing time between onset and diagnosis.[16] In addition to DIS and DIT, MRI assessment of lesion distribution and morphology helps differentiate MS from NMO and ADEM,[21,23–29] and disease-specific characterization may provide additional insight into disease pathogenesis.[30]

Importance of the blood-brain-barrier and myelin

Blood Brain Barrier

The brain requires a precisely regulated microenvironment to maintain reliable neuronal signaling and to prevent neuronal damage. Nutrients, proteins, and waste products move through the body through the blood; a special barrier, the blood-brain-barrier (BBB), controls exchange between the blood and the brain, protecting the central nervous system from blood-borne pathogens and solutes. Tight junctions between endothelial cells of the capillary walls prevent paracellular diffusion, but are sensitive to factors produced within the CNS. The

tight junctions forming the BBB are unique from the rest of the body, as most endothelia readily allow paracellular diffusion.[31]

While a wide range of lipid-soluble molecules, such as barbiturates and ethanol, and small gaseous molecules including CO_2 and O_2, are capable of passively crossing the BBB, most transport is tightly regulated by specialized solute carriers, transport proteins, and endocytotic mechanisms. In the presence of inflammation, circulating monocytes, macrophages, and mononuclear leukocytes are recruited to the site of inflammation, penetrate the barrier, and respond to injury. Importantly, in the a state of pathological inflammation the tight junctions may break down, allowing additional inflammatory cells and other pathological substrates that may damage brain tissue and disrupt neuronal function.[32]

Endothelial cells in the BBB are supported externally by astrocytes, pericytes, and microglia.[33] Pericytes along the outside of the capillaries partially surround the endothelial cells and contribute to the basement membrane (basal lamina), which completely surround pericytes and capillaries, as illustrated in Figure 1. Perivascular astrocytic endfeet communicate directly with the basement membrane and pericytes, forming a communication link between the vasculature and neurons, and also play a key role in maintaining the structural integrity of the BBB[34,35]. Astrocytic signaling is involved in both tightening and opening the BBB, both of which occur naturally in the healthy brain. In a pathological state of inflammation, astrocytes will signal the BBB to open to allow more rapid passage of ions and cells. Chronic inflammation can lead to permanent BBB dysfunction

resulting in irreversible tissue damage including demyelination and axonopathy.[31,32]

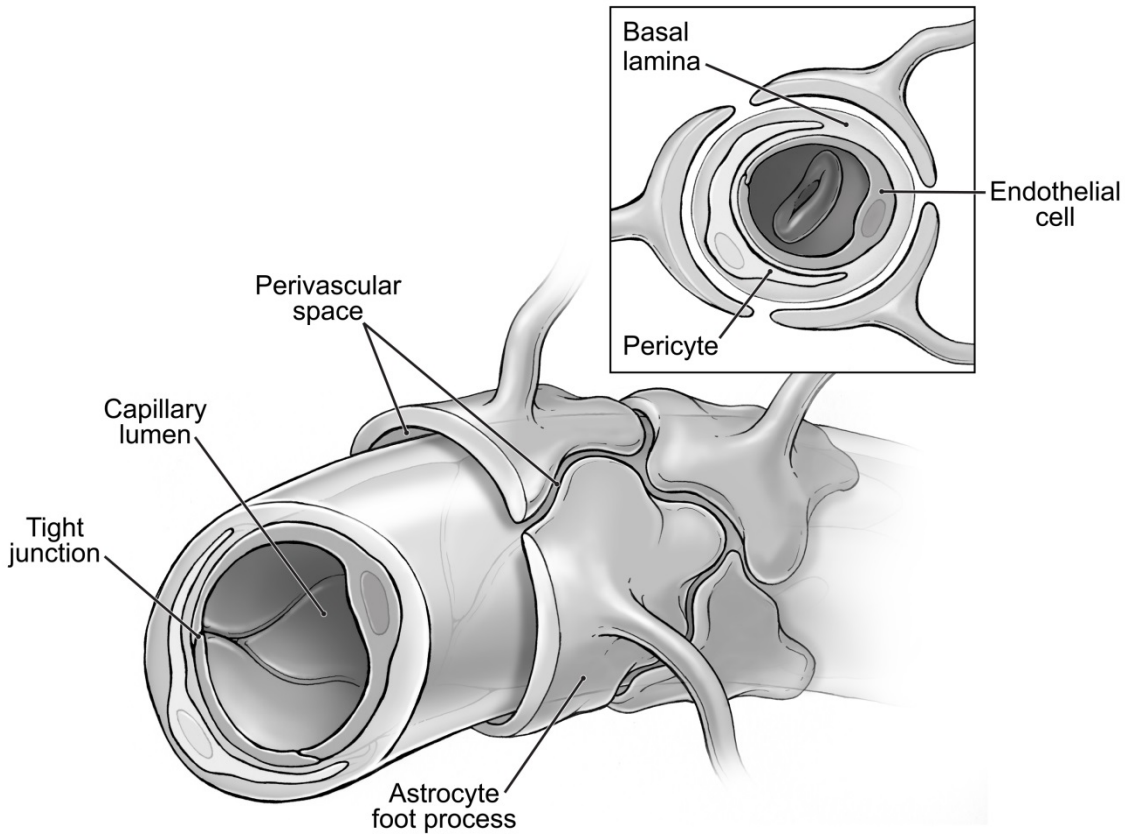

Figure 1. Structure of the Blood Brain Barrier. Pericytes and astrocytic endfeet tightly wrap around capillary walls forming an additional barrier beyond endothelial cell tight junctions. Reproduced with permission from V. Anderson and A. Rekito (Anderson, 2011[33])

Myelin

Neuronal projections (axons) are surrounded by a protective multi-layered cell membrane, the myelin sheath. CNS myelin is formed by oligodendrocytes, whereas Schwann cells are responsible for myelin in the peripheral nervous system. The myelin sheath provides trophic support to the neuron and enables

rapid signal transmission via saltatory conduction. Oligodendrocyte processes extend from the cell body and wrap around axons in the CNS creating a tight myelin sheath, as illustrated in Figure 2. The top panel shows processes from one oligodendrocyte providing myelin for multiple axons. An electron micrograph cross-section demonstrates many wraps creating a thick sheath around an axon. Ion channels are clustered in the nodes of Ranvier, small gaps between myelin segments that are essential for saltatory conduction. The number of processes extending from a single oligodendrocyte varies throughout the central nervous system, and the number of wraps, or lamellae, created around an axon is related to axonal diameter.[36] For example, the so-called white matter in the brain is heavily myelinated, denoted by a thick myelin sheath surrounding the majority of axons, whereas axons in the gray matter are less frequently myelinated.

During myelination the leading edge of the oligodendrocyte process wraps around the axon creating new layers by remaining in contact with the axon and sliding underneath the previously generated layers of myelin. The inner tongue is triangle-shaped, so lateral edges of each wrap are constantly in contact with the axon. The wraps extend laterally throughout the wrapping process, ultimately forming nodes of Ranvier. The layers of the myelin sheath are bound tightly together by intracellular myelin basic protein (MBP), which ensures uniform and reproducible spacing between layers. Compaction begins from the outer layers (closest to the oligodendrocyte cell body) and works its way inward toward the inner tongue. It is important that compaction proceed in an ordered and coordinated fashion to avoid creating uncompacted pockets; the protein 2’- 3’-

cyclic nucleotide-3'-phosphodiesterase (CNP), appears to be important in this process[37]. Maintaining compactness in myelin sheaths is essential for both myelin and neuronal function, and is also a marker of myelin health and quality.[38] The process of myelin sheath compaction is illustrated in the second panel of **Figure 2**.

Myelinated axons become dependent on their oligodendrocyte counterparts for maintenance of proper cytoskeletal arrangement, ion channel organization, and axonal transport. Disrupted ion channel organization leads to improper ion flux that impairs signal transduction and can lead to neurotoxicity and cell death. Oligodendrocytes are additionally critical in regulating slow and fast transport mechanisms within the axon. Dysfunction in axonal transport results in inefficient clearance of metabolic byproducts, slows nerve transmission, and can impair metabolic function.[34,35] Demyelinated axons typically have an increased demand for ATP to overcome inefficiencies in both transport and transmission, and to maintain proper ionic homeostasis. It is this increased metabolic demand that may make these axons more vulnerable to degeneration.[39,40]

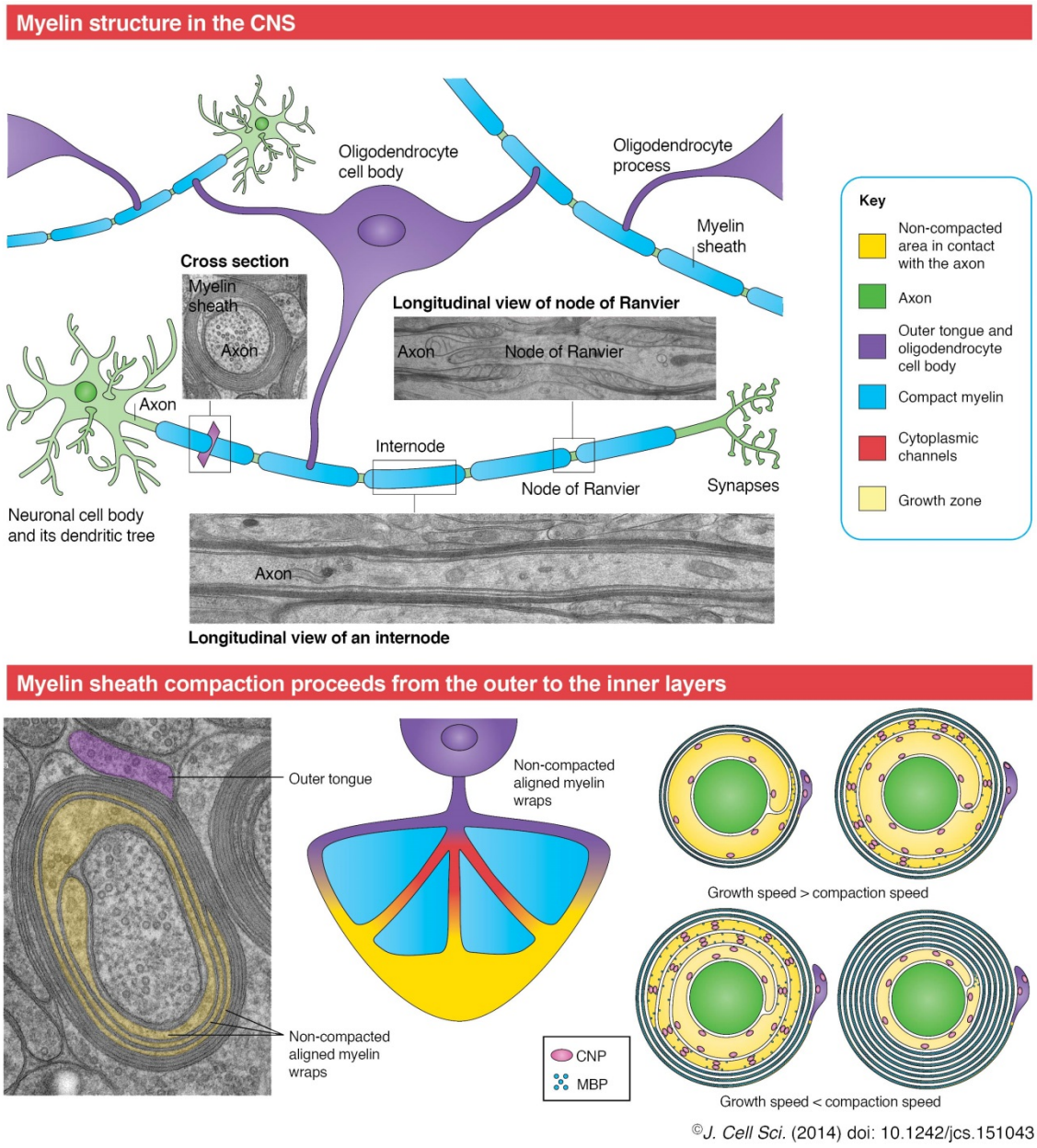

Figure 2. Myelin Structure in the CNS. Oligodendrocytes processes form myelin sheath segments on axons in the central nervous system; one oligodendrocyte will wrap segments on several axons as shown in the top panel. Nodes of Ranvier form between myelin segments where ion channels cluster to allow rapid signal transduction via salutatory conduction. The oligodendrocyte process forms a flat, triangle shaped sheet that wraps around the axon several times to create the multi-lamellar structure of the myelin sheath (bottom panel). Myelin layers are then bound tightly together in the process of compaction, which is a critical processes dependent on myelin proteins including MBP and CNP. Adapted from Snaidero, et al (2014),[35] with permission.

Remyelination after an acute injury or inflammatory event is possible in humans, but is variable and typically incomplete. Formation of a glial scar creates a physical and chemical barrier that reduces the ability of oligodendrocyte precursors and neural progenitor cells to respond to injury and differentiate into mature myelinating oligodendrocytes.[39] Remyelinated axons typically have thinner, less compact myelin sheaths than healthy tissue,[41] likely increasing their vulnerability to damage in the event of another inflammatory insult.[12] The central nervous system's capacity to repair diminishes both with age and disease duration. Progressive loss of oligodendrocytes and axons results in accumulation of disability.[42,43]

Pathology of Multiple Sclerosis

Focal demyelinated lesions, or plaques, on a background of inflammation within the CNS are the pathological hallmark of MS.[12] Lesions within the white matter exhibit varying degrees of inflammation depending on the age of the lesion and stage of disease. Demyelinating lesions also occur in the cortex, although they are believed to be less inflammatory than white matter lesions and are more difficult to identify on MRI.[6,44,45]

Acute active lesions in the white matter are heavily infiltrated by myelin-laded macrophages uniformly distributed across the lesion, forming the so-called "sea of macrophages." Proliferating astrocytes and cytotoxic T lymphocytes contribute to the pathology and inflammation in acute lesions. The extensive

inflammation in acute lesions leads to BBB damage that allows infiltration of additional imflammatory cells into the brain tissue. Oligodendroglial and axonal injury is variable in these lesions, leading to the suggestion from Lucchinetti and colleagues that pathological mechanisms of injury may vary between MS patients.[46] While areas of demyelination are frequently clearly demarcated, myelin damage can extend beyond the lesion border and affect normal-appearing white matter. Prolonged inflammation eventually leads to axonal injury, increasing with the number of lymphocytes and activated microglia present within a lesion.

As a lesion ages, the core of the lesion may become inactive and even remyelinate, forming a remyelinated shadow plaque with reduced myelin density and thin myelin sheaths,[12,47] while the border of the lesion remains inflamed and demyelination expands centrifugally with macrophage infiltration. Lesions demonstrating this combination of inactive core and active border are considered chronic active lesions.[12,47,48] The inactive core in these lesions has an intact BBB, while BBB permeability remains elevated in the active rim. Chronic inactive lesions are characterized by limited or no inflammation, complete demyelination, axonal damage, and formation of a glial scar. In the absence of inflammation, BBB remains intact and neurodegeneration decreases to sub-pathological levels.[12,49]

Early in disease, the CNS is capable of repairing damaged tissue and replacing lost myelin. Remyelination in lesions is incomplete, producing only a thin myelin sheath that remains highly vulnerable to future injury. Lesions with

inactive cores recruit oligodendrocyte precursor cells and attempt remyelination even if the border of the lesion remains actively demyelinating. Older remyelinated lesions that are not subsequently re-injured may eventually produce myelin sheaths nearly as thick as normal white matter. More frequently, remyelination of inactive lesions remains incomplete and shadow plaques form that are clearly distinct from normal white matter. Shadow plaques are most prevalent in progressive stages of MS (PPMS or SPMS) but are also seen in RRMS, consistent with ongoing remyelination attempts. However, remyelination gradually becomes less effective, concomitant with disease progression.[12,50]

It is clear that both the BBB and myelin are essential in maintaining brain health and are important areas of research in neurodegenerative disease. The molecular mechanisms of remyelination and its eventual failure are not entirely understood. It is critical that non- and/or minimally-invasive in-vivo biomarkers of pathological changes in the BBB and myelin, in both healthy and diseased brains, be developed to increase understanding and improve treatment of neurodegenerative conditions. This work will explore development, application, and validation of magnetic resonance imaging biomarkers of both myelin content and BBB permeability in vivo.

Magnetic Resonance Imaging in Multiple Sclerosis

Introduction to Magnetic Resonance Imaging

Magnetic resonance imaging plays an important role in diagnosis, monitoring, and the study of MS. MRI is unique from other imaging modalities in that the signal is derived from magnetic properties of hydrogen atom nuclei, or protons, which are abundant in the body in water, lipids, and proteins. A variety of advanced imaging techniques have been proposed to evaluate tissue properties including water content (e.g., increased interstitial water as in edema), myelin content (to assess demyelination and remyelination), vascular permeability (BBB breakdown in the case of neuroinflammatory diseases), and vascular density, all based on the unique signals produced by protons in various chemical environments within the body.

Fundamental MRI Contrast Mechanisms

MRI contrast mechanisms that are exploited to create standard clinical MR images are proton density (PD), and longitudinal (T_1) and transverse (T_2) relaxation time constants of protons in a magnetic field. While it is possible to create MR images using a variety of nuclei, hydrogen is the most abundant atom in the body (mostly in water molecules) and thus produces the strongest magnetic resonance signal. Modern MRI instruments are composed of a superconducting electromagnet, magnetic field strength measured in Tesla (T), and radiofrequency (RF) coils that are used to transmit and receive signals that ultimately create the MR image. Hydrogen nuclei (protons) have a net magnetic

moment that will align either with (parallel, along the z-axis) or against (anti-parallel) a strong external magnetic field as in an MRI instrument. However, the magnetic moments do not align exactly with the external magnetic field ($\boldsymbol{B_0}$) and instead will precess around the direction of $\boldsymbol{B_0}$ at the Larmor, or resonant, frequency. The Larmor frequency is determined by a physical property known as the gyromagnetic ratio, γ, and the magnetic field strength, $\boldsymbol{B_0}$:

$$\omega = \gamma \cdot \boldsymbol{B}_0, \quad (1)$$

where γ is measured in 10^6 rad s^{-1} T^{-1}, or

$$f = \left(\frac{\gamma}{2\pi}\right) \cdot \boldsymbol{B}_0, \quad (2)$$

where γ / 2π is measured in MHz T^{-1}.

For example, the Larmor frequency of protons in a 7T instrument is approximately 300 MHz (= 42.576 (MHz T^{-1}) * 7 (T)). Protons aligned parallel to $\boldsymbol{B_0}$ are in a low energy and stable state, whereas those aligned anti-parallel are in a higher energy and thus less stable state. The lower energy (parallel) state is slightly favored, so slightly more protons are aligned parallel to the field than anti-parallel, creating a small net magnetization vector, M_0, in the direction of $\boldsymbol{B_0}$. The magnitude of M_0 is determined by the number of protons in the sample, and the difference in number of protons aligned parallel versus antiparallel, which increases with magnetic field. Subsequently, the maximum available MR signal (S_0) in a tissue is proportional to M_0. However, the net magnetization vector

provides a small signal compared to $\boldsymbol{B_0}$ and is undetectable while at equilibrium and aligned with $\boldsymbol{B_0}$.

RF pulses applied at the Larmor frequency are capable of manipulating the net magnetization vector by inducing a secondary magnetic field, $\boldsymbol{B_1}$, typically orthogonal to the direction of $\boldsymbol{B_0}$, which then rotates M_0 into an orthogonal orientation compared to $\boldsymbol{B_0}$, known as the transverse plane. As soon as the RF pulses are turned off the net magnetization vector will begin to precess around the direction of $\boldsymbol{B_0}$ at the Larmor frequency, inducing a voltage in the nearby receiver RF coil aligned perpendicular to $\boldsymbol{B_0}$. The signal detected in the receive coil varies with time and oscillates at the Larmor frequency. Eventually the net magnetization vector will relax, or slowly realign with $\boldsymbol{B_0}$. The time constant required for the magnetization to realign with $\boldsymbol{B_0}$ and reach thermal equilibrium is called T_1 (measured in s), or the longitudinal relaxation time constant:

$$M_z(t) = M_0 - [M_0 - M_z(0)]e^{\left(\frac{-t}{T_1}\right)}, \qquad (3)$$

where $M_z(t)$ is the magnitude of the net magnetization vector along the z-axis at time t after excitation ($M_z(0) = M_0$). The inverse of T_1, or R_1 (measured in s^{-1}), is the longitudinal relaxation rate constant.

When the magnetization vector is initially tipped into the transverse plane, all of the protons are rotating around $\boldsymbol{B_0}$ at the same speed and in the same alignment: they are in phase. As the protons precess they experience small magnetic fields of their own that cause neighboring protons to temporarily precess at slightly higher or lower rates. The protons then precess at the Larmor

frequency, but are now out of phase. Dephasing of proton spins reduces the net magnetization vector in the transverse plane ($M_{x,y}$), causing the signal to decay due to incoherent summation, which is one type of transverse relaxation called T_2*. The amount of time it takes for the transverse signal to decay is called T_2, or the transverse relaxation time constant:

$$M_{x,y}(t) = M_0 e^{\left(\frac{-t}{T_2}\right)}, \quad (4)$$

It is important to note that T_2 relaxation of tissue ^1H_2O typically occurs faster than T_1 relaxation, and unlike T_1 relaxation, T_2 does not vary greatly with magnetic field strength.[51]

As mentioned previously, the density of protons in a tissue will determine the total available signal, S_0. In a PD-weighted image, bone and tendon will appear darker than fatty tissue, which are darker than fluids due to differences in tissue water content.[51] Image contrast in T_1-weighted (T_1-w) and T_2-weighted (T_2-w) images are similarly influenced by PD, and more importantly by tissue-specific properties that modify T_1 and T_2 relaxation time constants. The key property to consider here is known as the correlation time constant of a molecule, τ_c. The correlation time relates to how rapidly a molecule tumbles or rotates, translates, and vibrates, which is dependent on temperature, molecular size, and chemical environment. Water protons in free liquids such as cerebral spinal fluid (CSF) or blood have small τ_c ($\approx 3 \times 10^{-12}$ s) and are considered “mobile” protons. Protons in macromolecules and proteins have larger τ_c ($\approx 1 \times 10^{-8}$ s) and are considered “bound” or “restricted” protons.[52] T_2 relaxation is dependent on dipole-dipole interactions between molecules that create local field inhomogeneity that

subsequently dephase proton rotation resulting in transverse signal decay. The magnitude of effect created by local field inhomogeneities is directly related to correlation time constants.[51,52] Free protons with small time constants tumble very rapidly and, due to motional averaging, experience a relatively homogeneous local field and minimal dephasing, resulting in a large T_2. On the opposite end, restricted protons have large correlation time constants and tumble slowly, thus the local field inhomogeneities are not as subject to motional averaging and rotational dephasing occurs quickly, which produces a very small T_2. In fact, T_2 is so small for these protons that they are not MRI-visible using standard imaging techniques.[51–54]

Clinical Standards: T_1, T_2, and Contrast-Enhanced MRI

Fluids and tissues with large T_2 (e.g. CSF) will appear bright on T_2-weighted images, while tissues with smaller T_2 appear dark. Accordingly, MRI sequences are sensitive to changes in tissue water content (e.g., edema) and are commonly used in neuroimaging, particularly in diagnosing MS. Inflammatory demyelinating lesions typical of MS demonstrate bright, or hyperintense, signal on T_2-weighted MRI due to increased water content in inflamed tissue. These scans are highly sensitive, but lack specificity. Idiopathic white matter signal hyperintensities (WMSHs) are commonly found in healthy adults, and incidence increases with age. Thus, T_2 WMSHs can be indicative of a number of pathologies that induce edema, or may be of little clinical significance. Image contrast in T_1-weighted images is entirely different: fluids and tissues with long ^{1}H

T_1 will appear dark, while tissues with short ^1H T_1 give a stronger signal and appear bright. Heavily myelinated white matter has a short ^1H T_1, thus appears bright on T_1-w images. In MS lesions, demyelination, edema, and axonal loss simultaneously reduce macromolecular content and increase free water content, both of which lead to a longer ^1H T_1 and decreased signal intensity on T_1-w MRI. Examples of T_1-w, T_2-w, and PD-w images in an MS subject are shown in **Figure 3**. Note the bright WMSHs on the T_2-w image correspond to the hypointense signal on the T_1-w image.

The use of intravenously-delivered low molecular weight paramagnetic gadolinium based contrast agents (GBCA, e.g. gadoteridol molecular weight ~560 Da) in combination with serial T_1-w imaging, called contrast-enhanced MRI, is used clinically to identify acute, active white matter lesions with a leaky blood-brain-barrier (BBB). GBCAs bind transiently to water molecules, effectively shortening both T_1 and T_2 relaxation time constants of protons within the immediate vicinity of the contrast molecule. In healthy brain tissue, the BBB limits hydrophilic molecules from entering the brain, so extravasation of GBCAs is slow

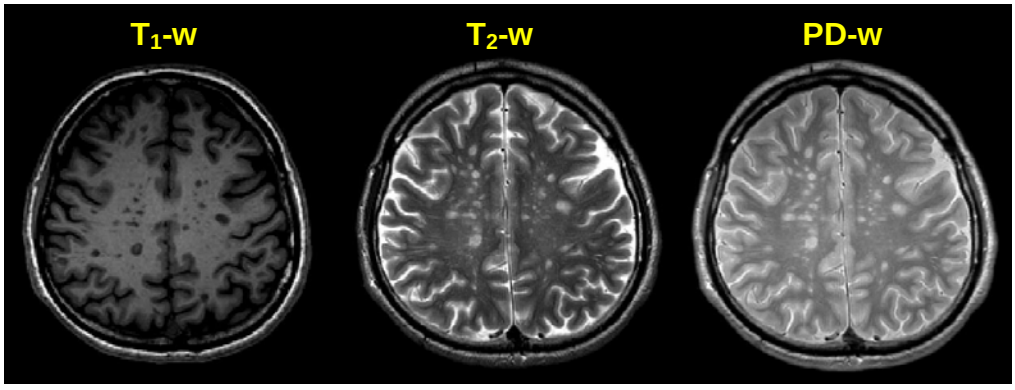

Figure 3. Image Contrasts in MRI. White matter lesions in MS appear dark (hypointense) on T_1-w images. The same lesions will appear bright (hyperintense) on both T_2-w and PD-w images. Images are from a 30 y/o male with RRMS.

and extremely limited.[55] In a state of pathological inflammation the BBB is compromised and GBCA leaks out of the vasculature and into the extravascular space where it accumulates and creates T_1-w hyperintensities shortly after administration.[18,56] Contrast-enhanced MRI may be used as a purely qualitative technique in which two T_1-w images are collected, one pre-contrast and one ~10 minutes post-contrast, and the differences in signal intensity are observed. T_1-w hypointensities that do not enhance after GBCA-administration are thought to be chronic, persistent lesions characterized pathologically by demyelination, axonal loss, and an intact BBB. T_1 lesions that are contrast-enhancing are in an acute, inflammatory stage, typically indicating formation of a new lesion, or continued activity in a persistent, smoldering lesion.[57,58]

However, as discussed previously, lesion pathology is highly heterogeneous both within and across MS patients and these qualitative measurements do not adequately address underlying pathology and disease mechanisms. Quantitative and semi-quantitative imaging techniques provide imaging biomarkers of disease with high pathological specificity, enabling more complete and non-invasive means of studying disease in-vivo. Two primary imaging biomarkers are investigated in this work: magnetization transfer ratio (MTR), a semi-quantitative measurement of macromolecular proton fraction, which is thought to be sensitive to demyelination, and K^{trans}, a measure of GBCA extravasation obtained via quantitative contrast-enhanced MRI.

Magnetization Transfer (MT) Imaging

Magnetization transfer imaging (MTI) produces a unique tissue contrast by taking advantage of the chemical exchange and ^{1}H T_1 relaxation coupling observed between normally MRI-invisible protons of macromolecules and macromolecule-interacting water, and the MRI-visible free water protons in tissue and fluid. Protons in environments with long effective correlation time constants and extremely short transverse relaxation time constants (T_2 < 0.1 ms, 'restricted pool') have broad spectral lines, while protons with small correlation times have relatively large T_2 (> 10 ms, 'free pool') and narrow spectral lines; both pools have approximately the same resonant frequency, as shown in **Figure 4**. A saturation pulse applied sufficiently far off-resonance will selectively saturate (reduce net magnetization to zero) the restricted pool, while having no effect on the free pool. Saturated magnetization from the restricted pool transfers to the free pool causing reduced free pool MR signal. Wolff and Balaban[59] accidentally discovered this imaging contrast and first demonstrated its use in 1989. In the more than 25 years since their initial observation, MTI has gained attention for its ability to indirectly quantify the fraction of protons within a sample that are bound to and/or interacting with macromolecules. This measurement has been applied as a surrogate imaging biomarker for myelin content in-vivo in patients with MS.[60–65]

The so-called free pool includes mobile protons in free bulk water and some lipids with short correlation times and transverse relaxation times sufficiently long (T_2 > 10ms) to be MRI-visible with conventional imaging

methods. The restricted pool is composed of protons associated with macromolecules, proteins, and cell membranes with long correlation times and extremely short T_2 (< 1ms). Equilibrium chemical exchange between the so-called hydration layer, water molecules bound to the macromolecular surface, is thought to be sufficiently fast to treat the hydration layer as part of the bulk free pool. Dipole-dipole interactions transfer magnetization between macromolecular protons and hydration layer protons, which then diffuse into the bulk water.[52,66]

Magnetization transfer ratio (MTR), a semi-quantitative biomarker, is trivial to calculate from only two images: M_{sat}, acquired with the off-resonance

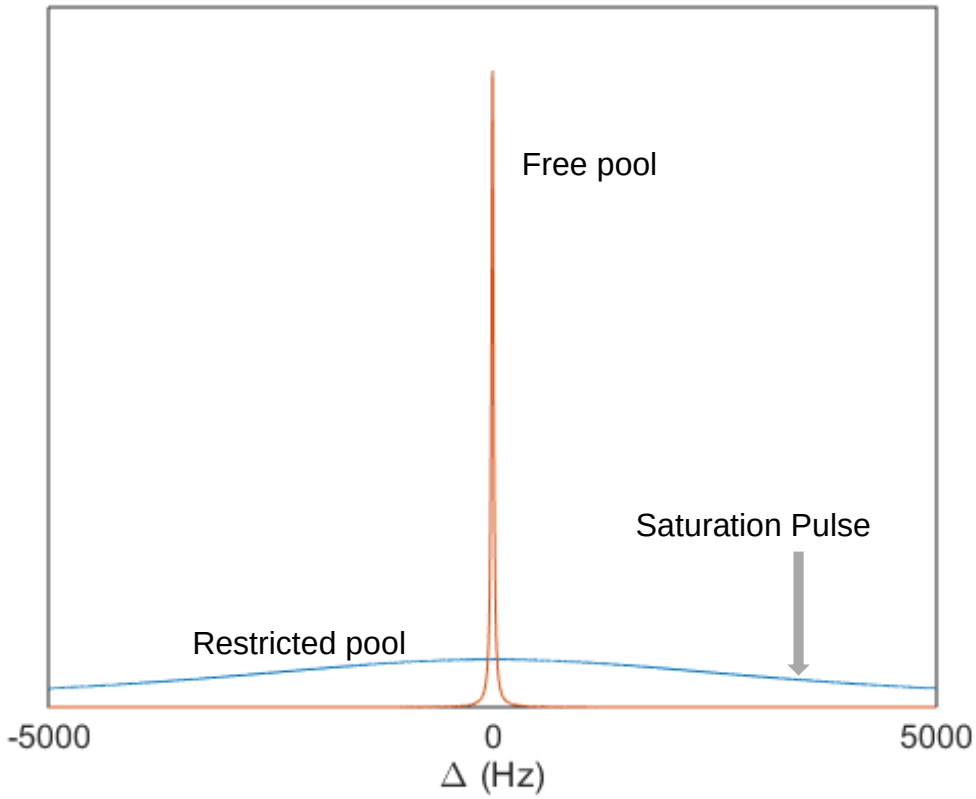

Figure 4. Simulated Spectral Linewidths. Protons in the free pool have a narrow peak (red line) at the Larmor frequency. Due to extremely short T_2, the restricted pool has a broad line (blue line) that is sensitive to off-resonance RF pulses.

saturation RF pulse applied; and M_0, the steady state image collected with identical imaging parameters except with the saturation pulse either disabled or so far off resonance (e.g., 100 kHz) as to have essentially no effect. MTR is calculated as follows:

$$MTR = \frac{M_0 - M_{sat}}{M_0}, \quad (5)$$

where M_{sat} is the net magnetization after a saturation pulse has been applied. MTR values are highly sensitive to $\boldsymbol{B_0}$ and image acquisition parameters, specifically the amplitude and offset of the off-resonance pulse. Saturation pulses applied too close to the Larmor frequency will necessarily introduce some direct saturation on the free pool, which will artificially increase the observed MT effect. Conversely, saturation pulses too far off resonance will produce little or no appreciable MT effect. Agar gel phantoms are routinely used to optimize MT experiments for a variety of tissue types, with increasing agar concentrations representing higher macromolecular content.[54,67,68]

A phantom containing pure saline (1% phosphate buffered saline) in one compartment and 4% agar by weight in another was constructed to characterize the MT response of a custom built surface receive RF coil on our 11.75 T horizontal bore instrument (Bruker Biospin, Billerica MA) equipped with a high-performance gradient coil (9 cm inner diameter). Magnetization transfer images were acquired using 3D gradient-recalled echo (GRE) sequences with 2.5ms echo time (TE), 30 ms recycle time (TR), 10° FA, and a pulsed MT saturation pulse of Gaussian shape, 20ms duration, 0.01ms interpulse delay, 137 Hz bandwidth, field of view (FOV) 1.44 cm x 1.92 cm x 0.96 cm, matrix size 144 x

192 x 96. In an effort to remain reasonably consistent with other work in humans[64,68,69] and mice.[70–75] I collected MT images at two $\boldsymbol{B_1}$ field strengths: 4.7 and 7.8 μT (corresponding to effective flip angles of 600° and 1000°, respectively). Twelve off-resonance frequencies were evaluated between +100 Hz and +100 kHz, for $\boldsymbol{B_1}$ = 7.8 μT, and eight off-resonance frequencies between +1.5 kHz and +100 kHz for $\boldsymbol{B_1}$ = 4.7 μT. The images collected with a 100 kHz off-resonance saturation pulse were used as M_0. Representative cross-sectional MR images of the phantom acquired with 7.8 μT $\boldsymbol{B_1}$ and saturation pulse offsets of +3 kHz and +100 kHz are shown along with the resulting MTR image in **Figure 6**. Regions of interest (ROIs) were placed in the saline and agar; normalized ROI average net magnetization values ($M_z = M_{sat}/M_0$) are plotted in **Figure 5**. Solid lines are added to guide the eye.

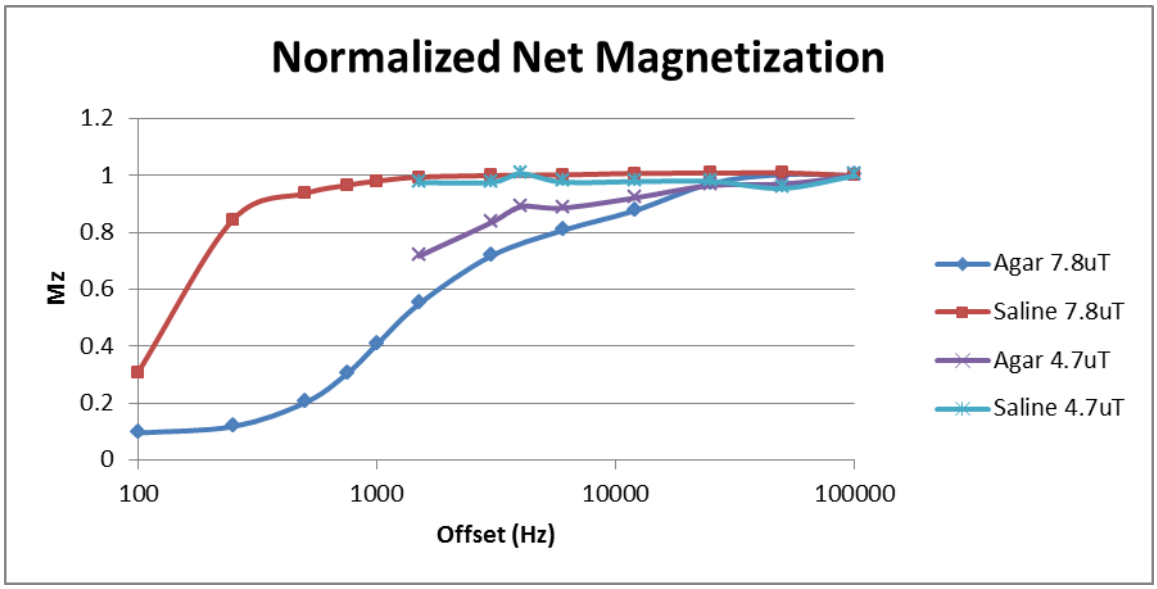

Figure 5. ROI average net magnetization. Data points indicate actual collected data; solid lines are drawn to guide the eye. Direct saturation is evident by decrease in saline M_z; offset frequencies greater than 1 kHz show no direct saturation (M_z = 1). MT effect is observed at 12 kHz offset with both $\boldsymbol{B_1}$ amplitudes; however, higher $\boldsymbol{B_1}$ amplitude increases the MT effect.

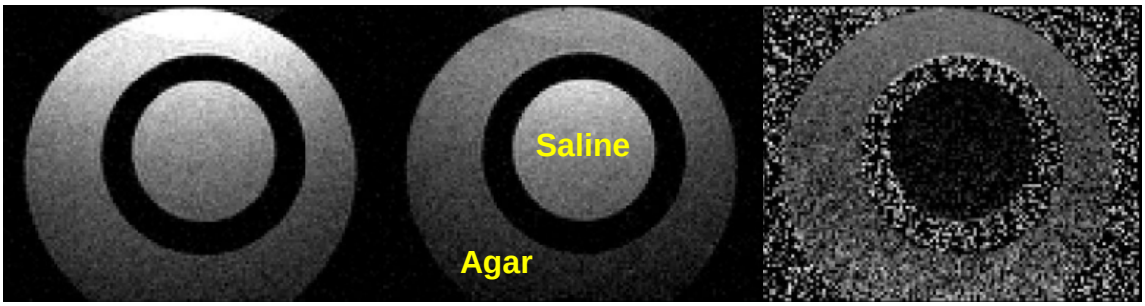

Figure 6. MT characterization at 11.75T in saline and agar phantom. MT images acquired with 7.8 μT B_1, and saturation pulses 100kHz (left) and 3kHz (middle) off-resonance. Calculated MTR image is shown on the right. Saline in the inner compartment appears identical between the two scans, and shows essentially zero MTR, except for noise. MRI signal in 4% agar in the outside compartment is appreciably darker with the 3 kHz off-resonance pulse applied compared to M_0 (100 kHz offset). Note that signal-to-noise ratio drops off with distance from the surface coil (positioned above the phantom).

Dynamic-Contrast-Enhanced MRI (DCE-MRI)

The advent of DCE-MRI provided a unique method of quantitatively characterizing tissue vascular properties *in-vivo*. Serial MR images are acquired before, during and after a bolus injection of contrast reagent (CR) to monitor the pharmacokinetics of the contrast reagent passage through tissues. Pharmacokinetic modeling of DCE-MRI data allows quantification of vascular properties (*PK parameters*) including blood volume, BBB permeability and transendothelial and transcytolemmal water exchange kinetics. These surrogate biomarkers are sensitive to disease state.[76] This work will focus on the CR transendothelial transfer constant, K^{trans}, which is a biomarker for CR extravasation (and thus a surrogate marker for BBB permeability). Early pharmacokinetic models[77] are commonly used in the study of MS; however, the early models inadvertently included a systematic error that ignored the indirect nature of CR detection and the differential distribution of CR and water (the MR

signal molecule), implicitly assuming that trans-compartmental water exchange kinetics in tissue occur effectively infinitely fast. Our group has derived a pharmacokinetic model, the Shutter-Speed Model (SSM),[78,79] that accounts for finite water exchange rate constants. The efficacy of our model has been shown in the study of many disorders including MS (white matter),[80–82] and breast[83,84] and prostate cancer.[85]

Quantitative R_1 ($\equiv 1/T_1$) maps can be calculated based on an inversion recovery experiment employing multiple magnetic prepared rapid acquisition gradient echo (MPRAGE) sequences with variable inversion times (TI). R_1 maps are then calculated by fitting the multi-TI signal intensity (S, where $S \propto M_0$) to a potentially multi-exponential inversion recovery equation:

$$S = k\rho \left(1 - 2e^{(-TI \cdot R_1)} + e^{(-TR \cdot R_1)}\right), \qquad (6)$$

where k is a proportionality constant and ρ is the proton density.

Contrast extravasation in the normal, healthy brain is nearly negligible at all time points after GBCA injection, certainly within the first few minutes of administration. However, extravasation is appreciable even at early time points (within 10 minutes post-injection) in pathologic brain tissue where the BBB is compromised. A schematic diagram of a capillary illustrating contrast extravasation is shown in **Figure 7**. Concentration of contrast reagent in the blood plasma is denoted by $[CR_p]$; concentration of contrast reagent in the interstitium is labeled $[CR_o]$, for CR outside. In homogeneous solution, R_1 has a linear dependence on [CR]:

$$R_1 = r_1 \cdot [CR] + R_{10}, \qquad (7)$$

where R_{10} is the pre-CR rate constant, and r_1 is the CR relaxivity. However, CR in blood is restricted to the plasma, so the equation is modified to account for the hematocrit (h):

$$R_{1b} = r_{1p} \cdot p_p \cdot [CR_p] + R_{1b0}, \quad (8)$$

where R_{1b} is the relaxation rate constant of blood, r_{1p} is relaxivity of CR in plasma, and p_p (= 1-h) is the mole fraction of extracellular blood water (i.e., plasma water). When CR extravastates from blood into interstitium the tissue relaxation rate constant (R_{1t}) calculation requires modification of Equation (7) to include a term that accounts for the fractional population of extracellular tissue water (p_o) available to interact with CR:

$$R_{1t} = r_{1o} \cdot p_o \cdot [CR_o] + R_{1t0}, \quad (9)$$

Equation (9) assumes that the extravascular space, including interstitial and cellular spaces, can be represented as a homogeneously mixed compartment, requiring that equilibrium water exchange between intra- and extracellular space is effectively infinitely fast, and ignores the intravascular space. This is physically impossible in tissue, and the intracellular or intravascular water molecule lifetime (τ_i or τ_b, respectively) can be calculated using the Shutter-speed model, which accounts for transcytolemmal and transendothelial water exchange:[78,86,87]

$$R_{1t}(t) = \frac{1}{2}\Big[\{R_{1exv} + R_{1b}(t) + \tau_b^{-1} + p_b/[\tau_b(1-p_b)]\} - \Big(\{R_{1exv} - R_{1b}(t) - \tau_b^{-1} + p_b/[\tau_b(1-p_b)]\}^2 + 4p_b/\tau_b(1-p_b)\Big)^{1/2}\Big] \quad (10)$$

where p_b is the mole fraction of tissue water in blood (=1 – p_{exv}), and R_{1exv} is the intrinsic, extravascular R_1.

Equations (7-9) reflect a constant concentration of CR; however, in DCE-MRI studies [CR_o] is a time-varying function dependent on [CR_p] and transendothelial CR extravasation, expressed by the Kety-Schmidt pharmacokinetic rate law:

$$[CR_o](T) = K^{trans} v_e^{-1} \int_0^T [CR_p](t) e^{-K^{trans} v_e^{-1}(T-t)} dt, \qquad (11)$$

where K^{trans} is the plasma volume fraction CR rate constant product, and v_e is the interstitial volume fraction (= $p_o f_w$, where f_w is the volume fraction accessible to mobile aqueous solutes).

Values for R_{1t} and R_{1b} are obtained from R_1 maps, which can then be used to estimate [CR_p] with Equation (8), and [CR_o] using modified Bloch equations as described elsewhere.[78,83,88] Estimates of extracellular, extravascular space (v_e) and CR extravasation (K^{trans}) can then be obtained by fitting Equation (11), where K^{trans} and v_e are the optimization parameters.

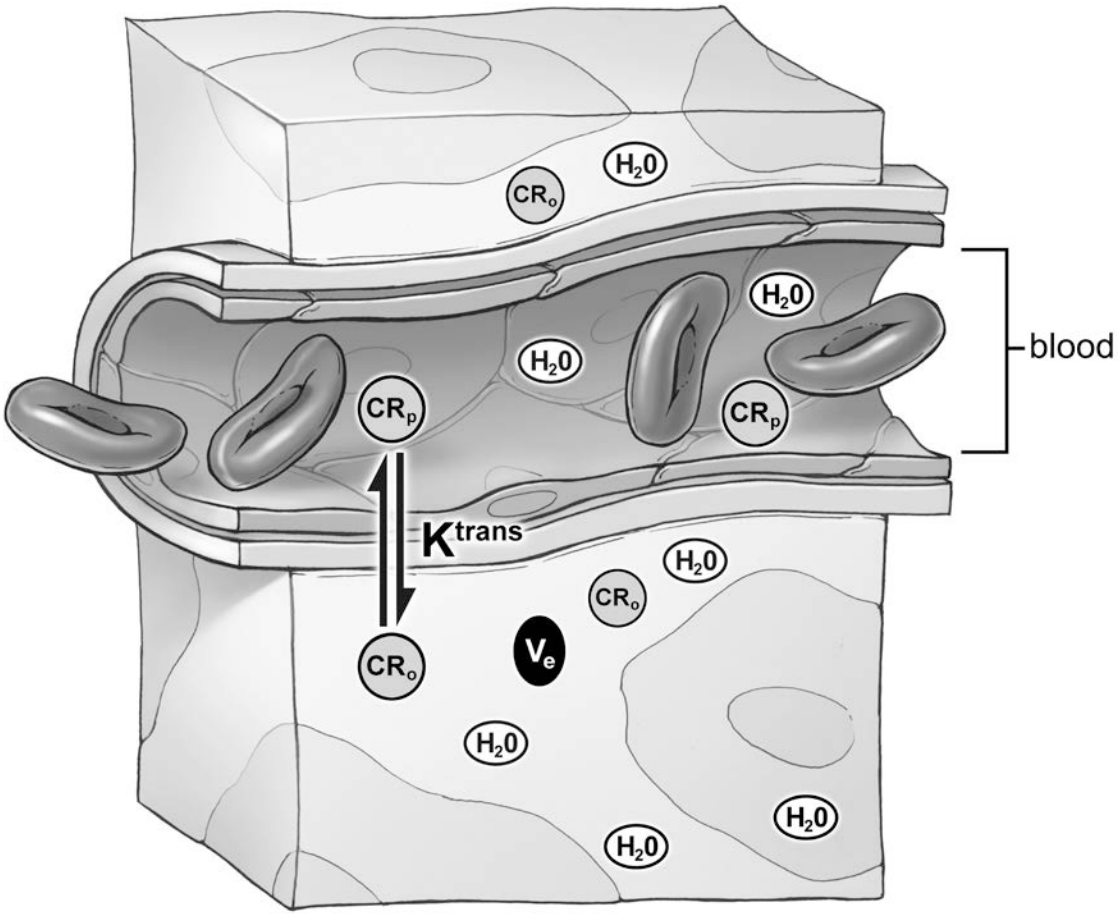

Figure 7. Schematic of CR extravasation. Contrast reagent administered intravenously extravasates from the blood into the extravascular space via tight junctions where it remains in the interstituium and does not enter the intracellular space. Modified from Anderson, 2011,[33] and reproduced with permission from V. Anderson and A. Rekito.

Animal Models of Multiple Sclerosis

A wide variety of animal models have been developed to study human diseases, providing access to crucial controlled studies of disease mechanism, pathology, and potential therapies that would otherwise be difficult or impossible to achieve clinically. Particularly important are studies aimed at validating potential imaging biomarkers that promise non-invasive methods of assessing disease state and pathology, and evaluating treatment strategies in-vivo; these have been thoroughly reviewed.[89,90] Post-mortem tissue dissected from euthanized animals can be analyzed using gold-standard histopathological and immunohistochemical techniques and retrospectively correlated with biomarkers obtained from imaging studies performed in-vivo. However, each model recapitulates only a subset of pathologic or clinical characteristics of MS, so care must be taken when designing and interpreting studies.

Perhaps the most widely used model of MS in animals is experimental autoimmune encephalomyelitis (EAE), which has been demonstrated across several species including rodents and non-human primates.[89–92] EAE provides a model of chronic inflammation and can be designed to exhibit monophasic, relapsing-remitting, chronic-progressive, and chronic relapsing disease courses. Homogenized CNS components or purified myelin proteins injected into the CNS induce an autoimmune response that targets myelin. Key common features between MS and EAE include demyelination, inflammation, axonopathy, and the variable development of numerous lesions disseminated in space and time.

Another model induces focal demyelinating lesions by injecting lysolecithin (lysophosphatidylcholine), an activator of phospholipase A2, into the area of interest in the CNS. Magnetization transfer imaging has been used to study demyelination and remyelination in rat and non-human primate lysolecithin models. An ongoing study at OHSU is using lysolecithin in mice to explore thyroid hormone (T3) treatment as a potential therapy to reduce demyelination and increase remyelination. MRI studies using T_2-w images and MTR readily visualize lesions created in the corpus callosum (CC) via lysolecithin injection. Preliminary analyses suggest that lesion volume estimates from MT imaging correlate well with those obtained by histology, which will provide an important in-vivo method of tracking lesion volume throughout treatment in this model. A potential benefit of the lysolecithin model is that each animal theoretically serves as its own control assuming that damage is completely localized to the lesion area. However, this model is extremely sensitive to needle placement during injection: injections penetrating the lateral ventricles have been seen to cause widespread edema and pathology throughout the entire corpus callosum (unpublished data).

The cuprizone model of MS demonstrates demyelination and spontaneous remyelination, the extents of which are variable across tissue types and depend on species, dose, sex, and age.[93–98] Cuprizone is a copper chelator that induces CNS demyelination when administered via chow, with spontaneous remyelination occurring upon removal of cuprizone from the diet. Acute, reversible demyelination is achieved in adult mice after 4-5 weeks of treatment, while a

chronic, permanent condition is induced after 12-13 weeks of continuous treatment. Axonopathy and inflammation are limited during acute demyelination in this model, but become appreciable in the chronic state. Disruption of the blood-brain-barrier is not observed in the cuprizone model. Demyelination in mice is most significant in the corpus callosum, though evidence of myelin loss has been observed throughout the brain. Interestingly, spinal cord white matter is preserved in this model despite systemic administration. The next chapter will explore the use of magnetization transfer imaging in studying demyelination and remyelination in this model and will provide new insight into the spatio-temporal pattern of cuprizone-induced demyelination in adult C57BL/6 mice.

All of the current animal models of MS provide valuable insight into disease pathological mechanisms, validation of non-invasive biomarkers, and potential therapeutic targets. However, none of these models capture the truly spontaneous nature of the disease as observed in humans. Japanese Macaque encephalomyelitis (JME) is a spontaneous inflammatory demyelinating disease affecting Japanese macaques (JMs) at the Oregon National Primate Research Center that demonstrates pathological, clinical, and imaging characteristics remarkably similar to MS.[99–101] Work presented in this thesis will endeavor to define imaging characteristics typical of JME including T_2 and contrast-enhancing lesion distribution, BBB permeability measured by quantitative DCE-MRI, and lesion evolution in individuals. Careful consideration of imaging features typical of JME will contribute to the ongoing description of this novel disease as well as its development as a potential model of human demyelinating disease.

Spatio-Temporal Patterns of Demyelination and Remyelination in the Cuprizone Mouse Model

Ian Tagge,[1,2]* Audrey O'Connor,[1] Priya Chaudhary,[3] Jim Pollaro,[1] Yosef Berlow,[1] Megan Chalupsky,[4] Dennis Bourdette,[3,5] Randy Woltjer,[4] Mac Johnson,[6] William Rooney[1,2,3]*

[1]Advanced Imaging Research Center, Oregon Health & Science University, 3181 SW Sam Jackson Park Rd, Portland, OR 97239, United States of America

[2]Biomedical Engineering, Oregon Health & Science University, 3181 SW Sam Jackson Park Rd, Portland, OR 97239, United States of America

[3]Neurology; Oregon Health & Science University, 3181 SW Sam Jackson Park Rd, Portland, OR 97239, United States of America

[4]Pathology; Oregon Health & Science University, 3181 SW Sam Jackson Park Rd, Portland, OR 97239, United States of America

[5]Portland VA Medical Center, 3710 SW US Veterans Hospital Rd, Portland, OR 97239, United States of America

[6]Vertex Pharmaceuticals Incorporated, 50 Northern Ave, Boston, MA 02210, United States of America

* Corresponding Authors
E-mail: taggei@ohsu.edu, rooneyw@ohsu.edu

Acknowledgements.
Evan Calkins, Danielle Galipeau, and David Clark provided excellent technical support in histological processing. We would like to express our thanks to the Advanced Light Microscopy Core (P30 NS061800) Facility at the Oregon Health & Science University. Immunohistochemical studies were performed in the laboratory of the Oregon Brain Bank and the Oregon Alzheimer's Disease Center (supported by NIA P30 AG008017).

A version of this chapter was published in PLoS ONE on April 7, 2016:
PLoS ONE 11(4): e0152480. doi: 10.1371/journal.pone.0152480

Abstract

Cuprizone administration in mice provides a reproducible model of demyelination and spontaneous remyelination, and has been useful in understanding important aspects of human disease, including multiple sclerosis. In this study, we apply high spatial resolution quantitative MRI techniques to establish the spatio-temporal patterns of acute demyelination in C57BL/6 mice after 6 weeks of cuprizone administration, and subsequent remyelination after 6 weeks of post-cuprizone recovery. MRI measurements were complemented with Black Gold II stain for myelin and immunohistochemical stains for associated tissue changes. Gene expression was evaluated using the Allen Gene Expression Atlas.

Twenty-five C57BL/6 male mice were split into control and cuprizone groups; MRI data were obtained at baseline, after 6 weeks of cuprizone, and 6 weeks post-cuprizone. High-resolution (100μm isotropic) whole-brain coverage magnetization transfer ratio (MTR) parametric maps demonstrated concurrent caudal-to-rostral and medial-to-lateral gradients of MTR decrease within corpus callosum (CC) that correlated well with demyelination assessed histologically. Our results show that demyelination was not limited to the midsagittal line of the corpus callosum, and also that opposing gradients of demyelination occur in the lateral and medial CC. T2-weighted MRI gray/white matter contrast was strong at baseline, weak after 6 weeks of cuprizone treatment, and returned to a limited extent after recovery. MTR decreases during demyelination were observed throughout the brain, most clearly in callosal white matter.

Myelin damage and repair appear to be influenced by proximity to oligodendrocyte progenitor cell populations and exhibit an inverse correlation with myelin basic protein gene expression. These findings suggest that susceptibility to injury and ability to repair vary across the brain, and whole-brain analysis is necessary to accurately characterize this model. Whole-brain parametric mapping across time is essential for gaining a real understanding of disease processes in-vivo. MTR increases in healthy mice throughout adolescence and adulthood were observed, illustrating the need for appropriate age-matched controls. Elucidating the unique and site-specific demyelination in the cuprizone model may offer new insights into in mechanisms of both damage and repair in human demyelinating diseases.

Introduction

Cuprizone [bis-cyclohexanone-oxaldihydrazone] is a low molecular weight copper chelator that induces reversible demyelination in both gray and white matter in the murine brain when added to chow in low concentrations for short periods. First described as a neurotoxin in rodents in the 1960's, cuprizone reliably produces toxic effects including demyelination, hydrocephalus, and astrogliosis.[102,103] Over the last two decades the cuprizone mouse model been widely accepted as an animal model capable of capturing some aspects of multiple sclerosis (MS), providing a model of demyelination and spontaneous remyelination. Non-focal demyelinating lesions in this model occur in the presence of microglial activation and oligodendrocyte apoptosis without lymphocytic infiltration, which can occur in some MS lesions.[46,47] Increased doses of cuprizone intensify both demyelination and mortality as severe liver damage occurs at doses above 0.3% (wt/wt).[94] Accordingly, 0.2% cuprizone (wt/wt) delivered in chow is the established optimal dose for inducing acute demyelination in the C57BL/6 mouse strain.

While cuprizone administration in the mouse has become a common approach used to study demyelination and remyelination processes relevant to human disease, the mechanism of cuprizone action and subsequent oligodendrocyte death is not well understood. Recent reports suggest cuprizone toxicity inhibits respiratory chain complex-2 in the mitochondria, leading to a cellular stress response and ultimately oligodendrocyte death.[98,104] Aged CD-1 mice given a copper-deficient diet showed a significant reduction of several key

metal ions (Fe, Al, Zn, and Ca) in the frontal areas of the brain and in the cerebellum.[105] A separate study in CD-1 mice demonstrated that cuprizone is not absorbed by the intestines, does not accumulate in the brain or the liver, does not cross neuronal plasma membranes (in-vitro), nor does it have any effect on viability or proliferation of cultured neurons.[106] Together, these results suggest that copper is chelated in the gut and the toxic effects are due to a copper-deficient diet rather than direct toxicity of the cuprizone molecule.

Copper is an essential cofactor for many integral enzymes involved in iron metabolism and the homeostasis of other key ions including Al, Zn, Mg and Ca. Cuprizone toxicity extensively modifies copper and zinc distribution in the brain, thereby potentially disrupting the function of the mitochondrial enzyme cytochrome c oxidase.[107] Pasquini, et al, demonstrated a marked decrease in cerebral mitochondrial complexes I, I-II, I-III, and II-III of the respiratory chain after cuprizone intoxication, strongly indicating mitochondrial dysfunction is associated with demyelination.[96] One study demonstrated that copper deficiency for 8 weeks alters gene expression of proteins involved in iron metabolism, and deficiency for 12 weeks results in anemia.[108] Since the brain has the greatest metabolic demands of all organs one would expect any deficiency or metabolic dysfunction to be observed in the central nervous system earlier and with greater severity than elsewhere in the body.

Microglia and macrophages appear around week 2 of treatment, even before gross demyelination is apparent. Notable demyelination is detected at 3 weeks of treatment, with peak demyelination occurring around the 5th week.[94]

Morphological changes occur in astroglia around week 3, concurrent with onset of demyelination. The level of astrogliosis and microglial/macrophage involvement increase until around the 5th week when demyelination is nearly complete.[71,94] Oligodendrocyte density drops dramatically upon cuprizone exposure, then increases beginning at week 3. Remyelination becomes notable during the 5th week of treatment,[109] and within two weeks of cuprizone removal oligodendrocyte density is similar to pre-treatment levels.[70] Electron microscopy reveals that the G-ratio (mean ratio of axon thickness to total fiber diameter including myelin) increases significantly after 6 weeks cuprizone challenge and then returns nearly to normal after 4-6 weeks recovery.[71,109] Continued cuprizone exposure leads to a cycle of demyelinating and remyelinating events that ultimately result in a state of chronic demyelination. Upon 10 weeks of continuous exposure a second episode of near-complete demyelination occurs, followed by incomplete remyelination two weeks later. At week 16 a third and final demyelinating episode persists until animals become moribund or are euthanized.[109] The role(s) of astrocytes and microglia in both demyelination and remyelination have been debated as it has been unclear how much each is responsible for damage or repair.[110,111] Astrocytes have been shown to signal microglial activity and thus modulate myelin debris clearance.[112] Indeed, without debris clearance oligodendrocyte precursor migration and differentiation, along with other repair mechanisms, are significantly impaired.[110]

Pathological heterogeneity in the cuprizone model has been demonstrated,[70,72,95,113–115] and the mechanism of demyelination may vary across structures. For example, it has been suggested that demyelination in the cerebral cortex is not associated with microglial activation,[113] but that demyelination in the corpus callosum is microglia-mediated.[96] Cortical demyelination and oligodendrocyte loss may be directly related to energy deficient oligodendrocytes.[106,113] Oligodendrocyte death and subsequent demyelination occur in the cerebral cortex with little or no microglial activation or T-cell infiltration, which suggests that cuprizone directly interferes with mitochondrial function in oligodendrocytes.[113] Conversely, demyelination in the corpus callosum likely involves microglia activation and is induced by pro-inflammatory cytokines.[96,112] While the full mechanism of cuprizone toxicity as a source of demyelination is not fully understood, it is generally accepted that metabolic aberrations in oligodendrocytes are downstream effects of treatment with cuprizone that eventually lead to caspase-independent, apoptosis-inducing, factor-mediated cell death.[116] Perhaps due to structural and genetic variations,[117] response varies markedly across animals and is sex-, dose-, and age-dependent.[93–98] While inflammation and axonal loss are minimal, if not entirely negligible, during acute demyelination in young mice,[71] axonal loss is significant in aged (6-8 months) mice. Additionally, macrophage and astrocyte responses are different in aged mice than in young (8-10 weeks) mice.[118] Because histological analyses are invasive and time-intensive, non-invasive imaging techniques are well suited to complement histology and provide a more

comprehensive perspective of pathophysiology, particularly with respect to longitudinal studies. Careful histological analyses are important to validate emerging quantitative and semi-quantitative in-vivo imaging techniques.

Several magnetic resonance imaging (MRI) based methods of non-invasively quantifying demyelination in-vivo in the cuprizone mouse model have been explored including diffusion tensor imaging (DTI),[119,120] diffusion kurtosis imaging,[121] T_1 and T_2 quantitative parametric mapping,[71,122] and MR elastography.[123] Magnetization Transfer (MT) has been widely used as a fast and precise measurement capable of semi-quantitative estimation of macromolecular content by calculating the MT ratio (MTR). Myelin content correlates with MTR, but, axonal density and other tissue components can also influence MTR values.[65] Quantitative magnetization transfer (qMT) techniques have been proposed to obtain quantitative measures of macromolecular proton fraction in tissue in an attempt to overcome the potentially non-specific nature of MTR.[62–64,69,124] However, qMT relies heavily on extensive image sets, additional quantitative R_1 imaging, or a number of assumptions regarding intrinsic tissue properties, and are thus prohibitively time or labor intensive. Quantitative R_1 ($\equiv 1/T_1$) acquisitions are necessarily time intensive as parametric modeling and mapping requires excellent signal-to-noise ratio (SNR), thus adding to the complexity and scan time burden of qMT experiments. However, qR_1 measurements may provide more comprehensive information in their own right and warrant further investigation.[125]

Due to SNR limitations, particularly when imaging small rodents, in-vivo MRI experiments tend to utilize single-slice acquisitions, or multi-slice acquisitions with thick slices (0.5 – 1.0mm) and limited coverage.[72,121,122,126] Mouse brains are roughly 10mm across compared to 120mm in humans. A voxel size of 100μm^3 or less is thus required to achieve resolution comparable to the 1mm^3 voxel size in human neuroimaging. Some recent work has obtained 3D whole-brain MT images with good resolution (200x200x230μm^{370} or 117μm isotropic[71,73]), although results presented included only either single-slice or region-of-interest (ROI) analysis. While ROI analysis is useful for boosting SNR and performing coarse regional evaluations, it necessarily introduces exaggerated partial-volume dilution and obscures fine regional and structural variations. This latter point is of particular interest because pathology and morphology are known to be highly heterogeneous both regionally and across animals in the cuprizone model.[70,72,93,95,113,115,127,128]

In this study we investigated non-invasive methods of characterizing demyelination and remyelination in-vivo. We employed T_2-weighted and magnetization transfer imaging sequences, established semi-quantitative MRI techniques designed to achieve whole-brain coverage with exceptional spatial resolution (100μm isotropic), to elucidate the spatial distribution of acute cuprizone-induced demyelination, and subsequent remyelination, in adult C57BL/6 male mice. Acute demyelination was induced by 6 weeks of cuprizone diet; spontaneous remyelination was observed after 6 weeks of recovery on normal chow post-cuprizone. Changes in MRI contrast in cuprizone-treated

mouse brains were interrogated in-vivo using T_2-weighted and MTR imaging sequences. Gold-standard histological analyses were used to evaluate the extent to which MTR was a specific measure of myelin content in-vivo. We thus confirm and expand upon earlier work[70,95] as we present the first comprehensive overview of spatially varying cuprizone-induced demyelination in the mouse corpus callosum (CC) and external capsule (EC).

Materials and Methods

This study was specifically reviewed and approved by the Oregon Health & Science University (OHSU) Institutional Animal Care and Use Committee (IACUC), as protocol IS00001282. All animal handling, care and treatment was carried out in strict accordance with the OHSU IACUC regulations. C57BL/6 mice were obtained from Charles River. Mice (n = 12 controls, 14 cuprizone) were studied longitudinally for up to twelve weeks. Mice were monitored daily for signs of distress including lethargy, hunching, and self-mutilation. Each mouse was weighed weekly and values recorded. Sustained weight loss, failure to recover from anesthesia, and general poor health were defined as humane end points. A malocclusion led to malnourishment and eventual humane euthanasia in one mouse during the acclimation period. One cuprizone-treated mouse died of unknown causes the day after successfully recovering from Week 6 MRI. No other adverse events occurred in this study.

Twenty-six male C57BL/6 mice were received at 4 weeks of age and singly housed on-site under normal light/dark cycle conditions. After a 3-week acclimation period, 14 mice began a 0.2% (wt/wt) cuprizone diet (Sigma-Aldrich, St Louis, MO) with free access to food. All animals were given pelletized chow for the duration of the study (Purina Mills, LLC, TestDiet division). MRI examinations were performed longitudinally at three time points: (1) immediately prior to initiation of cuprizone diet (age 7 weeks; Baseline), (2) at the end of treatment (age 13 weeks; Week 6) and (3) 6 weeks later (age 19 weeks; Week 12 for controls, Week 6+6 for cuprizone animals: i.e., 6 weeks on cuprizone and 6 weeks normal chow post-cuprizone administration). After 6 weeks of treatment a subgroup (n = 9 treatment and 6 age-matched controls) were sacrificed immediately following MRI for histological analyses. The remaining mice were returned to a normal diet for 6 weeks of recovery at which time a final MRI was obtained and all remaining subjects were sacrificed for histology. Euthanasia was accomplished by isoflurane overdose followed by cervical dislocation.

MRI

MRI data were collected using an 11.75 Tesla (T) instrument (Bruker Biospin, Billerica MA) equipped with a high-performance gradient coil (9cm inner diameter), and radiofrequency (RF) volume coil transmitter and surface receiver. The RF coils are sequentially detuned to reduce interactions between the transmitter and receiver RF coils. The surface coil was custom-built and had an oval geometry with 1.2cm long axis and 0.8cm short axis. Prior to image acquisition, a gradient-based magnetic field optimization routine was performed

to adjust electrical currents in first, second, and third-order room-temperature shims. Mice were initially sedated via an intraperitoneal injection of a xylazine/ketamine cocktail, and then maintained with 1-2% isofluorane, adjusted to maintain respiration (approx. 90±10 breaths/min), in 100% oxygen for the duration of the MRI (approx. 2.5 hrs). Rectal temperature and respiration rate were monitored throughout the study using a small animal physiological monitor (SA Instruments, Inc., Stony Brook, NY). The magnet bore was heated with forced warm air using the rectal thermometer as controller. Core body temperature was maintained at 37° ± 1° C. Custom-built head-holders restrained the sedated animal to minimize respiration-induced motion artifacts.

A two-dimensional multislice T_2-weighted RARE sequence was acquired (refocus flip angle (FA) 180°, field-of-view (FOV) 1.3cmx1.6cm (132x160 matrix, 100x100μm^2 in-plane resolution), 25 0.5mm thick coronal slices). Magnetization transfer (MT) MRI data were acquired using whole-brain 3D gradient-recalled echo (GRE) sequences with 2.5ms echo time (TE), 30ms recycle time (TR), 10° FA, and a pulsed MT saturation pulse of Gauss shape, 20ms duration, 0.01ms interpulse delay, 137Hz bandwidth.

Tissue processing

Brains were extracted whole within 10 minutes of sacrifice, immediately immersed in 4% paraformaldehyde and microwaved for 75 min using the PELCO BioWave® Pro (Ted Pella, Inc., Redding, CA). The entire brain was sectioned into 30μm slices using a Leica VT1000s Vibratome. About 20 representative

sections between bregma -2mm and bregma +1.5mm were stained with Black Gold II and imaged using a Zeiss AxioImager M2 bright field microscope.

Myelin staining and analysis

Brain sections (30µm) were stained with Black Gold II (AG105, Millipore Corp, Billerica, MA) according to manufacturer's instructions. Briefly, the sections were dehydrated for 60-90 minutes on a slide warmer and then rehydrated with purified water ("Milli-Q" water purified using a Millipore system). Pre-warmed Black Gold II solution was added onto sections and incubated at 60°C. The average incubation time was 15 min. The slides were rinsed with Milli-Q water twice. Pre-warmed 1% sodium thiosulfate was added to the slides and incubated for 3 min. The slides were rinsed thrice with Milli-Q water before 3-minute incubation with cresyl violet stain. Sections were rinsed again and dehydrated using a series of gradated alcohols and finally in a xylene substitute for 2 min and coverslipped with mounting media. The area of demyelination in the corpus callosum was manually measured using MetaMorph (ver 7.7.5, Molecular Devices, CA) and represented as percent demyelination. Analysis of demyelinated area was restricted to the MRI-visible extents of the corpus callosum.

Immunohistochemical studies

Fixed brain tissue was used to prepare 6 µm paraffin-embedded sections. After deparaffinization and antigen retrieval (5 min treatment at room temperature with 95% formic acid, followed by 30 min incubation in citrate buffer, pH 6.0, at 90 degrees C. Tissue sections were blocked with 5% nonfat dry milk in

phosphate-buffered saline and labeled with antibodies to GFAP (G9269 from Sigma, St. Louis, MO), microglia (Iba1 from Wako USA, Richmonda, VA), and PDGFR-alpha (R&D systems, Minneapolis, MN). Development was accomplished with either diaminobenzidine-based Elite (for Iba1) or Vector Red (other immunostains) kits (Vector Laboratories, Burlingame, CA).

Data Analysis

Pre-processing and Coregistration

An elliptical 3D Gaussian apodization filter (sigma = 0.42) was applied to raw k-space data to improve SNR by down-weighting high-frequency signals and noise. Filtered k-space data were reconstructed to create magnitude and phase images using custom software written in Python[129] scripting language. Magnitude images were coregistered using a multi-step process. Briefly, images from each animal were skull-stripped with FSL's BET[130] and then linearly registered to a single high-quality reference data set using FSL's FLIRT[130]. A population average image was created and all data sets were linearly registered to the population average. Final registration to the population average was achieved via FSL's nonlinear registration tool, FNIRT[130], with the affine matrix from the second linear registration step as a starting estimate.

Corrections and Parametric Mapping

All skull-stripped, coregistered images were corrected for inter-day variation in receiver gain settings by linearly scaling histogram intensities – while preserving native contrast - to match the reference images used in the initial coregistration step. The magnetization transfer ratio (MTR) was calculated as:

$$MTR = (M_0 - M_{sat}) / M_{0,} \qquad (12)$$

where M_{sat} and M_0 are magnetization obtained from 3D GRE sequences with and without the saturation RF pulse, respectively (see MRI above). MTR maps were calculated for all animals and timepoints individually, and then pooled according to timepoint (Baseline, Week 6, Week 6+6) to create population averages. All corrections and parametric estimations were performed with code written in-house.

Statistical Analysis

Non-parametric permutation-based analyses were performed using FSL's RANDOMIZE tool employing Threshold-Free Cluster Enhancement[131] with corrections for repeated measures consistent with our longitudinal design. No assumptions were made regarding distribution of means or variances. Paired and un-paired non-parametric t-tests compared voxel-wise MTR values in cuprizone-treated mice between Baseline and Week 6, Baseline and Recovery, and Week 6 and Recovery to identify significant changes at each time point.

Gene Expression

The Allen Institute for Brain Sciences Anatomic Gene Expression Atlas (AGEA)[132,133] was used to assess relative genetic homogeneity within the CC.

“Seed” voxels were chosen at multiple points within the CC along the rostrocaudal and mediolateral axes. Both correlation and cluster maps for each seed voxel were visually inspected. The Gene Finder utility was then used to identify genes of interest (those with highest correlation or highest fold change compared to other structures) in our seeds in the CC. In situ hybridizaton (ISH) slides for the returned genes were then manually reviewed to ensure accuracy. Candidate genes were identified based on a visual inspection of anatomical distribution of gene expression energy. Three-dimensional renders of candidate gene expression energy and density[132,133] throughout the C57BL/5 P56 male mouse brain were then visualized using the Allen Institute’s Brain Explorer 2 desktop application. Expression energy distribution was qualitatively compared to patterns of demyelination observed in our 3D MTR maps.

Results

Longitudinal MTR data were obtained from eleven controls and fourteen cuprizone-treated animals immediately prior to initiation of cuprizone administration (7 weeks old; Baseline), after 6 weeks of cuprizone (13 weeks old; Week 6). Immediately after week 6 MRI, a subgroup (n = 9 treatment and 6 age-matched controls) were sacrificed for histological analyses. The remaining mice were studied by MRI 6 weeks later (19 weeks old; Week 6+6 for treatment, Week 12 for controls), and immediately sacrificed for histology (**Figure 8**).

Black Gold II stain for myelin was used at Week 6 and Week 6+6 to histologically assess myelin content in both cuprizone and healthy control mice,

and to provide additional validation of the MTR measurements. Whole-brain MRI coverage revealed a complex spatial pattern in MRI contrast during acute demyelination in the medial corpus callosum (CC) and lateral CC/external capsule (EC) that is a combination of gradients along the caudal-to-rostral and medial-to-lateral axes. Mild MTR decrease was also observed in the caudoputamen, thalamus, cortex, and cerebellum (CBLL). MTR correlated well with histological quantification of myelin content in the CC. Visual inspection of myelin basic protein (MBP) gene expression revealed an inverse correlation between MBP and areas of significant demyelination and decreased MTR in the CC.

Reduced weight gain is associated with cuprizone diet

Animals lost approximately 5% of their body weight during the first week of cuprizone feeding ($p<0.005$) followed by gradual weight gain over the next 5 weeks, consistent with previous observations.[94,95,97,116] Non-cuprizone fed mice gained weight roughly 3 times faster (0.65g/wk vs 0.23g/wk) than cuprizone-fed mice during treatment, and group weight averages were significantly different until one week after the treatment group returned to normal chow as shown in **Figure 8**.

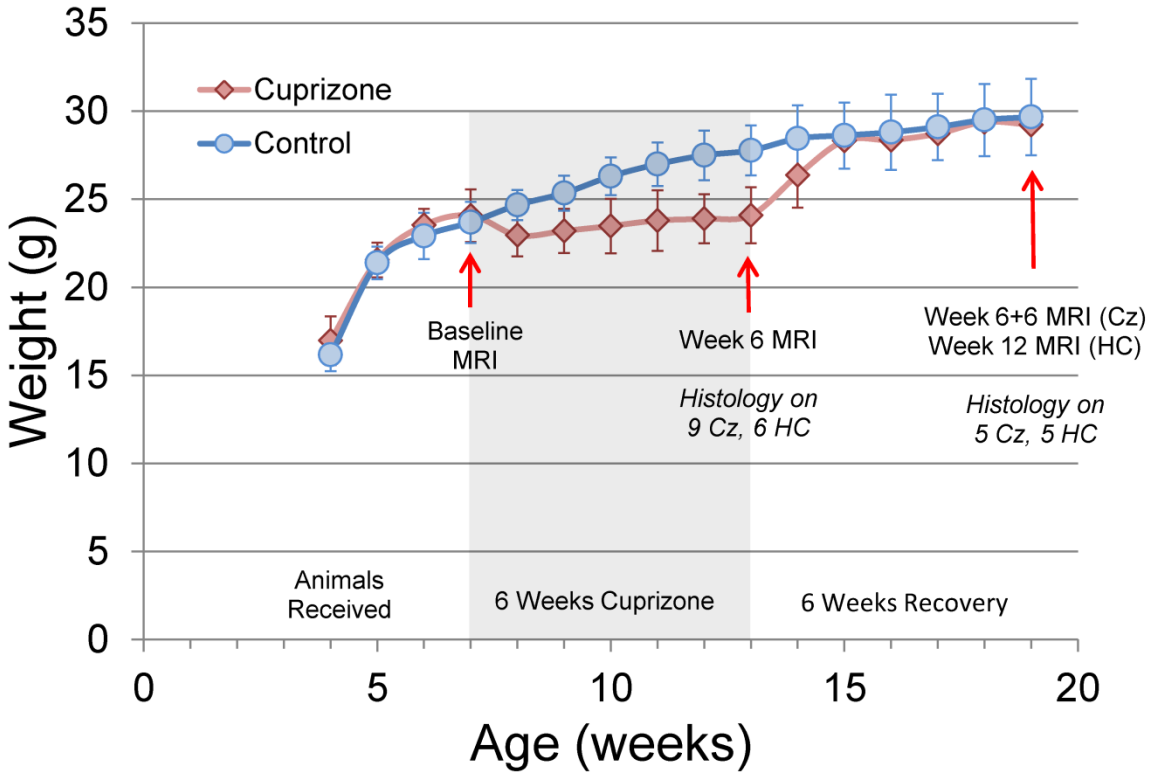

Figure 8. Weight Gain and Study Design. Average weight of animals over the course of the study (error bars represent one standard deviation). Cuprizone diet was administered for 6 weeks (shaded area) beginning 3 weeks after delivery. After one week on cuprizone the treatment group (Cz) exhibited lower weight than healthy controls (HC; *p<0.005); weight gain increased one week after cuprizone was removed from the diet, and two weeks into recovery no difference can be seen between the two groups' weights.

Longitudinal ROI analysis of MTR demonstrates regional heterogeneity in demyelination and remyelination

We pooled callosal structures into two categories for ROI analysis: medial and lateral corpus callosum, referred to here as med-CC and lat-CC, respectively. Caudal med-CC likely includes adjacent structures such as fornix, dorsal hippocampal commissure, and cingulum. **Figure 9** shows the distinction used here for lateral and medial corpus callosum. Three coronal slices were selected representing genu of CC (gCC, Bregma +1mm), isthmus of CC (iCC, Bregma -1mm), and splenium of CC (sCC, Bregma -2mm). Briefly, the med-CC

corresponds to the center-most region demarcated by the apex of the lateral arches, consistent with similar studies; lat-CC thus includes all MRI-visible white matter distal to the apex of the lateral arches. We adopted this approach for two primary reasons: (1) various atlases disagree on location and extent of EC; (2) while distinguishable on histology, MRI partial volume effects limit differentiation of CC from small adjacent white matter structures. Longitudinal changes in population-average MTR values are demonstrated in **Figure 10** for all cuprizone mice (solid lines) and healthy controls (dashed lines) at Baseline, Week 6, and Week 6+6.

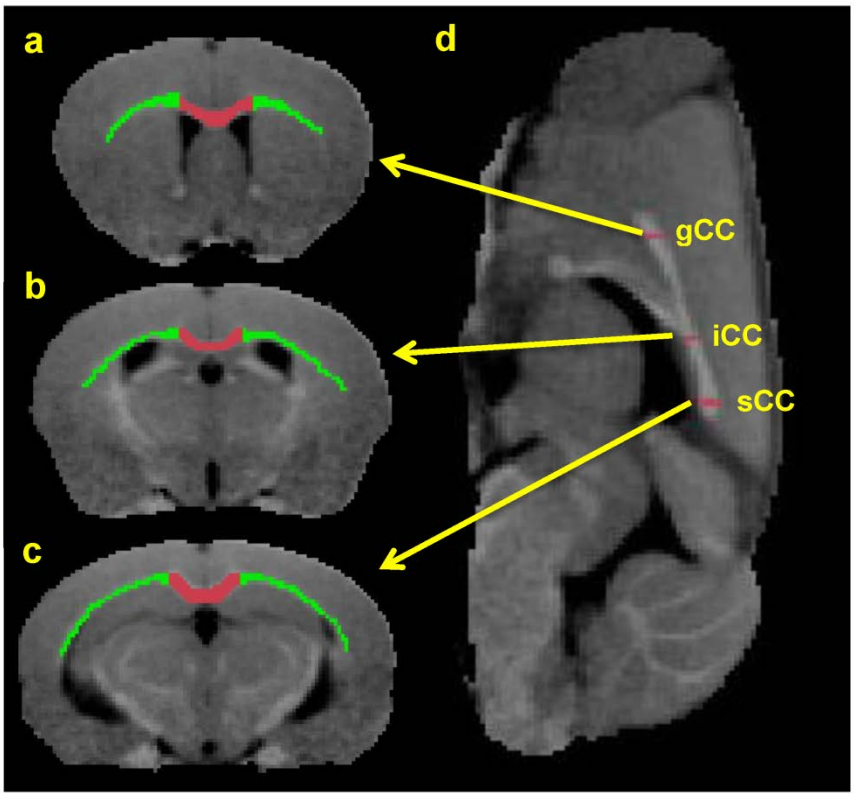

Figure 9. ROI Selection on Coronal MR Images. Coronal sections of the mouse brain with colored ROIs used in scatter plots below. Medial CC is red, lateral CC (including EC) is colored in green. A sagittal view with arrows corresponding to the locations of the coronal slices shown in (a-c), corresponding to genu (gCC), body/isthmus (iCC), and splenium (sCC), respectively, is shown in panel (d).

Substantial reductions in MTR were seen along the entire length of the CC midline after 6 weeks of cuprizone (iCC $p < 0.5x10^{-6}$, sCC $p = 0.001$), with an increase in absolute change following a rostro-caudal gradient. Lateral CC MTR decrease was significant in the genu ($p=0.0005$) and isthmus ($p < 0.05$). Importantly, a striking rostro-caudal gradient of decreasing effect is observed in the lat-CC – opposite of med-CC. Indeed, only a small change was seen in lat-CC at the level of the isthmus, and caudal lat-CC appears essentially preserved. MTR returned to near-baseline values in all regions after 6 weeks recovery on normal chow (Week 6+6). MTR values at Week 6+6 generally hover right between those obtained at Baseline and Week 6, suggesting gradual return to some level of contrast at Week 6+6 that resembles Baseline.

MTR in all structures in control mice matched well with those of the cuprizone group at baseline. However, by week 6, MTR in control mice had increased in all ROIs compared to baseline, and generally continued to increase throughout the 12 week study. **Figure 10** compares MTR changes in controls versus cuprizone mice at Baseline, Week 6, and Week 6+6 (recovery).

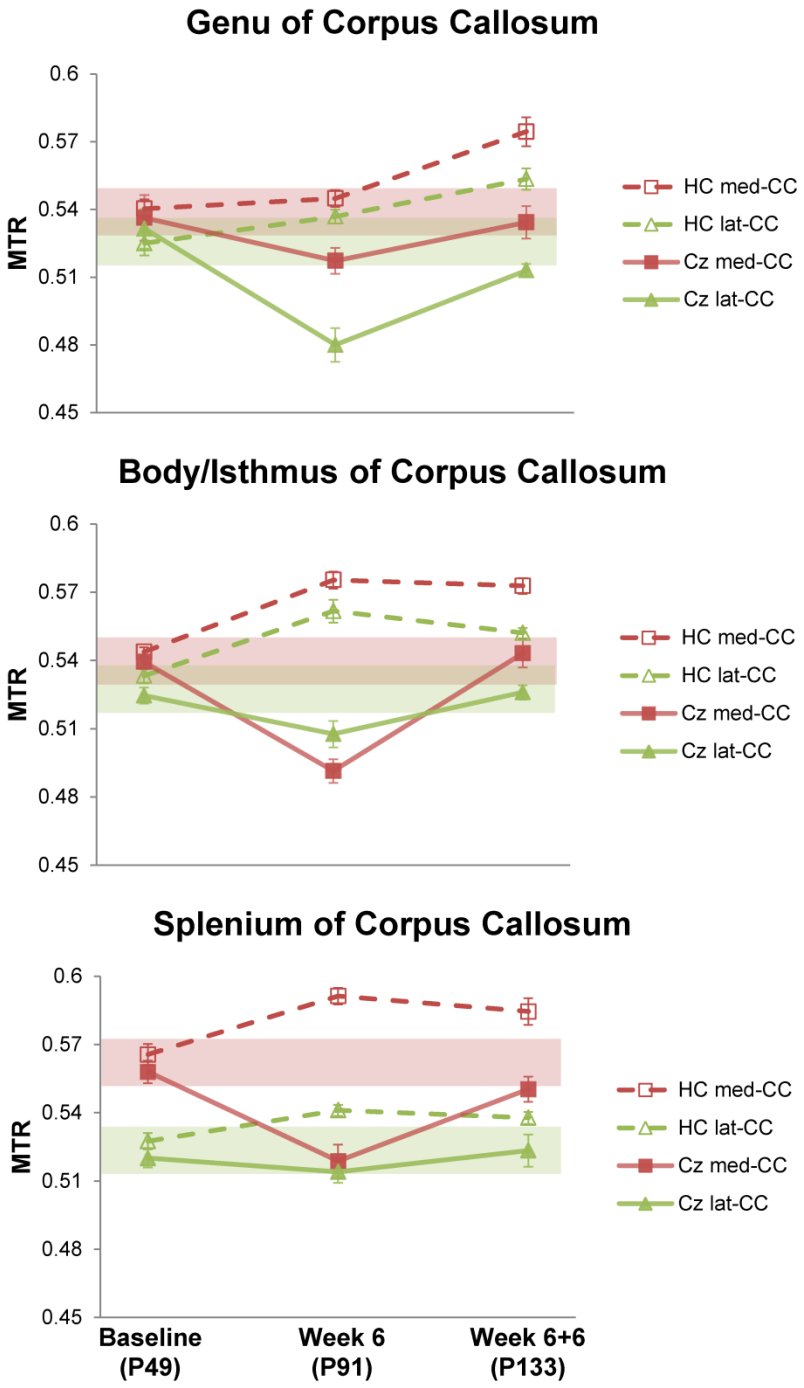

Figure 10. Longitudinal ROI-average MTR Compared to Healthy Age-Matched Controls. ROI-average MTR scatter plots for the medial- and lateral-CC ROIs illustrated in Figure 2 (a-c). Values represent population average within an ROI. Dashed lines/hollow markers represent data from healthy age-matched controls (n = 10, 4, 5, for Baseline (age postnatal (P) 49), Week 6 (P91), Week 6+6 (P133), respectively); data from cuprizone treated animals are shown with solid lines/filled markers (n = 14, 14, 5, for Baseline, Week 6, Week 6+6, respectively). Error bars represent mean standard error for each group. The shaded bands illustrate the 95% confidence interval for baseline values (±0.01) for medial (red) and lateral (green) ROIs.

MTR parametric maps reveal complex pattern of demyelination across whole brain

Population average MTR maps for Baseline, Week 6, Week 6+6 (cuprizone recovery) and Week 12 (control) are compared in **Figure 11**. Baseline images for one control animal were discarded due to incomplete image acquisition. An MTR intensity projection along the midsagittal CC (**Figure 11**a,b) shows natural variance in MTR along the CC in healthy animals at baseline (blue line). This caudal-rostral gradient is entirely eliminated after 6 weeks cuprizone (red line), and only partially recovers after 6 weeks of normal chow post-cuprizone (green line). At Cz Week 6, rostral lat-CC/EC and caudal med-CC have become isointense with surrounding gray matter, suggestive of distinct demyelination (**Figure 11**c, yellow arrows). Limited corpus callosum contrast returns at Week 6+6, but remains hypointense compared to control (white arrows). **Figure 12** shows the population average baseline MTR map with the statistically significant (paired t-test $p < 0.01$) average ΔMTR (= $MTR_{Baseline} - MTR_{Week6}$) values overlaid in color. Panel (a) shows a horizontal slice demonstrating decreased MTR in the rostral lat-CC. A midsagittal view is shown in panel (b); the caudal-rostral pattern of decreased MTR in the medial CC is evident (yellow arrow: caudal demyelination; white arrow: rostral myelin preserved). A coronal slice (approximately bregma -1mm) is shown in panel c; here the medial CC displays decreased MTR whereas the lateral CC was unaffected. MTR at recovery was not significantly different from either Week 6 or Baseline, suggesting substantial yet incomplete recovery. Consistent with

previous reports, ventricular enlargement occured at week 6 but was largely resolved after 6 weeks of recovery.[70,93,102,134] MTR depressions scattered throughout the ventral cerebral cortex may be artifactual and can be attributed to SNR decreasing with distance from the surface receive coil. Decreased MTR was observed in the CBLL peduncles and limited diffuse decreases throughout deep gray matter and cortex were seen in parametric maps ($p < 0.05$; not shown).

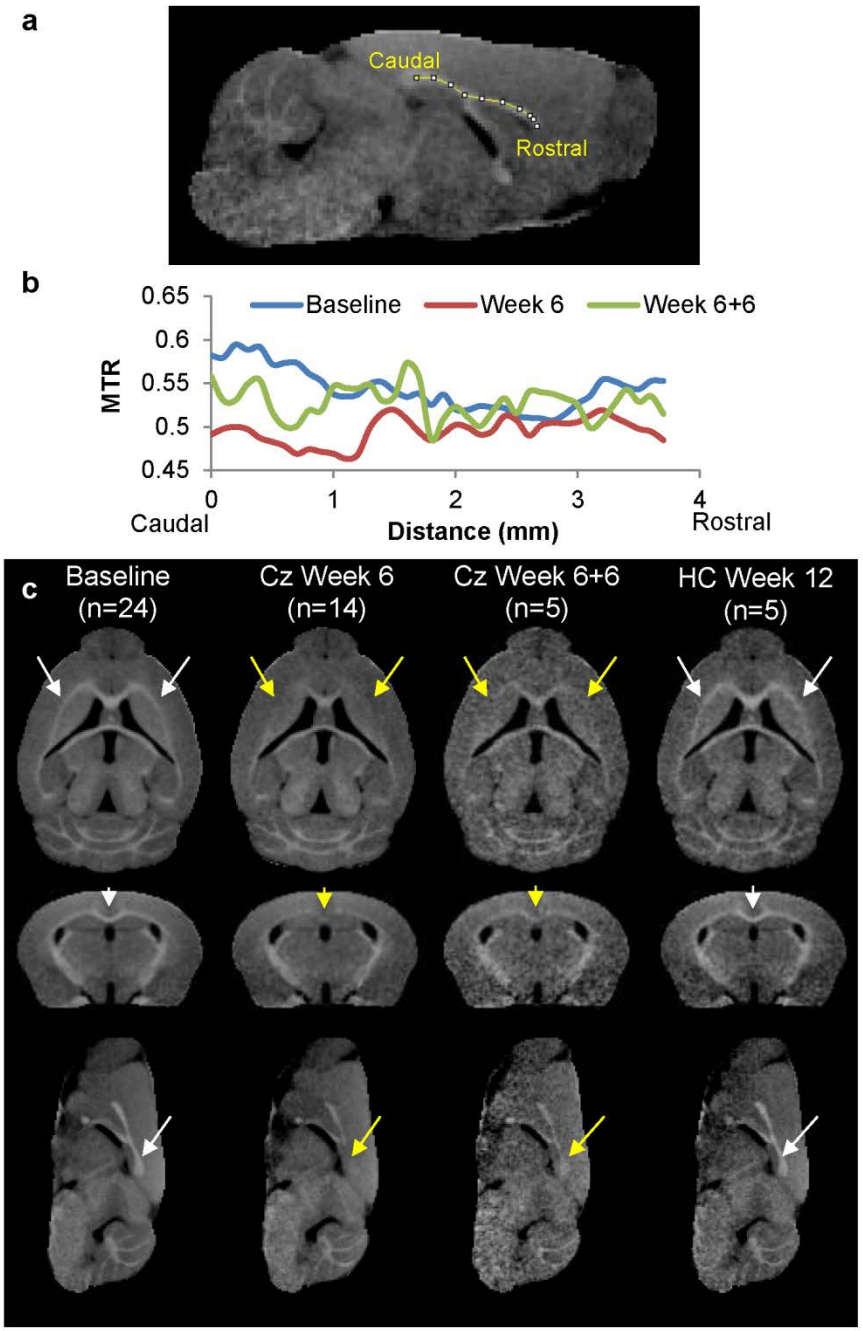

Figure 11. Population Average MTR Parametric Maps. (a,b) Population average MTR projection along midsagittal CC from Caudal (splenium) to Rostral (genu) at Baseline (blue), Week 6 (red), and Week 6+6 (green). (c) Population-average MTR maps at baseline, Cz Week 6, Cz Week 6+6, and HC Week 12. Note that SNR decreases with fewer number of images averaged, resulting in poorer image quality in Cz Week 6+6 and HC Week 12 images.

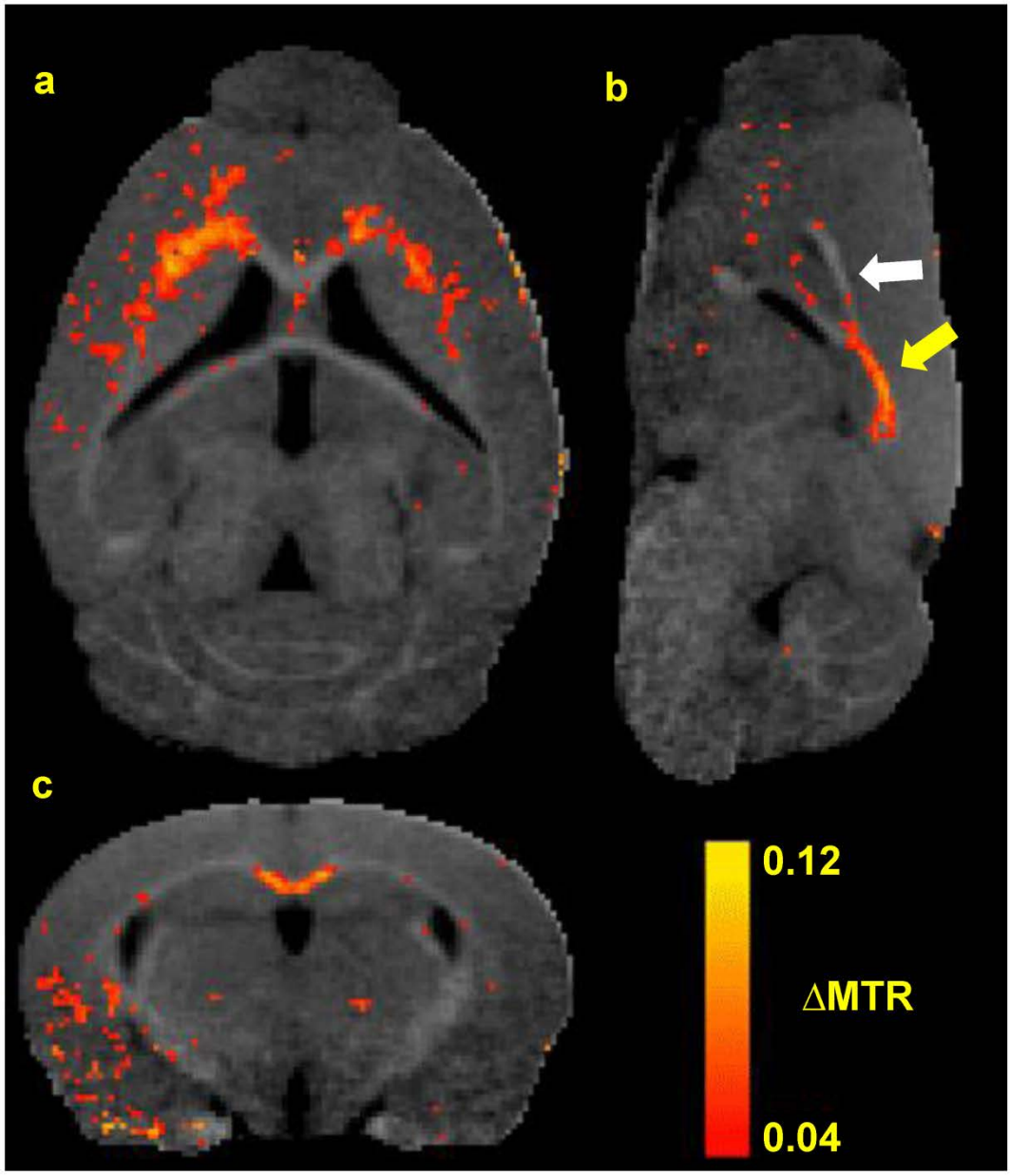

Figure 12. Population Average Week 6 ΔMTR Parametric Maps. Horizontal (a), sagittal (b), and coronal (c) views of the mouse brain. Color overlay represents areas of MTR decrease (paired t-test, $p<0.01$) after 6 weeks of cuprizone as compared to baseline. The caudal-rostral pattern of demyelination along the midline is illustrated in panel b (arrows).

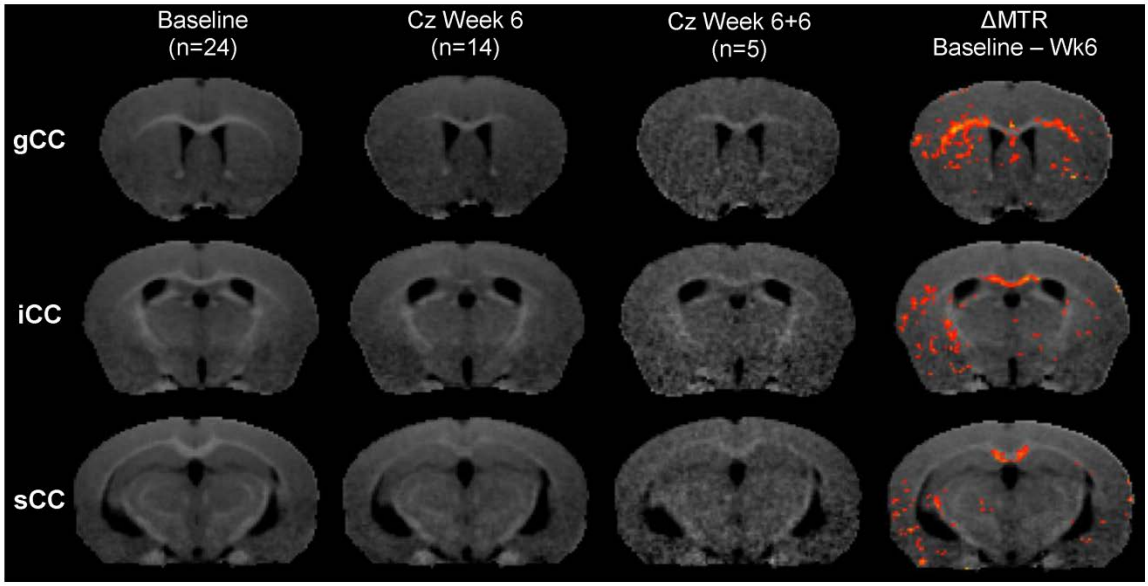

Figure 13. Population Averaged Coronal MTR Maps. MTR maps at the level of gCC (top row), iCC (middle row), and sCC (bottom row). ΔMTR ($p < 0.01$) values are overlaid in false color (see Fig 5 for color bar) in the far right column. Note reduced image quality at Cz Week 6+6 due small number of images included in the average (n=5) compared to Baseline (n=24) and Cz Week 6 (n=14).

Quantitative histological analyses correlate well with MTR

Quantitative analyses of tissue samples with BGII stain for myelin are summarized in **Table 1**. Any part of lat-CC/EC that was not MRI-visible, and thus not included in the green ROIs shown in **Figure 9**, was excluded from this analysis. Demyelination is evident and variable along the length of the CC. Both MTR and ΔMTR average ROI values correlated well with the percentage of demyelinated area; Pearson's correlation coefficients (r) are shown in **Table 2** along with linear regression parameters. Overall, ΔMTR was more highly correlated with percent demyelinated area than was MTR. Sections obtained at bregma +1mm stained with BGII shown in **Figure 14** illustrate myelination in the

lat-CC in a healthy control (a), after 6 weeks cuprizone challenge (b), and 6 weeks cuprizone + 6 weeks recovery (c). Complete demyelination is evident in the rostral lat-CC after 6 weeks of cuprizone, yet med-CC myelin is preserved. Comparing panels a and c it is evident that remyelination in the lat-CC is incomplete after 6 weeks recovery following 6 weeks of cuprizone. Panels d-f demonstrate patterns of myelination at bregma -1.5mm in healthy control (d), after 6 weeks cuprizone (e), and after 6 weeks recovery post-cuprizone (f). Caudal med-CC is heavily demyelinated (arrowhead, e), and lat-CC/EC show moderate demyelination compared to control (d). All structures show dense stain for myelin after 6 weeks of recovery (f). Hybrid images created from BGII and MTR images in **Figure 15** demonstrate that MTR contrast reflects BGII staining in gCC, iCC, and sCC at Baseline, Cz Week 6, and Cz Week 6+6. Limits of MRI-visible EC compared to the full extent of the structure are clearly evident.

Table 1. BGII stain for myelin in corpus callosum - demyelination as percent area

Group	Section	% BGII Demyelination (SD)		
		Whole CC	Medial CC	Lateral CC
6 Weeks Cz	gCC	9.7 (±0.6)	2.3 (±1.9)	17.2 (±3.6)
	iCC	8.2 (±0.9)	20.7 (±4.8)	3.4 (±0.8)
	sCC	16.3 (±2.6)	30.7 (±8.5)	8.9 (±3.0)
6 Weeks Cz + 6 Weeks Recovery	gCC	2.6 (±0.3)	0.9 (±0.4)	4.0 (±0.6)
	iCC	4.9 (±0.9)	6.5 (±2.4)	4.3 (±0.9)
	sCC	2.3 (±1.0)	3.6 (±2.1)	1.8 (±1.0)

Table 2. BGII-MTR linear regression

Region	BGII vs MTR			BGII vs ΔMTR		
	Equation	*r*	*p*	*Equation*	*r*	*p*
Whole CC	y = -1.7x + 0.1	-0.55	0.26	y = 2.1x + 0.04	0.63	0.18
Medial CC	y = -3.3x + 1.8	-0.58	0.23	y = 4.8x + 0.02	0.82	<0.05
Lateral CC	y = -2.4x + 1.3	-0.87	<0.05	y = 2.4x + 0.03	0.83	<0.05

Pearson's correlation coefficients (r) demonstrate BGII % demyelination is negatively correlated with MTR, and positively correlated with ΔMTR. Linear regression parameters: *y* represents BGII % demyelination; *x* is either MTR % or ΔMTR (%).

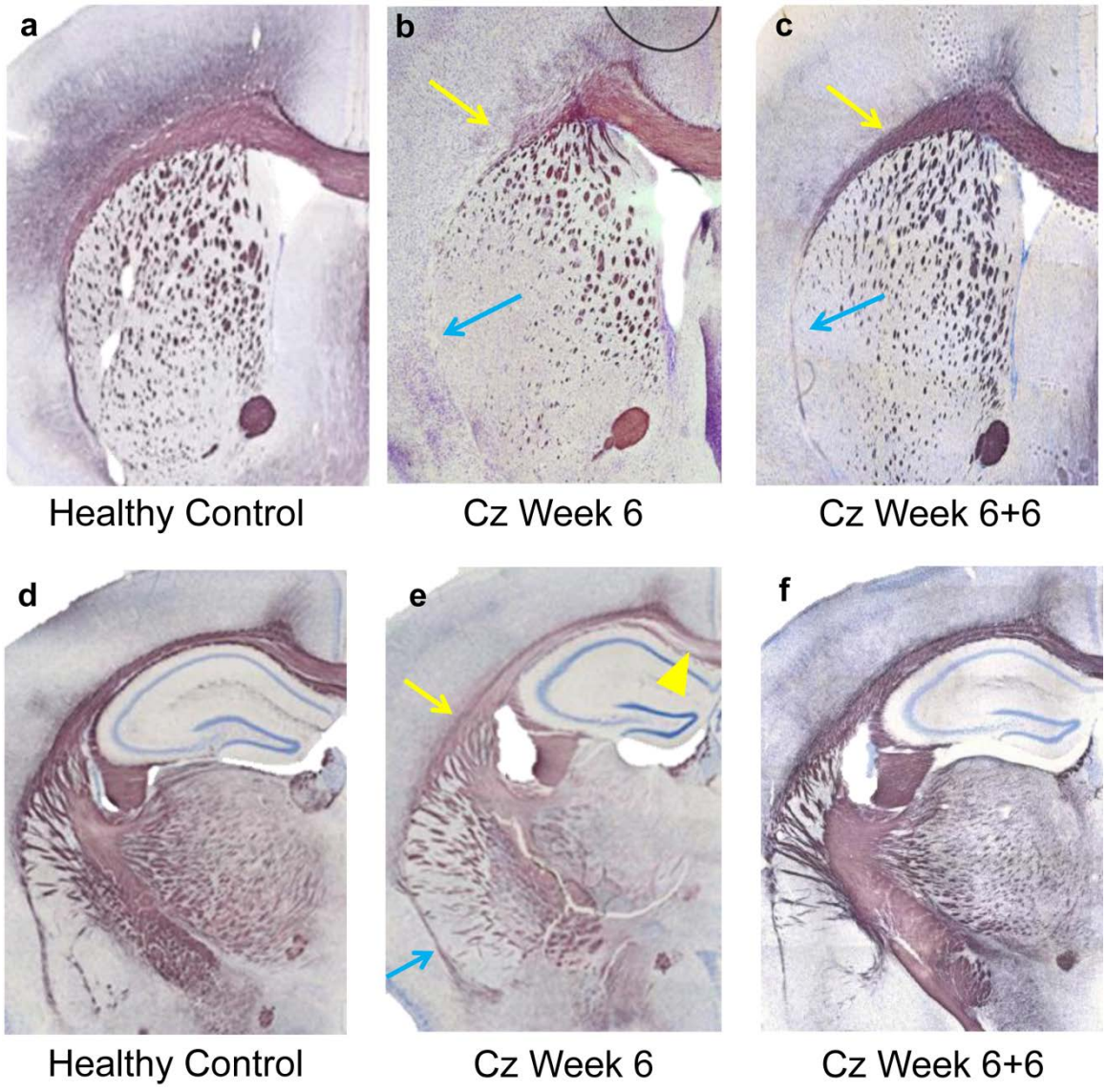

Figure 14. Black Gold II Stain for Myelin in Rostral and Caudal CC. BGII stains roughly corresponding to gCC (a-c) and sCC (d-f) ROIs in Fig. 2. Age-matched control with normal myelinated lat-CC/EC (a); substantial demyelination in rostral lat-CC/EC (arrows) after 6 weeks Cz (b); lat-CC/EC partially recovered after 6 weeks on regular chow (c). Reduction in myelinated fibers in caudoputamen is observed both at Week 6 and Week 6+6 compared to control. Stark demyelination is evident in the caudal med-CC (e, arrowhead), while lat-CC/EC (arrow) is only mildly demyelinated after 6 weeks cuprizone (e) compared to control (d). Remyelination in lat-CC/EC and med-CC is substantial yet incomplete after 6 weeks recovery (f). Blue arrows indicate demyelination in EC beyond the extents of MRI-visible lat-CC/EC.

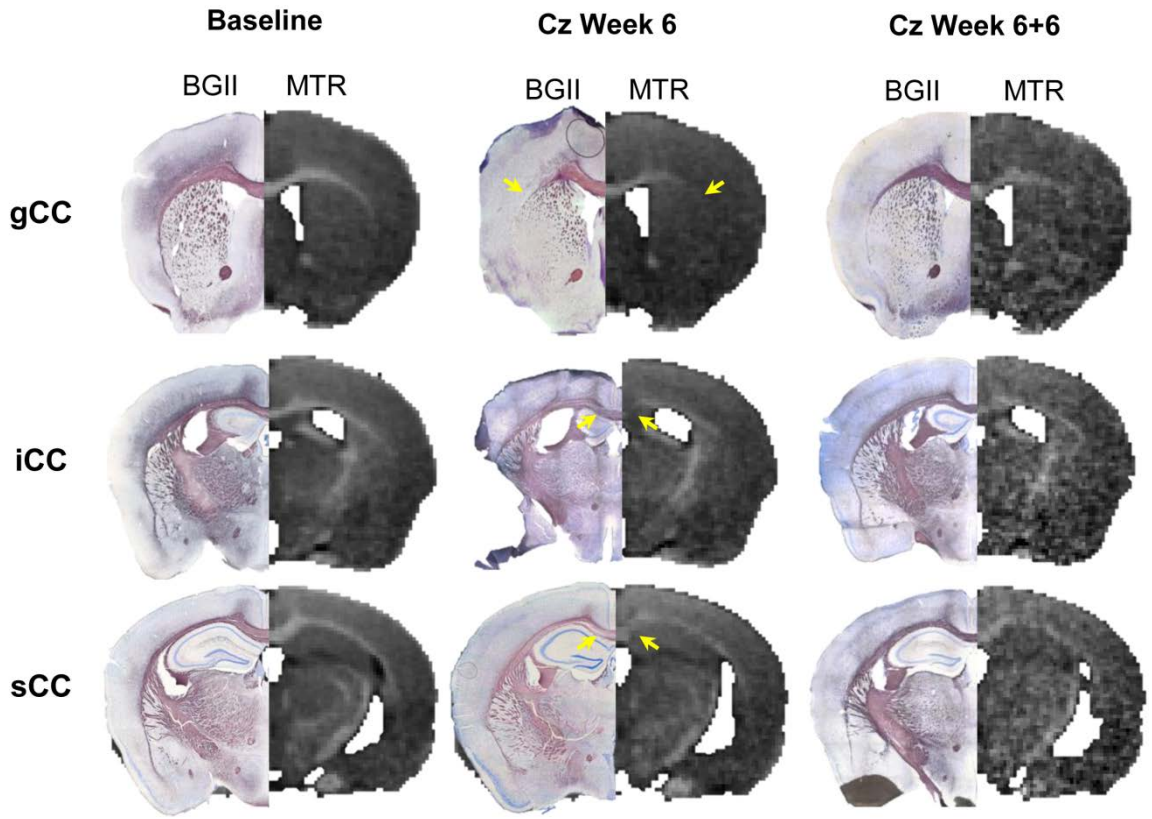

Figure 15. BGII/MTR Hybrid Images. BGII sections compared to MTR maps in gCC, iCC, and sCC. Hybrid BGII/MTR images demonstrate MTR contrast and corresponding BGII staining at the level of gCC (first row), iCC (second row), and sCC (third row) at Baseline (left), Cz Week 6 (middle.), and Cz Week 6+6 (right). Loss of MTR contrast at Week 6 matches changes in BGII staining, representing demyelination (yellow arrows). The black circle in the cortex above gCC at Cz Week 6 is a coverslip bubble and should be ignored.

T_2-weighted images provide qualitative estimates of myelin content

T_2-weighted (T_2-w) images give excellent GM/WM contrast in-vivo. In age-matched healthy controls, the med-CC and lat-CC both are clearly hypointense compared to GM as shown in **Figure 16**a,c. After 6 weeks of cuprizone treatment the GM/WM contrast is eliminated as callosal regions are isointense with GM, consistent with loss of myelin as shown via histology in **Figure 16**b inset. Remyelination is indicated by increased GM/WM contrast in T_2-w images (**Figure**

16d) 6 weeks after removal of cuprizone. Black Gold II stain for myelin is fairly homogenous in the CC in healthy controls (panels a,c insets) compared to the disorganized and inhomogeneous appearance in demyelinated CC (panel b inset). Myelination appears somewhat more organized and homogenous after 6 weeks of recovery (panel d inset), indicating partial, yet incomplete remyelination.

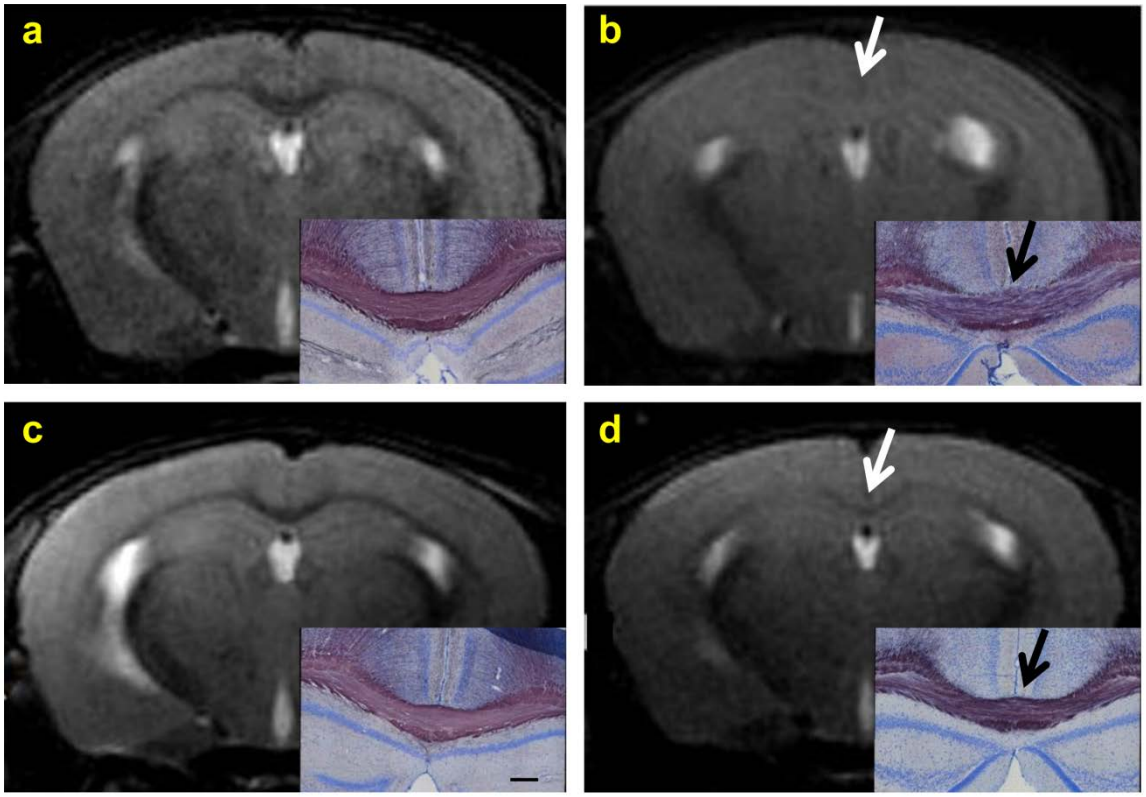

Figure 16. T_2-w MRI Compared to BGII. T_2-w RARE coronal images and pathologic sections stained with Black Gold II for myelin (insets, scale bar 200µm) from mice fed normal chow (a and c), after 6 weeks on cuprizone chow (b) and 6 weeks after stopping cuprizone chow (d). MRI from age-matched control mice (a and c) show low signal intensity in the corpus callosum and corresponding normal myelin on histology. After 6 weeks of cuprizone exposure (b), the corpus callosum has increased signal intensity (now isointense with cortex) and corresponding decreased staining for myelin on histology. Six weeks after being taken off of cuprizone, MRI shows return of hypointensity in the corpus callosum and corresponding increased staining for myelin on histology (d).

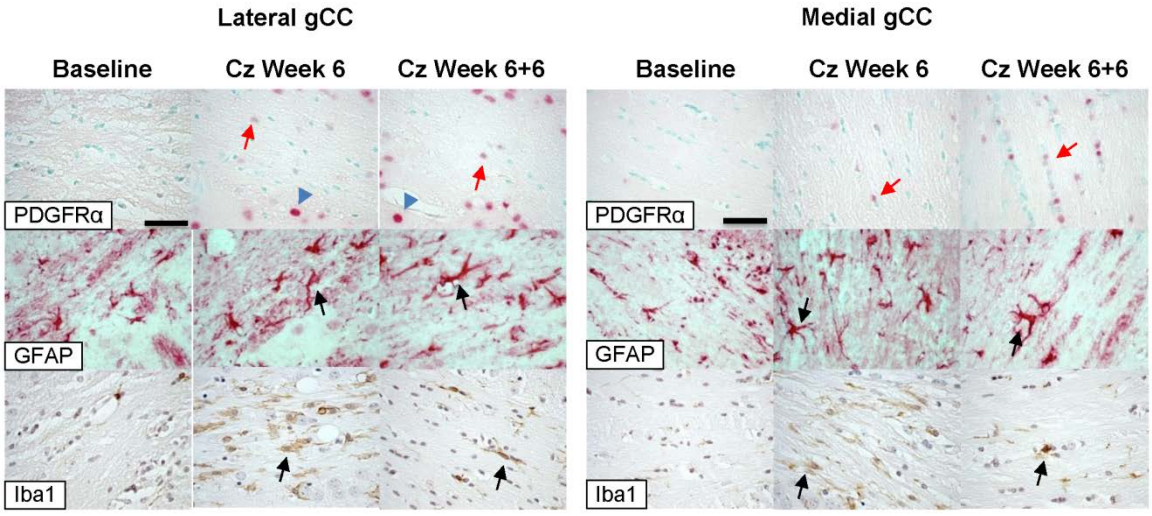

Figure 17. Immunohistochemical Analyses of gCC. OPCs stained with PDFRα appear red (red arrows), often in a tight line with other cells, in the top row (25µm scale bar applies to all images). Note that neurons (blue arrowheads) expressing PDGFRα exhibit large, round nuclei. Activated astrocytes, stained red, are identified by an enlarged cell body and stalky processes in the second row (arrows). Microglia appear brown in the bottom row (arrows).

We performed additional immunohistochemical analysis of baseline, Cz Week 6, and Cz Week 6+6 mice using antibodies to glial fibrillary acid protein (GFAP, an astrocyte marker), microglia (Iba1), and PDGFRα (a marker of proliferating oligodendroglial precursors). Microglia were markedly increased in affected areas of the corpus callosum after cuprizone treatment compared to baseline animals, with incomplete normalization of microglial signal after 6 weeks recovery. Microglial burden at Cz Week 6 corresponded approximately to the degree of demyelination at various sites: greater microglial burden in lateral gCC than medial gCC, and less microglial burden in lateral iCC and sCC than in medial iCC and sCC, respectively. Oligodendroglial proliferation, as assessed by PDGFRα expression, was modestly increased after cuprizone treatment, and

more strikingly so in the recovery phase, throughout all affected areas of the corpus callosum. **Figure 17** shows representative high-magnification images of medial and lateral gCC stained for GFAP, PDGFRα, and Iba1, at Baseline, Cz Week 6, and Cz Week 6+6.

Gene expression in the CC is heterogenous and aligns with patterns of demyelination and MTR depression

Distinct zones of unique gene expression are evident within the CC, exhibiting caudo-rostral and medio-lateral gradients of regional gene expression correlation. Example seed positions in AGEA: 7.113, 1.873, 5.620 for caudal medial CC; 4.477, 3.302, 5.620 for rostral medial CC. Myelin basic protein (MBP) in-situ hybridization (ISH) expression energy (experiments 112202838 and 79632288)[132,133,135] exhibits the opposite rostro-caudal and medio-lateral patterns of decreased MTR – and demyelination – observed after 6 weeks of cuprizone exposure. That is to say, less demyelination and MTR decrease was observed in the CC where MBP expression is greatest, demonstrating an inverse correlation between MBP mRNA expression and demyelination/MTR decrease.

Discussion

The primary findings of this study were: (i) acute cuprizone-induced demyelination is region-specific and varies along both rostrocaudal and mediolateral gradients; and, (ii) histological estimates of myelin content correlated well with MTR values obtained in-vivo in this model. We further showed that MTR increases in healthy mice throughout adolescence and

adulthood, which may indicate continued myelin development and maturation, demonstrating the need for appropriate age-matched controls in these studies.

Cuprizone induced demyelination showed marked spatial heterogeneity with strong caudal-to-rostral and medial-to-lateral patterns. The caudal-to-rostral pattern of cuprizone-induced demyelination in the medial corpus callosum is knownhas previously been described.[11,16,23,38] Less known is the medial-to-lateral demyelination pattern that we observed in conjunction with the caudal-to-rostral pattern. We are among the first to perform report in-vivo 3D MTR mapping in the cuprizone mouse model and here present the highest resolution 3D characterization of spatial patterns of cuprizone-induced demyelination in medial and lateral CC to date.

Histological estimates of myelin content correlated well with MTR values ($r = -0.58$ and -0.87 in medial and lateral CC, respectively) obtained in-vivo. While MTR changes associated with demyelination were modest (~5-10%) compared to histological assessment of myelin loss (up to 30%), ΔMTR was more highly correlated with demyelination throughout the CC ($r = 0.82$ and 0.83 in medial and lateral CC, respectively).

We demonstrated that acute cuprizone-induced demyelination is not uniform across the mouse brain, or even within individual brain structures. The corpus callosum is the most heavily studied brain structure in the cuprizone model of demyelination in mice. Much previous work has focused on only one subsection of the CC (primarily caudal med-CC) that exhibits a unique spatio-temporal pattern of demyelination that differs from the rest of the structure. The

caudal-rostral gradient of demyelination along the midline of the CC is well defined in the literature; however, substantial discussion of the medial-lateral gradient is lacking. Whole-brain coverage in our MRI experiments clearly shows that the lateral CC/EC experiences a pattern of demyelination essentially opposite of the medial CC, following a rostral-caudal gradient of demyelination rather than caudal-rostral. When viewed together, it becomes evident that the cuprizone-induced injury-repair dynamic is complex and highly varied across the brain. Perhaps varying genetic niches within the corpus callosum, and likely in other regions in the central nervous sytem, contribute to the region-specific nature of demyelination in this model. Gene expression is heterogeneous throughout the CC, and patterns of demyelination may coincide with patterns of basal gene expression. This regional heterogeneity may be essential in not only understanding the mechanisms involved in this model, but also in appropriately and effectively applying it to study human disease.

MTR is a sensitive, but not specific, measure of demyelination in-vivo

MTR is sensitive to demyelination but is not specific: MTR values are substantially changed, typically decreased, by demyelination, but also by inflammation and edema.[65,71] Because the cuprizone model does not induce substantial edema or axonopathy, we can be confident that the changes observed in MTR here are reflective more of demyelination than any other pathology. Preserved axonal density combined with increased astrocyte infiltration and activated microglia (**Figure 17**) will contribute to MTR values and likely obscure MTR decreases due to demyelination alone. So, ΔMTR may be

viewed as a measure of injury outpacing repair and development in this model. Histological staining with BGII (**Figure 14**) and subsequent quantification (**Table 1**) match well with patterns of MTR changes shown in **Figure 10** - **Figure 13**, thus validating MTR as a good measure of demyelination in this model.

Attenuated MTR in multiple sclerosis lesions may be an effect of a degraded macromolecular matrix, damaged myelin or axonal membranes, or by inflammatory edema, all of which tend to dilute the macromolecular pool.[72] We have also seen extensive MTR changes in the lysolecithin model of demyelination that extend well beyond the lesion boundary, are unrelated to demyelination, and are most likely due to edematous inflammation (unpublished). Interpretation of MTR measurements in other rodent models of MS is more complex than in cuprizone: lysolecithin induces substantial global edema, and EAE involves significant inflammation and axonopathy with limited demyelination.

MTR decreases in cerebellum, thalamus, cerebral cortex have been reported;[70] we observed similar patterns but did not focus on these tissues in this analysis. That pathological mechanisms in the CBLL are distinct from the CC seems clear, but the exact nature of each is yet unknown. Zaaouri, et al, used thalamus as a reference tissue for nomalization and reported lower MTR values in the CC (35-25% compared to 55-45%) than in the present work. However, the thalamus is not a suitable reference region as demyelination and reduced MTR after 6 weeks of cuprizone treatment have been demonstrated in this area.[70] Thiessen, et al, report MTR at 7T in rostral CC with slightly lower baseline (50%) and greater depression at Week 6 (38%) than what is shown in this paper.

Thicker slices used in that work may lead to understimated MTR due to partial volume effects. Fjær, et al (2013), performed a similar longitudinal MTR study using a horizontal bore 7T instrument and MT imaging parameters similar to ours. However, because absolute MTR values were not reported, their findings cannot be directly compared to our results. Instead, ΔMTR values are reported, which are in excellent agreement with our findings. Rates of demyelination and remyelination calculated with a Linear Mixed Effects Regression vary across structures and support the theory that multiple mechanisms of damage and repair exist in the cuprizone model. Their work also demonstrated that MTR was correlated with myelin content in both CC and deep gray matter, but MTR did not appear to be influenced by oligodendrocyte density in the CC. Magnitude of response to demyelination is substantially lower in MTR compared to histology, but is nevertheless clear and significant. The attenuation in MTR effect may be due to infiltration of astrocytes, microglia and macrophages, which may increase observed MTR and confound the measurement. The correlation we observed between MTR and myelin content is consistent with previous reports.[72]

MTR values varied slightly between mice and across days, likely due to natural biological variance, and fluctuation in the MRI hardware. Deviations of approximately 5% (**Figure 10** a-c, shaded bands) are consistent with what has been previously reported at 2.35T,[71,73] 7T,[70] and 9.4T.[72] Myriad data normalization techniques have been proposed to overcome instrument variation. Here, a basic global histogram matching approach was selected as it limits the assumptions required of a reference tissue and still allows for evaluation of

absolute MTR values. Histogram shapes were preserved during scaling, thus preserving tissue contrasts. The histogram matching technique is not perfect: all images are necessarily biased toward the signal intensities of the reference images. Calculated MTR values are dependent upon experimental methods (magnitude and offset of saturation pulse), thus will vary across studies unless acquisition parameters are identitical. Regardless of differing acquisition details, the trend of significantly decreased MTR corresponding to demyelination is consistent across studies. **Figure 10** MTR values show some variance across structures at baseline, most notably in the splenium of the CC. Lateral CC/EC MTR values are significantly lower than medial CC ($p < 0.01$) in both splenium and isthmus of CC, which can be attributed to partial volume effects inherent in selecting narrow structures that are on the order of 1-2 voxels wide. That the medial sCC shows significantly higher baseline MTR ($p < 0.01$) than isthmus or genu is surprising, but may be attributed to the inclusion of other heavily-myelinated structures including the dorsal hippocampal commisure, fornix, and cingulate.

In addition to the corpus callosum, MTR decreases in cerebellum, thalamus, cerebral cortex have been reported;[70] we observed similar patterns but did not focus on these brain regions in this analysis. Zaaouri, et al, used thalamus as a reference tissue for normalization and reported[72] lower MTR values in the CC (0.35-0.25 compared to 0.55-0.45) than in the present work. However, the thalamus is not a suitable reference region as demyelination and reduced MTR after 6 weeks of cuprizone treatment have been demonstrated in

this area.[70] Thiessen, et al,[122] reported MTR at 7T in rostral CC with slightly lower baseline (0.5) and greater depression at Week 6 (0.38) than what is shown in this paper. Fjær, et al,[70] performed a similar longitudinal MTR study using a 7T MRI instrument and MT imaging parameters similar to ours, and report ΔMTR that are in excellent agreement with our findings. The correlation we observed between MTR and histologically-determined myelin content is consistent with the work of Fjær and others.[72] The magnitude of response to demyelination is substantially lower in MTR compared to histology, but is nevertheless clear and significant. The attenuation in MTR effect size may be due to MTR's sensitivity to axonal density and infiltration of astrocytes, microglia and macrophages, which may increase observed MTR and confound the measurement.

Acute demyelination is region-specific and expresses heterogenous pathology

Estimates of percentage of myelinated axons present in the adult CC vary greatly due to inconsistencies in definitions of 'mature,' and application of minimum axonal diameter thresholds. Early studies reported only roughly 30% of mature axons in CC are myelinated;[44] conversely, more recent studies indicate that 80-90% of axons are myelinated in the healthy mouse CC.[16,17,45] Our method of quantifying myelination assesses the area of tissue that stains for myelin compared to total area of interest. Using this technique we report baseline as 100% myelination and then demyelination is reported as a fractional area in the CC that does not stain for myelin.

Qualitatively, microglial burden tracked with severity of demyelination and MTR reductions. Microglial infiltration was observed in all CC ROIs, with higher

burden in areas exhibiting greatest demyelination. Reactive astrocytes were identified by their GFAP-positive cytoplasmic processes. This morphologic feature of reactive astrocytes is more difficult to assess quantitatively and is further complicated by subtle variations in astrocyte morphology in the relatively loose lateral corpus callosum compared to the more dense medial tissue. Additionally, given the regional differences in astrocyte morphology, making comparisons between lateral and medial CC astrocyte infiltration is challenging. Quantitative analysis of PDGFα receptor stains can also be ambiguous due to (1) non-specific staining of OPCs and neurons, (2) often only a small number of positive oligodendroglia were observed, so sampling variation can lead to gross under- or overestimation of effect, and, (3) the staining of oligodendroglia, in contrast to neurons, was quite variable and sometimes light in these sections. This may be due to the fact that as oligodendrocytes mature they lose expression of this antigen, thus reflecting biological phenomenon rather than a technical problem.

Some investigators have suggested that regional vulnerability to demyelination is related to the order of maturation, and thus the age of oligodendrocytes and myelin sheaths.[134] The CC and dorsal hippocampal commissure are among the last white matter tracts to reach maturity and become fully myelinated.[136,137] Newly formed oligodendrocytes myelinate an increasing number of axonal segments as the animal ages, and as such have extremely high metabolic demands, leaving them particularly vulnerable to damage.[138] This suggests that oligodendrocytes in the CC and dorsal hippocampal commissure

should be equally vulnerable to damage, and more so than any other structure in the brain. However, the timing of myelination is not uniform: the caudal parts of the CC are myelinated earlier in development than are rostral regions. If we accept that the newer oligodendrocytes (rostral CC) wrap more axonal segments than older oligodendrocytes (caudal CC), we would expect the rostral medial CC to experience greater demyelination than the caudal medial CC. However, we observe the opposite pattern, so this explanation is unsatisfactory.

Axonal caliber varies along a rostrocaudal gradient in the human CC,[139,140] and may influence susceptibility to demyelination and capacity for future remyelination. While true in humans, ultrastructural studies have demonstrated that initial axon caliber does not vary significantly across the mouse CC,[109,119] and remains constant with age,[137] and thus does not predict demyelination in this model. However, a more thorough characterization of axon caliber across the whole CC as the brain ages will be necessary to adequately address this possibility.

Histopathological heterogeneity between the small white matter structures adjacent to CC has been observed at a variety of time points and illustrates the importance of distinguishing between structures such as CC and dorsal hippocampal commissure, among others.[95] This distinction is interesting histologically, but is challenging to detect using MRI. Despite having collected the highest resolution in-vivo MRI to date, our resolution was too low to reliably distinguish these structures. Thus, separate comparisons between histology and MRI for these structures were not performed. ROI analysis separating lat-CC and

med-CC reveals a complex pattern of demyelination both histologically (**Table 1**) and via MRI (**Figs. 2-5)**: rostral CC demyelinates laterally but is relatively unaffected medially; caudal CC demyelinates medially, but is preserved laterally. So, there is a clear caudal-to-rostral and medial-to-lateral pattern of demyelination within the CC. A very recent study demonstrated a rostro-to-caudal pattern of demyelination in the cortical gray matter similar to what is shown here in lateral CC, wherein demyelination occurs earlier and with greater severity in motor cortices (rostral, proximal to gCC) than in the somatosensory cortices (caudal, proximal to iCC).[141] This result supports our observation of a complex pattern of demyelinating gradients throughout the mouse brain. We stress the importance of obtaining parametric maps to reveal the intricate and subtle spatial patterns of demyelination that correspond to those seen on histology, as shown in Figs 7-8.

It has been suggested that the lateral and medial CC can be combined for analysis in the rostral CC;[71] our results establish that the distinction between medial CC and lateral CC/EC is critical in accurately evaluating extent of demyelination and remyelination. Loss of myelin in the rostral lateral CC/EC adjacent to unaffected med-CC consistent with our observations has been previously shown,[98,134] though little analysis has been provided. Clearly, pooling medial CC and lateral CC in ROI analysis obscures underlying pathological heterogeneity and neglects essential model characteristics.

We observed few OPCs in demyelinated CC ROIs after 6 weeks of cuprizone treatment, consistent with the modest remyelination attempts prior to

removal of cuprizone. Accordingly, greater numbers of OPCs were observed in the recovering CC 6 weeks after cuprizone removal (Fig. 10). Oligodendrocyte precursor migration and differentiation is determined by a complex system of long-range and short-range cues and growth factors expressed during development,[142–144] and the process of progenitor migration and fate in the adult brain, particularly in disease state, is still unclear. Neural progenitor cells (NPCs) reside primarily in the subventricular zone (SVZ) in adult brains, located along the lateral wall of the lateral ventricles, and are also found in the subgranular zone (SGZ), adjacent to dentate gyrus.[145,146] A number of studies have explored the roles of the SVZ and SGZ in responding to cuprizone-induced demyelination.[147–152] The results from these studies combined with the patterns of demyelination and remyelination observed in the present work suggest that the rostral med-CC is preferentially supported by progenitor cells from the SVZ via the rostral migration stream, while the SGZ responds to injury in the caudal med-CC. Additional histopatholigical studies achieving more complete brain coverage are needed to elucidate how the different populations of progenitor cells contribute to repair and regeneration in this model, particularly with respect to the lat-CC/EC.

Caudal-rostral gradients are reduced in chronic demyelination

The rostro-caudal gradient of demyelination in the midline of the CC is distinct and well-known under acute demyelination. Interestingly, demyelination is much more uniform along the midline when chronic demyelination is achieved. Xie, et al, demonstrated that sCC contains similar levels of myelinated fibers in

both acute and chronic stages of demyelination, whereas the differences between acute and chronic demyelination are striking in both the iCC and gCC. This indicates that demyelination is substantially delayed in iCC and gCC compared to sCC, but, given enough time, the caudal-rostral gradient becomes appreciably less severe. Additionally, myelin thickness is not different from baseline after 4 or 12 weeks of cuprizone challenge.[119]

Axonal diameter and myelin thickness do not vary significantly rostrocaudally or mediolaterally in the healthy mouse CC. However, a moderate caudal-rostral gradient in axonal diameter is observed after 4 weeks cuprizone challenge and persists with a slightly increasing gradation after 12 weeks cuprizone.[119,120] Caudal CC experiences the greatest reduction in axonal diameter, consistent with severity of demyelination. Perhaps the temporal variations are indicative of some underlying mechanism of protection or repair in rostral CC that is either not present or is less effective in caudal CC.

Cerebral white matter may continue to develop in healthy mice throughout adolescence and adulthood

Previous DTI studies of maturation in the mouse brain suggest development plateaus around 5-6 weeks after birth,[153] and maturation is spatially and temporally heterogeneous throughout development.[154] Other work has suggested that MTR maps in the healthy mouse brain do not change with age and that age-matched controls may be superfluous.[71] However, a very recent study demonstrated age-related changes in T_2-w and diffusion kurtosis imaging in the medial sCC, body of CC, gCC, and cortex between eight and twenty weeks

of age.[141] Our results also indicate that age-matched controls are in fact essential in this model, particularly for quantitative MRI studies. **Figure 10** shows MTR increases after Baseline in both medial and lateral CC in healthy controls, suggesting ongoing development and maturation. Indeed, the Week 6 MTR effect size increased when values were compared to age-matched controls rather than Baseline (average Cohen's d = 1.5 [range 0.5-3.3] compared to Baseline; d = 2.7 [range 1.7-5.2] compared to age-matched controls). Further, it is clear that even 6 weeks after cuprizone cessation, MTR remains abnormally low compared to healthy age-matched controls. These data suggest that recovery to Baseline MTR does not represent true normalization with respect to healthy age-matched controls.

Proximity to sources of neural progenitor cells may determine extent of demyelination and remyelination

As an alternate to previous theories of region-specific demyelination and remyelination, one may look to the origin and migration of oligodendrocyte progenitor cells (OPCs), neural progenitor cells (NPCs), and neural stem cells (NSCs) in the adult brain for some clarity. NPCs reside primarily in the subventricular zone (SVZ) in adult brains, located along the lateral wall of the lateral ventricles, and are also found in the subgranular zone, adjacent to dentate gyrus.[145,146] Oligodendrocyte precursor migration and differentiation is determined by a complex system of long-range and short-range cues and growth factors expressed during development,[142,143] and the process of progenitor migration and fate in the adult brain, particularly in disease state, is still unclear.

Mason, et al, (2000)[147] demonstrated a significant increase in OPCs and NSCs in the SVZ and posterior fornix in under 4 weeks of cuprizone exposure, prior to accumulation within the adjacent demyelinated med-CC. Their conclusion that these progenitor cells migrate to the adjacent CC and presumably contribute to the eventual remyelination and repair of damaged tissue was later confirmed.[148] Guglielmetti, et al, labeled SVZ neuroblasts *in-vivo* and showed that while progenitors from the SVZ do not contribute to remyelination in the splenium of the CC, rostral migration of neuroblasts from the SVZ increases following cuprizone treatment.[149] The majority of neuroblasts in the SVZ are oriented to migrate along the rostral migration stream.[150] So, in agreement with recent reports,[151,152] we suggest that the splenium of the CC is too far caudal to receive support from cells labeled in the SVZ but that remyelination in rostral medial CC is likely supported by this cell population. Progenitor cells originating in the SGZ rather than the SVZ may be responsible for repairing the splenium of the CC. Additional studies achieving more complete brain coverage are needed to elucidate how the different populations of progenitor cells contribute to repair and regeneration in this model.

Regional differences in gene expression may contribute to region-specific vulnerability

Regional heterogeneity in resistance and vulnerability to demyelination in the cuprizone model almost certainly involves complicated interactions of numerous enzymes, proteins, cofactors, and signaling pathways. Heterogeneous gene expression in the mouse CC suggests genetically distinct zones within the

CC that coincide with varying degrees of demyelination. It was initially surprising to us that MBP is most abundant in those parts of the CC/EC that are most resistant to cuprizone-induced demyelination. MBP associated with the myelin membrane is responsible for the multilamellar structure of myelin and is highly sensitive to metal ion concentrations. Cuprizone administration can create imbalances in copper and zinc ion concentration, which could subsequently destabilize the MBP-membrane association, reduce myelin compaction, and degrade myelin quality. Perhaps it is the regionally increased expression of MBP that is responsible for, or at least an important contributor to, resistance to cuprizone-induced demyelination.

Heterogeneous gene expression in the mouse CC suggests genetically distinct zones within the CC that coincide with varying degrees of demyelination. MBP most certainly plays an important role in this model, but it is likely not the only factor at play; however, a complete proteomic analysis is beyond the scope of this paper. We recommend additional, more complete proteomic studies of the healthy CC and surrounding structures to thoroughly characterize the genetic environment that may affect demyelination and remyelination in neurodegenerative disorders.

Regional heterogeneity may hold the key to understanding the model

Compelling evidence has been given to suggest that the primary action of cuprizone is metabolic disruption, which leads to oligodendrocyte death. Our findings suggest a more complex story. Regional heterogeneity in demyelination and remyelination suggests distinctly varying microenvironments exist in the CC.

Perhaps it is the varying spatial proximity to various NPC niches[142,143,145–152] coupled with heterogeneous expression of MBP RNA that determines, at least partially, the regional and site-specific nature of demyelination and remyelination in the cuprizone mouse model. A better understanding of spatial and temporal pathological patterns in the model is essential to determining how and why damage and repair occur. Thus, further study employing imaging techniques that are sensitive to demyelination and are capable of whole-brain coverage is necessary. MRI is ideal for longitudinal studies to examine temporal progression of demyelination and subsequent remyelination in-vivo, and obtaining comprehensive histological data will help to better understand these processes. MRI studies can indicate when and where to focus histological analyses, thus increasing both efficiency and effectiveness of histological comparisons.

To date, few studies have commented on the medio-lateral patterns of demyelination, and its importance is certainly underappreciated. Demyelination is significant in the rostral lateral CC by week 6 and possibly even earlier. We suggest that only through true 4D studies, assessing the changes in the whole brain as a complete 3D organ over time, will we be able to paint a thorough picture of the cuprizone model of demyelination and remyelination. A similar comprehensive study of spatial patterns of demyelination in the chronic state has yet to be completed and will help to answer many of the questions raised here regarding mechanisms of both damage and repair. Understanding the patterns and mechanisms of site-specific damage and repair in the cuprizone model can

be helpful in understanding and treating human diseases, such as multiple sclerosis.

The ROI analysis in this study is informative, but has limitations. At first glance it appears that MTR is more sensitive to demyelination in lateral iCC than in lateral sCC when comparing ROI analysis in Fig. 3 to BGII results from **Table 1**. However, two primary factors may obfuscate results from ROI analysis of MRI data in these regions: (1) partial volume effects from surrounding gray matter could artificially decrease MTR at all time points, effectively reducing sensitivity to subtle MTR changes within the CC; (2) enlarged ventricles observed at Week 6 could exaggerate MTR decreases in lateral iCC more than in other regions, giving the appearance of high sensitivity in iCC and no sensitivity in sCC. Lateral CC is quite narrow (2-3 voxels) in both iCC and sCC, thus increasing the potential for partial volume effects in ROI analyses. Although, average MTR maps indicate clear preservation of contrast in all periventricular regions of all slices (Fig 6), which supports our ROI results. Nevertheless, potential for partial volume effects emphasizes importance of high-resolution parametric mapping to demonstrate fine regional variations that may be obscured by ROI analysis alone. Additionally, our BGII quantification approach introduces limits in interpretation of histological results. In some cases only a small number of mounted tissue sections were useable for analysis. Demyelination calculated as percent area as we have done here requires the observer to estimate the extents of CC, which is particularly challenging in heavily demyelinated lateral CC and EC. Limited tissue coverage and biological variation are likely sources of error in

myelin content estimation and will contribute to apparent inconsistency in matchup between BGII and MTR values in the narrow lateral extents of the iCC and sCC.

Our results support previous findings that MTR correlates well with demyelination and is a sensitive, if not specific, marker of myelin content in-vivo. We expanded upon previous knowledge of the cuprizone model through a more complete characterization of the spatial pattern of demyelination in the corpus callosum after 6 weeks of cuprizone challenge and demonstrate the importance of appropriate age-matched controls. While the caudal-rostral pattern of demyelination has been shown, this study demonstrates an additional medio-lateral pattern of demyelination in the cuprizone model. This site-specific demyelination may be related to regional gene expression variation and/or spatial proximity to distinct sources of progenitor cells. It is evident that the unique and site-specific demyelination in the cuprizone model has much to teach us about the complex mechanisms of both damage and repair in demyelinating disease.

Toward a standardized quantitative imaging protocol for multiple sclerosis: a multisite study of magnetization transfer and quantitative T_1 imaging techniques

Ian Tagge,[1] Daniel Schwartz,[1] Katherine Powers,[1] Rohit Bakshi,[2] Peter Calabresi,[3] Todd Constable,[4] John Grinstead,[1,5] Roland Henry,[6] Govind Nair,[7] Jiwon Oh,[3,8] Nico Papinutto,[6] Daniel Pelletier,[9] Daniel Reich,[7] Nancy Sicotte,[9] William Rooney,[1] and the NAIMS Cooperative

[1]Oregon Health & Science University, Portland, OR

[2]Brigham and Women's Hospital,Harvard Medical School, Brookline, MA

[3]Johns Hopkins, Baltimore, MD

[4]Yale, New Haven, CT

[5]Siemens Medical Solutions, USA, Portland, OR

[6]University of California San Francisco, San Francisco, CA

[7]National Institute of Neurological Disease and Stroke, National Institute of Health, Bethesda, MD, United States

[8]University of Toronto, Toronto, ON, Canada

[9]University of Southern California, Keck School of Medicine, Los Angeles, CA, United States

Introduction.

The North American Imaging in Multiple Sclerosis (NAIMS) Cooperative was formed with the goal of developing sensitive, reliable imaging-based surrogates for disease progression in MS. The current lack of standardization in MRI protocols leads to increased variability, particularly in semi-quantitative techniques such as MTR, and makes comparisons between studies almost impossible.[68] An essential step in establishing a standardized protocol is demonstrating that the proposed protocol can be reliably implemented at multiple sites, by independent investigators, and on a variety of MRI systems. Subsequently, careful quality assurance measures must be performed to verify consistency not only in image quality, but also in results obtained from semi-quantitative and quantitative imaging techniques. To this end, a single MS subject travelled to seven NAIMS sites to undergo identical imaging sessions, providing a robust means of comparing protocol implementation and performance at each site. These efforts will accelerate MS research by creating standardized quantitative and semi-quantitative imaging protocols, a centralized database, multiple analytic tools, and data sharing across NAIMS sites.

Quantitative magnetization transfer (qMT) techniques have been proposed to determine macromolecular proton fraction in tissue in an attempt to overcome the semi-quantitative variability and potentially non-specific nature of MTR.[62–64,69,124] However, qMT modeling requires additional quantitative T_1 (qT_1) imaging, which can increase acquisition time beyond what is clinically feasible. In this work

we set out to obtain all images required for qMT modeling in less than ten minutes in an attempt to remain within clinically reasonable time limits.

Methods.

Healthy control subjects were recruited at each site for initial development and validation of the study protocol. A 44 year old male subject with clinically definite, stable RRMS (13 years disease duration, no new lesions or significant clinical progression for at least 400 days prior to this study) was selected from a cohort at the National Institutes of Health (NIH). The subject travelled to seven North American sites and underwent two distinct 3T MRI sessions at each site. Informed consent was obtained at each imaging center: Harvard Brigham and Women's Hospital (BWH), Cedars-Sinai (Cedars), Johns Hopkins University (JHU), National Institute of Neurological Disorders and Stroke (NIH), Oregon Health & Science University (OHSU), University of California, San Francisco (UCSF), and Yale. Hardware and software details for each participating site are shown in **Table 3**. The subject was scanned at NIH both at the beginning and at the end of the study; see the timeline in **Figure 18**.

MRI

All sites collected data using a 3T Siemens instrument (additional details in **Table 3**). The variable flip angle (VFA) method was employed to create whole-brain quantitative T_1 (qT_1) maps. VFA images were acquired using whole-brain 3D gradient recalled echo (GRE) sequences with 2.3 ms echo time (TE), 20 ms

recycle time (TR), four read-RF pulses of nominal flip angle (FA): 3°, 6°, 10°, 20°; field of view (FOV) 19.2 cm x 25.6 cm, 192 x 256 matrix, 48 slices, 3 mm slice thickness, 1 min 20 sec acquisition time per FA. $\boldsymbol{B_1}$ field maps were acquired using a Siemens service protocol with TR 1000 ms, TE 14 ms, FA 90°, FOV $(25.6\ cm)^2$, 64 x 64 matrix, 48 slices, and 5 mm thick slices, 1 min 9 sec acquisition time. Magnetization transfer images were acquired with two saturation pulse offset frequencies (4kHz, 100kHz) at 8 μT amplitude, sufficient for magnetization transfer ratio (MTR) calculation. Other acquisition parameters include: TR 43 ms, TE 2.3 ms, FA 10°, FOV 19.2 cm x 25.6 cm, 192 x 256 matrix, 48 slices, 3 mm slice thickness, 2 min 45 sec for each MT contrast.Total acquisition time for all qMT images was 11 min 59 sec. High resolution T_1-w 3D MPRAGE (TE 2.52 ms, TR 1900 ms, inversion time (TI) 900 ms, FA 9°, 256 x 246 matrix, FOV $(25\ cm)^2$, 176 sagittal slices, 1mm slice thickness), and T_2-w FLAIR (TE 355 ms, TR 4800 ms, TI 1800 ms, FA 120°, 256 x 258 matrix, FOV $(25.6\ cm)^2$, 176 sagittal slices, 1 mm slice thickness), were used for segmentation.

Table 3. NAIMS Sites and Equipment

Site	Manufacturer	Model	Software	Receive Coil
BWH	Siemens	Skyra	D13	32 channel
Cedars	Siemens	Verio	B17	32 channel
JHU	Siemens	Trio	VB17	32 channel
NIH	Siemens	Skyra	VD13A	32 channel
OHSU	Siemens	Trio	VB17	32 channel
UCSF	Siemens	Skyra	VS13C	64 channel
Yale	Siemens	Skyra	C13	32 Channel

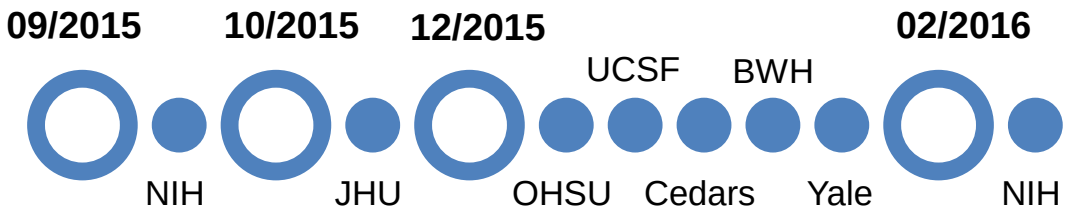

Figure 18. MS Subject Site Visit Timeline.The MS subject received a baseline scan at NIH in September, 2015, before traveling to the rest of the sites in October and December. A final set of scans were obtained at NIH in February, 2016.

Image Processing

All images were coregistered into a common space with FSL's FLIRT.[130] Briefly, all base MT and VFA images from one site (OHSU Session 1, reference set) were averaged to create a reference image for coregistration. All base MT images from every site and session were coregistered to the averaged image created from the reference set and averaged to create a new reference image. All images, including those from the original reference set, were coregistered to the new reference image. All base images in the new common space were averaged, and a brain mask was created with FSL's BET.[130] MTR maps were calculated for each individual imaging session from the coregistered base images using Equation 12, where M_0 is voxel signal intensity of the image collected with a 100 kHz offset saturation pulse, and M_{sat} is voxel signal intensity of the image collected with a 4 kHz offset saturation pulse applied. Tissue and lesion masks were created from the anatomical MPRAGE and FLAIR images using LesionTOADS software as described elsewhere.[155,156] Individual lesions in the thalamus, periventricular white matter (PVWM), and centrum semiovale (CSO) were manually selected for region of interest (ROI) analysis. T_1 maps were calculated by fitting voxel signal intensity (S_i) using the following equation:

$$S_i(TR,\alpha) = M_{0i}\frac{\sin(B_{1i}\cdot\alpha)\cdot(1-e^{-TR/T_{1i}})}{1-e^{-TR/T_{1i}}\cdot\cos(B_{1i}\cdot\alpha)}, \qquad (13)$$

where $\boldsymbol{B_1}$ is the FA correction factor calculated from the acquired $\boldsymbol{B_1}$ map, α is the nominal FA, and S_i is the voxel signal intensity from the VFA images.

Results.

Imaging sessions were successfully completed at all sites between October 2015 and February 2016. Coregistered axial MTR maps for all sites and imaging sessions are shown in **Figure 19**. Whole-brain average cerebral WM, cortical GM, and lesion MTR values were obtained using the respective masks obtained from LesionTOADS segmentation. Mean (±standard deviation) white matter, cortical gray matter, and lesion MTR values for all imaging sessions were: 0.27 (0.005), 0.20 (0.009), and 0.21 (0.006), respectively. MTR values were in good agreement across sites and imaging sessions. Whole-brain MTR histograms for all imaging sessions are plotted together in **Figure 20**. A scatter plot of mean MTR in WM and GM is shown in **Figure 21**. One site demonstrated unusually low session 1 GM MTR; all other sites showed good agreement between sessions and values were consistent across sites. Mean intra-site MTR variance in WM, GM, and lesions was 0.0001 across all sites. Similar agreement across sites and sessions was observed in three manually selected lesions, as shown in **Figure 22** and **Figure 23**.

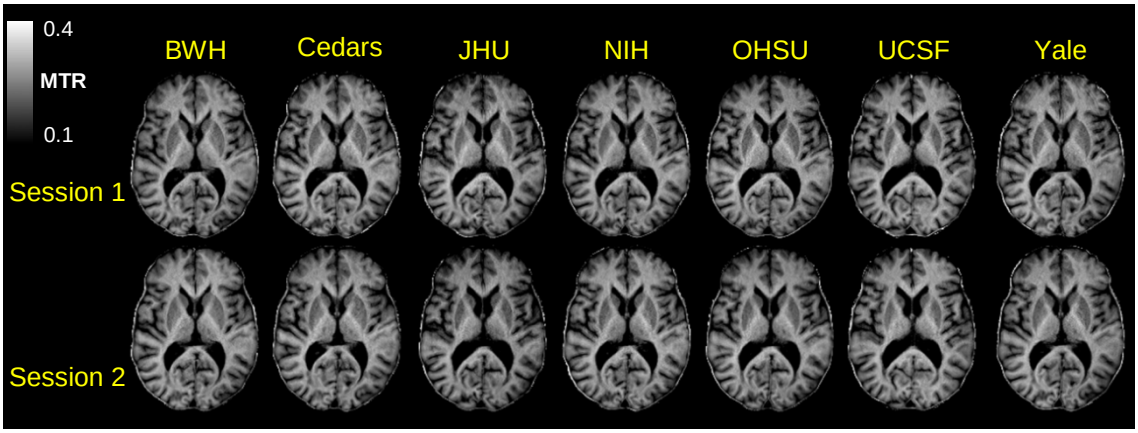

Figure 19. Axial MTR maps across sites and sessions in the MS Subject. Axial MTR maps are shown for all sites (horizontal) from both sessions (Session 1 top, Session 2 bottom). MTR maps show consistent contrast and values across all sites and sessions.

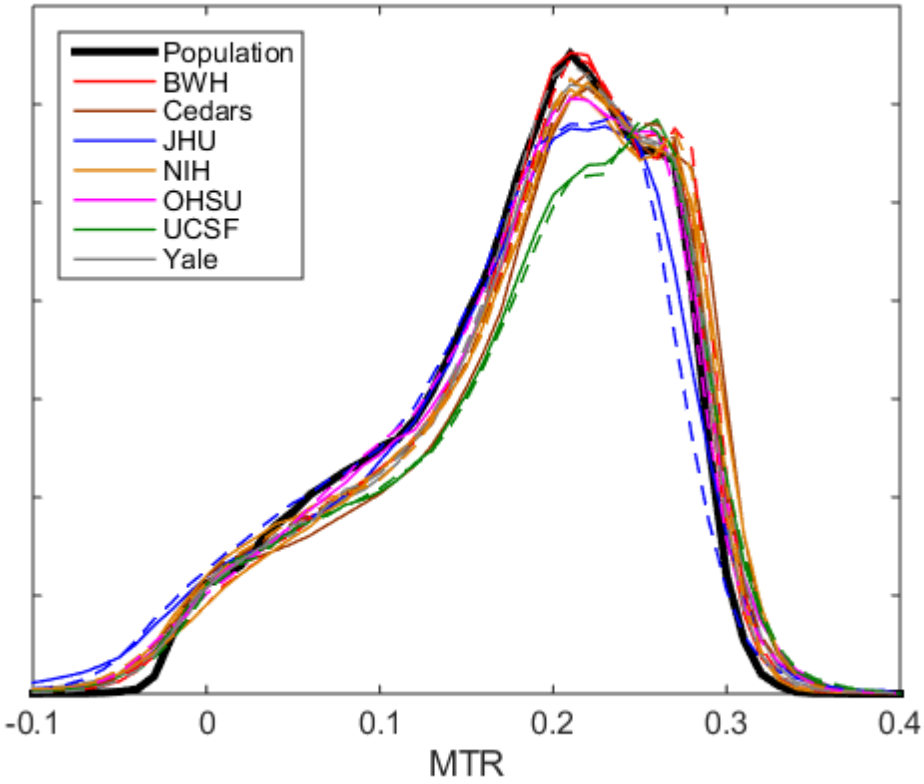

Figure 20. Whole-brain MTR Histograms. Voxel MTR histograms are in excellent agreement for all imaging sessions. The Session 1 histogram for each site is shown in a solid line, and dashed lines indicate Session 2. The histogram for the population average is shown in a solid black line. Note the departure of JHU and UCSF curves from the average is due to limited infratentorial brain coverage, thus lower voxel counts.

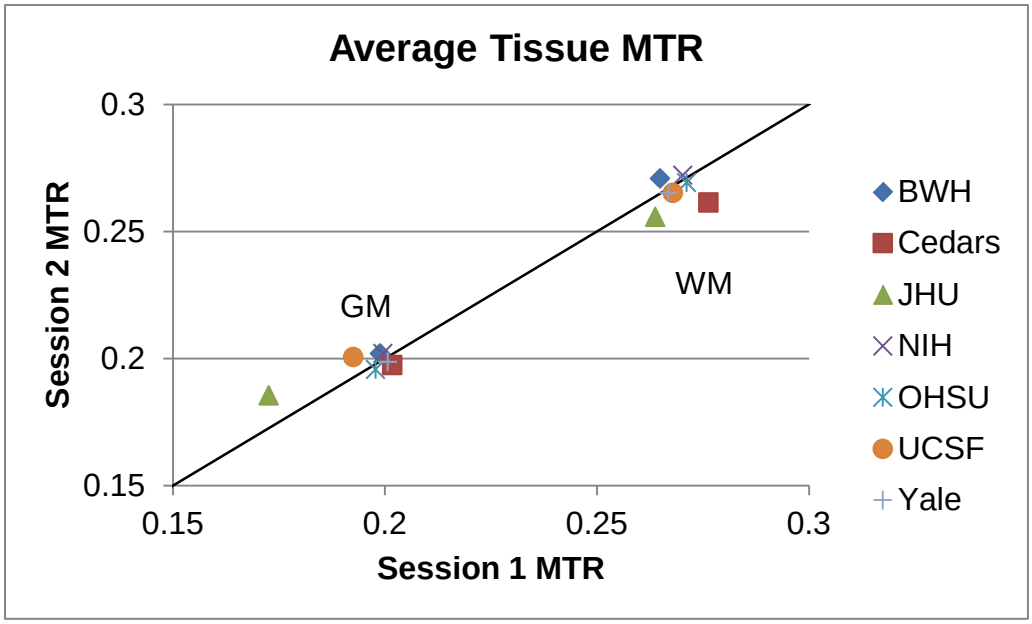

Figure 21. MTR Reproducibility in Tissue. Average MTR values in WM and GM are plotted for Session 1 vs Session 2. The black solid line represents unity, or perfect agreement between Session 1 and Session 2 MTR values. Aside from one Session 1 outlier, all data points are clustered around the unity line demonstrating reproducibility across sessions and sites.

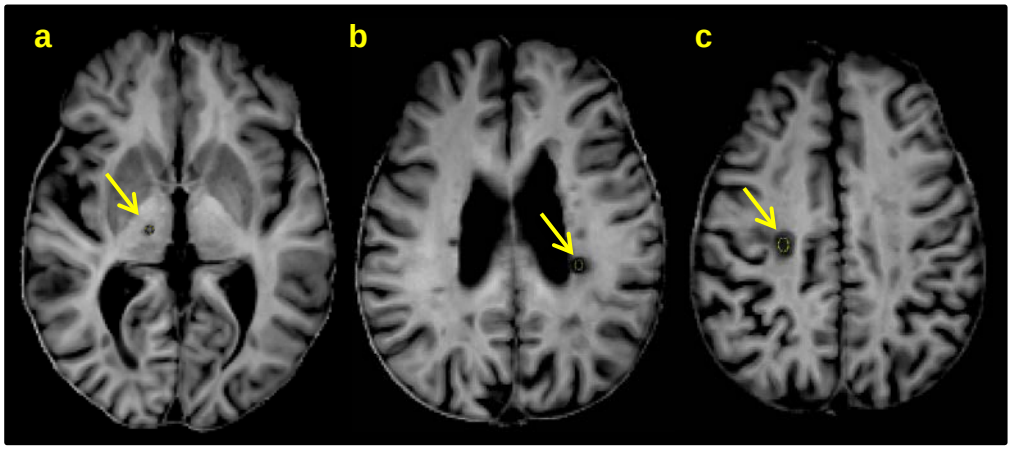

Figure 22. Lesion ROI Selection. Yellow arrows highlight ROIs within lesion areas selected in the thalamus (panel a), periventricular WM (panel b), and CSO (panel c) from the population average MTR map.

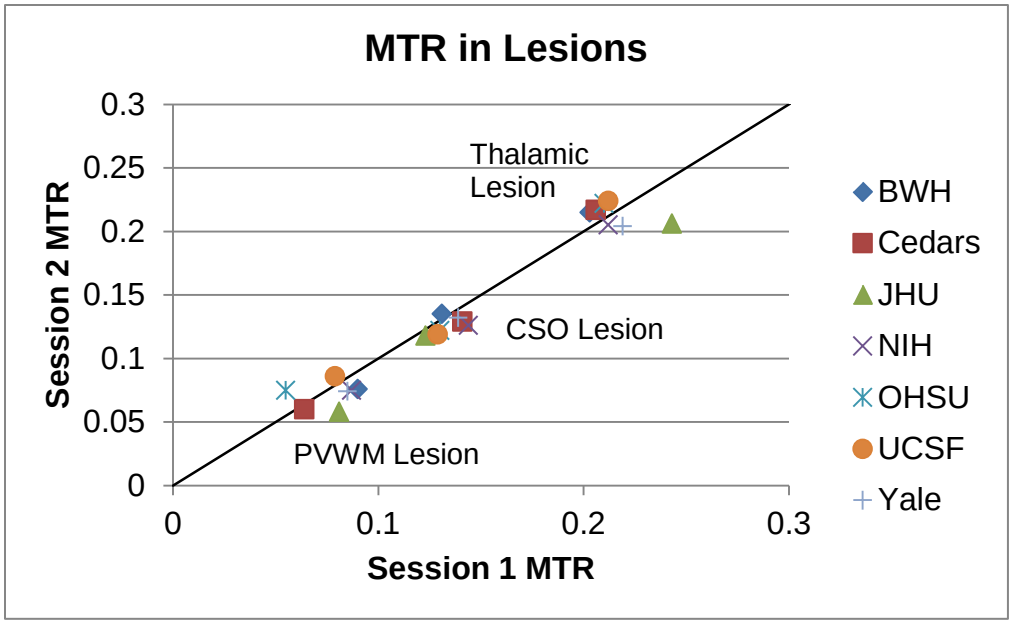

Figure 23. MTR Reproducibility in Lesion ROIs. Average MTR values from the lesions in Figure 3 are plotted for Session 1 vs Session 2. The black solid line represents the line of unit slope, or perfect agreement between Session 1 and Session 2 MTR values. Aside from one Session 1 outlier in the thalamic lesion, perhaps due to coregistration errors or partial volume effects, all data points are clustered around the unity line demonstrating reproducibility across sessions and sites.

Despite applying corrections, $\boldsymbol{B_1}$ inhomogeneity contributed to substantial inconsistencies in qT_1 maps, particularly in the most superior and inferior regions of the brain where radio frequency coil performance is variable and sensitive to subject placement within the instrument. Axial R_1 ($\equiv 1/T_1$) maps are shown in **Figure 24** for the MS subject collected across all sites and sessions. Even in this mid-brain slice where $\boldsymbol{B_1}$ deviations are expected to be smallest, some R_1 maps show inhomogeneity suggestive of insufficient $\boldsymbol{B_1}$ corrections and variable $\boldsymbol{B_1}$ field both across and within sites.

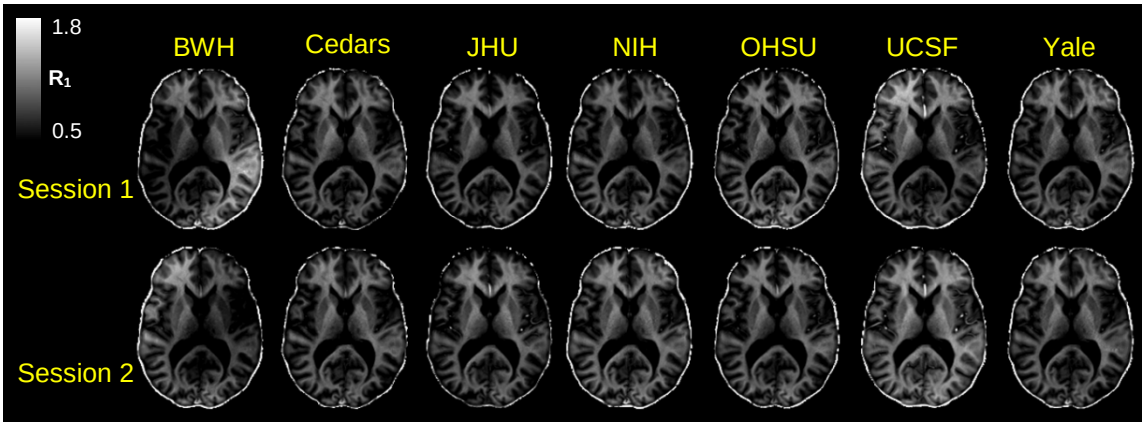

Figure 24. Axial R_1 in the MS Subject. Axial R_1 map sare shown for all sites (horizontal) from both sessions (Session 1 top, Session 2 bottom). Substantial inhomogeneity is seen in many of the R_1 maps, most notably those from BWH (left). Inhomogeneity varies both between sites and between sessions within sites.

Discussion.

Magnetization transfer imaging has found widespread use in assessing tissue changes in multiple sclerosis.[60,61,157–161] However, unlike purely quantitative measures such as qT_1, MTR is semi-quantitative and absolute MTR values are determined by acquisition parameters as much as they are by tissue characteristics. Thus, comparing studies or establishing a definite correlation between specific MTR values and disease state remains challenging, if not impossible. MTR is still attractive as an imaging biomarker because it does correlate with tissue pathology,[162,163] can be rapidly acquired, and parametric calculation is trivial. Additionally, MTR is effectively a self-bias-correcting technique so little or no additional post-processing or corrections are necessary.

Main sources of MTR variance in this study include imperfect coregistration and segmentation, which were compounded by the thick slices

used in this study. The total acquisition time allotted for MTR, qT_1, and $\boldsymbol{B_1}$ mapping was 10 minutes, requiring reduced spatial resolution to meet the target scan time. Allowing more time to acquire MTR images would increase spatial resolution and would likely improve coregistration, segmentation, and overall MTR agreement across sites. qT_1 map quality was highly variable, demonstrating significant $\boldsymbol{B_1}$ inhomogeneity artifacts. More work is necessary to apply sufficient corrections to VFA qT_1 fittings and also to acquire more consistent VFA images across sites.

The imaging protocol developed for this pilot study was designed specifically to take advantage of the best available technology, and thus is limited in scope of immediate widespread adoption. However, it is important to develop a the leading edge of technology in order to provide deployment-ready protocols as soon as new technology (e.g., 32-channel head coils) becomes widely available in research centers and clinics. Additionally, the MTR and $\boldsymbol{B_1}$ Map sequences required special development by Siemens scientists and are not currently available all Siemens systems. An important next step will be to develop and test the same protocol on MRI systems from other vendors.

We showed here that MTR can be highly reproducible not only within one site across multiple imaging sessions, but also across several sites using a variety of MRI systems and equipment. Carefully standardized protocols produce consistent semi-quantitative measurements across sites in MS brain tissue in-vivo. Future work will improve qT_1 mapping and combine the qT_1 and MTR maps for quantitative calculations of myelin water fraction.

Characterization of MRI Findings in Japanese Macaque Encephalomyelitis (JME)

Introduction

A spontaneous non-human primate demyelinating disease, Japanese Macaque Encephalomyelitis (JME), with striking similarities to human demyelinating diseases has recently been described.[99–101,164–166] JME bears marked clinical and pathological similarities to multiple sclerosis (MS) , acute disseminated encephalomyelitis (ADEM), and neuromyelitis optica (NMO). Additionally, asymptomatic animals presenting with non-enhancing white matter lesions have been identified, suggesting a sub-acute disease course or perhaps unrelated radiologic isolated syndrome (RIS).[164] To date, JME is the only known naturally-occurring MS-like disease in non-human primates. The first acute cases of JME were identified in 1985 at the Oregon National Primate Research Center (ONPRC) colony of free roaming Japanese macaques (*Macaca fuscata*, JMs). Affected animals present with clinical symptoms including ataxia, paresis, or optic involvement. Disease course is characterized by an acute clinical onset with rapid progression, often leading to debilitating paresis necessitating humane euthanasia within days of the initial observation. A relapsing-remitting course has been observed in a small number of animals (approx. 7% of all cases identified). Pathological hallmarks of JME include intense focal neuroinflammation, macrophage infiltration, demyelination, and BBB compromise. Disease etiology is unknown; however a novel γ2-herpesvirus has been isolated from active lesions.[99] Virus exposure typically occurs within the first year of life, though

disease may not be clinically evident until years later. Select maternal lineages are differentially susceptible to the disease, suggesting important genetic risk factors.[100]

Dynamic-contrast-enhanced MRI (DCE-MRI) provides a unique method of quantitatively characterizing tissue vascular properties in-vivo. Transedothelial GBCA extravasation is extremely limited in normal brain, but is appreciable in presence of BBB breakdown. Pharmacokinetic (PK) modeling of DCE-MRI data allows quantification of microvascular properties including blood volume, BBB permeability and transendothelial water exchange, all of which are sensitive to disease state. A two-site-exchange (2SX) PK model[78,79,167] has been used to monitor lesion evolution in individuals with multiple sclerosis (MS),[76] and may be useful in understanding disease pathogenesis and therapy efficacy.

This work describes neuroimaging characteristics typical of JME including lesion distribution and morphology, presence of GBCA-enhancing versus non-enhancing T_1 lesions, and BBB permeability. These features will be compared to what is typically seen in MS, NMO, and ADEM. We also present a short-term longitudinal study on a subset of JME cases to investigate the time-scale of morphological and microvascular changes in active lesions during acute JME episodes. In doing so, we provide a clearer picture of JME's similarities and dissimilarities to human disease and further explore its potential as a novel non-human primate model of human demyelinating disease. We seek to determine whether JME is a non-human primate model of MS, NMO, ADEM, or perhaps a unique demyelinating disease inclusive of many aspects of each of these human

diseases. This represents an important step in not only understanding this disease, but also in making meaningful comparisons to human demyelinating diseases

Methods

Animals were monitored daily in the free-roaming colony at the Oregon National Primate Research Center. JMs demonstrating signs of neurological symptoms of JME, which include ataxia, paresis, or visual impairment, were brought in for a complete physical examination and supportive care. Suspected JME cases underwent MRI examinations shortly after first symptomatic presentation (median 1 day, range 1-5 days). In this study, MRI was performed on 21 animals during an acute episode of JME between 2008 and 2015. Animals with debilitating disability were humanely euthanized after MRI, and brain and spinal cord tissues were collected for histological examination.

Animal Handling

Animals were initially sedated with Telazol, intubated and maintained on 1% isoflurane in 100% O_2 and were continuously monitored by pulse oximetry, respiration, and end-tidal CO_2 levels during the study. The study protocol was reviewed and approved by the Oregon National Primate Research Center (ONPRC) Institutional Animal Care and Use Committee (IACUC). All animal handling and care were performed in strict accordance with the ONPRC IACUC regulations. In some cases, treatment with corticosteroids was administered for up to twelve days before animals reached the humane endpoint requiring

euthanasia. One animal was observed for 7 days without steroid treatment before reaching the humane endpoint (JM 30760). Animals were monitored daily and corticosteroid doses were increased if symptoms worsened.

MRI

All MRI data were acquired on a whole-body Siemens 3 Tesla (T) Tim Trio MRI instrument (Erlangen, Germany) located at ONPRC. Images were collected with either a 2- or 15-channel transmit/receive extremity radiofrequency (RF) coil. In-vivo imaging for all animals included sagittal proton density (PD, FOV 160 x 60 160 mm^3, Matrix 256 x 60 x 256), axial PD and T_2-weighted (T_2-w) turbo-spin echo (TSE, FOV 120 x 160 x 66 mm^3; Matrix 240 x 320 x 66) anatomical sequences. Axial 2D fluid attenuated inversion recovery (FLAIR; FOV 108 x 144 x 36 mm^3; Matrix 144 x 192 x 24) images were collected on fifteen animals. Quantitative R_1 ($\equiv 1/T_1$) mapping was performed with a multiple-inversion recovery experiment employing 3D T_1-weighted magnetic prepared rapid acquisition gradient echo (MPRAGE) sequence (TR: 2500 ms; TE: 3.49 ms; FA: 8°; FOV 130 x 97.5 mm^2, matrix: 192x144; 96 0.8 mm thick slices; TI: 200, 900, 2000ms, no inversion). R_1 maps were acquired before and after bolus injection of 0.2 mmol/kg GBCA (ProHance, Bracco Diagnostics).

Image Processing

A combination of post-contrast difference ($=R_{1post\text{-}CA\text{-}i} - R_{1pre\text{-}CA}$; where $R_{1post\text{-}CA\text{-}i}$ represents the i^{th} post-contrast timepoint) and standard deviation ($=stdev(R_{1pre\text{-}CA}, R_{1post\text{-}CA\text{-}1}, R_{1post\text{-}CA\text{-}2}, R_{1post\text{-}CA\text{-}3}, R_{1post\text{-}CA\text{-}4})$) maps were created and used to manually identify GBCA-enhancing lesions and determine

enhancement volumes. Lesion masks were manually created based on the R_1 difference and standard deviation maps for GBCA-enhancing lesions for each case. In the case of animals with longitudinal data, lesion masks were created for each MRI exam and combined to illustrate cumulative lesion distribution within that animal over time. T_2 white matter signal hyperintensities (WMSHs) were manually identified on T_2-w images, and lesion masks were similarly drawn by hand for each subject. T_2-w and R_1 reference images were created from 6 healthy JMs (median age 9 yrs, range 4 yr 10 mo – 20 yr, 3 M and 3 F). Briefly, all R_1 maps were skull-stripped with FSL's BET,[130] linearly coregistered to a single animal using FSL's FLIRT,[130] then summed to create an average R_1 map. All images were then linearly coregistered to the average image, averaged again, then nonlinearly coregistered to the new average using FSL's FNIRT.[130] In this way we reduce spatial and morphological bias toward any one subject. The nonlinearly coregistered images were then averaged to create a common reference space for analysis. Forgoing skull-stripping, a reference T_2-w image was created following the same procedures. R_1 maps and T_2-w images from JME cases were nonlinearly coregistered to the appropriate reference image, and lesion masks were transformed accordingly. Binarized lesion masks in the reference space were then summed to create final lesion distribution probability maps.

A two-site-exchange (2SX) pharmacokinetic model[78,79,167] was applied to R_1 DCE-MRI data in subject native space on a voxel-by-voxel basis to estimate K^{trans}, a measure of GBCA blood-brain-barrier extravasation. Plasma

concentration functions representing blood plasma GBCA concentration for each animal were obtained from a region of interest (ROI) manually selected in the sagittal sinus.

Longitudinal Observation

Short-term longitudinal MRI data were collected from nine of the twenty-one animals in this study. Up to three follow-up exams occurred between 1 and 12 days after the initial MRI session. Five animals were scanned twice; three animals received three MRI exams; and one received four MRI exams over the span of 12 days. Follow-up MRI for two animals included only anatomical imaging and no DCE-MRI was acquired.

Results

Lesion Distribution

A total of 110 GBCA-enhancing lesions were identified in 21 Japanese macaques (median 5 lesions per animal, range 2-12) presenting with clinical symptoms typical of JME: ataxia, paresis, or optic involvement. The median age was 2 years [range 0.3-26 years] and 43% were female. Animals most commonly presented with lesions in the cerebellum (including peduncles, CBLL; n=18; 86% of animals), followed by the upper cervical spinal cord (SC; n=12; 57%), brainstem (n=11; 52%), and internal capsule (IC; n=8; 38%), as demonstrated in **Figure 25**a. Overall lesion load across the population was greatest in the cerebellum (n=56 lesions), followed by the SC (n=15), IC (n=14), and brainstem

(n=13). Lesions were also identified in the periventricular white matter (PVWM, n=5), corpus callosum (CC, n=4), and cerebral white matter (CWM, n=3). Lesions were frequently observed bilaterally within cases, and did not demonstrate hemispheric preference (**Figure 25**b). Comorbidities occasionally observed included extended lateral ventricles and hydrocephalus; evidence of stroke was observed in one case.

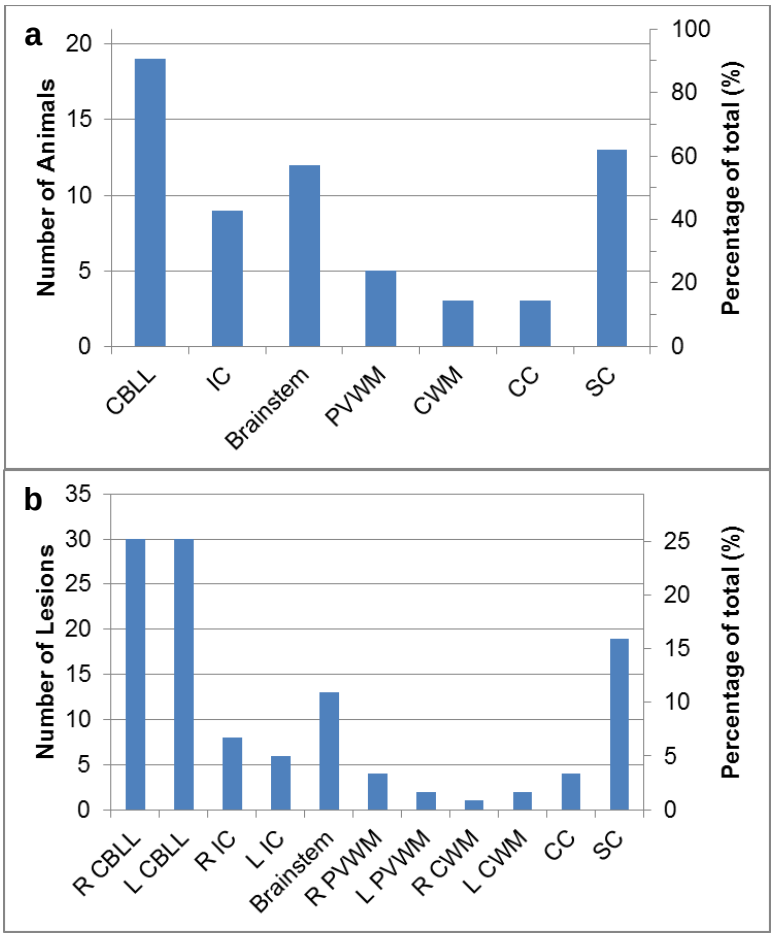

Figure 25. JME Lesion Locations and Prevalence. Panel (a) illustrates the number of animals presenting with at least one lesion, and its location. Total lesion counts across all animals in each structure are given in panel (b). Regions are separated by hemisphere where applicable to assess hemispheric preference. R – right; L – left; CBLL – cerebellum; IC – internal capsule; PVWM – periventricular white matter; CWM – cerebral white matter; CC – corpus callosum; SC – cervical spinal cord.

Seven subjects exhibited T_2-w hyperintensities corresponding to non-enhancing R_1 hypointensities (animal ID / lesion location(s): 27571 / IC, CWM; 27616 / R CBLL peduncle and L IC; 27624 / L IC connected to enhancing; 28422 / L CBLL/peduncle; 30493 / L CBLL peduncle and R IC; 30760 / CBLL, basillary pons connected to IC, confluent with enhancing IC and PVWM; 32150 / CBLL, IC, SC), which are consistent with chronic, burned-out lesions found in MS. One example of such a lesion is shown in **Figure 26.** Spinal cord lesions spanning at least 1-2 cervical vertebrae were observed in 29% of cases on sagittal PD images (animals 13221, 20482, 26174, 30493, 30760, 30773), **Figure 27** a,b.

Lesions extending from the spinal cord into the brainstem were observed on sagittal PD images in 29% cases (22019 / pons, 27571 / lateral medulla, 30760 / periependymal lesion involving the pons, 30773 / medulla/pons, 31852 / medulla, 31869 / medulla/pons, 34027 / medulla/pons). Two examples are shown in **Figure 27** a,d. Additionally, post-mortem tissue analysis revealed a longitudinally extensive lesion in one case (30773) spanning up to two-thirds of

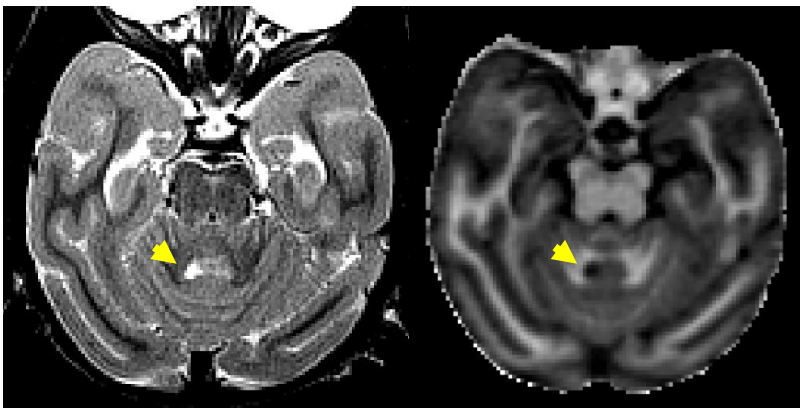

Figure 26. Chronic non-enhancing lesion. T_2-w (left) and R_1 (right) images at the same horizontal level are shown for one case demonstrating a WMSH corresponding to a non-enhancing R_1 hypointensity (arrows), consistent with burned-out (non-enhancing) chronic lesions observed in MS.

the spinal cord length. This lesion was outside the DCE-MRI field-of-view so GBCA-enhancing status is unknown.

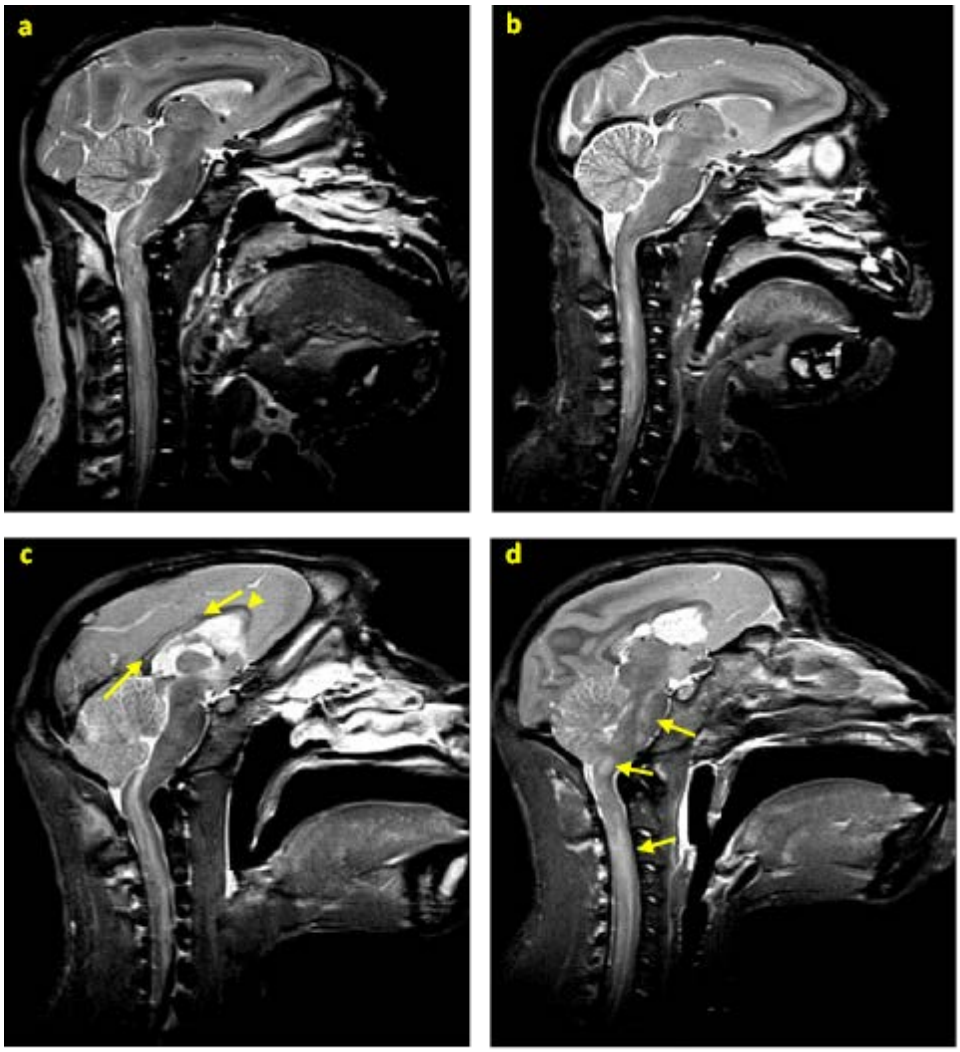

Figure 27. Longitudinally Extensive SC and CC Lesions. Longitudinally extensive spinal cord lesions appear bright in three separate cases in panels a, b, and d (animals 31869 (a), 32150 (b), and 29756 (c,d)). Two slices are shown from an individual animal in panels c and d demonstrating NMO-like CC and SC lesions (arrows). Although not obvious from a single slice, the lesions indicated by arrows in panel d are confluent. A focal lesion is also seen in the genu of the CC (arrowhead). Note abnormal SC and CBLL in panel c (29756).

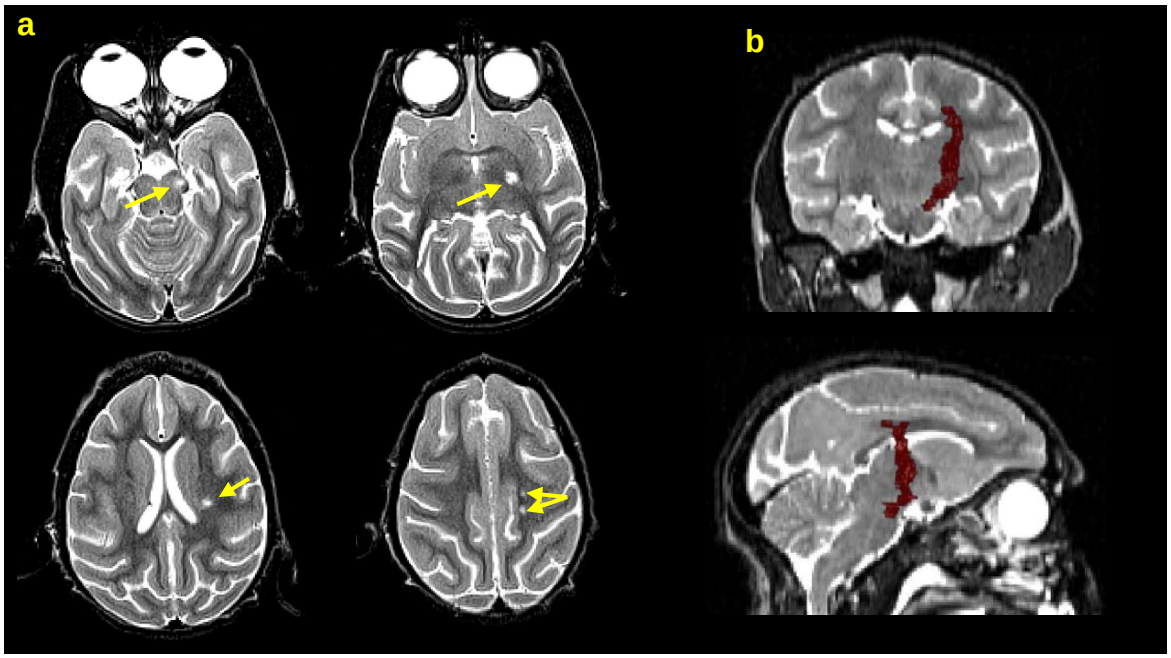

Figure 28. Longitudinally Extensive CWM Lesion. T_2-w axial slices show a lesion (hyperintensity, arrows) extending from the pons through the IC all the way up to CWM superior to the lateral ventricle in animal 30773. Note that the superior aspect of the lesion has bifurcated (lower right image in panel a). A representative line is overlaid on a sagittal PD slice of the same animal illustrating the extent of the lesion in panel b.

Lesions extending from the brainstem to at least the IC were observed in four cases (19%), three of which extended into the superior PVWM (27571, 27624, 30493, 30733). A lesion extending from the pons into white matter superior to the lateral ventricles on axial T_2-w images in **Figure 28a**. Reconstructed coronal and sagittal T_2 views are shown in **Figure 28b** with a 3-dimensional render of the lesion overlaid in red. One case demonstrated bilateral confluent lesions ascending from IC into cerebral white matter superior to lateral ventricles (31852). Sixty-six percent of animals with CC involvement demonstrated long, linear T_2 lesions spanning much of the length of the CC (**Figure 27**c arrows) that are thought to be exceptional for MS and perhaps

suggestive of NMO (29756, 27624).[21,168] One case showed bilateral ventricular horn hyperintensities on T_2-w FLAIR (29756), consistent with MS (**Figure 29**).

Within subjects, T_2-w WMSHs corresponded to both R_1 hypointense and GBCA-enhancing lesions, although T_2-w lesions were generally more extensive and diffuse in nature. Lesion probability maps for T_2-w and R_1 lesions in **Figure 30** demonstrate that T_2-w WMSHs appear throughout the brain with nearly the same distribution and probability as R_1 GBCA-enhancing lesions; however, T_2-w lesions tend to be larger and more diffuse than the focal GBCA-enhancing lesions. Indeed, multiple GBCA-enhancing lesions were often observed within large diffuse T_2 lesions. Longitudinally extensive lesions in the CC are best visualized on sagittal PD images as shown in **Figure 27**, and are typically only 1-2 voxels wide and (0.625 mm x 0.625 x 1 mm voxel size). Because of their small size, and relatively thick slices (1mm thick) in T_2 axial acquisitions, these lesions are not represented on the T_2 lesion probability map.

Asymptomatic T_2-w white matter signal hyperintensities were identified in

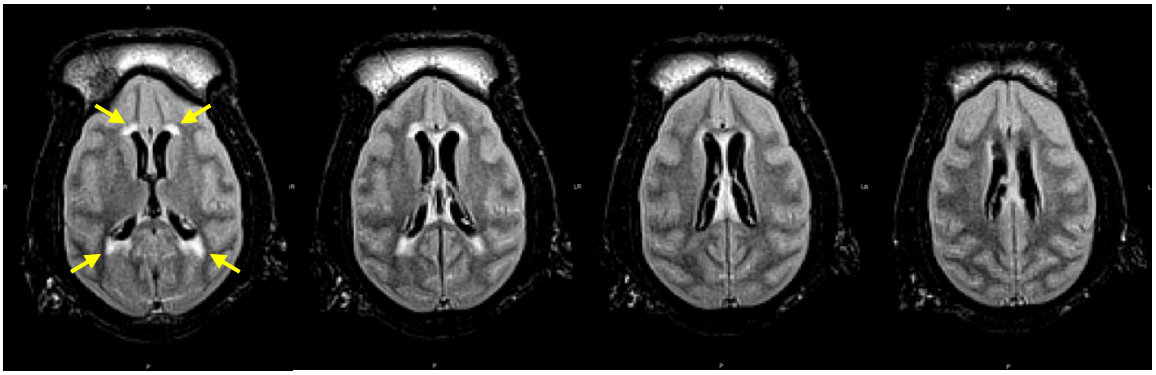

Figure 29. Hyperintense Ventricular Horns and CC. One case demonstrated striking hyperintense ventricular horns on axial FLAIR images, reminiscent of findings on FLAIR in MS.

approximately 10% of animals enrolled in a screening study in 2009.[164] Lesions were most frequently found in periventricular white matter (n=4 animals), followed by brainstem (n=2), spinal cord (n=2), cerebellar peduncles (n=2), and cerebral white matter (n=2). One lesion was found in the corpus callosum, and one in the internal capsule.

DCE-MRI and Pharmacokinetic Modeling

All 21 cases of acute JME examined in this analysis exhibited GBCA-enhancing lesions. Pharmacokinetic modeling reveals BBB permeability in acute JME lesions similar to that seen in acute human MS lesions, as measured by K^{trans} and shown in **Table 4**.[76]

Table 4. K^{trans} in Normal-Appearing White Matter and Lesions

	NAWM	**pre-acute**	**acute**	**post-acute**
MS K^{trans} (min^{-1})	$1x10^{-5}$	$3x10^{-4}$	$1x10^{-2}$	$6x10^{-4}$
JME K^{trans} (min^{-1})	$1x10^{-4}$	$1x10^{-3}$	$1x10^{-2}$	$5x10^{-3}$

JME GBCA-enhancing lesions were typically focal and ovoid, demonstrating highest BBB permeability in the lesion core, which is consistent with newly developed acute, focal MS lesions shown in **Figure 31**.[57,169] However, one partially enclosed ring-enhancing lesion was observed in the CBLL of an animal with particularly high lesion burden (34027). In this case, the T_2-w lesion is a focal hyperintensity that corresponds to the non-enhancing R_1 hypointensity in the center of the lesion, shown in **Figure 32**. This lesion demonstrates a centripetal enhancement pattern marked by initial enhancement in the rim of the

lesion that slowly fills in toward the center. Six minutes after intravenous GBCA administration the rim is brightly enhanced while the core of the lesion remains hypointense. Forty minutes after injection the core of the lesion shows some enhancement, though it remains slightly hypointense compared to the rim.

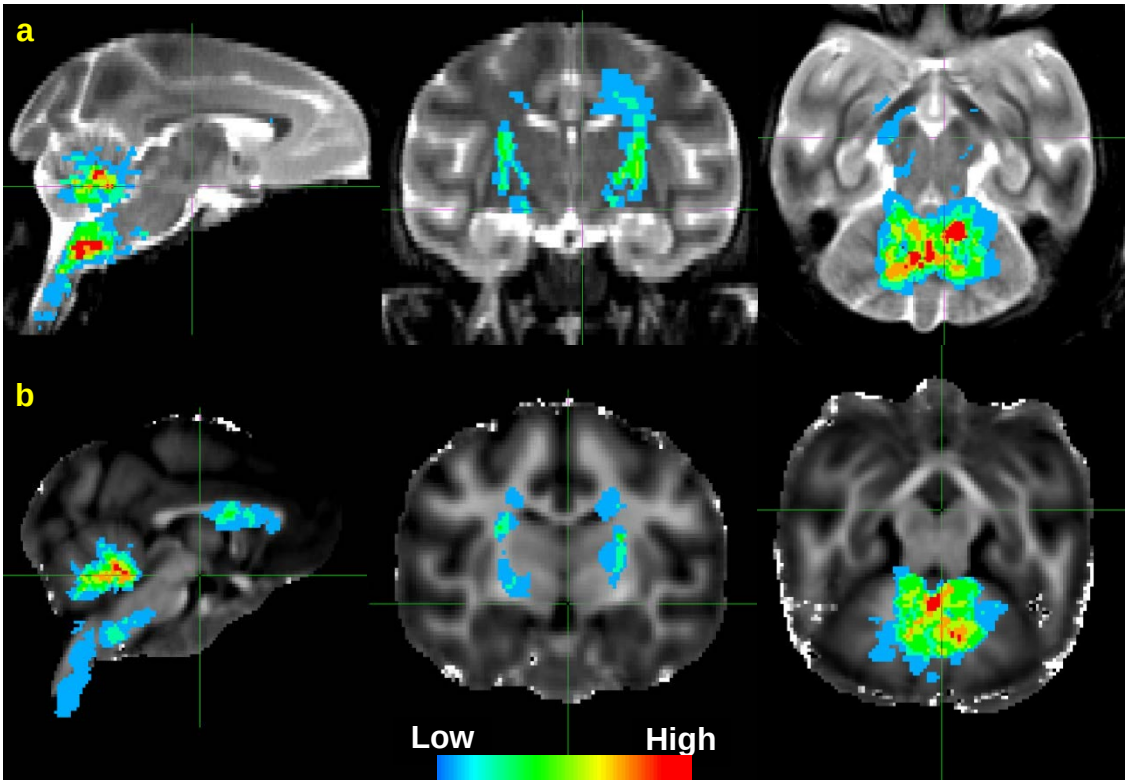

Figure 30. Lesion Distribution Probability Maps. Lesion distribution probability maps are overlaid in false color on reference images created from six healthy control animals. T_2-w WMSH lesions (top row, 3 views) demonstrate the same general spatial distribution and probability as GBCA-enhancing lesions on R_1 maps (bottom row). Both maps show high infratentorial lesion load and bilateral ascending CWM lesions between the IC and CWM superior to the lateral ventricles. Partial volume effects due to thicker slices in T_2-w images than in R_1 maps account for paucity of CC lesions visualized on the axial T_2-w images (a, left) compared to R_1 (b, left).

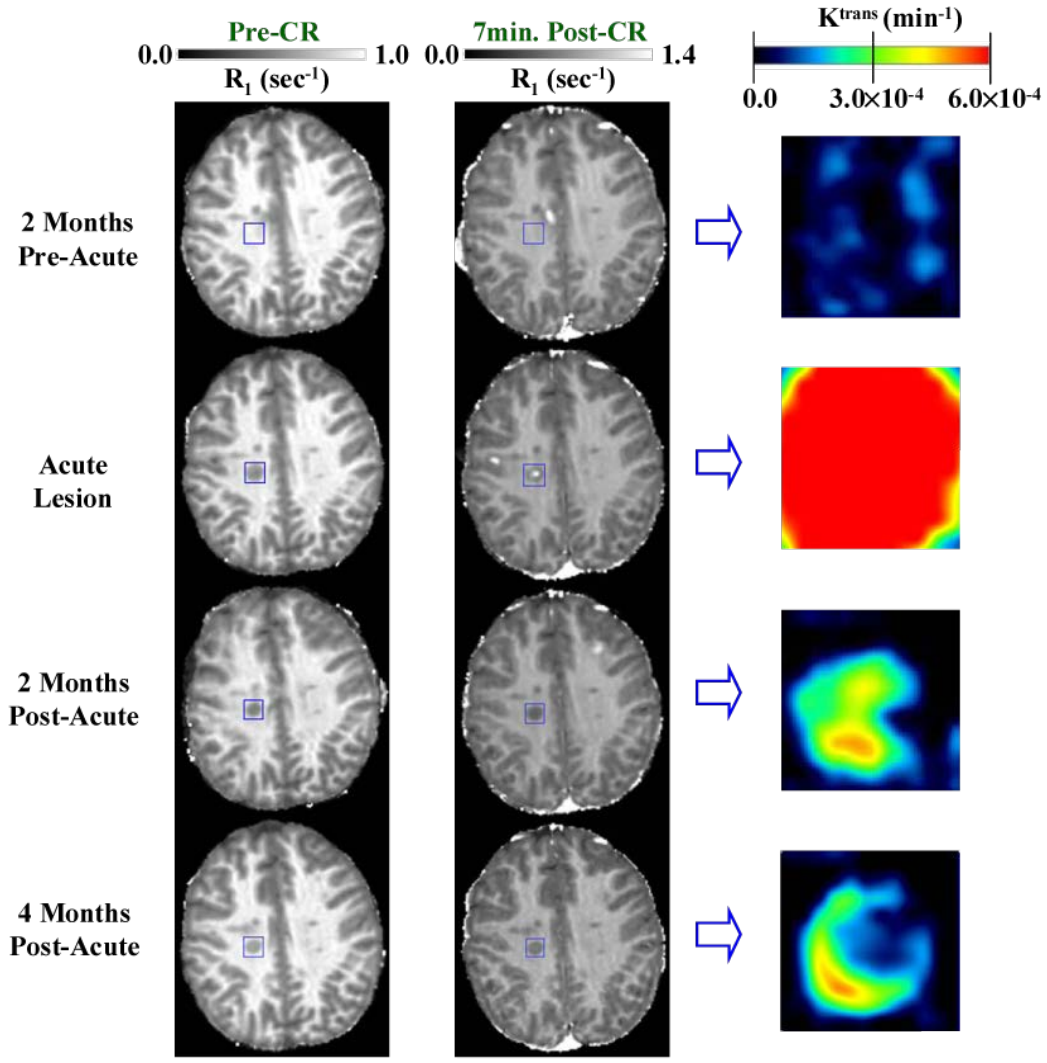

Figure 31. Lesion Evolution in MS. DCE-MRI were acquired every two months for six months in a patient with relapsing-remitting MS. The blue square overlaid on R_1 maps circumscribes a new GBCA-enhancing lesion that appears at the second MRI exam (second row). Zoomed K^{trans} maps from the blue square are shown on the right. K^{trans} is elevated during the acute stage, then gradually reduces over time as the lesion transitions into a post-acute stage. Not that K^{trans} is slightly elevated above normal (K^{trans} ~$1x10^{-5}$) even two months before enhancement is obvious (acute). As the lesion ages, BBB extravasation decreases most significantly in the center of the lesion and remains elevated in the periphery, suggesting a transition from centrifugal enhancement to centripetal enhancement. Modified from Njus,et. al., 2008.[76]

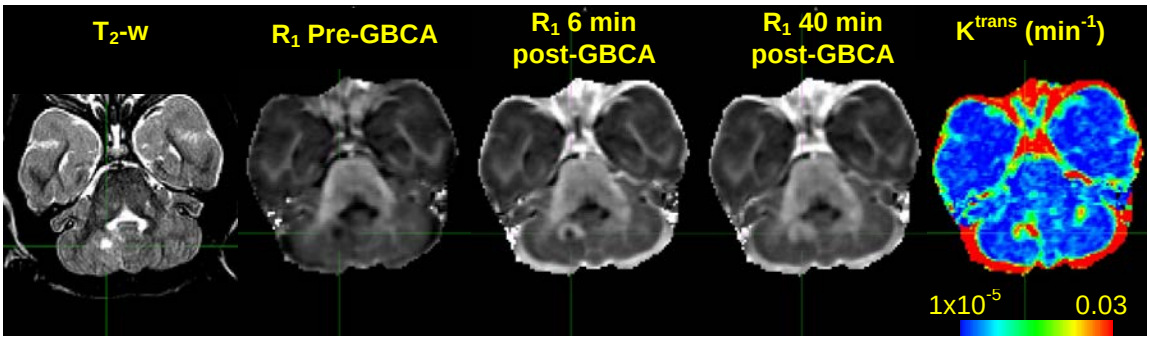

Figure 32. Ring-Enhancing JME Lesion. T_2-w MRI shows a punctate hyperintensity in the right CBLL corresponding to a similar hypointensity on the pre-GBCA R_1 map. GBCA-enhancement is clear in the periphery of the lesion immediately after injection, then slowly fill into the center by 40 mins after injection. The corresponding K^{trans} map accordingly shows higher K^{trans} around the edge of the lesion where enhancement initiated than in the center of the lesion. This lesion appears to have already transitioned from centrifugal to centripetal enhancement consistent with an old lesion that has an inactive core and active edges.

Longitudinal Observations

Four (20482, 28422, 32150, 32914) of the seven animals with longitudinal DCE-MRI exhibited new GBCA-enhancing lesions on follow-up exams at least two days after the initial exam. The three animals that did not present new lesions had follow-up exams one (n=2; 19615, 31869) or two (n=1; 30493) days after the initial exam. Details for all nine animals observed longitudinally are summarized in **Table 5**. Sagittal, coronal, and axial views of K^{trans} maps overlaid on R_1 images are shown in **Figure 33** for three animals that received multiple DCE-MRI exams. K^{trans} values are variable across lesions and change with time. The large brainstem lesion visible on Day 1 (one day after clinical symptoms were first observed) shows marked decrease in K^{trans} with time, while new lesions are simultaneously developing in the cerebellum. Average K^{trans} values for the brainstem lesion and one CBLL lesion (**Figure 33**a arrows) are shown in **Figure 34**. Error bars represent one standard deviation over the lesion volume. Elevated

K^{trans} observed in newly formed lesions is characteristic of tight junction breakdown and increased BBB permeability associated with inflammatory processes. The two imaging sessions for the animal in **Figure 33**b were only 24hrs apart to observe effects of short-term treatment. Clinical symptoms worsened and average K^{trans} values increased in all lesions in this animal during the 24hr treatment period. A second animal was imaged twice within 24 hours, but was not given corticosteroid treatment (not shown). In that case, K^{trans} decreased slightly or did not change in the majority of lesions, and increased in one lesion. **Figure 33**c shows K^{trans} maps from an animal scanned at three time points; data are shown from the first and last days. Acute lesions were identified in the IC (not shown), CBLL, and brainstem. One new enhancing lesion was observed in the CBLL on Day 7 (not shown). Interestingly, a strongly enhancing CBLL lesion on Day 1 was completely non-enhancing ($K^{trans} \sim 1x10^{-5}$) by Day 7 (**Figure 33**c arrows).

Table 5. Longitudinal JME Case Summary

ID	# Exams	MRI Days (post-onset)	GBCA on all days?	New GBCA+ lesions/Notes	Treatment*
19615	2	1,2	Yes	No	Prednisolone
20482	4	1,5,11,13	Yes	Yes - some better, some worse, some new (K^{trans})	Prednisolone
28422	3	1,3,7	Yes	Yes – most lesions normalizing K^{trans}, one new CBLL	Prednisolone
30493	2	1,3	Yes	No	Dexamethasone/Prednisolone
30760	2	5,6	No	N/A	None
31509	2	1,4	No	N/A	Dexamethasone/High Dose Prednisolone
31869	2	2,3	Yes	No – some better, some worse, some no change (K^{trans})	None
32150	3	1,5,12	Yes	Yes – Some resolve, some new (K^{trans})	High Dose Methylprednisolone
32914	2	2,4	Yes	Yes – New/worse K^{trans} in SC and CWM	High dose Methylprednisolone before first MRI

*See Appendix A – JME Symptom and Treatment Details

New lesions demonstrating compromised BBB on MRI arise from normal-appearing tissue in as few as two days, while BBB permeability normalization required several days and was incomplete, even with corticosteroid treatment. All four animals exhibiting new lesions during the longitudinal observation were receiving corticosteroid treatment. Two cases (20482, 28422) received anti-inflammatory doses of corticosteroids (2-8 mg/kg/day methylprednisolone); the remaining two received higher doses (32150, 32914; 24-26 mg/kg/day methylprednisolone). Two of the three animals with no new lesion presentation received anti-inflammatory doses of prednisolone; the third (31869) received no

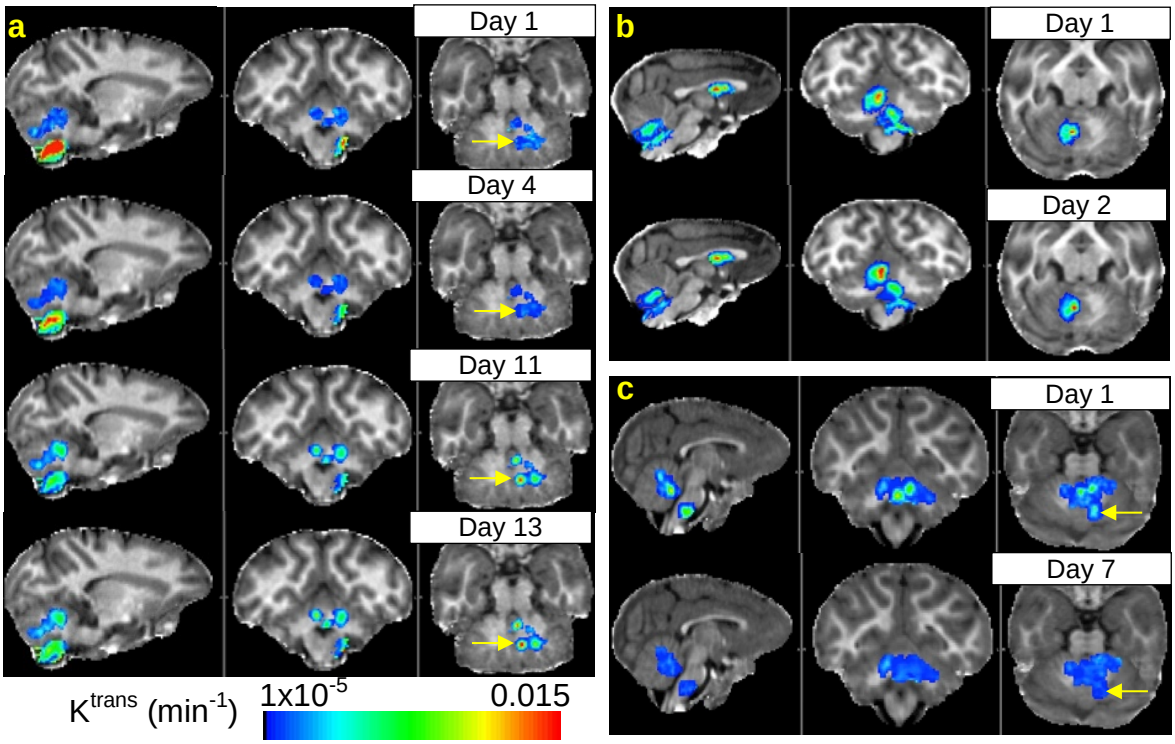

Figure 33. Lesion Evolution in JME. K^{trans} parametric maps in lesion areas overlaid on pre-GBCA R1 maps showing lesion evolution over time for 3 separate animals: (a) initial large brainstem lesion and developing CBLL lesions evaluated four times over twelve days in animal 20482; (b) lesions in CC and CBLL demonstrate slightly elevated K^{trans} 24 hrs after initial exam (animal 19615); (c) CBLL and brainstem lesions appear largely resolved after 6 days of treatment with prednisolone (animal 28422).

treatment. Low-dose corticosteroid treatment appeared to have little or no effect overall: clinical symptoms continued to worsen, new lesions were not prevented, and K^{trans} in the original lesions only partially resolved in some cases. High-dose corticosteroid treatment similarly had a limited and inconsistent positive effect on clinical symptoms and did not prevent new lesion development. Average K^{trans} values for nine enhancing lesions from one animal on high-dose corticosteroids (32150) are shown in **Figure 35.** Lesions with the highest average K^{trans} at Day 1 show decreasing K^{trans} over time, while those with the lowest average K^{trans} at Day 1 have markedly increased K^{trans} by Day 12. Clinical details including symptoms, treatments, and procedures for this animal are shown in **Table 6**.

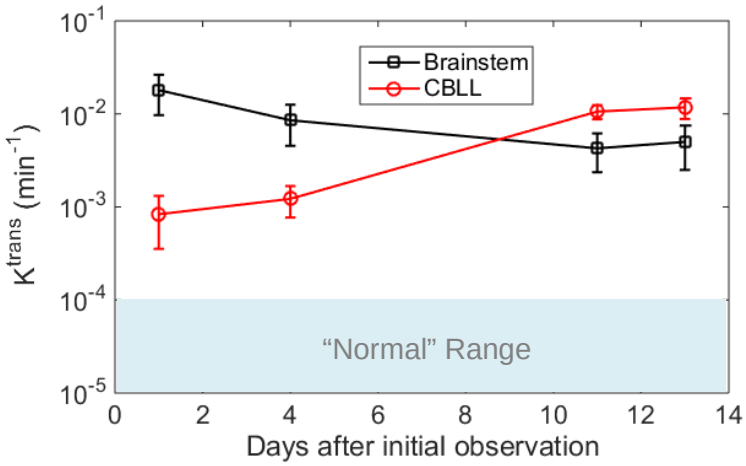

Figure 34. Lesion Average K^{trans} in JM 20482. Ktrans changes over time in Figure 25a CBLL (arrows) and brainstem lesions demonstrate simultaneous progression and resolution of lesions in an individual over the course of 12 days. Error bars represent K^{trans} standard deviation within the lesion. Solid connecting lines are drawn to guide the eye

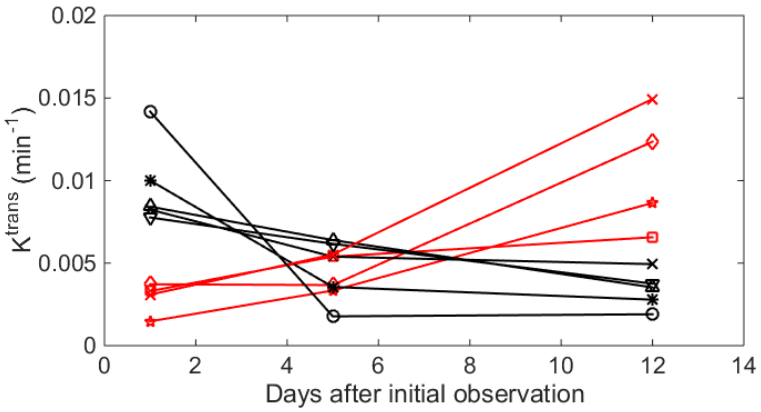

Figure 35. Lesion Average K^{trans} in JM 32150. Average K^{trans} in each lesion in one individual is shown over time. The five black data sets each represent a lesion with high K^{trans} on the first day consistent with a very active acute lesion with a leaky BBB, then resolve to a post-acute (but still elevated compared to normal tissue) level by Day 12. The four red data sets show the opposite trend – at Day 1 they were pre-acute and unremarkable; by Day 12 they all had higher K^{trans}, indicating lesion progression and increased pathological activity. Solid connecting lines are included to guide the eye.

Discussion

Assessments of lesion morphology and distribution are important in obtaining a correct differential diagnosis in demyelinating diseases.[16] This work describes T_2-w and GBCA-enhancing lesion distribution typical of JME, a novel spontaneous demyelinating disease in non-human primates. Biomarkers associated with inflammatory response including blood volume, blood-brain-barrier permeation, and myelin water fraction, which can be calculated from MRI data and subsequently validated with histology. JME is a unique disease that, like human MS and its mimics, is still not entirely understood. Investigation of JME and development of non-invasive imaging biomarkers will contribute to the understanding and study of human demyelinating diseases.

Table 6. Clinical Details for JM 32150.

Day	Symptoms	Procedures	Corticosteroid	Dose / Frequency	Methylpred equivalent (mg/kg/day)
0	L leg paralysis, abrasion on dorsal L foot	PE			
1	L leg limp, R leg used exclusively	MRI, CSF, BAL	Methylpred	125 mg SID	24
2	L leg shows limited but some function		Methylpred	125 mg SID	24
3	Uses L leg for support still limited use		Methylpred	125 mg SID	24
4	No use of L leg observed		Methylpred	125 mg SID	24
5	Same	MRI	Methylpred	125 mg SID	24
6	Same		Prednisone	5 mg SID	0.8
7	Same		Prednisone	5 mg SID	0.8
8	Possible R leg paresis		Prednisone	5 mg SID	0.8
9	Using arms predominantly to move but R leg still partially functional		Prednisone	5 mg SID	0.8
10	Same		Prednisone	5 mg SID	0.8
11	Both legs nonfunctional		Prednisone	5 mg SID	0.8
12		MRI, necropsy			

SID – once per day; PE – physical exam; CSF – cerebrospinal fluid sample; BAL – bronchoalveolar lavage; Methylpred - methyprednisolone

Several key characteristics JME, MS, ADEM, and NMO are compared in **Table 7**. MS lesions are typically found in periventricular (Dawson fingers), juxtacortical, infratentorial, and spinal cord white matter (WM). Cortical lesions and gray matter (GM) atrophy are common in MS and contribute significantly to disability.[3,12,45,170–175] Additionally, tissue damage in MS can be detected outside focal lesions, which is generally not present in NMO or ADEM.[15,161] Imaging findings characteristic of NMO include longitudinally extensive transverse myelitis (LETM), optic nerve involvement, lesions that extend from spinal cord to brainstem, dorsal medullary involvement, and long lesions following the corticospinal tract (contiguous through CBLL peduncle and IC).[21] ADEM is characterized by acute encephalopathy, and frequently presents with optic neuritis or transverse myelitis. Relapses are common in both MS and NMO, while ADEM is typically monophasic.[176] Diagnostic criteria for ADEM exist for pediatric patients,[177] yet diagnosis in adults is poorly defined and unrelated conditions may be misdiagnosed as ADEM in adults.[178] Lesions identified in neuroimaging examinations of ADEM patients are most commonly found to be multifocal and asymmetric in the cerebral WM,[20,179] symmetric (bilateral) in the GM (including thalamus and basal ganglia)[180], and occasionally are found in the spinal cord and medulla. Unlike MS, ADEM lesions are expected to all have arisen at nearly the same time, consistent with its normally monophasic time course, and thus would not demonstrate evidence of DIT (dissemination in time). However, recurrent ADEM is observed, compounding the challenge of distinguishing between ADEM and MS.[178]

Table 7. Key Characteristics of JME, MS, ADEM, and NMO

Feature	JME	MS	ADEM	NMO
Lesion Locations and Features				
Cerebellum	X	X	X	X
Cerebral WM	X	X	X	X
DIS	X	X	X	X
DIT	X	X		
High infratentorial lesion load	X	X[a]		X
Lateral SC	X	X		
LETM				X
Long lesions following corticospinal tract	X			X
Medial SC	X			X
Optic Nerve	X	X	X	X
PVWM (Dawson Fingers)		X		
Other Features				
BBB Compromise	X	X	X	X
Genetic Predisposition	X	?		
More common in pediatric group	X		X	
Response to Corticosteroids	X[b]	X[c]	X[d]	X[c]
Relapsing	X[e]	X	X[e]	X

[a]True of pediatric MS, exceptional for adult MS
[b]High-dose corticosteroids (20-30mg/day methylprednisolone) may be beneficial
[c]3-5 days high dose IV corticosteroids (e.g., 1000 mg/day methylprednisolone)[181,182]
[d]Several days of IV corticosteroids (e.g., 10-30 mg/kg/day methylprednisolone)[183]
[e]Observed in a small percentage of total cases

Brainstem and SC lesions in JME are found both medially and laterally, complicating the direct comparison to MS and NMO. Spinal cord lesions occupying the central gray matter, extending from cervical SC into the brainstem, or extending 2 or more vertebral segments in length, are uncommon in adult MS and are thus perhaps the most specific neuroimaging marker of NMO.[21] In contrast, MS spinal cord lesions generally are localized to the peripheral white matter and are shorter than those in NMO, typically only one vertebral segment or less. A variety of GBCA-enhancing lesions in the cervical spinal cord and

brainstem have been identified in JME that could fit the descriptions for either MS or NMO. Longitudinally extensive myelitis observed in nearly 30% of this cohort suggests some similarity to NMO.[21,184] The field of view in our DCE-MRI sequences provides only limited cervical spine coverage, so we are unable to characterize the full extent of spinal cord involvement in this disease with MRI alone. Pre-contrast sagittal PD-weighted images offer some additional insight into spinal cord involvement in this disease. Indeed, a longitudinally extensive spinal cord lesion spanning up to two-thirds of the spinal cord length has been identified (not shown) by post-mortem tissue analysis. However, the spinal cord lesions extending more than two vertebral segments in length in JME are typically restricted to the peripheral white matter, so may in fact be more similar to MS despite their length. Immunological analysis of spinal cord lesions also suggests a similarity here to MS rather than its mimics.[99,101] JME lesions identified in the central gray matter of the cervical spinal cord tend to be limited in length, and often do extend into the brainstem and medulla, which is highly suggestive of NMO when seen in humans.

CWM lesions are often sub- or juxtacortical in JME; distinguishing between PVWM and CWM can be challenging due to small JM brain size and close proximity of structures. Indeed, a WM lesion could be simultaneously classified as periventricular and juxtacortical. As these two lesion types are both typical of MS, the absolute distinction here may be of limited importance. However, perpendicular PVWM lesions known as Dawson fingers characteristic of MS were not observed in these JME cases. Bilateral extensive lesions

extending from the IC into the CWM have been noted in NMO.[21,168] Such lesions were observed in one JME case extending from IC to CWM superior to the lateral ventricles, while unilateral lesions of a similar nature were observed in three others, giving these cases an appearance reflective of NMO.

Compared to adults with MS, pediatric MS patients are more likely to present with infratentorial white matter lesions and have lower supratentorial lesion burden. Brainstem lesions, specifically in the pons, have been shown to be more characteristic of pediatric MS than the broad category of infratentorial lesion burden.[28,56] High infratentorial lesion load found in JME, noting the prevalence of brainstem lesions, suggests JME may be more similar to pediatric than adult MS. Accordingly, JME typically occurs in animals prior to sexual maturity (72% of this cohort) and shows no sex predilection, similar to pediatric MS. However, children with MS have a low risk of becoming disabled early in disease progression, which conflicts with the rapid and aggressive progression of disease and disability found in JME.

Longitudinal Observations

Substantial morphological and vascular changes can occur in as few as 2-3 days in JME-affected brain tissue. We demonstrate here that acute lesions with elevated BBB permeability arise from normal-appearing white matter (NAWM) rapidly, even in the presence of treatment with corticosteroids. Interestingly, lesion sites show mildly elevated K^{trans} (~0.001 min^{-1}) in days leading up to the acute stage (**Figure 33**a, arrows). Low K^{trans} found in lesions at Day 1 in **Figure 33** suggests that these are either developing or resolving lesions; comparison

with Day 7 reveals these lesions are likely already exiting the acute phase at Day 1. Indeed, one lesion (**Figure 33**c arrows) appears to have normalized completely with respect to K^{trans} from the acute stage at Day 1 to a post-acute state at Day 7. Similar to MS, lesion development and resolution is variable in both time and space in JME, with new lesions developing while others are resolving or transitioning to an inactive state. DCE-MRI measurements of lesion evolution in JME track well with previously reported MS data; K^{trans} values are summarized in **Table 4**.[76]

It is important to note that the MS pre- and post-acute stages in **Figure 31** were measured 2 months before and after the acute stage, respectively. It is likely that K^{trans} values in JME and MS would be more similar were they measured on the same time intervals relative to the acute stage.

Further, it is interesting to note that the MS lesion shown in **Figure 31** transitions from a focal ovoid lesion that demonstrates highest BBB permeation in the center of the lesion during the acute phase to a ring-shaped lesion with greater permeability along the rim of the lesion in the post-acute phase. This is consistent with the transition from centrifugal (enhancement moving from center to periphery) to centripetal (enhancement moving from periphery to center) patterns of enhancement that have recently been shown associated with varying stages of lesion activity and pathology.[12,49,169] Gaitán, et al., demonstrate that acute GBCA-enhancing lesions initially enhancing centrifugally can convert to centripetal enhancement as the core of the lesion becomes chronic and inactive provided that inflammatory processes persist in the rim of the lesion.

Extrapolating from these results we can look more closely at the rim-enhancing lesion shown in **Figure 32**, and, combined with T_2 images, say that this same transition occurs in at least some JME lesions. We would accordingly expect that this lesion is not new; rather the center of the lesion has already become chronic and inactive, while the border of the lesion remains active and expanding. Gaitán, et al, further demonstrate that observation of ring-like enhancement can be dependent on how quickly images are acquired after GBCA administration. That is to say, a lesion may demonstrate ring-like enhancement within the first few minutes after GBCA administration then will fill in and appear nodular at later time points. The lesion in **Figure 32** is an exceptional case; it is possible that many more JME lesions would exhibit ring-like enhancement immediately after GBCA injection. However, without rapidly sampled post-contrast T_1-w images, and given our limited longitudinal data, it is difficult to say if this is common in JME.

A significant limitation to this analysis is the poor visualization of JM optic nerves by MRI. While optical involvement has been clinically reported in JME cases, and observed by histology, we were unable to reliably detect T_2 or GBCA-enhancing lesions in the optic nerves of these animals. Identification of such lesions is important in distinguishing between NMO, ADEM and MS, and would certainly provide valuable insight in comparing JME to these human diseases. Additionally, image coregistration across the population was imperfect, so the lesion distribution maps primarily serve illustrative purposes rather than precise

quantification. In spite of these limitations, the lesion distribution probability maps presented are informative and contribute to the ongoing characterization of JME.

Obtaining the correct diagnosis of MS, ADEM, NMO, or something else entirely is of utmost importance in patient care as treatments vary based on disease, and incorrect treatment can be detrimental to patient health. Similarly, understanding the pathogenesis and establishing key characteristics in JME will help identify appropriate therapy for monkeys affected by JME. Animals treated with corticosteroids typically show little or no clinical improvement. Any clinical improvement observed after high-dose corticosteroids reversed soon after dose tapering. This may warrant exploring the effects of prolonged treatment with high-dose corticosteroids, as it may improve clinical symptoms given enough time. In addition to rapid progression of physical disability, long-term treatment of JME is further complicated by challenges associated with reintroducing animals to the colony after an extended absence during treatment. Social dynamics within the colony are complex, and reintroductions are considered on a case-by-case basis. Primary factors considered when determining whether reintroduction will be successful or not include: animal's age, social rank and status, gender, and how long the animal has been integrated within their specific group. Typically, females, younger animals, and those with good social ranking are easiest to reintroduce.

Further characterization of disease progression and etiology in JME may lead to new insights into MS. Since most JME animals are euthanized for humane reasons, the availability of high-quality brain and spinal cord tissue

specimens is outstanding and facilitates the development and validation of MRI biomarkers relevant to MS. Additional characterization of disease natural history, CSF assays, and immunohistochemical analyses will be necessary before confident comparisons can be made between JME and human disease. JME is a novel and promising non-human primate model of inflammatory and demyelinating disease with potential applications in understanding MS and MS-like diseases.

DCE-MRI assessment of cortical gray matter changes in multiple sclerosis

Introduction

Clinically, acute white matter lesions in MS are identified using contrast-enhanced MRI.[22] The typical MR contrast agents are FDA approved low molecular weight gadolinium (Gd) chelates. The combination of contrast agent administration and time series acquisition of T_1-weighted MR images is known as dynamic contrast enhanced (DCE) MRI. Pharmacokinetic (PK) modeling of DCE-MRI data quantifies physiologically important parameters such as blood volume, blood flow, blood-brain barrier (BBB) permeability, and contrast agent distribution volume (mostly interstitial space). Indeed, one of the first quantitative DCE-MRI PK experiments examined BBB permeability in MS lesions.[77] Our group has derived a pharmacokinetic model, the Shutter-Speed Model (SSM),[78,79,167] which accounts for the indirect nature of MR contrast agent detection, and has been shown effective in the study of a variety of pathologies, including MS.[76,80–85,185–187] Further, research from the last decade has shown that gray matter tissue damage is a key component of MS, occurs early in disease, is related to cognitive impairment, and influences accumulation of disability.[7,8,12,45,170–172,174,175,188,189] Increased interest in cortical GM pathology, specifically as it relates to early measures of disease progression and clinical disability, motivates new in-vivo investigations explicitly designed for the cortical GM.

Imaging and Visualization of MS Lesions

Cortical lesions are not easily detected *in-vivo* by standard MRI techniques due to poor spatial resolution, low signal-to noise ratio, and insufficient image contrast. Therefore, the study of gray matter damage in MS has largely relied on post-mortem tissue analysis with *ex-vivo* MRI and histologic staining, both of which have revealed cortical demyelination. Cortical lesions are generally believed to have a limited inflammatory response, yet some researchers have suggested that cortical damage in early MS may be associated with considerable inflammation while more progressive stages of the disease exhibit less cortical inflammation.[190] Because autopsy-derived specimens predominantly represent a chronic disease state, post-mortem studies reveal little about underlying disease processes and potential inflammatory response.[191] Hence, the pathology of early cortical MS lesions is essentially unknown.[173] Further, evidence that damage spreads into the normal-appearing cortex coupled with the difficulty of imaging cortical lesions increases the need to study diffuse, non-lesional changes in the cortical microenvironment in MS.[192] Novel imaging techniques that allow for minimally- or non-invasive longitudinal measurements of focal and diffuse changes in the cortical gray matter microenvironment are required to characterize the temporal relationship between physiological changes and clinical and pathological disease progression.[7,44,161,193,194]

MRI readily detects white matter lesions and has long been used in diagnosing and studying MS. Inflamed tissue exhibits a significantly higher water concentration than surrounding, normal-appearing tissues. This difference in

water concentration produces contrast in MR images and is the reason white matter lesions are MRI-visible. However, gray matter lesions generally are considerably less inflammatory than white matter lesions. Thus, the difference in water concentration between lesions and normal-appearing gray matter is small, rendering them effectively MR-invisible by conventional methods.[190] A recently introduced MRI technique, double inversion recovery (DIR),[195] has shown promise in imaging gray matter lesions and has provided additional evidence of gray matter's importance in MS.[44,171] Though an improvement over previous methods, DIR has poor sensitivity to gray matter lesions – detecting only 18% of cortical lesions[196] - and is generally riddled with confusing artifacts that contribute to poor specificity.[197–199] When combined with Phase Sensitive Inversion Recovery, DIR has shown improved sensitivity and mitigated artifacts with high field (3 Tesla) MR.[198] While these methods demonstrate improvements in lesion visualization, none of them access physiological parameters specific to microenvironment changes. Other MR imaging protocols (Magnetization Transfer Ratio, Diffusion Tensor Imaging) are able to reveal diffuse microscopic cortical damage but are unable to show focal changes. It is well known that vascular changes occur in the gray matter in MS, but the temporal expression of such changes and their relationship to pathological disease progression are not well understood.[193,194]

The introduction of high field (3T) and ultrahigh-field (>7T) MRI in research settings has made possible vast improvements over clinically achievable images. Increased magnetic field, and novel image acquisition acceleration techniques,[200]

allow for substantial improvements in signal-to-noise ratio (SNR), spatial resolution and image contrast. Our group,[76,80,185–187] and others,[191,197] have shown that high field (4T) and ultrahigh-field (7T, 9.4T [*ex-vivo*][191]) MRI are capable of detecting MS white matter pathology better than lower field strength instruments in both *ex-vivo* and *in-vivo* white matter tissue.

Our preliminary DCE-MRI data - acquired at both 4T and 7T - demonstrate that PK modeling with the SSM[167] provides a means of quantitatively measuring and characterizing vascular properties in brain tissue with high spatial resolution. One theory of pathogenesis of tissue damage in MS describes a hypoxia-like insult resulting from inflammation-induced vascular damage.[50,201] Moreover, a 'metabolic hypoxia'[202] leads to a mitochondrial respiratory dysfunction that may contribute to progressive neurodegeneration in MS. Accordingly, an MRI biomarker sensitive to metabolic dysfunction has immense potential in exposing the mechanisms underlying lesion pathogenesis and disease progression. One of the key parameters returned from SSM modeling, τ_b - the mean capillary water molecule lifetime, has been shown to be directly related to metabolic activity.[203–206] This work explores feasibility of mapping the physiologically relevant PK parameters, p_b and τ_b, in human cortical gray matter in-vivo at 7T.

Preliminary Data

Initial analyses of 12 healthy controls and 15 MS subjects imaged at 4T (Varian Inova, acquired at Brookhaven National Laboratory) revealed an increase of blood volume fraction by about 20% in MS normal appearing subcortical gray

matter (NAGM) and 13% in normal appearing white matter (NAWM) as compared to controls, independent of sex (see **Table 1**).[187] This suggests a notable change in the vasculature associated with MS occurs in gray matter and is quantifiable via PK modeling.

Table 8. MS vs. Control group comparisons of blood volume fraction (p_b) for normal appearing white matter (NAWM) and normal appearing gray matter (NAGM).[187]

		Control	**MS**	**% Diff**
		(n = 12)	**(n = 15)**	**MS > Control**
p_b:	NAWM	0.013 (±0.003)	0.015 (±0.005)	13%
	NAGM	0.023 (±0.003)	0.027 (±0.007)	20%

Values shown are mean (± SD)

Imaging at 7T provides substantial increases in spatial resolution and image contrast. Increasing spatial resolution reduces partial volume averaging and improves access to PK parameters in cortical gray matter. Indeed, the intensity profile of the white/gray matter boundary exhibits a substantially sharper cutoff at 7T than 3T. Anatomical image acquisition parameters can be tuned, and image phase information used, to provide even greater contrast between and within gray matter and white matter[207] for robust cortical segmentation for PK parameter measurement.

Methods

Subjects were recruited to participate in high-field DCE-MRI studies of MS at Oregon Health & Science University (OHSU) between 2009 and 2013. MS

subjects were previously diagnosed with clinically definite MS. DCE-MRI data were collected from 18 RRMS (9M/9F, 42 (±7) years) and 7 healthy control (HC; 6F/1M, 27 (±6.5) years) subjects.

MRI Methods

All studies were performed at OHSU's Advanced Imaging Research Center with a 7T whole body MRI instrument (Siemens) equipped with an actively-shielded AVANTO whole body gradient system (45 mT/m in 250 μsec). Images were obtained with either an 8-channel (n=4 HC, 3 RRMS) or 24-channel (n = 3 HC, 14 MS) radiofrequency head coil. A turboFLASH sequence employing a global adiabatic pulse and 4 inversion times (TI=200, 900, 2200 ms and no inversion; 64 2mm thick slices, 1mm in-plane; 8 min acquisition time) was used to create quantitative whole-brain R_1 ($\equiv T_1$) maps before and after each injection of contrast. A catheter placed within an antecubital vein was used to deliver a total of 0.1 mmol/kg Gd(HP-DO3A) [Gadoteridol; ProHance] with a power injector. Total contrast dose was calculated then split into three separate injections of stepwise increasing doses: $1/7^{th}$ total dose, $2/7^{ths}$ total dose, and $4/7^{ths}$ total dose.

Rapidly-sampled single-slice dynamic MRI data were collected with a single axial slice (10 mm thick) inversion-recovery (IR) turboFLASH sequence with 8 inversion times, and 2.3 second sampling interval. Other acquisition parameters were FA 6°, TR 285 ms, TE 1.15 ms, FOV 19.2 x 25.6 cm, 128 x 96 matrix. Fifty IR image sets were acquired during each IV contrast injection.

DCE-MRI Pre-Processing

All whole-brain images were co-registered to the initial anatomical MR image for each subject and subsequently bias-corrected and segmented as previously described.[208] Lesion maps were manually drawn and lesion areas were removed from GM and WM maps created in the original segmentation. Parametric R_1 maps were calculated by voxelwise fittings of the signal intensity at each inversion time with a full Bloch simulation accounting for all RF pulses and pulse delays. Inversion recovery modeling was achieved with a single exponential inversion recovery equation using a gradient expansion algorithm. Single-slice DCE-MRI data were segmented by fitting Gaussian functions to histographic data to obtain peak positions and determine WM and GM areas.[209] An example is shown in **Figure 38**. Briefly, a bimodal Gaussian function was fit to image histograms yielding peak values and standard deviations for gray and white matter peaks. GM and WM voxels were identified by setting integration limits one standard deviation above and below the respective peak. Integration limits were automatically adjusted to eliminate GM/WM overlap.

Pharmacokinetic modeling

Non-linear shutter-speed modeling of DCE-MRI data (detailed elsewhere)[78–80,88,210] was used to extract estimates of blood water fraction (p_b), and τ_b^{-1} (unidirectional rate constant for equilibrium water extravasation). Average R_1 values for WM and GM were extracted from each subject using the segmentation maps created during pre-processing. An ROI placed in the sagittal sinus of each subject was used to obtain R_1 values in the blood (R_{1b}). The

average R_1 values for WM and GM were then fit using the SSM to extract estimates of R_{1i}, p_b, and τ_b for each subject. Regions of interest (ROIs) were manually drawn on single-slice data to obtain values for pure NAWM and NAGM in all subjects.

Results

Sparsely Sampled Whole-Brain R_1 Maps

Figure 36 shows average R_1 in the white matter for a representative subject plotted against R_{1b}. The blue solid curve is the fit from the 2-parameter 2-site-exchange Shutter-Speed Model; the black dotted line is a linear fit to the data. Limited R_{1b} dynamic range results in data confined to the fast-exchange

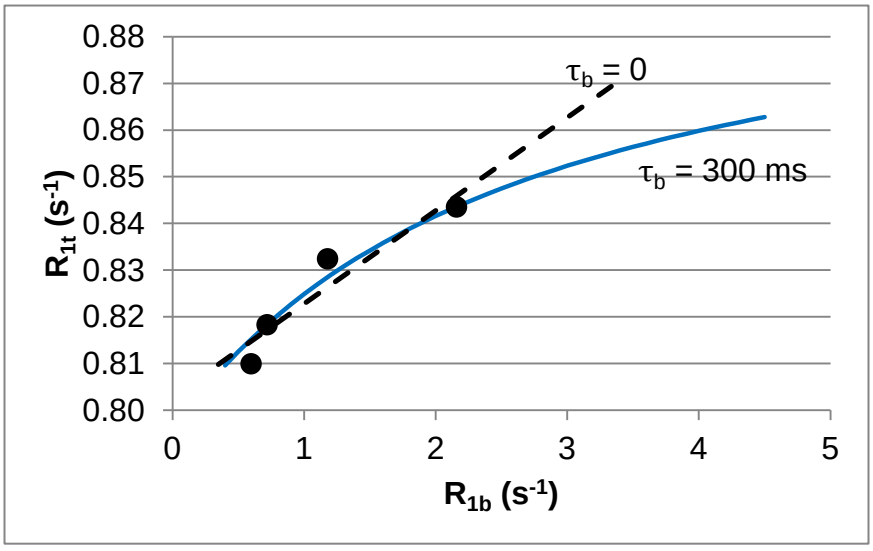

Figure 36. Average WM Fitting of Temporally Sparse Data. Data points are the whole-brain WM average R_1 in a 38 year old female RRMS subject. The dotted line demonstrates a fitting obtained from a linear model assuming τ_b is effectively ≈0; i.e., exchange is infinitely fast. The blue line is the SSP fitting assuming τ_b is 300 ms. Given the limited dynamic range in R_{1b}, we cannot reliably obtain τ_b estimates from these data.

regime in which the relationship between R_{1b} and R_{1t} can appear linear (τ_b effectively zero) rather than nonlinear (non-zero τ_b) and is thus not suitable for producing τ_b estimates. Data was thus determined insufficient for the desired analyses, so parametric mapping was not performed on the whole-brain data.

Single-Slice DCE-MRI Data

Using identical scanning protocols, the 24-channel coil achieves more than twice the signal-to-noise ratio (SNR) of the 8-channel coil (SNR 74 vs SNR 28 in the examples shown in Figure 2, respectively). Contrast between WM and GM was typically better with the 24-channel coil than the 8-channel coil, allowing more reliable segmentation. However, some GM areas were misclassified as WM in nearly all cases, which is likely due to low spatial resolution and a simplistic segmentation technique.

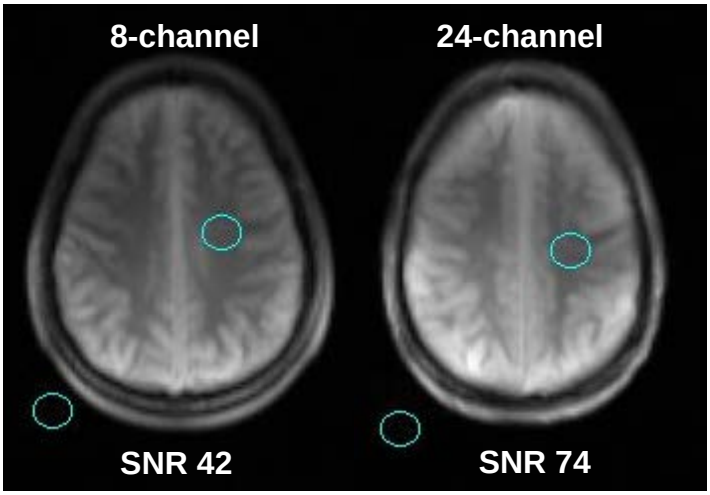

Figure 37. SNR Comparisons between 8- and 24-Channel Head RF Coils. SNR and tissue contrast are increased with the 24-channel coil (image obtained from 33 y/o female RRMS subject) compared to the 8-channel coil (image obtained from 30 y/o male RRMS subject). ROIs used for SNR calculation are overlaid on the first inversion time from the base IR image sets.

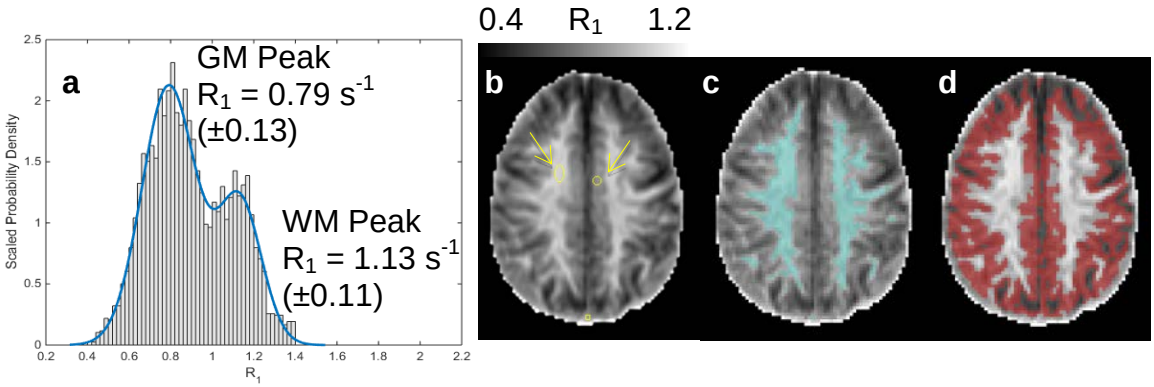

Figure 38. Histographic Segmentation. Single-slice R_1 map histogram data from a 33 year old female RRMS subject is shown on the left (a) with the Gaussian fits overlaid in blue. WM and GM peaks are readily identified and the resulting fits produce reasonable WM (c) and GM (d) masks. Tissue ROIs are drawn in yellow on the R_1 map in panel b (arrows).

Rapidly-sampled single-slice DCE-MRI data acquired during injection of contrast agent capture the first-pass dynamics of contrast agent before extravasation becomes appreciable. During this time the contrast molecule agent remains largely intravascular and R_1 in the blood reaches levels sufficiently high to be sensitive to τ_b. **Figure 39**c is an analogous plot to that shown in **Figure 36** demonstrating the R_1 in a NAWM ROI plotted against R_{1b}. The relationship between R_1 in tissue and R_{1b} is now appreciably nonlinear and pharmacokinetic modeling produces a τ_b estimate of 360 ms. Data from the 8-channel coil were sufficient for reliable ROI PK modeling and produced results consistent with those from the 24-channel coil. Average ROI PK parameters are summarized in **Table 9**.

R_{1i} (longitudinal relaxation rate constant of the tissue corrected for contributions from blood) values are decreased in both NAGM and NAWM in MS compared to HC, suggestive of diffuse tissue damage and consistent with a

recent report.[205] Elevated MS τ_b and p_b are consistent with observations previously reported to be related to important vascular and metabolic changes related to disease activity in MS brain.[87,187] Importantly, elevated τ_b indicates longer water molecule lifetimes in blood, consistent with reduced metabolic activity.

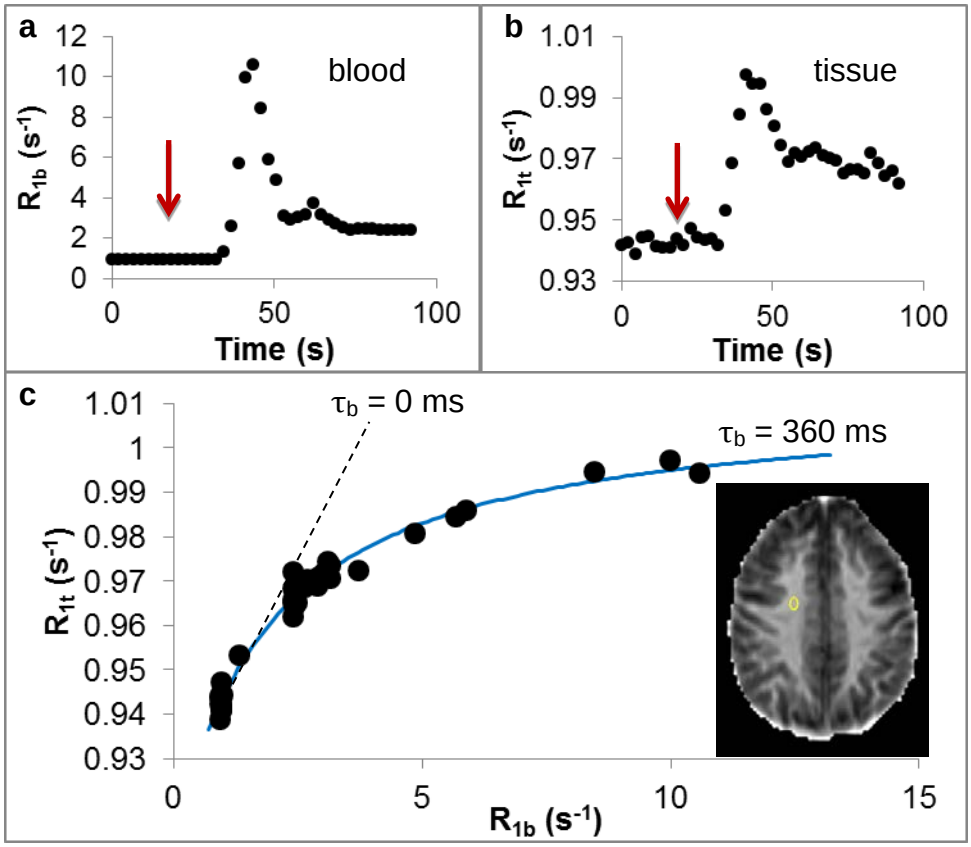

Figure 39. WM ROI Single-Slice Data. Blood (a) and tissue (b) response curves are shown values from the second injection (2/7^{ths} total dose) from a 38 year old female HC subject. GBCA injection is indicated by the red arrow. Black dots in panel c represent tissue R_1 plotted against R_{1b}. The fitted curve is shown in blue. R_{1b} reaches maximum values much higher than those in the sparse sampled data (Figure 33), thus driving the system well beyond the fast-exchange regime and providing access to τ_b estimates. The gray dashed line represents the linear response expected when τ_b is assumed to be effectively zero. WM ROI selection is demonstrated in panel c inset.

Table 9. Population-averaged SSP DCE-MRI Parameter Values

	SSP DCE-MRI		
	R_{1i} (s^{-1})	p_b	τ_b (s)
Health Controls (n=7)		mean (±SD)	
NWM	1.036 (±0.076)	0.018 (±0.005)	0.263 (±0.083)
NGM	0.741 (±0.068)	0.049 (±0.021)	0.367 (±0.150)
RRMS (n=18)			
NAWM	1.015 (±0.053)	0.020 (±0.005)	0.288 ±(±0.081)
NAGM	0.738 (±0.081)	0.056 (±0.029)	0.411 (±0.197)
% Diff MS vs HC			
NAWM	-2%	12%	10%
NAGM	-3%	14%	12%

Parametric maps were created by performing voxelwise fits of the R_1 data. Image sets collected with the 24-channel coil typically had high enough SNR to produce reliable parametric maps. Representative p_b and τ_b maps are shown in **Figure 40** for one healthy control and one MS subject; both sets were collected with the 24-channel coil. Consistent with the ROI averages, p_b and τ_b values are generally elevated in the MS maps compared to that of the healthy control. Indeed, parametric mapping demonstrates the real strength of these imaging techniques: we can visualize diffuse spatial variations in tissue properties that are relevant to disease state. Importantly, cortical areas are distinctly demarcated from the white matter, particularly in the p_b maps, demonstrating that this technique is capable of producing high fidelity parametric maps in human brain in-vivo.

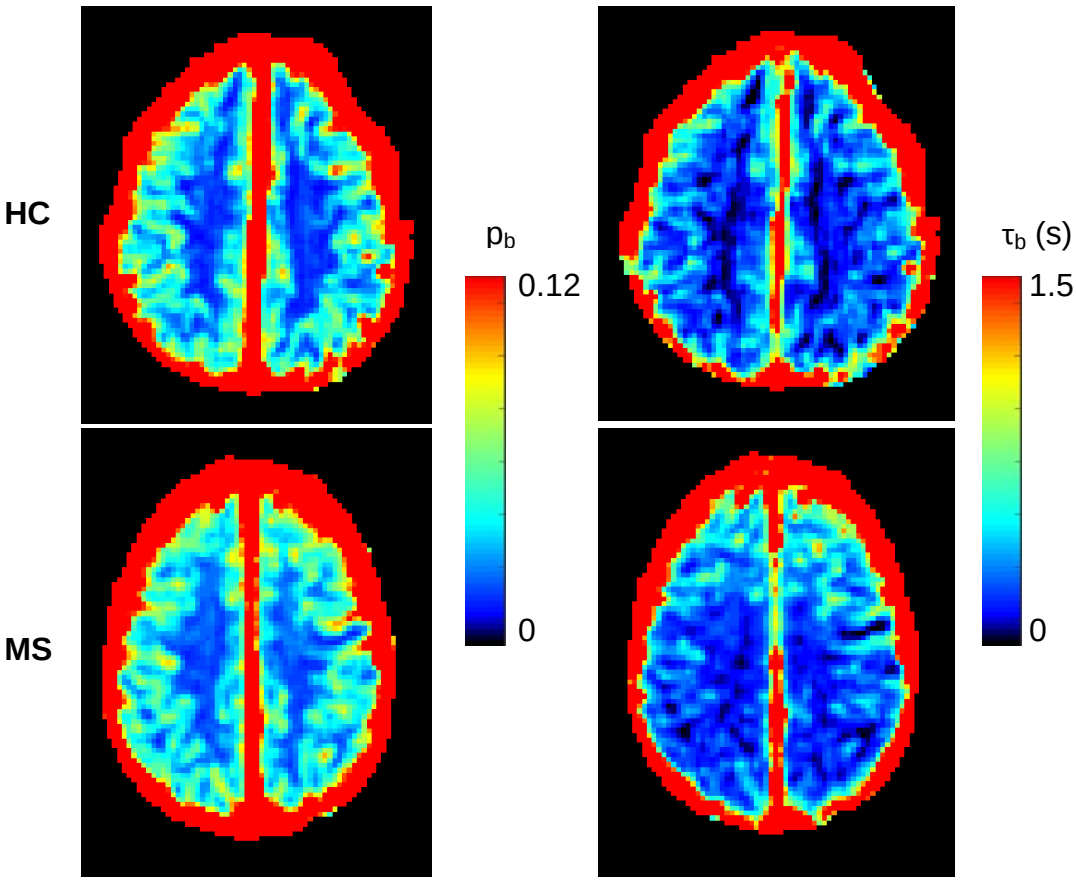

Figure 40. Single-Slice Parametric Maps. Parametric maps for a 34 year old HC male (top) and the 33 year old female RRMS subject (bottom) in Figure 35. Blood volume is higher in GM than in WM, consistent with the highly vascularized nature of the cortex compared to WM. The τ_b maps reflects anatomy, suggesting reliable fittings. Both data sets were acquired with the 24-channel RF coil. Elevated subarachnoid values are artefactual.

Discussion

Despite long acquisition times and careful measurement, whole-brain R_1 measurements were too noisy to reliably create R_1 maps necessary for voxel-by-voxel parametric mapping of PK parameters. Moreover, the R_{1b} range observed in these sparsely-sampled whole-brain images was not sufficiently broad to provide sensitivity to τ_b. Rapidly-sampled single-slice data achieved sufficient

dynamic range in R_{1b} values to allow estimation of τ_b in ROI analysis in all subjects. Image quality produced by the 24-channel coil was sufficient in most cases to produce reliably parametric maps demonstrating tissue microvascular characteristics. The values obtained for both p_b and τ_b in this study are in agreement with previous reports at both 4T and 7T,[87,187,205] demonstrating that this is a robust and reproducible technique.

While tissue segmentation in whole-brain volumes is routinely performed, segmenting single-slice data can be more challenging as the standard tissue atlases used in some volumetric segmentation platforms[130,156] are not readily applied to 2D data. The histographic segmentation applied in this analysis has been shown effective,[209] but ultimately is a simplistic approach that depends on high tissue contrast and high SNR. Increasing the spatial resolution of the current turboFLASH IR experiment will reduce partial volume effects and improve segmentation results.

Cortical segmentation was achieved in a subset of the images obtained in this study, which is essential for more comprehensive analysis specific to the cortical gray matter. However, because segmentation was not reliably achieved in all image sets, even those obtained with the 24-channel coil, it is important that imaging sequences be tuned to achieve higher spatial resolution. Indeed, imaging sequences tuned for the 8-channel coil were used in this study to produce a more accurate side-by-side comparison of the two coils and to maintain study consistency over time. Higher resolution images are feasible with the 24-channel coil, an improvement that will provide more robust cortical

segmentation and allow cortical gray matter to be analyzed separately from white matter with reduced partial volume averaging.

PK parametric mapping of the cortex has the capacity to elucidate global, regional and focal vascular changes associated with MS. SSM analysis of cortical gray matter accesses quantitative measurements of vascular properties (blood volume, transendothelial water exchange) and BBB permeability *in-vivo*. Indeed, τ_b parametric maps suggest disrupted metabolic activity in normal-appearing MS brain tissue and lesions, potentially offering increased lesion conspicuity.[87] Key changes in vasculature and metabolic activity are likely temporally related to and are indicative of pathological mechanisms contributing to sustained and increased disease.[87,194,211] DCE-MRI measurements are minimally invasive and repeatable, thus ideal for longitudinal studies, and thus is poised as an important tool for studying MS disease progression.

This work has demonstrated that SSM analysis of DCE-MRI data acquired at ultra-highfield can access important physiological properties of the human cortical gray matter and is thus ideal for both cross-sectional and longitudinal studies providing thorough characterization of MS disease processes in the cortex. These imaging techniques could be further utilized to monitor treatment efficacy and may lead to new therapeutic approaches specifically targeting early MS cortical gray matter degeneration.

Discussion and Summary

Multiple sclerosis (MS) is an inflammatory disease of the central nervous system (CNS) and is a leading cause of non-traumatic neurological disability in young and middle-aged adults. Breakdown of the blood-brain barrier (BBB) in MS produces inflammatory lesions by increasing permeability to macromolecules, blood-borne solutes, pathogens, and immune cells including $CD4^+$, $CD8^+$ T cells and B cells.[12,17] The combination of inflammation and an immune response leads to oligodendrocyte death, demyelination, and eventually neuronal loss.[6,12,17,46,163,171,190] Patients with MS experience highly varied symptoms including sensations of numbness, vision impairment, fatigue, loss of coordination, and bladder dysfunction.[50] Symptoms are not limited to physical disability; cognitive impairments including attention deficits, memory loss, and reduced mental processing also affect a large number of patients.[3–8] Disease etiology is yet unknown; investigation of tissue pathology is challenging in humans and requires invasive biopsy procedures or post-mortem analysis.

Magnetic resonance imaging (MRI) plays a vital role in not only diagnosing MS, but also in the characterization of disease and in monitoring treatment efficacy.[18,56,212,213] Non-invasive imaging biomarkers provide access to markers of pathology in-vivo. However, it is essential that each imaging biomarker be properly validated by comparison to histological and immunohistochemical measurements. The use of animal models provides the opportunity to carefully control disease state, obtain in-vivo MRI, and then correlate MRI findings with

post-mortem tissue analysis. Human studies are inherently less controlled, include many potentially confounding factors, and rarely afford the opportunity to compare in-vivo MRI with comprehensive tissue analyses. A wide variety of animal models have been developed and proposed to study MS, each with their own strengths and weaknesses.[89,90,92] In this work I investigated magnetization transfer ratio (MTR) as a surrogate biomarker of myelin content in the cuprizone mouse model of demyelination and remyelination. I also investigated imaging biomarkers in Japanese macaque encephalomyelitis, a novel spontaneous inflammatory demyelinating disease found in Japanese macaques, that bears striking similarities to human demyelinating diseases.[99,214] MTR and DCE-MRI biomarkers were also presented in human studies at 3T and 7T, respectively.

Clinicians rely on both T_2-w and T_1-w MRI contrasts to diagnose MS and evaluate disease progression. Inflammation and loss of both myelin and neurons produce hyperintense signal on T_2-w scans, and hypointense signal on T_1-w images. The use of gadolinium-based contrast agents (GBCA) with MRI in contrast-enhanced MRI provides qualitative insight into BBB integrity: T_1-w images acquired before and after intravenous injection of GBCA identify enhancing lesions, indicating increased BBB permeation. Quantitative analysis of dynamic-contrast-enhanced MRI (DCE-MRI) yields surrogate biomarkers of disease state such as BBB permeability (K^{trans}), blood volume fraction (p_b), and transendothelial water exchange (τ_b^{-1}). Beyond the qualitative analysis of whether or not a lesion enhances, K^{trans} provides a more sensitive assessment of BBB permeability that has important implications in evaluating lesion progression

and response to therapy. Indeed, K^{trans} exposes BBB permeability in pre- and post-acute lesions even when frank GBCA-enhancement is not obvious, as shown in **Figure 31**. Longitudinal evaluation of even subtle changes in BBB permeability will certainly help reveal the nature of lesion evolution, provide a sensitive method of evaluating therapeutic response, and may provide insight into new therapeutic targets.

Magnetization transfer (MT) imaging produces a novel image contrast by taking advantage of the unique properties of hydrogen protons in macromolecules such as myelin. Selective saturation of protons associated with macromolecules in the so-called restricted pool is possible by applying a radio-frequency (RF) pulse offset from the Larmor (resonant) frequency by several hundreds or even thousands of Hertz.[59,215] A carefully selected off-resonance saturation pulse will eliminate the net magnetization of the restricted pool without substantially decreasing the net magnetization of bulk water protons (the free pool).[52] Dipole-dipole interactions between restricted protons and water protons loosely bound to macromolecules in a hydration layer transfer magnetization between the pools, effectively reducing the net magnetization, and thus the MR signal, of the free pool.[66] Diffusion of water molecules from the hydration layer into the bulk water promotes magnetization transfer in the free pool. The magnetization transfer ratio is a semi-quantitative marker of macromolecular content in-vivo.[54] Myelin is rich in macromolecules and is thus a major contributor of macromolecules in the white matter of the CNS; accordingly MTR has been applied as a surrogate marker of myelin content in vivo.[65,72,124] Calculation of

MTR is trivial and requires only two images: one acquired with the saturation pulse applied, and one either without the saturation pulse, or with the pulse sufficiently far off-resonance to have no appreciable effect on the restricted pool.

The cuprizone mouse model produces reasonably reliable demyelination with little mortality, making it an ideal model for longitudinal studies of demyelination and spontaneous demyelination. In my investigation of MTR as a marker of myelin content in the cuprizone mouse model I found that MTR decreases in the corpus callosum (CC) after 6 weeks of cuprizone diet (0.2% wt/wt), then increases after 6 weeks of recovery post-cuprizone. MTR values correlated well with histological measurements of myelin content, suggesting that MTR is a sensitive marker of myelin in-vivo. However, MTR is also sensitive to edema and axonal density, thus it is not specific to myelin content.[65,71] Acute cuprizone-induced demyelination occurs without substantial axonopathy or inflammation, so changes seen in MTR in this model can be attributed primarily to changes in myelination. While MTR has been previously explored in the cuprizone model, [70,95] the work presented here confirms and expands upon earlier work by presenting the first comprehensive overview of spatially varying cuprizone-induced demyelination in the mouse corpus callosum (CC) and external capsule (EC). Indeed, it is the exceptional spatial resolution and whole-brain coverage that revealed a unique spatio-temporal pattern in demyelination and remyelination that was previously not described.

A caudal-to-rostral pattern of demyelination has been described in the literature, along with moderate demyelination in the gray matter and

cerebellum.[70] I demonstrate here that there is a more complex pattern of demyelination including opposing rostral-to-caudal and caudal-to-rostral gradients of demyelination in the lateral and medial CC, respectively. Future studies exploring the etiology of these patterns will certainly lead to new understanding of not only the model, but also of mechanisms of damage and repair vary throughout the CNS. While the mechanism of cuprizone's action on the CNS is unknown, it is currently believed that cuprizone administration disrupts ion homeostasis in the brain, leading to mitochondrial dysfunction and oligodendroglial death. However, the important question of why are some parts of the CC preferentially vulnerable to demyelination and others are relatively preserved remains unanswered. My work has led me to two primary theories, each with multiple possible mechanisms that require further investigation. In short, is the regional heterogeneity in demyelination due to (1) some regionally varying morphology or functionality that protects oligodendrocytes from cuprizone-induced demyelination, or, (2) areas more effective at repair may obscure underlying pathology.

Patterns of demyelination in this model appear to correspond to (a) sources of neural progenitor cells (NPCs) and oligodendroglial precursor cells (OPCs), and (b) location along the rostral migration stream (RMS).[142,143,145–152] OPCs and NPCs migrate rostrally from the subventricular zone (SVZ) into the olfactory bulbs via the RMS. Increased migration from the SVZ following cuprizone exposure has been shown.[149] This normally-occurring migration of NPCs could provide considerable early and ongoing support to the rostral midline

of the CC that would not be seen in the lateral CC or in any part of the caudal CC. This could explain the limited demyelination in the medial rostral CC, significant demyelination in lateral rostral CC, and also the significant demyelination in the medial caudal CC. Yet, only limited demyelination is observed in the lateral caudal CC. Looking now at the proximity to the SVZ in the lateral ventricles, it is evident that lateral caudal CC and medial rostral CC are both spatially closer to the SVZ than their medial and lateral counterparts, respectively. So, perhaps these areas have preferential access to NPCs and OPCs, resulting in rapid response to injury and more substantial repair even during acute demyelination, than other areas that appear more heavily affected. However, larger and more complex brains, such as those found in humans and non-human primates, may have additional progenitor cell zones and migration pathways,[216] so mechanistic conclusions drawn from the cuprizone model may not translate directly to human disease.

Alternatively, or perhaps additionally, the differences in vulnerability to demyelination may be genetic. In situ hybridization (ISH) analysis of myelin basic protein (MBP) messenger ribonucleic acid (mRNA) performed by the Allen Institute for Brain Sciences[132,133] demonstrates heterogeneity of gene expression throughout the CC. When compared to changes in MTR observed in the experiments presented here, there appears to be an inverse correlation between MBP mRNA expression and severity of demyelination, as shown in **Figure 41.** It is possible, though entirely unknown, that increased levels of basal mRNA for MBP provides greater capacity for MBP production, which may be upregulated in

response to MBP dissociating from myelin sheaths during cuprizone-induced demyelination. This certainly is an evolving theory that may warrant further investigation.

In summary, cuprizone is an interesting model that reliably (allowing some inter-animal variance) produces demyelination and spontaneous remyelination. Its use has been shown in developing non-invasive imaging biomarkers of disease. However, until the mechanisms responsible for the spatial heterogeneity

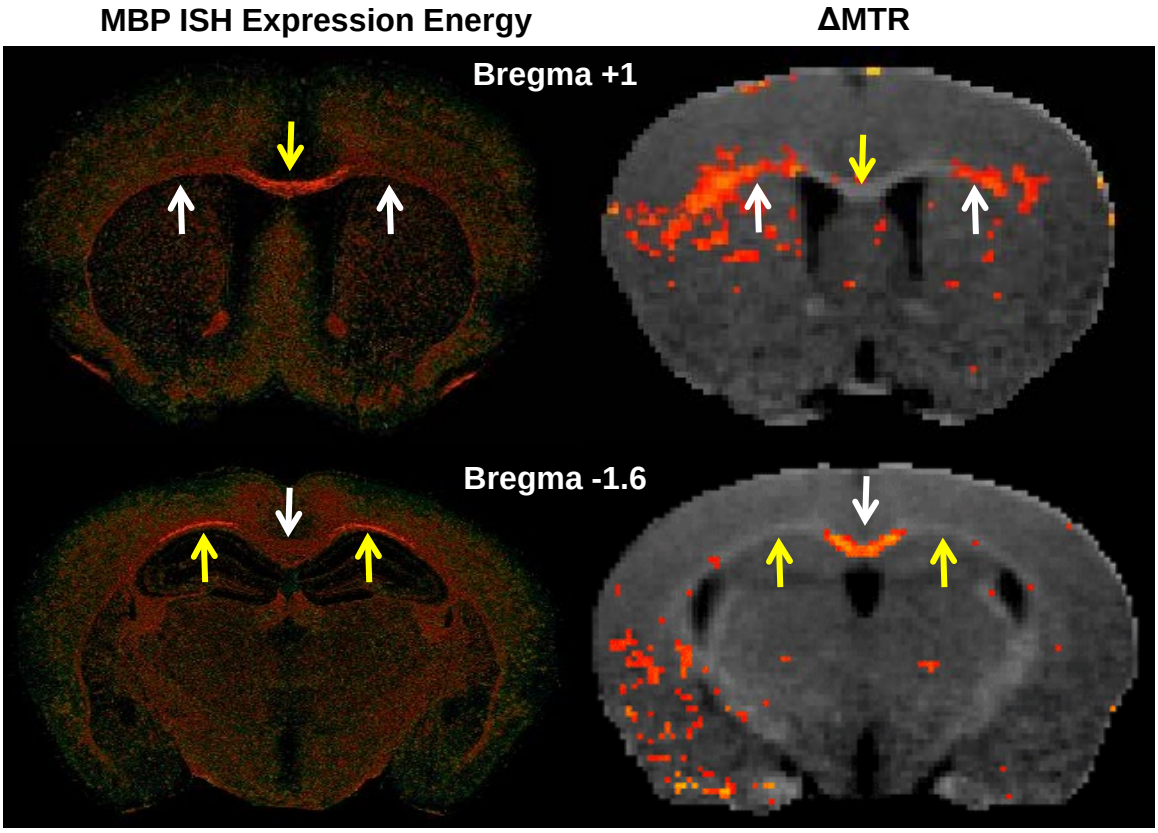

Figure 41. MBP mRNA Expression vs ΔMTR. MBP ISH data compared to ΔMTR at two levels in the mouse brain (top row: rostral, approx. bregma +1; bottom row: caudal, approx. bregma -1.6). Yellow arrows indicate areas of higher MBP mRNA expression and little change in MTR. White arrows indicate areas of lower MBP mRNA expression and significant MTR changes. An inverse correlation between MBP mRNA expression and ΔMTR is visually striking. See Figure 11 for ΔMTR color scale. ISH color scale relative; orange/yellow indicates high expression energy, green is low.

of demyelination are more carefully considered, extreme caution should be exercised when comparing any mechanistic study of pathology or therapy in this model to human disease. Indeed, it is likely that the uniquely variable vulnerability to cuprizone-induced demyelination in mouse CNS tissues will actually demonstrate far more about pathological mechanisms than previously expected from this model.

An important extension to this work developed a standardized imaging protocol demonstrating reproducible MTR maps across multiple sites. The North American Imaging in Multiple Sclerosis (NAIMS) Cooperative was formed with the goal of developing sensitive, reliable imaging-based surrogates for disease progression in MS. The current lack of standardization leads to increased variability, particularly in MTR. Increased variability reduces reliability, and makes quantitative comparisons between studies almost impossible. This study demonstrated that with careful standardization MTR can be a highly reproducible biomarker, both within and across sites. One subject with clinically stable RRMS traveled to seven NAIMS sites and underwent two imaging sessions at each site on a 3T Siemens instrument. We thus were able to compare MTR values within sites by looking at Session 1 versus Session 2 results, as well as across sites. Imaging sequences were developed for the latest technology, using custom-created protocols, so the technique is not entirely off-the-shelf and is thus limited in current applicability. However, the results of this study are encouraging and will lay a solid framework for creating standardized protocols in the future.

Current animal models of MS provide valuable insight into a variety of disease phenotypes and mechanisms, yet so far none capture the truly spontaneous nature of the disease. JME is a spontaneous demyelinating disease that recapitulates many features of MS including inflammatory immune response, demyelination, and disability, and is thus an exciting potential non-human primate model of MS. In an effort to more fully characterize the disease and thus broaden our understanding of how this disease may reflect MS, I described imaging biomarkers commonly used in human studies, T_2 and contrast-enhancing T_1 lesions, and BBB permeability, to compare JME to MS and its mimics. Lesion distribution probability maps offer important insight into disease pathogenesis, vulnerable tissues, and describe what is typical of JME to help differentiate it from other diseases and syndromes. Three-dimensional renders of the lesion distribution probability maps from **Figure 30** provide a clearer overview of how and where lesions cluster in this disease. Three views through the brain are presented in **Figure 42**: a view from the right, from the back (anterior) and from the top (superior); T_2 lesion maps are in the top row, R_1 (GBCA-enhancing) in the bottom row.

JME lesions are most frequently found in the cerebellum, followed by the spinal cord, brainstem, and internal capsule. Indeed, in many cases, spinal cord lesions were confluent with brainstem lesions, and brainstem lesions were often confluent with internal capsule lesions. Two JMs presented with lesions only in the cerebellum, and one presented with lesions only in the spinal cord and brainstem. In all other cases lesions were observed in at least two spatially

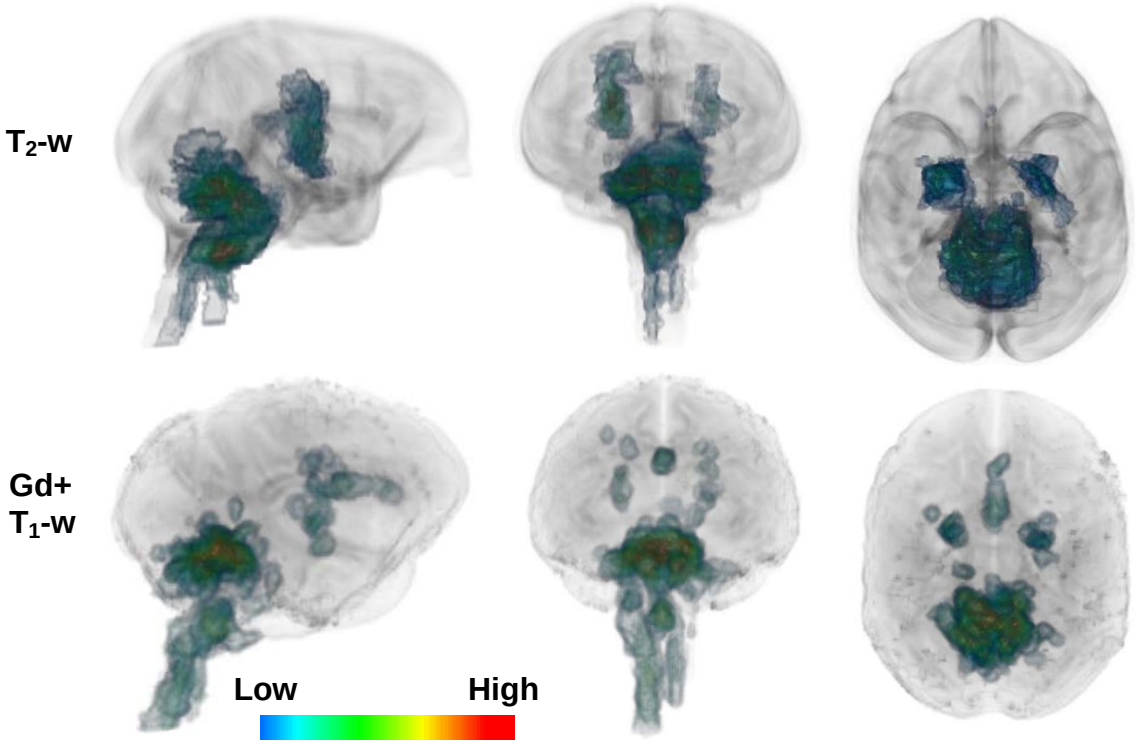

Figure 42. JME Lesion Distribution Probability in 3D. 3D renders of lesion probability maps for T_2 hyperintensities (top row) and contrast-enhancing lesions (bottom row). Note that corpus callosum lesions are not well represented in the T_2 map due to poorer through-plane spatial resolution and warping and blurring artifacts inherent in image coregistration. T_2-w images were not skull-stripped, so anatomy outside of the brain is visible.

distinct tissue regions. Lesion distribution as characterized in this cohort of 21 JME cases does not exactly match any of the human demyelinating diseases explored in this work. Striking immunological similarities between JME and MS have recently been published.[101] So, as with other animal models, JME is an imperfect yet useful model of MS and other human demyelinating diseases. Perhaps most exciting is the spontaneous nature of JME, providing a unique opportunity to investigate mechanisms of disease evolution that will likely provide key insights into the etiology of human disease.

Lesions evolve rapidly in this disease, and progression of disability is aggressive. High dose corticosteroid therapy has been attempted in only a few

recent cases, and it is still unclear how much clinical benefit is gained from this treatment. However, looking at the lesion evolution and changes in K^{trans} in conjunction with treatment in **Figure 35** and **Table 6**, a relationship might be suggested between when steroid dosage was tapered and when new lesions and symptoms develop. High dose steroids were delivered for five days, during which time K^{trans} in existing lesions decreases dramatically, and disease progression (accumulation and worsening of clinical disability) decelerated. However, when the treatment dosage was reduced on day 6, this was followed almost immediately by increased physical disability and new acute lesions on MRI by day 12. It is important to note that retrospective analysis of new lesions on day 12 shows K^{trans} is already increasing by day 5 compared to day 1, albeit more slowly than between day 5 and day 12. Perhaps continued treatment with high dose steroids would have prevented these new lesions from becoming florid and the animal's clinical symptoms may have improved or at least remained stable. Based on the positive clinical outcomes in treating acute episodes human disease with high dose corticosteroids, further exploration is warranted to see whether prolonged treatment with high dose corticosteroids can stop or even reverse disease progression in JME.

Preliminary work has been done exploring a ultrasmall superparamagnetic iron oxide (USPIO) contrast agent, ferumoxytol (FeO), as a possible marker for both blood volume and macrophage activity (see Appendix B – Refereed Conference Proceedings: Vascular Expansion and Blood-Brain-Barrier Permeability: A Comparative Volumetric Study in Acute Japanese Macaque

Encephalomyelitis). Unlike GBCAs, ferumoxytol is too large (non-monodisperse molecular weight 750 kDa, size range 17-31 nm), to extravasate appreciably through the blood-brain-barrier; it remains within the blood at early time points after injection and is thus considered a blood pool, or intravascular, contrast agent.[217] Signal enhancements in tissue observed on T_1-w images acquired ~10 mins after FeO injection may represent areas of increased vascularity. This early enhancement has been observed in some JME lesions; immunohistochemical analyses will provide more clarity about vascular density and will help to validate this as a potential marker of blood volume. FeO has a half-life in the blood of roughly 12 hours in humans, and is slowly cleared from the blood by phagocytes in the liver, spleen, and bone.[218]. In the presence of inflammation, circulating monocytes are recruited to the site of injury and are able to pass through the blood brain barrier.[23,219,220] It follows that macrophages and circulating immune cells containing FeO will be recruited to the site of injury and will demonstrate some accumulation of FeO in the area. Enhancement on T_1-w images 24 hours post-injection of FeO is thus a likely marker of increased macrophage activity and inflammation.[221] Antibodies against the carbohydrate coating used in preparing FeO can be used to stain specifically for FeO in tissue samples. However, tissue must be collected within 24 hours of injection otherwise the carbohydrate degrades and the antibodies are ineffective. We have recently collected tissue from JME cases within this timeframe, and investigation is ongoing. JME provides a unique opportunity to explore these minimally-invasive imaging biomarkers of vascular pathology in-vivo with the essential benefit of post-

mortem tissue analysis that enables validation against gold-standard histological techniques.

The real value of any of these biomarkers is the application in studying human disease. DCE-MRI data were collected from healthy control and MS subjects at 7T in an effort to obtain estimates of blood volume fraction (p_b) and brain metabolic activity (via τ_b^{-1}, the inverse of the brain capillary water molecule lifetime[87]) at high resolution. Temporally sparsely sampled whole-brain qR_1 maps combined with low molecular weight GBCA did not achieve sufficiently high R_{1b} to estimate either p_b or τ_b in this study. Rapidly-sampled single-slice data acquired during contrast injection did achieve sufficient dynamic range in R_{1b} values to allow estimation of τ_b in ROI analysis in all subjects. I qualitatively compared mage quality produced by the older 8-channel and the new 24-channel RF head coils and determined that data from both coils were suitable for ROI analysis. However, parametric mapping is more informative than ROI analysis and also requires much higher image fidelity. Data from the 24-channel coil was sufficient in most cases to reliably produce parametric maps demonstrating tissue microvascular characteristics.

Cortical segmentation was achieved in a subset of the images obtained in this study, which is essential for more comprehensive analysis specific to the cortical gray matter. Importantly, imaging protocols were initially developed for the 8-channel coil, so the full benefits of the 24-channel coil have not yet been realized. Careful optimization of these protocols to fully utilize the new coil will

provide better spatial resolution and increased SNR that will ultimately allow more reliable parametric mapping and cortical segmentation.

This study found that both p_b and τ_b are elevated in normal-appearing brain tissue in MS subjects compared to control, consistent with previous reports.[87,187,205] Indeed, elevated τ_b may reflect down-regulated active transendothelial water cycling, which is directly related to metabolic activity.[87,204,206] Thus, elevated τ_b in MS normal-appearing tissue suggests that metabolic dysfunction occurs not only in lesions,[202] but is present throughout the brain.[87] Together, these results add to the mounting evidence that these biomarkers are (1) sensitive to disease, (2) reproducible in-vivo, and (3) will be important in unraveling disease processes underlying MS and other neurological diseases. Perhaps most importantly, these markers represent a novel method of assessing brain metabolic activity in vivo, without the use of ionizing radiation and radiotracers, and at high enough spatial resolution to isolate and analyze the cortex separate from white matter.

Developing imaging biomarkers of disease using animal models, where access to post-mortem tissue allows careful validation and interpretation of imaging results, is important in studying and treating human disease. Biomarkers, such that those presented in this work, capable of accessing tissue and vascular properties related to underlying disease pathology are perfectly suited for non-invasive, longitudinal investigations of disease and treatments. Application of these biomarkers in human studies will improve treatment of

human disease by elucidating disease mechanisms and processes, help identify new therapeutic targets and strategies, and advance patient care and outcomes.

References

1 WHO. Neurological disorders: a public health approach. *Neurol Disord public Heal challenges* 2006; : 41–176.

2 No Title. http://www.nationalmssociety.org.

3 De Stefano N, Matthews PM, Filippi M, Agosta F, De Luca M, Bartolozzi ML *et al.* Evidence of early cortical atrophy in MS: Relevance to white matter changes and disability. *Neurology* 2003; **60**: 1157–1162.

4 Amato MP, Bartolozzi ML, Zipoli V, Portaccio E, Mortilla M, Guidi L *et al.* Neocortical volume decrease in relapsing-remitting MS patients with mild cognitive impairment. *Neurology* 2004; **63**: 89–93.

5 Calabrese M, Grossi P, Favaretto A, Romualdi C, Atzori M, Rinaldi F *et al.* Cortical pathology in multiple sclerosis patients with epilepsy: a 3 year longitudinal study. *J Neurol Neurosurg Psychiatry* 2011; **83**: 49–54.

6 Geurts JJ, Barkhof F. Grey matter pathology in multiple sclerosis. *Lancet Neurol* 2008; **7**: 841–851.

7 Calabrese M, Agosta F, Rinaldi F, Mattisi I, Grossi P, Favaretto A *et al.* Cortical lesions and atrophy associated with cognitive impairment in relapsing-remitting multiple sclerosis. *Arch Neurol* 2009; **66**: 1144–1150.

8 Horakova D, Kalincik T, Blahova Dusankova J, Dolezal O. Clinical correlates of grey matter pathology in multiple sclerosis. *BMC Neurol* 2012; **12**: 10.

9 Strober LB, Christodoulou C, Benedict RHB, Westervelt HJ, Melville P, Scherl WF *et al.* Unemployment in multiple sclerosis: the contribution of personality and disease. *Mult Scler* 2012; **18**: 647–53.

10 Polman CH, Rudick R a. The multiple sclerosis functional composite: a clinically meaningful measure of disability. *Neurology* 2010; **74 Suppl 3**: S8–15.

11 Cutter GR, Baier ML, Rudick RA, Cookfair DL, Fischer JS, Petkau J *et al.* Development of a multiple sclerosis functional composite as a clinical trial outcome measure. *Brain* 1999; **122 (Pt 5**: 871–882.

12 Popescu BFG, Pirko I, Lucchinetti CF. Pathology of multiple sclerosis: where do we stand? *Continuum (Minneap Minn)* 2013; **19**: 901–21.

13 Ge Y, Law M, Johnson G. Dynamic susceptibility contrast perfusion MR imaging of multiple sclerosis lesions: characterizing hemodynamic impairment and inflammatory activity. *Am J …* 2005; **26**: 1539–1547.

14 Solomon AJ, Klein EP, Bourdette D. 'Undiagnosing' multiple sclerosis: The challenge of misdiagnosis in MS. *Neurology* 2012; **78**: 1986–1991.

15 Miller DH, Weinshenker BG, Filippi M, Banwell BL, Cohen J a, Freedman MS *et al.* Differential diagnosis of suspected multiple sclerosis: a consensus approach. *Mult Scler* 2008; **14**: 1157–1174.

16 Polman CH, Reingold SC, Banwell B, Clanet M, Cohen JA, Filippi M *et al.* Diagnostic criteria for multiple sclerosis: 2010 revisions to the McDonald criteria. *Ann Neurol* 2011; **69**: 292–302.

17 McFarland HF, Martin R. Multiple sclerosis: a complicated picture of autoimmunity. *Nat Immunol* 2007; **8**: 913–9.

18 Wattjes MP, Steenwijk MD, Stangel M. MRI in the Diagnosis and Monitoring of Multiple Sclerosis: An Update. *Clin Neuroradiol* 2015. doi:10.1007/s00062-015-0430-y.

19 Chou I-J, Whitehouse WP, Wang H-S, Tanasescu R, Constantinescu CS. Diagnostic modalities in multiple sclerosis: perspectives in children. *Biomed J* 2014; **37**: 50–9.

20 Hynson JL, Kornberg AJ, Coleman LT, Shield L, Harvey AS, Kean MJ. Clinical and neuroradiologic features of acute disseminated encephalomyelitis in children. *Neurology* 2001; **56**: 1308–12.

21 Wingerchuk DM, Brenda Banwell F, Jeffrey Bennett FL, Cabre P, Carroll W, Chitnis T *et al.* International consensus diagnostic criteria for neuromyelitis optica spectrum disorders. *Neurology* 2015; **85**: 177–189.

22 Grossman RI, Gonzalez-Scarano F, Atlas SW, Galetta SL, Silberberg DH. Multiple sclerosis: gadolinium enhancement in MR imaging. *Radiology* 1986; **161**: 721–5.

23 Vellinga MM, Vrenken H, Hulst HE, Polman CH, Uitdehaag BMJ, Pouwels PJW *et al.* Use of ultrasmall superparamagnetic particles of iron oxide (USPIO)-enhanced MRI to demonstrate diffuse inflammation in the normal-appearing white matter (NAWM) of multiple sclerosis (MS) patients: an exploratory study. *J Magn Reson Imaging* 2009; **29**: 774–9.

24 Rovira À, Wattjes MP, Tintoré M, Tur C, Yousry T a., Sormani MP *et al.* Evidence-based guidelines: MAGNIMS consensus guidelines on the use of MRI in multiple sclerosis—clinical implementation in the diagnostic process. *Nat Rev Neurol* 2015; **11**: 1–12.

25 Raz E, Loh JP, Saba L, Omari M, Herbert J, Lui Y *et al.* Periventricular lesions help differentiate neuromyelitis optica spectrum disorders from multiple sclerosis. *Mult Scler Int* 2014; **2014**: 986923.

26 Kincses ZT, Ropele S, Jenkinson M, Khalil M, Petrovic K, Loitfelder M *et al.* Lesion probability mapping to explain clinical deficits and cognitive performance in multiple sclerosis. *Mult Scler* 2011; **17**: 681–689.

27 Kuchling J, Ramien C, Bozin I, Dörr J, Harms L, Rosche B *et al.* Identical lesion morphology in primary progressive and relapsing-remitting MS -an ultrahigh field MRI study. *Mult Scler J* 2014; **20**: 1866–71.

28 Ghassemi R, Narayanan S, Banwell B, Sled JG, Shroff M, Arnold DL. Quantitative determination of regional lesion volume and distribution in children and adults with relapsing-remitting multiple sclerosis. *PLoS One* 2014; **9**: e85741.

29 Sinnecker T, Dorr J, Pfueller CF, Harms L, Ruprecht K, Jarius S *et al.* Distinct lesion morphology at 7 Tesla MRI differentiates neuromyelitis optica from multiple sclerosis. *Neurology* 2012; **18**: 708–714.

30 Lee M a., Smith S, Palace J, Narayanan S, Silver N, Minicucci L *et al.* Spatial mapping of T2 and gadolinium-enhancing T1 lesion volumes in multiple sclerosis: Evidence for distinct mechanisms of lesion genesis? *Brain* 1999; **122**: 1261–1270.

31 Abbott NJ, Rönnbäck L, Hansson E. Astrocyte-endothelial interactions at the blood-brain barrier. *Nat Rev Neurosci* 2006; **7**: 41–53.

32 Abbott NJ, Patabendige AAK, Dolman DEM, Yusof SR, Begley DJ. Structure and function of the blood–brain barrier. *Neurobiol Dis* 2010; **37**: 13–25.

33 Anderson VC, Lenar DP, Quinn JF, Rooney WD. The blood-brain barrier and microvascular water exchange in Alzheimer's disease. *Cardiovasc Psychiatry Neurol* 2011; **2011**: 615829.

34 Lee Y, Morrison BM, Li Y, Lengacher S, Farah MH, Hoffman PN *et al.* Oligodendroglia metabolically support axons and contribute to neurodegeneration. *Nature* 2012; **487**: 443–448.

35 Snaidero N, Simons M. Myelination at a glance. *J Cell Sci* 2014; **127**: 2999–3004.

36 Bechler ME, Byrne L, ffrench-Constant C. CNS Myelin Sheath Lengths Are an Intrinsic Property of Oligodendrocytes. *Curr Biol* 2015; **25**: 2411–2416.

37 Snaidero N, Möbius W, Czopka T, Hekking LHP, Mathisen C, Verkleij D *et al.* Myelin Membrane Wrapping of CNS Axons by PI(3,4,5)P3-Dependent Polarized Growth at the Inner Tongue. *Cell* 2014; **156**: 277–290.

38 Colmanm D, Filbin M. Cell Adhesion Molecules in Myelination. In: *Basic Neurochemistry: Molecular, Cellular and Medical Aspects. 6th edition.* Philadelphia: Lippincott-Raven, 1999http://www.ncbi.nlm.nih.gov/books/NBK28158/.

39 Alizadeh A, Dyck SM, Karimi-Abdolrezaee S. Myelin damage and repair in pathologic CNS: challenges and prospects. *Front Mol Neurosci* 2015; **8**: 1–27.

40 Quarles RH, Macklin WB, Morell P. Myelin Formation, Sturcture, and Biochemistry. *Basic Neurochem Mol CellulR, ns Med Asp* 2006; : 51–71.

41 Bramow S, Frischer JM, Lassmann H, Koch-Henriksen N, Lucchinetti CF, Sorensen PS *et al.* Demyelination versus remyelination in progressive multiple sclerosis. *Brain* 2010; **133**: 2983–2998.

42 Tallantyre EC, Bø L, Al-Rawashdeh O, Owens T, Polman CH, Lowe JS *et al.* Clinico-pathological evidence that axonal loss underlies disability in progressive multiple sclerosis. *Mult Scler* 2010; **16**: 406–411.

43 Haines JD, Inglese M, Casaccia P. Axonal damage in multiple sclerosis. *Mt Sinai J Med* 2012; **78**: 231–43.

44 Calabrese M, Gallo P. Magnetic resonance evidence of cortical onset of multiple

sclerosis. *Mult Scler* 2009; **15**: 933–941.

45 Filippi M, Rocca M a, Horsfield M a, Hametner S, Geurts JJG, Comi G *et al.* Imaging cortical damage and dysfunction in multiple sclerosis. *JAMA Neurol* 2013; **70**: 556–64.

46 Lucchinetti C, Brück W, Parisi J, Scheithauer B, Rodriguez M, Lassmann H. Heterogeneity of multiple sclerosis lesions: implications for the pathogenesis of demyelination. *Ann Neurol* 2000; **47**: 707–17.

47 Prineas JW, Parratt JDE. Oligodendrocytes and the early multiple sclerosis lesion. *Ann Neurol* 2012; **72**: 18–31.

48 Barnett MH, Prineas JW. Relapsing and remitting multiple sclerosis: Pathology of the newly forming lesion. *Ann Neurol* 2004; **55**: 458–468.

49 Maggi P, Macri SMC, Gaitán MI, Leibovitch E, Wholer JE, Knight HL *et al.* The formation of inflammatory demyelinated lesions in cerebral white matter. *Ann Neurol* 2014; **76**: 594–608.

50 Compston A, Coles A. Multiple sclerosis. *Lancet* 2008; **372**: 1502–1517.

51 McRobbie DW, Moore EA, Graves MJ, Prince MR. *MRI: From Picture to Proton,*. 2003 doi:10.1097/00004032-200310000-00020.

52 de Boer RW. Magnetization Transfer Contrast Part 1: MR Physics. *Medica Mundi (Philips Heal* 1995; **40**: 64–63.

53 Bernstein MA, King KE, Zhou XJ, Fong W. Handbook of MRI Pulse Sequences. Med. Phys. 2005; **32**: 1452.

54 Henkelman RM, Stanisz GJ, Graham SJ. Magnetization transfer in MRI: a review. *NMR Biomed* 2001; **14**: 57–64.

55 Montagne A, Toga AW, Zlokovic B V. Blood-Brain Barrier Permeability and Gadolinium Benefits and Potential Pitfalls in Research. *JAMA Neurol* 2015; **73**: E1–E2.

56 Callen DJ a, Shroff MM, Branson HM, Lotze T, Li DK, Stephens D *et al.* MRI in the diagnosis of pediatric multiple sclerosis. *Neurology* 2009; **72**: 961–7.

57 Gaitán MI, Sati P, Inati SJ, Reich DS. Initial investigation of the blood-brain barrier in MS lesions at 7 tesla. *Mult Scler* 2013; **19**: 1068–73.

58 Martinelli Boneschi F, Rovaris M, Comi G, Filippi M. The use of magnetic resonance imaging in multiple sclerosis: lessons learned from clinical trials. *Mult Scler* 2004; **10**: 341–347.

59 Wolff SD, Balaban RS. Magnetization transfer contrast (MTC) and tissue water proton relaxation in vivo. *Magn Reson Med* 1989; **10**: 135–144.

60 Chen JT, Easley K, Schneider C, Nakamura K, Kidd GJ, Chang A *et al.* Clinically feasible MTR is sensitive to cortical demyelination in MS. *Neurology* 2013; **80**: 246–252.

61 Hayton T, Furby J, Smith KJ, Altmann DR, Brenner R, Chataway J *et al.* Clinical and imaging correlates of the multiple sclerosis impact scale in secondary progressive multiple sclerosis. *J Neurol* 2012; **259**: 237–245.

62 Levesque IR, Pike GB. Characterizing healthy and diseased white matter using quantitative magnetization transfer and multicomponent T(2) relaxometry: A unified view via a four-pool model. *Magn Reson Med* 2009; **62**: 1487–1496.

63 Kolind SH, Mädler B, Fischer S, Li DKB, MacKay AL. Myelin water imaging: Implementation and development at 3.0T and comparison to 1.5T measurements. *Magn Reson Med* 2009; **62**: 106–15.

64 Tardif CL, Bedell BJ, Eskildsen SF, Collins DL, Pike GB. Quantitative magnetic resonance imaging of cortical multiple sclerosis pathology. *Mult Scler Int* 2012; **2012**: 742018.

65 Vavasour IM, Laule C, Li DKB, Traboulsee AL, MacKay AL. Is the magnetization transfer ratio a marker for myelin in multiple sclerosis? *J Magn Reson Imaging* 2011; **33**: 713–8.

66 Grossman RI, Gomori JM, Ramer KN, Lexa FJ, Schnall MD. Magnetization transfer: theory and clinical applications in neuroradiology. *Radiographics* 1994; **14**: 279–290.

67 Sled JG, Pike GB. Quantitative interpretation of magnetization transfer in spoiled gradient echo MRI sequences. *J Magn Reson* 2000; **145**: 24–36.

68 Sled JG, Pike GB. Quantitative imaging of magnetization transfer exchange and relaxation properties in vivo using MRI. *Magn Reson Med* 2001; **46**: 923–931.

69 Yarnykh VL. Fast macromolecular proton fraction mapping from a single off-resonance magnetization transfer measurement. *Magn Reson Med* 2012; **68**: 166–178.

70 Fjær S, Bø L, Lundervold A, Myhr K-M, Pavlin T, Torkildsen O *et al.* Deep gray matter demyelination detected by magnetization transfer ratio in the cuprizone model. *PLoS One* 2013; **8**: e84162.

71 Merkler D, Boretius S, Stadelmann C, Ernsting T, Michaelis T, Frahm J *et al.* Multicontrast MRI of remyelination in the central nervous system. *NMR Biomed* 2005; **18**: 395–403.

72 Zaaraoui W, Deloire M, Merle M, Girard C, Raffard G, Biran M *et al.* Monitoring demyelination and remyelination by magnetization transfer imaging in the mouse brain at 9.4 T. *Magma* 2008; **21**: 357–362.

73 Boretius S, Escher A, Dallenga T, Wrzos C, Tammer R, Brück W *et al.* Assessment of lesion pathology in a new animal model of MS by multiparametric MRI and DTI. *Neuroimage* 2012; **59**: 2678–88.

74 Portnoy S, Stanisz GJ. Modeling pulsed magnetization transfer. *Magn Reson Med* 2007; **58**: 144–155.

75 Stanisz GJ, Odrobina EE, Pun J, Escaravage M, Graham SJ, Bronskill MJ *et al.*

T1, T2 relaxation and magnetization transfer in tissue at 3T. *Magn Reson Med* 2005; **54**: 507–512.

76 Njus JM, Vigeland L, Springer Jr. CS, Taylor M, Telang FW, Coyle PK *et al.* DCE-MRI Ktrans Mapping of MS Lesion Evolution in Individuals. In: *International Society for Magnetic Resonance in Medicine*. 2008, p 3431.

77 Tofts PS, Kermode AG. Measurement of the blood-brain barrier permeability and leakage space using dynamic MR imaging. 1. Fundamental concepts. *Magn Reson Med* 1991; **17**: 357–367.

78 Yankeelov TE, Rooney WD, Li X, Springer Jr. CS. Variation of the relaxographic 'shutter-speed' for transcytolemmal water exchange affects the CR bolus-tracking curve shape. *Magn Reson Med* 2003; **50**: 1151–1169.

79 Li X, Huang W, Yankeelov TE, Tudorica A, Rooney WD, Springer Jr. CS. Shutter-speed analysis of contrast reagent bolus-tracking data: Preliminary observations in benign and malignant breast disease. *Magn Reson Med* 2005; **53**: 724–729.

80 Rooney WD, Yankeelov TE, Coyle PK, Telang FW, Springer Jr. CS. Regional Blood Volumes and Intravascular Water Lifetimes in Human Brain. In: *International Society of Magnetic Resonance in Medicine*. 2003, p 2188.

81 Li Kohama, G, Hobbs, TR, Rooney, WD, Jerosch-Herold, M, Springer, CS X. 3T MRI Detection of Contrast Reagent Extravasation in the Normal Primate Brain. In: *Int Soc Magn Reson Med*. Proceedings of the 15th Annual Meeting ISMRM, Berlin, Germany, 2007, p 1434.

82 Li Rooney, WD, Springer, CS X. Quantitative aspects of measuring contrast reagent extravasation in the healthy human brain. In: *Int. Soc. Magn. Reson. Med.* Proceedings of the 14th Annual Meeting ISMRM, Seattle, USA., 2006, p 2650.

83 Li X, Huang W, Morris EA, Tudorica LA, Seshan VE, Rooney WD *et al.* Dynamic NMR effects in breast cancer dynamic-contrast-enhanced MRI. *Proc Natl Acad Sci U S A* 2008; **105**: 17937–17942.

84 Huang W, Li X, Morris EA, Tudorica LA, Seshan VE, Rooney WD *et al.* The magnetic resonance shutter speed discriminates vascular properties of malignant and benign breast tumors in vivo. *Proc Natl Acad Sci U S A* 2008; **105**: 17943–17948.

85 Li X, Priest RA, Woodward WJ, Tagge IJ, Siddiqui F, Huang W *et al.* Feasibility of shutter-speed DCE-MRI for improved prostate cancer detection. *Magn Reson Med* 2013; **69**: 171–178.

86 Landis CS Telang FW, Molina PE, Palyka I, Vetek G, Springer CS LX. Equilibrium Transcytolemmal Water-Exchange Kinetics in Skeletal Muscle In Vivo. *Magn Reson Med* 1999; **42**: 467–478.

87 Rooney WD, Li X, Sammi MK, Bourdette DN, Neuwelt E a., Springer CS. Mapping human brain capillary water lifetime: high-resolution metabolic neuroimaging. *NMR Biomed* 2015; : n/a–n/a.

88 Landis CS, Li X, Telang FW, Coderre J a, Micca PL, Rooney WD *et al.* Determination of the MRI contrast agent concentration time course in vivo following bolus injection: effect of equilibrium transcytolemmal water exchange. *Magn Reson Med* 2000; **44**: 563–74.

89 Nathoo N, Yong VW, Dunn JF. Using magnetic resonance imaging in animal models to guide drug development in multiple sclerosis. *Mult Scler* 2014; **20**: 3–11.

90 Nathoo N, Yong VW, Dunn JF. Understanding disease processes in multiple sclerosis through magnetic resonance imaging studies in animal models. *NeuroImage Clin* 2014; **4**: 743–56.

91 Sati P, Silva AC, van Gelderen P, Gaitan MI, Wohler JE, Jacobson S *et al.* In vivo quantification of T_2 anisotropy in white matter fibers in marmoset monkeys. *Neuroimage* 2012; **59**: 979–85.

92 Gaitán MI, Maggi P, Wohler J, Leibovitch E, Sati P, Calandri IL *et al.* Perivenular brain lesions in a primate multiple sclerosis model at 7-tesla magnetic resonance imaging. *Mult Scler* 2013. doi:10.1177/1352458513492244.

93 Gudi V, Gingele S, Skripuletz T, Stangel M. Glial response during cuprizone-induced de- and remyelination in the CNS: lessons learned. *Front Cell Neurosci* 2014; **8**: 73.

94 Hiremath MM, Saito Y, Knapp GW, Ting JP, Suzuki K, Matsushima GK. Microglial/macrophage accumulation during cuprizone-induced demyelination in C57BL/6 mice. *J Neuroimmunol* 1998; **92**: 38–49.

95 Steelman AJ, Thompson JP, Li J. Demyelination and remyelination in anatomically distinct regions of the corpus callosum following cuprizone intoxication. *Neurosci Res* 2012; **72**: 32–42.

96 Pasquini L a, Calatayud C a, Bertone Uña a L, Millet V, Pasquini JM, Soto EF. The neurotoxic effect of cuprizone on oligodendrocytes depends on the presence of pro-inflammatory cytokines secreted by microglia. *Neurochem Res* 2007; **32**: 279–92.

97 Stidworthy MF, Genoud S, Suter U, Mantei N, Franklin RJM. Quantifying the early stages of remyelination following cuprizone-induced demyelination. *Brain Pathol* 2003; **13**: 329–39.

98 Kipp M, Clarner T, Dang J, Copray S, Beyer C. The cuprizone animal model: new insights into an old story. *Acta Neuropathol* 2009; **118**: 723–36.

99 Axthelm MK, Bourdette DN, Marracci GH, Su W, Mullaney ET, Manoharan M *et al.* Japanese macaque encephalomyelitis: a spontaneous multiple sclerosis-like disease in a nonhuman primate. *Ann Neurol* 2011; **70**: 362–73.

100 Estep RD, Hansen SG, Rogers KS, Axthelm MK, Wong SW. Genomic Characterization of Japanese Macaque Rhadinovirus , a Novel Herpesvirus Isolated from a Nonhuman Primate with a Spontaneous Inflammatory Demyelinating Disease. *J Virol* 2013; **87**: 512–23.

101 Blair TC, Manoharan M, Rawlings-Rhea SD, Tagge IJ, Kohama SG, Woltjer R *et al.* Immunopathology of Japanese macaque encephalomyelitis is similar to multiple sclerosis. *J Neuroimmunol* 2016; **291**: 1–10.

102 Carlton W. Studies on the induction of hydrocephalus and spongy degeneration by cuprizone feeding and attempts to antidote the toxicity. *Life Sci* 1967; **6**: 11–9.

103 Carlton W. Response of mice to the chelating agents sodium diethyldithiocarbamate, alpha-benzoinoxime, and biscyclohexanone oxaldihydrazone. *Toxicol Appl Pharmacol* 1966; **8**: 512–21.

104 Goldberg J, Daniel M, Heuvel Y van H, Victor M, Beye C, Clarner T *et al.* Short-Term Cuprizone Feeding Induces Selective Amino Acid Deprivation with Concomitant Activation of an Integrated Stress Response in Oligodendrocytes. *Cell Mol Neurobiol* 2013; **33**: 1087–1098.

105 Bolognin S, Pasqualetto F, Mucignat-Caretta C, Scancar J, Milacic R, Zambenedetti P *et al.* Effects of a copper-deficient diet on the biochemistry, neural morphology and behavior of aged mice. *PLoS One* 2012; **7**: e47063.

106 Benetti F, Ventura M, Salmini B, Ceola S, Carbonera D, Mammi S *et al.* Cuprizone neurotoxicity, copper deficiency and neurodegeneration. *Neurotoxicology* 2010; **31**: 509–17.

107 Zatta P, Raso M, Zambenedetti P, Wittkowski W, Messori L, Piccioli F *et al.* Copper and zinc dismetabolism in the mouse brain upon chronic cuprizone treatment. *Cell Mol Life Sci* 2005; **62**: 1502–13.

108 Auclair S, Feillet-Coudray C, Coudray C, Schneider S, Muckenthaler MU, Mazur A. Mild copper deficiency alters gene expression of proteins involved in iron metabolism. *Blood Cells Mol Dis* 2006; **36**: 15–20.

109 Mason JL, Langaman C, Morell P, Suzuki K, Matsushima GK. Episodic demyelination and subsequent remyelination within the murine central nervous system: changes in axonal calibre. *Neuropathol Appl Neurobiol* 2001; **27**: 50–58.

110 Skripuletz T, Hackstette D, Bauer K, Gudi V, Pul R, Voss E *et al.* Astrocytes regulate myelin clearance through recruitment of microglia during cuprizone-induced demyelination. *Brain* 2013; **136**: 147–67.

111 Janßen S, Gudi V, Prajeeth CK, Singh V, Stahl K, Heckers S *et al.* A pivotal role of nonmuscle myosin II during microglial activation. *Exp Neurol* 2014; **261**: 666–676.

112 Clarner T, Janssen K, Nellessen L, Stangel M, Skripuletz T, Krauspe B *et al.* CXCL10 Triggers Early Microglial Activation in the Cuprizone Model. *J Immunol* 2015. doi:10.4049/jimmunol.1401459.

113 Wergeland S, Torkildsen Ø, Myhr K-M, Mørk SJ, Bø L. The cuprizone model: regional heterogeneity of pathology. *APMIS* 2012; **120**: 648–57.

114 Gudi V, Moharregh-Khiabani D, Skripuletz T, Koutsoudaki PN, Kotsiari A, Skuljec J *et al.* Regional differences between grey and white matter in cuprizone induced

demyelination. *Brain Res* 2009; **1283**: 127–38.

115 Goldberg J, Clarner T, Beyer C, Kipp M. Anatomical Distribution of Cuprizone-Induced Lesions in C57BL6 Mice. *J Mol Neurosci* 2015. doi:10.1007/s12031-015-0595-5.

116 Acs P, Kalman B. *Autoimmunity*. Second. Humana Press: Totowa, NJ, 2012 doi:10.1007/978-1-60761-720-4.

117 Gozzo S, Renzi P, D'udine. Morphological differences in cerebral cortex and corpus callosum are genetically determined in two different strains of mice. *Int J Neurosci* 1979; **9**: 91–96.

118 Irvine K, Blakemore WF. Age increases axon loss associated with primary demyelination in cuprizone-induced demyelination in C57BL/6 mice. *J Neuroimmunol* 2006; **175**: 69–76.

119 Xie M, Tobin JE, Budde MMD, Chen C-I, Trinkaus K, Cross AH *et al.* Rostro-Caudal Analysis of Corpus Callosum Demyelination and Axon Damage Across Disease Stages Refines Diffusion Tensor Imaging Correlations with Pathological Features. *J Neuropathol Exp Neurol* 2010; **69**: 704–16.

120 Tobin J, Xie M, Le T, Song S-K, Arms. Reduced Axonopathy and Enhanced Remyelination Following Chronic Demyelination in Fibroblast Growth Factor-2 (Fgf2) Null Mice: Differential Detection with Diffusion Tensor Imaging. *J Neuropathol Exp Neurol* 2011; **70**: 157–165.

121 Falangola M, Guilfoyle D, Tabesh A, Hui E, Nie X, Jensen J *et al.* Histological correlation of diffusional kurtosis and white matter modeling metrics in cuprizone-induced corpus callosum demyelination. *NMR Biomed* 2014; **27**: 948–957.

122 Thiessen JD, Zhang Y, Zhang H, Wang L, Buist R, Del Bigio MR *et al.* Quantitative MRI and ultrastructural examination of the cuprizone mouse model of demyelination. *NMR Biomed* 2013; **26**: 1562–81.

123 Schregel K, Tysiak EW, Garteiser P, Gemeinhardt I, Prozorovski T, Aktas O *et al.* Demyelination reduces brain parenchymal stiffness quantified in vivo by magnetic resonance elastography. *PNAS* 2012; **109**: 6650–6655.

124 Underhill HR, Rostomily RC, Mikheev AM, Yuan C, Yarnykh VL. Fast bound pool fraction imaging of the in vivo rat brain: association with myelin content and validation in the C6 glioma model. *Neuroimage* 2011; **54**: 2052–2065.

125 Labadie C, Lee J-H, Rooney WD, Jarchow S, Aubert-Frécon M, Springer CS *et al.* Myelin water mapping by spatially regularized longitudinal relaxographic imaging at high magnetic fields. *Magn Reson Med* 2014; **71**: 375–87.

126 Wu Q-Z, Yang Q, Cate HS, Kemper D, Binder M, Wang H-X *et al.* MRI identification of the rostral-caudal pattern of pathology within the corpus callosum in the cuprizone mouse model. *J Magn Reson Imaging* 2008; **27**: 446–53.

127 Skripuletz T, Bussmann J-H, Gudi V, Koutsoudaki PN, Pul R, Moharregh-Khiabani D *et al.* Cerebellar cortical demyelination in the murine cuprizone model. *Brain*

Pathol 2010; **20**: 301–12.

128 Schmidt T, Awad H, Slowik a, Beyer C, Kipp M, Clarner T. Regional heterogeneity of cuprizone-induced demyelination: topographical aspects of the midline of the corpus callosum. *J Mol Neurosci* 2013; **49**: 80–8.

129 Van Rossum G. Python programming language. In: *USENIX Annual Technical Conference*. 2007.

130 Jenkinson M, Beckmann CF, Behrens TEJ, Woolrich MW, Smith SM. Fsl. *Neuroimage* 2012; **62**: 782–90.

131 Smith SM, Nichols TE. Threshold-free cluster enhancement: addressing problems of smoothing, threshold dependence and localisation in cluster inference. *Neuroimage* 2009; **44**: 83–98.

132 Allen Institute for Brain Science. Allen Mouse Brain Atlas. *Http://MouseBrain-MapOrg/* 2014; : 1–26.

133 Lein ES, Hawrylycz MJ, Ao N, Ayres M, Bensinger A, Bernard A *et al.* Genome-wide atlas of gene expression in the adult mouse brain. *Nature* 2007; **445**: 168–76.

134 Yang H-J, Wang H, Zhang Y, Xiao L, Clough RW, Browning R *et al.* Region-specific susceptibilities to cuprizone-induced lesions in the mouse forebrain: Implications for the pathophysiology of schizophrenia. *Brain Res* 2009; **1270**: 121–30.

135 Allen Institute for Brain Science. Allen Mouse Brain Atlas [Internet]. 2015.http://connectivity.brain-map.org.

136 Nair HP, Collisson T, Gonzalez-Lima F. Postnatal development of cytochrome oxidase activity in fiber tracts of the rat brain. *Dev Brain Res* 1999; **118**: 197–203.

137 Sturrock R. Myelination of the mouse corpus callosum. *Neuropathol Appl Neurobiol* 1980; **6**: 415–420.

138 Doucette JR, Jiao R, Nazarali AJ. Age-related and cuprizone-induced changes in myelin and transcription factor gene expression and in oligodendrocyte cell densities in the rostral corpus callosum of mice. *Cell Mol Neurobiol* 2010; **30**: 607–29.

139 Aboitiz F, Scheibel AB, Fisher RS, Zaidel E. Fiber composition of the human corpus callosum. *Brain Res* 1992; **598**: 143–153.

140 Aboitiz F, Montiel J. One hundred million years of interhemispheric communication: the history of the corpus callosum. *Braz J Med Bio Res* 2003; **36**: 409–420.

141 Guglielmetti C, Veraart J, Roelant E, Mai Z, Daans J, Audekerke J Van *et al.* Diffusion kurtosis imaging probes cortical alterations and white matter pathology following cuprizone-induced demyelination and spontaneous remyelination. *Neuroimage* 2016; **125**: 363–377.

142 Jarjour A a, Kennedy TE. Oligodendrocyte precursors on the move: mechanisms directing migration. *Neuroscientist* 2004; **10**: 99–105.

143 Cate HS, Sabo JK, Merlo D, Kemper D, Aumann TD, Robinson J *et al.* Modulation of bone morphogenic protein signalling alters numbers of astrocytes and oligodendroglia in the subventricular zone during cuprizone-induced demyelination. *J Neurochem* 2010; **115**: 11–22.

144 Back SA, Rosenberg PA. *Pathophysiology of Glia in Perinatal White Matter Injury*. 2014 doi:10.1016/j.micinf.2011.07.011.Innate.

145 Kaneko N, Kako E, Sawamoto K. Prospects and limitations of using endogenous neural stem cells for brain regeneration. *Genes (Basel)* 2011; **2**: 107–30.

146 Donegà M, Giusto E, Cossetti C, Pluchino S. Systemic neural stem cell-based therapeutic interventions for inflammatory CNS disorders. *Neural Stem Cells - New Perspect* 2013.http://www.intechopen.com/books/neural-stem-cells-new-perspectives/systemic-neural-stem-cell-based-therapeutic-interventions-for-inflammatory-cns-disorders (accessed 4 Dec2014).

147 Mason JL, Jones JJ, Taniike M, Morell P, Suzuki K, Matsushima GK. Mature Oligodendrocyte Apoptosis Precedes IGF-1 Production and Oligodendrocyte Progenitor Accumulation and Differentiation During Demyelination / Remyelination. *J Neurosci Res* 2000; **61**: 251–262.

148 Petratos S, Gonzales MF, Azari MF, Marriott M, Minichiello R a, Shipham K a *et al.* Expression of the low-affinity neurotrophin receptor, p75(NTR), is upregulated by oligodendroglial progenitors adjacent to the subventricular zone in response to demyelination. *Glia* 2004; **48**: 64–75.

149 Guglielmetti C, Praet J, Rangarajan JR, Vreys R, De Vocht N, Maes F *et al.* Multimodal imaging of subventricular zone neural stem/progenitor cells in the cuprizone mouse model reveals increased neurogenic potential for the olfactory bulb pathway, but no contribution to remyelination of the corpus callosum. *Neuroimage* 2014; **86**: 99–110.

150 Sawamoto K, Wichterle H, Gonzalez-Perez O, Cholfin JA, Yamada M, Spassky N *et al.* New neurons follow the flow of cerebrospinal fluid in the adult brain. *Science (80-)* 2006; **311**: 629–632.

151 Beatrice B, Magalon K, Pascale D, Cayre M. Region and dynamic specificities of adult neural stem cells and oligodendrocyte precursors in myelin regeneration in the mouse brain. *Biol Open* 2015; : 1–13.

152 Silvestroff L, Bartucci S, Soto E, Gallo V, Pasquini J, Franco P. Cuprizone-Induced demyelination in CNP::GFP transgenic mice. *J Comp Neurol* 2010; **518**: 2261–2283.

153 Baloch S, Verma R, Huang H, Khurd P, Clark S, Yarowsky P *et al.* Quantification of brain maturation and growth patterns in C57BL/6J mice via computational neuroanatomy of diffusion tensor images. *Cereb Cortex* 2009; **19**: 675–87.

154 Larvaron P, Boespflug-tanguy O, Renou J, Bonny J. In vivo analysis of the post-

natal development of normal mouse brain by DTI. *NMR Biomed* 2007; **20**: 413–421.

155 Shiee N, Bazin PL, Zackowski KM, Farrell SK, Harrison DM, Newsome SD *et al.* Revisiting brain atrophy and its relationship to disability in multiple sclerosis. *PLoS One* 2012; **7**: e37049.

156 Shiee N, Bazin PL, Ozturk A, Reich DS, Calabresi PA, Pham DL. A topology-preserving approach to the segmentation of brain images with multiple sclerosis lesions. *Neuroimage* 2010; **49**: 1524–1535.

157 Mottershead JP, Schmierer K, Clemence M, Thornton JS, Scaravilli F, Barker GJ *et al.* High field MRI correlates of myelin content and axonal density in multiple sclerosis: A post-mortem study of the spinal cord. *J Neurol* 2003; **250**: 1293–1301.

158 Brown RA, Narayanan S, Arnold DL. Imaging of repeated episodes of demyelination and remyelination in multiple sclerosis. *NeuroImage Clin* 2014; **6**: 20–25.

159 Gareau PJ, Rutt BK, Karlik SJ, Mitchell JR. Magnetization transfer and multicomponent T2 relaxation measurements with histopathologic correlation in an experimental model of MS. *J Magn Reson Imaging* 2000; **11**: 586–95.

160 Oh J, Saidha S, Chen M, Smith S a, Prince J, Jones C *et al.* Spinal cord quantitative MRI discriminates between disability levels in multiple sclerosis. *Neurology* 2013; **80**: 540–7.

161 Filippi M, Rocca MA. Novel MRI approaches to assess patients with multiple sclerosis. *Curr Opin Neurol* 2010; **23**: 212–217.

162 Tagge I, O'Connor A, Chaudhary P, Pollaro J, Berlow Y, Chalupsky M *et al.* Spatio-Temporal Patterns of Demyelination and Remyelination in the Cuprizone Mouse Model. *PLoS One* 2016; **11**: e0152480.

163 Sahraian M a., Radue EW, Haller S, Kappos L. Black holes in multiple sclerosis: Definition, evolution, and clinical correlations. *Acta Neurol Scand* 2010; **122**: 1–8.

164 Rooney WD, Kohama SG, Wang P, Njus JM, Wong SW, Sherman S *et al.* MRI Estimation of Sub-Clinical Disease in Japanese Macaque Encephalomyelitis. In: *Proc Int Soc Magn Reson Med*. 2009, p 6973.

165 Tagge IJ, Kohama SG, Pollaro J, Sherman LS, Bourdette DN, Woltjer R *et al.* Vascular Expansion and Blood-Brain-Barrier Permeability: A Comparative Volumetric Study in Acute Japanese Macaque Encephalomyelitis. In: *Proc Int Soc Magn Reson Med*. 2015, p 4331.

166 Tagge I, Kohama S, Pollaro J, Sherman L, Bourdette D, Woltjer R *et al.* Blood-Brain-Barrier Permeability and Lesion Volume Changes in Acute Japanese Macaque Encephalomyelitis. *Proc Int Soc Magn Reson Med* 2015; **23**: 0238.

167 Li X, Rooney WD, Springer Jr. CS. A unified magnetic resonance imaging pharmacokinetic theory: intravascular and extracellular contrast reagents. *Magn*

Reson Med 2005; **54**: 1351–9. [Erratum: Magn Reson Med 2006;55:1217.].

168 Nakamura M, Misu T, Fujihara K, Miyazawa I, Nakashima I, Takahashi T *et al.* Occurrence of acute large and edematous callosal lesions in neuromyelitis optica. *Mult Scler* 2009; **15**: 695–700.

169 Gaitán MI, Shea CD, Evangelou IE, Stone RD, Fenton KM, Bielekova B *et al.* Evolution of the blood-brain barrier in newly forming multiple sclerosis lesions. *Ann Neurol* 2011; **70**: 22–29.

170 Popescu BF, Lucchinetti CF. Meningeal and cortical grey matter pathology in multiple sclerosis. *BMC Neurol* 2012; **12**: 11.

171 Lucchinetti CF, Popescu BFG, Bunyan RF, Moll NM, Roemer SF, Lassmann H *et al.* Inflammatory cortical demyelination in early multiple sclerosis. *N Engl J Med* 2011; **365**: 2188–2197.

172 Pirko I, Lucchinetti CF, Sriram S, Bakshi R. Gray matter involvement in multiple sclerosis. *Neurology* 2007; **68**: 634–642.

173 Popescu BFG, Bunyan RF, Parisi JE, Ransohoff RM, Lucchinetti CF. A case of multiple sclerosis presenting with inflammatory cortical demyelination. *Neurology* 2011; **76**: 1705–1710.

174 Zivadinov R, Pirko I. Advances in understanding gray matter pathology in multiple sclerosis: Are we ready to redefine disease pathogenesis? *BMC Neurol* 2012; **12**: 9.

175 Sbardella E, Petsas N, Tona F, Prosperini L, Raz E, Pace G *et al.* Assessing the correlation between grey and white matter damage with motor and cognitive impairment in multiple sclerosis patients. *PLoS One* 2013; **8**: e63250.

176 Wingerchuk DM, Weinshenker BG. Acute disseminated encephalomyelitis, transverse myelitis, and neuromyelitis optica. *Continuum (Minneap Minn)* 2013; **19**: 944–67.

177 Krupp LB, Banwell B, Tenembaum S. Consensus definitions proposed for pediatric multiple sclerosis and related disorders. *Neurology* 2007; **68**: 7–12.

178 Steiner I, Kennedy PGE. Acute disseminated encephalomyelitis : current knowledge and open questions. *J Neurovirol* 2015; : 473–479.

179 Wingerchuk DM. Post-infectious encephalomyelitis. *Curr Neurol Neurosci Rep* 2003; **3**: 256–264.

180 Tenembaum S, Chamoles N, Fejerman N. Acute disseminated encephalomyelitis: a long-term follow-up study of 84 pediatric patients. *Neurology* 2002; **59**: 1224–1231.

181 Krieger S, Sorrells SF, Nickerson M, Pace TWW. Mechanistic insights into corticosteroids in multiple sclerosis: war horse or chameleon?. *Clin Neurol Neurosurg* 2014; **119**: 6–16.

182 Kimbrough DJ, Fujihara K, Jacob A, Lana-Peixoto MA, Leite MI, Levy M *et al.*

Treatment of Neuromyelitis Optica: Review and Recommendations. *Mult Scler Relat Disord* 2012; **1**: 180–187.

183 Alexander M, Murthy J. Acute disseminated encephalomyelitis: Treatment guidelines. *Ann Indian Acad Neurol* 2011; **14**: Suppl S1:60–64.

184 Kremer S, Renard F, Achard S, Lana-Peixoto M a., Palace J, Asgari N *et al.* Use of Advanced Magnetic Resonance Imaging Techniques in Neuromyelitis Optica Spectrum Disorder. *JAMA Neurol* 2015; **72**: 815–822.

185 Njus JM, Li X, Springer Jr. CS, Taylor M, Greisel T, Telang FW *et al.* Changes in Blood-Brain-Barrier Permeability and Blood Volume During MS Lesion Development and Evolution. In: *International Society for Magnetic Resonance in Medicine*. 2008, p 3434.

186 Njus JM, Pollaro JR, Snodgrass MT, Cunneen J, Muldoon E, Warren VB *et al.* Intravascular Water Molecule Lifetime in the Japanese Macaque Brain. In: *Proceedings 17th Scientific Meeting, International Society for Magnetic Resonance in Medicine*. 2009, p 1480.

187 Njus JM, Vigeland L, Li X, Springer Jr. CS, Taylor M, Telang FW *et al.* Quantitative DCE 1H2O R1 Measurements Suggest Increased Fractional Blood Water in MS Normal Appearing Brain Tissue. In: *International Society for Magnetic Resonance in Medicine*. 2007, p 2193.

188 Hulst HE, Geurts JJ. Gray matter imaging in multiple sclerosis: what have we learned? *BMC Neurol* 2011; **11**: 153.

189 Mainero C, Benner T, Radding A, van der Kouwe A, Jensen R, Rosen BR *et al.* In vivo imaging of cortical pathology in multiple sclerosis using ultra-high field MRI. *Neurology* 2009; **73**: 941–948.

190 Walker CA, Huttner AJ, O'Connor KC. Cortical injury in multiple sclerosis; the role of the immune system. *BMC Neurol* 2011; **11**: 152.

191 Schmierer K, Parkes HG, So P-W, An SF, Brandner S, Ordidge RJ *et al.* High field (9.4 Tesla) magnetic resonance imaging of cortical grey matter lesions in multiple sclerosis. *Brain* 2010; **133**: 858–867.

192 Vrenken H, Pouwels PJ, Geurts JJ, Knol DL, Polman CH, Barkhof F *et al.* Altered diffusion tensor in multiple sclerosis normal-appearing brain tissue: cortical diffusion changes seem related to clinical deterioration. *J Magn Reson Imaging* 2006; **23**: 628–636.

193 Seabrook TJ, Littlewood-Evans A, Brinkmann V, Pollinger B, Schnell C, Hiestand PC. Angiogenesis is present in experimental autoimmune encephalomyelitis and pro-angiogenic factors are increased in multiple sclerosis lesions. *J Neuroinflammation* 2010; **7**: 95.

194 Kirk S, Frank JA, Karlik S. Angiogenesis in multiple sclerosis: is it good, bad or an epiphenomenon? *J Neurol Sci* 2004; **217**: 125–130.

195 Calabrese M, De Stefano N, Atzori M, Bernardi V, Mattisi I, Barachino L *et al.*

Detection of cortical inflammatory lesions by double inversion recovery magnetic resonance imaging in patients with multiple sclerosis. *Arch Neurol* 2007; **64**: 1416–1422.

196 Seewann A, Kooi EJ, Roosendaal SD, Pouwels PJ, Wattjes MP, van der Valk P *et al.* Postmortem verification of MS cortical lesion detection with 3D DIR. *Neurology* 2012; **78**: 302–308.

197 Sinnecker T, Mittelstaedt P, Dörr J, Pfueller CF, Harms L, Niendorf T *et al.* Multiple Sclerosis Lesions and Irreversible Brain Tissue Damage: A Comparative Ultrahigh-Field Strength Magnetic Resonance Imaging Study. *Arch Neurol* 2012; **69**: 739–45.

198 Nelson F, Poonawalla AH, Hou P, Huang F, Wolinsky JS, Narayana PA. Improved identification of intracortical lesions in multiple sclerosis with phase-sensitive inversion recovery in combination with fast double inversion recovery MR imaging. *AJNR Am J Neuroradiol* 2007; **28**: 1645–1649.

199 Sethi V, Muhlert N, Ron M, Golay X, Wheeler-Kingshott C a., Miller DH *et al.* MS Cortical Lesions on DIR: Not Quite What They Seem? *PLoS One* 2013; **8**: e78879.

200 Grinstead JW, Wang D, Bhat H, Deshpande V, Cauley S, Setsompop K *et al.* Slice-Accelerated Inversion Recovery T1 Mapping. In: *Proc Int Soc Magn Reson Med*. 2014, p 3215.

201 Mahad D, Ziabreva I, Lassmann H, Turnbull D. Mitochondrial defects in acute multiple sclerosis lesions. *Brain* 2008; **131**: 1722–1735.

202 Ge Y, Zhang Z, Lu H, Tang L, Jaggi H, Herbert J *et al.* Characterizing brain oxygen metabolism in patients with multiple sclerosis with T2-relaxation-under-spin-tagging MRI. *J Cereb Blood Flow Metab* 2012; **32**: 403–412.

203 Springer CS, Broberg CS, Rooney WD. Metabolic imaging of in vivo myocardium. *J Cardiovasc Magn Reson* 2015; **17**: P251.

204 Rooney WD, Li X, Grinstead JW, Neuwelt EA, Springer Jr. CS. Taub: A Metabolic Neuroimaging Biomarker. In: *Proc Int Soc Magn Reson Med*. 2014, p 4600.

205 Rooney WD, Sammi MK, Li X, Moloney B, Berlow YA, Bourdette DN *et al.* High-Resolution Metabolic Neuroimaging. In: *Proc Int Soc Magn Reson Med*. 2014, p 3387.

206 Zhang Y, Poirier-Quinot M, Springer Jr. CS, Balschi JA. Active trans-plasma membrane water cycling in yeast is revealed by NMR. *Biophys J* 2011; **101**: 2833–2842.

207 Duyn JH, van Gelderen P, Li TQ, de Zwart JA, Koretsky AP, Fukunaga M. High-field MRI of brain cortical substructure based on signal phase. *Proc Natl Acad Sci U S A* 2007; **104**: 11796–11801.

208 Berlow YA, Sammi MK, Mcmahon LE, Tagge I, Moloney B, Rooney WD. Unified Segmentation at 7T. In: *Proc Int Soc Magn Reson Med*. 2014, p 4911.

209 Rooney WD, Johnson G, Li X, Cohen ER, Kim SG, Ugurbil K *et al.* Magnetic field and tissue dependencies of human brain longitudinal 1H2O relaxation in vivo. *Magn Reson Med* 2007; **57**: 308–318.

210 Li Rooney, W.D., Varallyay, C., Goodman, J.A., Selzer, A., Tagge, I., Pike, M.M., Neuwelt, E.A., Springer, C.S., Jr. X. DCE-MRI Rat Cerebral Glioma Blood Volume Determination with Extravasating CR. In: *Int Soc Magn Reson Med*. Proceedings of the 16th Annual Meeting ISMRM, Toronto, Canada, 2008, p 3827.

211 Rooney WD, Li X, Bourdette DN, Springer CS. Mapping Human Cerebral Vascular/Metabolic Activity Coupling at High-Resolution. In: *Proc 20th Int Soc Magn Reson Med*. 2015, p 3889.

212 Fisher E, Reich DS. Imaging new lesions: Enhancing our understanding of multiple sclerosis pathogenesis. *Neurology* 2013; **81**: 202–3.

213 Filippi M, Preziosa P, Rocca M a. Magnetic resonance outcome measures in multiple sclerosis trials : time to rethink ? *Curr Opin Neurol* 2014; **27**: 290–299.

214 Blair TC, Manoharan M, Rawlings-Rhea SD, Tagge I, Kohama SG, Hollister-Smith J *et al.* Immunopathology of Japanese macaque encephalomyelitis is similar to multiple sclerosis. *J Neuroimmunol* 2016; **291**: 1–10.

215 Hua J, Hurst GC. Analysis of on- and off-resonance magnetization transfer techniques. *J Magn Reson Imaging2* 1995; **5**: 113–120.

216 Paredes MF, Sorrells SF, Garcia-Verdugo JM, Alvarez-Buylla A. Brain size and limits to adult neurogenesis. *J Comp Neurol* 2016; **524**: 646–664.

217 Weinstein JS, Varallyay CG, Dosa E, Gahramanov S, Hamilton B, Rooney WD *et al.* Superparamagnetic iron oxide nanoparticles: diagnostic magnetic resonance imaging and potential therapeutic applications in neurooncology and central nervous system inflammatory pathologies, a review. *J Cereb Blood Flow Metab* 2010; **30**: 15–35.

218 Várallyay C. *Iron Oxide Nanoparticles as MRI Contrast Agents in CNS Imaging ; Perfusion assessment of brain tumor therapy using ferumoxytol*. 2012.

219 Corot C, Petry KG, Trivedi R, Saleh A, Jonkmanns C, Le Bas J-F *et al.* Macrophage Imaging in Central Nervous System and in Carotid Atherosclerotic Plaque Using Ultrasmall Superparamagnetic Iron Oxide in Magnetic Resonance Imaging. *Invest Radiol* 2004; **39**: 619–625.

220 Neuwelt A, Sidhu N, Hu C-A a., Mlady G, Eberhardt SC, Sillerud LO. Iron-Based Superparamagnetic Nanoparticle Contrast Agents for MRI of Infection and Inflammation. *Am J Roentgenol* 2015; **204**: W302–W313.

221 Dósa E, Guillaume D. Magnetic resonance imaging of intracranial tumors: intra-patient comparison of gadoteridol and ferumoxytol. *Neuro Oncol* 2010; **13**: 251–260.

Appendix A – JME Symptom and Treatment Details

Definitions:

BAL – bronchoalveolar lavage

BID – twice per day

CSF – cerebrospinal fluid sample

Methylpred - methyprednisolone

PE – physical exam

SID – once per day

19615

Day	Symptoms	Procedures	Corticosteroid	Dose / Frequency	Methylpred equivalent (mg/kg/day)
0	R eyelid swelling with discharge and peripheral scratches. R head tilt.				
1	Bilateral ataxia of hindlimbs, difficulty standing.	MRI, CSF, BAL			
2	Laterally recumbent, R side paresis/paralysis, unable to feed self or reach lixit.	MRI, Necropsy	Prednisilone	50 mg once	3.125

20482

Day	Symptoms	Procedures	Corticosteroid	Dose / Frequency	Methylpred equivalent (mg/kg/day)
0	Ataxia, L head tilt		Prednisilone	140 mg SID	7.7
1	L head tilt	MRI	Prednisilone	140 mg SID	7.7
2	No change		Prednisilone	140 mg SID	7.7
3	No change		Prednisilone	70 mg BID	7.7
4	No change	MRI	Prednisilone	70 mg BID	7.7
5	No change	CSF tap	Prednisilone	35 mg BID	3.9
6	No change		Prednisilone	35 mg BID	3.9
7	Head tilt not present		Prednisilone	35 mg SID	1.9
8			Prednisilone	35 mg SID	1.9
9	Head tilt present		Prednisilone	15 mg SID	0.8
10					
11		MRI, BAL			
12			Prednisilone	70 mg BID	7.7
13	L leg paresis	MRI, Necropsy 1230	Prednisilone	70 mg AM	3.9

28422

Day	Symptoms	Procedures	Corticosteroid	Dose / Frequency	Methylpred equivalent (mg/kg/day)
0	Severe left head tilt, intention tremors	MRI, CSF, BAL	Prednisilone	1.8 mg BID	1.6
1	Abdominal bloat		Prednisilone	1.8 mg BID	1.6
2		MRI	Prednisilone	1.8 mg BID	1.6
3	Intention tremors		Prednisilone	10 mg (?)* BID	8.8
4	Same		Prednisilone	10 mg (?)* BID	8.8
5	Tremors worse		Prednisilone	10 mg (?)* BID	8.8
6		MRI, CSF, necropsy 1030			

* Possibly 2mg BID instead

30493

Day	Symptoms	Procedures	Corticosteroid	Dose / Frequency	Methylpred equivalent (mg/kg/day)
0	Paresis of L leg				
1	Paresis of both L leg/arm, reduced rectal tone, inguinal dermatitis	MRI, CSF, BAL	Dexamethasone	2 mg SID	2.7
2	Not using L arm, L leg dragging		Dexamethasone, Prednisilone	Dex - 2 mg SID, Pred - 5 mg BID	Dex - 2.7, Pred - 2, Total - 4.7
3	Same	MRI, Necropsy	Prednisilone	5 mg once	1

31509

Day	Symptoms	Procedures	Corticosteroid	Dose / Frequency	Methylpred equivalent (mg/kg/day)
0	L head tilt and head turn				
1	Same	MRI, CSF	Dexamethasone	2 mg SID	3.2
2	Same		Dexamethasone	3 mg SID	4.8
3	Head tilt improved		Prednisone	10 mg BID	4.7
4	Slight head tilt	MRI	Prednisone	10 mg BID	4.7
5	Same		Prednisone	10 mg BID	4.7
6	Same		Prednisone	7.5 mg BID	3.5
7	R leg being dragged		Prednisone	7.5 mg BID	3.5
8	Both legs dragged		Prednisone	7.5 mg BID	3.5
9		Necropsy 0830			

32150

Day	Symptoms	Procedures	Corticosteroid	Dose / Frequency	Methylpred equivalent (mg/kg/day)
0	L leg paralysis, abrasion on dorsal L foot	PE			
1	L leg limp, R leg used exclusively	MRI, CSF, BAL	Methylpred	125 mg SID	24
2	L leg shows limited but some function		Methylpred	125 mg SID	24
3	Uses L leg for support still limited use		Methylpred	125 mg SID	24
4	No use of L leg observed		Methylpred	125 mg SID	24
5	Same	MRI	Methylpred	125 mg SID	24
6	Same		Prednisone	5 mg SID	0.8
7	Same		Prednisone	5 mg SID	0.8
8	Possible R leg paresis		Prednisone	5 mg SID	0.8
9	Using arms predominantly to move but R leg still partially functional		Prednisone	5 mg SID	0.8
10	Same		Prednisone	5 mg SID	0.8
11	Both legs nonfunctional		Prednisone	5 mg SID	0.8
12		MRI, necropsy			

32914

Day	Symptoms	Procedures	Corticosteroid	Dose / Frequency	Methylpred equivalent (mg/kg/day)
0	R leg paresis, some toe movement				
1	Same		Methylpred	100 mg SID	26
2	Same	MRI, CSF	Methylpred	100 mg SID	26
3	Same		Methylpred	100 mg SID	26
4	R leg flaccid, L leg paresis	MRI	Methylpred	100 mg SID	26
5	L leg appears improved, R leg flaccid	Necropsy	Methylpred	100 mg SID	26

Appendix B – Refereed Conference Proceedings

High Resolution Mapping of Intravascular Water Molecule Lifetime in Rhesus Macaque Brain

Tagge, I. Li, X. Kohama, S. Kroenke, C. Berlow, Y. Warren, V. Hobbs, T. Horrocks, S. Cady, N. Purnell, J. Springer, C. S. Jr. Rooney, W.

Proceedings of the International Society of Magnetic Resonance in Medicine 2014; **22**:4911

Introduction

Dynamic contrast-enhanced (DCE) MRI is useful in examining cerebral pathology. Pharmacokinetic modeling of DCE-MRI data provides access to physiologically relevant parameters that characterize vascular properties *in-vivo*. Parameters such as blood volume fraction (v_b) and mean intravascular water molecule lifetime (τ_b) are sensitive to vascular changes related to disease state (*submitted)*. Quantitative T_1 mapping techniques have been shown to be sensitive to vascular water exchange, but these techniques are time intensive and often have limited tissue coverage. 3D Gradient Recalled Echo (GRE) sequences offer full brain coverage with a relatively short acquisition time, allowing for high spatial and temporal resolution DCE-MRI measurements. Here, we investigate the feasibility of measuring v_b and τ_b with 3D GRE DCE-MRI in Rhesus Macaque brain. Contrast Agent (CA) does not extravasate to any

appreciable extent during CA first-pass in the normal brain; following this assumption, a 2-site-exchange [2SX] shutter-speed paradigm [SSP] DCE-MRI analysis can be employed to obtain v_b and τ_b.(1,2)

Methods

Four healthy adult males were selected from our free-range colony. All images were acquired on a Siemens 3T TIM Trio instrument with a 15 channel Tx/Rx coil (Quality Electrodynamics, Mayfield, OH). The DCE-MRI measurement was achieved with a 3D FLASH sequence (TR/TE/FA: 9 ms/2.46 ms/20°) with 32 2.0-mm transverse head slices. The nominal in-plane resolution was $[1.25\ mm]^2$. Animals were anesthetized and a 0.3 mmol(gadoteridol)/kg CR bolus was administered, in the left s.v. in 10 - 15 s, ten or twenty image frames after starting the DCE-MRI acquisition, which lasted 18 minutes. The inter-image interval was 18 s. The arterial input function (AIF) was obtained from the DCE-MRI time-course of a *sagittal sinus* region-of-interest (ROI). The AIF from one animal was selected for use in all analyses and amplitude adjusted based on quantitative 3D R_1 maps obtained before and after the DCE time series acquisition. All images were coregistered and segmented using FSL's FLIRT and FAST tools, respectively.(3,4) Whole-brain WM and GM intensity-average signals were fitted with the Fast-Exchange-Regime-allowed SSP (5) to extract v_b, and τ_b values. Parametric maps were similarly created by voxel-wise fittings. Parameter estimation precision was evaluated via 1000 Monte Carlo simulations on each ROI fitting.

Results

Whole-brain ROI population average parameter values are given in the **Table** with standard deviation of means for the four animals given in parentheses**.** Parameter precisions are high based on Monte Carlo simulations with mean τ_b, v_b variances of 9.5 ms, 0.07% and 10 ms, 0.14% for WM and GM, respectively. **Figure 1** shows a representative high resolution transverse quantitative R_1 ($\equiv 1/T_1$) map (**a**) and corresponding τ_b (**b**) and v_b (**c**) parametric maps; the color scale is given adjacent to each map. Increased τ_b and v_b values in the subarachnoid and ventricular cerebrospinal fluid are artificial due to model insufficiency. Representative whole-brain signal-averaged WM and GM tissue response curves (hollow data points) and their respective fitted curves (solid lines) are shown in **Figure 2**. The AIF used for all analyses is displayed in the inset.

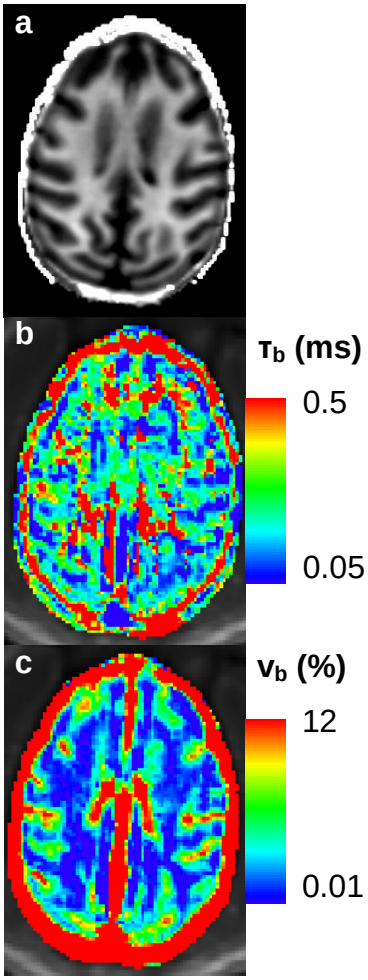

Figure 1. Parametric Maps

Tissue	τ_b (msec)	v_b (%)
WM (SD)	178 (±36.3)	3.17 (±0.46)
GM (SD)	291 (±28.6)	7.59 (±0.77)

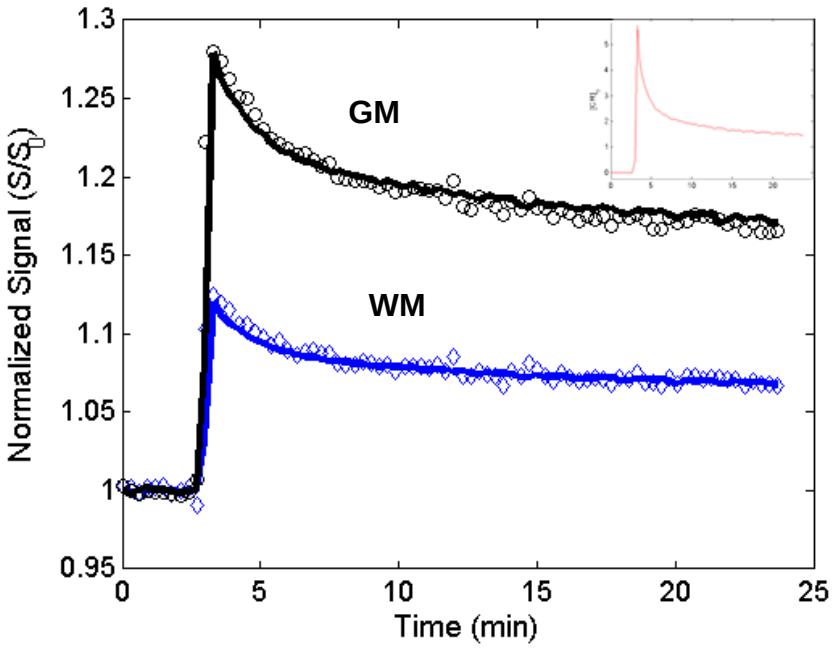

Figure 2. Representative signal intensity response in gray matter (GM, black circles) and white matter (WM, blue diamonds) and fitted pharmacokinetic model response (solid lines). Arterial input function is shown in the inset.

Discussion

WM τ_b values found here are smaller than have been previously reported (~300ms) in humans or Japanese Macaque.(6) GM τ_b values are also lower than reported in human brain (~260ms)(1); although human brain measurements were collected in the un-sedated state. Average WM v_b are in good agreement with that previously reported in Japanese Macaque.(6) Elevated GM v_b compared to WM is consistent with its highly vascularized nature. Importantly, the measurements in (6) were sparsely sampled over nearly an hour and required a K^{trans} correction, which had significant effects on parameter estimation. Reported human parameters are for conscious subjects; the effects of anesthesia on τ_b is unknown. Even though these data were not $\boldsymbol{B_1}$ corrected, our initial experience is

that the corrections are minor. Measurements across animals showed consistent results with low variance and high parameter precision, suggesting that our approach does indeed extract v_b, and τ_b values from 3D GRE DCE-MRI data. These parameters have potential as novel biomarkers of disease-related vascular changes *in-vivo*; the ability to collect whole-brain maps of these parameters in a clinically appropriate scan time has been demonstrated and may be of great importance in studying disease processes and in evaluation of therapy efficacy.

Grant Support

NIH: ULI-RR024140; RO1-NS040801; UO1-CA154602; OD011092.

References:

1. Rooney, *et al*, *PISMRM* 11:2188 (2003). **2.** Rooney, *et al, PISMRM* 12:1390 (2004). **3.** Jenkinson, *et al*, *NeuroImage* 17(2):825-841 (2002). **4.** Zhang**,** *et al*, *IEEE Trans Med Imag* 20(1):45-57 (2001). **5.** Li, *et al, JMR* 218:77-85 (2012). **6.** Njus, *et al, PISMRM* 17:1480 (2009).

Blood-Brain-Barrier Permeability and Lesion Volume Changes in Acute Japanese Macaque Encephalomyelitis

Tagge, I. Kohama, S. Pollaro, J. Sherman, L. Bourdette, D. Woltjer, R. Wong, S. Rooney, W.

Proceedings of the International Society of Magnetic Resonance in Medicine 2015; **23**:0238

Introduction:

Dynamic-contrast-enhanced magnetic resonance imaging (DCE-MRI) provides a unique method of quantitatively characterizing tissue vascular properties *in-vivo*. Contrast agent (CA) extravasation is extremely limited in normal brain but is appreciable with compromised blood-brain barrier (BBB). Pharmacokinetic (PK) modeling of DCE-MRI data allows quantification of microvascular properties including blood volume, BBB permeability and transendothelial water exchange, all of which are sensitive to disease state. A two-site-exchange (2SX) PK model[78,79,167] has been used to monitor lesion evolution in individuals with multiple sclerosis (MS).[76] A spontaneous non-human primate demyelinating disease with striking similarities to human MS, Japanese Macaque Encephalomyelitis (JME), has recently been described.[99,100,164] Here we adopt a short-term longitudinal study design to investigate the time scale of morphological and microvascular changes in active lesions during acute JME episodes.

Methods:

Five animals (3M, 2F; mean age 5.9yrs, range 9mo-14yrs) experiencing an acute episode of JME were identified and underwent repeated MRI examinations. Follow-up exams occurred between 1 and 12 days after the initial MRI session. Four animals were scanned twice; one received four MRI exams over the course of 12 days. Follow-up MRI for two animals included only anatomical imaging and no DCE-MRI was acquired. All MRI data were acquired on a whole-body Siemens 3 Tesla MRI instrument (Erlangen, Germany) using a quadrature radiofrequency (RF) coil with inner diameter of 15 cm. Animals were initially sedated with Telazol, intubated and maintained on 1% isoflurane in 100% O_2 and were continuously monitored by pulse oximetry, respiration, and end tidal CO_2 levels during the study. Quantitative R_1 ($\equiv 1/T_1$) mapping was performed with a multiple-inversion recovery experiment employing 3D T1-weighted magnetic prepared rapid acquisition gradient echo (MPRAGE) sequence (TR: 2500 ms; TE: 3.49 ms; FA: 8°; FOV 130 mm x 97.5 mm x 96 mm, matrix: 192x144x96; TI: 200, 900, 2000, no inversion). R_1 maps were acquired before and at four time points after bolus injection of 0.2mmol (gadoteridol)/kg CA. Difference maps were created ($=R_{1post\text{-}CA} - R_{1pre\text{-}CA}$) and used to manually identify lesions and determine enhancement volumes. Only active acute (defined by CA-enhancement) lesions were considered in this analysis. PK parameters (K^{trans} and v_e) were estimated on a voxel-by-voxel basis and parametric maps were created for all animals.

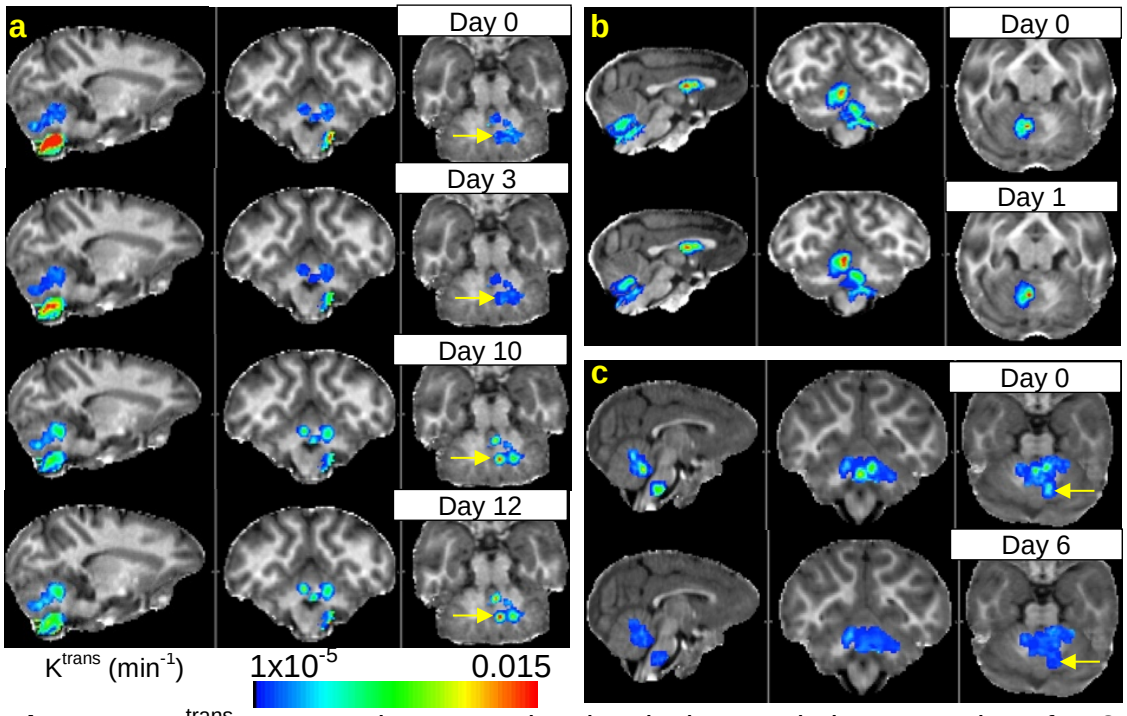

Figure 1. K^{trans} parametric maps showing lesion evolution over time for 3 separate animals.

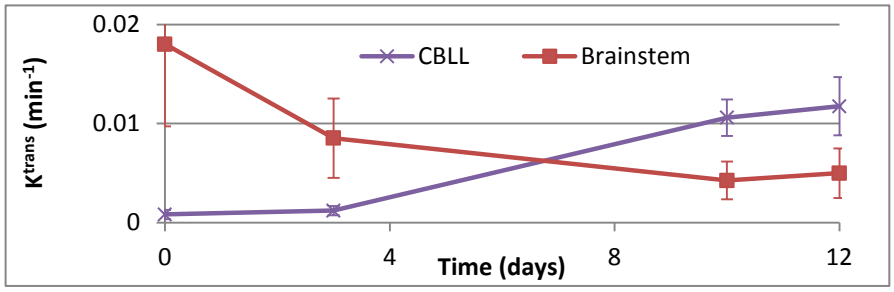

Figure 2. K^{trans} changes over time in Fig 1a CBLL (arrows) and brainstem lesions

Results:

Acute active (CA-enhancing) lesions were observed in the cerebellum (CBLL), brainstem, spinal cord, internal capsule (IC), corpus callosum (CC), and cerebral white matter. Cerebellar and periventricular chronic inactive lesions were also observed in some cases. Sagittal, coronal, and axial views of K^{trans}

maps overlaid on R_1 images are shown in **Figure 1** for the three animals that received multiple DCE-MRI exams. K^{trans} values are variable across lesions and change with time. The two imaging sessions for the animal in **Fig 1b** were only 24hrs apart to assess test-retest reliability. Lesion volumes and parameter estimates are consistent, confirming measurement stability. **Fig 1a** shows the course of lesion development over 12 days. The large brainstem lesion visible on Day 0 shows marked decrease in K^{trans} with time, while simultaneously new lesions are developing in the cerebellum. Average K^{trans} values for the brainstem lesion and one CBLL lesion (**Fig 1a** arrows) are shown in **Figure 2.** Error bars represent 1 standard deviation over the lesion volume. Elevated K^{trans} observed in newly formed lesions is characteristic of tight junction breakdown and increased BBB permeability. **Fig 1c** shows K^{trans} maps from an animal scanned at two time points. Acute lesions were identified in the IC (not shown), CBLL, and brainstem. One new enhancing lesion is observed in the CBLL on Day 6 (not shown). Interestingly, a strongly enhancing CBLL lesion on Day 0 is completely non-enhancing (K^{trans} ~ $1x10^{-5}$) by Day 6 (**Fig 1c** arrows). Volume changes for enhancing lesions in this animal are shown in **Table 1**.

Table 1	**Main CBLL (mm^3)**	**Left CBLL (mm^3)**	**Right CBLL (mm^3)**	**Superior Right CBLL (mm^3)**	**Brainstem (mm^3)**	**IC (mm^3)**
Day 0	392.4	54.3	0	32.6	119.6	15.4
Day 6	160.3	0	36.6	23.8	34.5	6.6
Change	-232.1	-54.3	+36.6	-8.8	-85.1	-8.8

Table 2	**NAWM**	**pre-acute**	**acute**	**post-acute**
MS K^{trans} (min^{-1})	$1x10^{-5}$	$3x10^{-4}$	$1x10^{-2}$	$6x10^{-4}$
JME K^{trans} (min^{-1})	$1x10^{-4}$	$1x10^{-3}$	$1x10^{-2}$	$5x10^{-3}$

Discussion:

JME lesions are observed to be fairly stable within approximately 24 hrs, but substantial morphological and vascular changes can occur in as few as 3 days. We demonstrate here that acute lesions with elevated BBB permeability arise from normal-appearing white matter (NAWM) rapidly (less than 7 days). Interestingly, lesion sites show mildly elevated K^{trans} (0.001 min^{-1}) in days leading up to the acute stage (**Figure 1a**, arrows). Low K^{trans} found in lesions at Day 0 in **Fig 1c** suggests either developing or resolving lesions; comparison with Day 6 reveals these lesions are likely already exiting the acute phase at Day 0. Indeed, one lesion (**Fig 1c** arrows) appears to have normalized completely with respect to K^{trans} from the acute stage at Day 0 to a post-acute state at Day 6. Lesion development and resolution is variable in both time and space in JME, with new lesions developing while others are resolving or transitioning to an inactive state. DCE-MRI measurements of lesion evolution in JME track well with previously reported MS data; K^{trans} values are summarized in **Table 2**.[76] It is important to note that the pre- and post-acute stages were measured 2 months before and after the acute stage, respectively, in humans. It is likely that K^{trans} values in JME would be more similar to those reported in MS were they measured months,

rather than days, before or after the acute stage. Further characterization of disease progression and etiology in JME may lead to new insights into MS. Since most JME animals are euthanized for humane reasons, the availability of high-quality brain and spinal cord tissue specimens is outstanding and facilitates the development and validation of MRI biomarkers relevant to MS.

Grant Support:

OHSU/Vertex SRA-05-07; Oregon Opportunity, DOD CDMRP-00486280; NIH: P51-RR00163-49; UL1-RR024140-S1; S10 OD018224 01.

References:

1. Yankeelov, *et al*, *MRM* 50:1151–1169 (2003). **2.** Li, *et al*, *MRM* 53:724–729 (2005). **3.** Li, *et al*, *MRM* 54:1351–9 (2005). **4.** Njus, *et al, PISMRM* 16:3431 (2008). **5.** Axthelm, *et al, Ann. Neurol.* 70:362–73 (2011). **6.** Rooney, *et al*, *PISMRM* 17:6973 (2005). **7.** Estep, et al, *J. Virol. 87:512–23* (2013).

Vascular Expansion and Blood-Brain-Barrier Permeability: A Comparative Volumetric Study in Acute Japanese Macaque Encephalomyelitis

Tagge, I. Kohama, S. Pollaro, J. Sherman, L. Bourdette, D. Woltjer, R. Wong, S. Rooney, W.

Proceedings of the International Society of Magnetic Resonance in Medicine 2015; **23**:4331

Introduction

Inflammation, blood brain barrier (BBB) compromise, and impaired microvascular function are common in multiple sclerosis (MS).[1,2] BBB permeability can be visualized with contrast-enhanced MRI using gadolinium based contrast agents (GBCA). Quantifying blood volume fractions in brain areas with a broken BBB requires sophisticated correction algorithms or use of a blood-pool contrast agent that does not readily extravasate. Japanese Macaque Encephalomyelitis (JME) is a spontaneous demyelinating disease that has many similarities to MS including intense focal neuroinflammation, macrophage infiltration, demyelination, and BBB compromise.[3,4] Acute JME lesions are commonly found in the brainstem, cerebellum (CBLL), internal capsule (IC), cerebral white matter, and corpus callosum (CC). Here we use bolus injection of ferumoxytol (FeO), an ultrasmall superparamagnetic iron oxide, to investigate vascular expansion during acute episodes of JME. Enhancement volume and location is compared between FeO and GBCA.

Methods

Five animals experiencing an acute episode of JME were identified and selected for MRI examination. All MRI data were acquired on a whole-body Siemens 3 Tesla (T) MRI instrument (Erlangen, Germany) using a quadrature radiofrequency (RF) coil with inner diameter of 15 cm. Animals were initially sedated with Telazol, intubated and maintained on 1% isoflurane in 100% O_2 and were continuously monitored by pulse oximetry, respiration, and end tidal CO_2 levels during the study. Quantitative R_1 ($\equiv 1/T_1$) mapping was performed with a multiple-inversion recovery experiment employing 3D T_1-weighted magnetic prepared rapid acquisition gradient echo (MPRAGE) sequence (TR: 2500 ms; TE: 3.49 ms; FA: 8°; FOV 130 mm x 97.5 mm x 96 mm, matrix: 192x144x96; TI: 200, 900, 2000ms, no inversion). R_1 maps were acquired before and after bolus injection of 0.2mmol/kg GBCA (Prohance). A bolus injection of 0.4mg/kg FeO was administered approximately 60 minutes after GBCA. Axial 2D T_1-weighted TSE sequence (TR:800 ms; TE 14 ms; FOV 160 mm x 120 mm, matrix 192x144, ST 1.0mm) was acquired before GBCA injection and after FeO injection on all animals. T_1-weighted images were acquired immediately before FeO injection on two animals. Relative blood volume maps were created for these two animals as a ratio of signal intensity between the pre- and post-FeO T_1 TSE images: $(S_{post\text{-}FeO} - S_{pre\text{-}FeO})/S_{pre\text{-}FeO}$. Difference maps were created by subtracting pre-contrast images from post-contrast images for both R_1 and T_1-weighted image sets to determine GBCA and FeO enhancement volumes, respectively, and lesions were identified manually. Two animals were returned to MRI for follow-up examination

one or three days after FeO injection. R_1 maps and T_1-weighted images were acquired without additional exogenous contrast administration. Follow-up images were coregistered to corresponding images from the initial visit and difference maps were created to evaluate extent of FeO accumulation in tissue ($\Delta R_1 = R_{1Day3} - R_{1Day0}$).

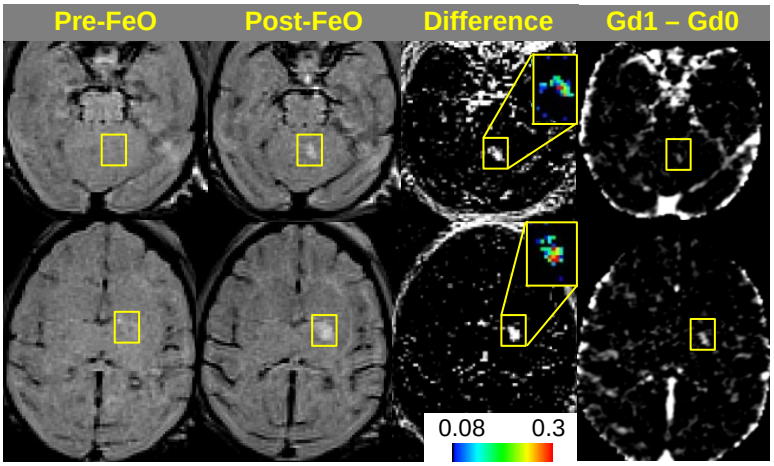

Figure 1. Comparison of gadolinium and early ferumoxytol enhancement in one subject. Top row shows a lesion in the cerebellum; bottom row demonstrates an enhancing lesion in the internal capsule.

Table – Enhancing Lesion Volumes corresponding to **Figure 1.**

Lesion Location	FeO Ratio (± SD)	FeO Volume (mm^3)	Gd Volume (mm^3)
CBLL	0.12 (± 0.07)	84	37
IC	0.15 (± 0.08)	81	48

Results

Fourteen lesions were identified in five animals, with at most 5 lesions in an individual animal. Ten of the fourteen lesions exhibited larger FeO

enhancement volume than GBCA. The remaining four lesions (one animal) showed FeO volumes equal (n=2) to or less (n=2) than GBCA. On Average FeO apparent lesion volume was 37% (+/- 25%) larger than GBCA lesion volume, but a wide variance was observed. **Figure 1** shows axial T_1-weighted slices through the CBLL (top row) and IC (bottom row). Pre-FeO images were acquired immediately prior to FeO injection, thus difference maps reflect only FeO enhancement. False-color maps of FeO enhancement ratio are shown in the inset. FeO enhancement appears fairly even, but ratio maps demonstrate lesion heterogeneity. Panels on the far right demonstrate GBCA enhancement ($=R_{1post} - R_{1pre}$). Lesion volumes for this animal are shown in the **Table**. Regions of interest selected in contralateral normal appearing brain tissue (NABT) showed zero average enhancement. **Figure 2** shows CBLL lesions in a second animal. Multi-focal enhancement is observed post-GBCA R_1 maps (top row). FeO accumulation after 3 days is visualized in R_1 difference maps (bottom row). Diffuse FeO accumulation is evident in CBLL after 3 days (**Figure 2**), and extends far beyond focal GBCA enhancement as evident in **Figure 2**, top row. Focal accumulation of FeO was observed in IC and CBLL of separate animal after 24 hrs (data not shown).

Discussion

We observe two types of FeO enhancement in JME; i) early, determined within minutes after FeO administration when plasma levels are high, and ii) late, typically 24-72 hrs post FeO administration when FeO plasma levels are low. FeO does not show significant extravasation at early times after administration,

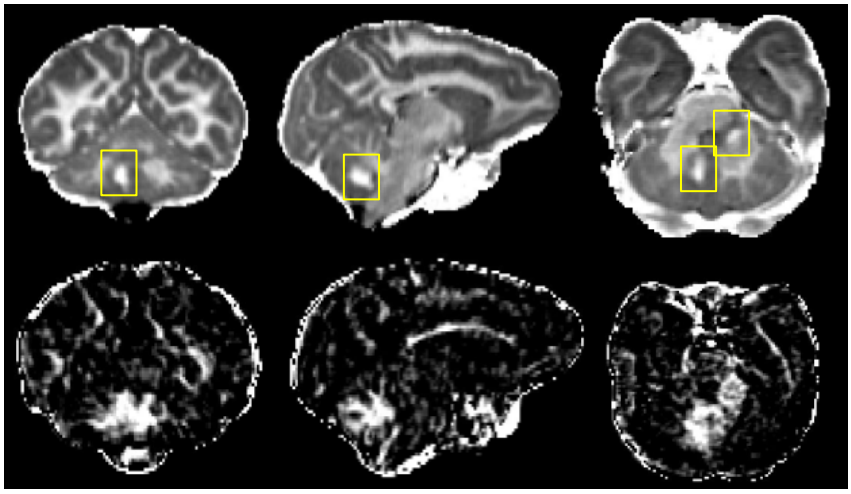

Figure 2. Comparison of GBCA and late FeO enhancement in coronal (left), sagittal (middle), and axial (right) views. Top row shows cerebellar lesions enhancing 6 mins post-GBCA injection. Bottom row ΔR_1 map shows FeO accumulation 72 hours after injection.

even in leaky glioblastoma tumors.[5] Taken as a surrogate for rCBV, early FeO enhancement ratio demonstrates heterogeneous blood volume increase within acute lesions. Based on previous estimations of white matter blood volume in Japanese Macaque NABT (2.7%),[6] FeO relative enhancements suggest lesion blood volumes ranging from 3-8%. JME lesions are frequently centered on venules or small veins; vascular dilation or alternatively, new blood vessel formation, may account for large blood volumes near the core of the lesions seen in **Figure 1** inlays. GBCA and FeO enhancements are colocalized, with the FeO volume generally exceeding that of GBCA. These findings suggest that vascular expansion extends well beyond the area of BBB compromise. FeO accumulation in tissue over 24-72 hours indicates heavy macrophage activity in and around acute lesions in JME, and extends well beyond areas of BBB breakdown visualized by GBCA. That there is a relationship between

inflammation and BBB compromise is well accepted, but the temporal nature of the relationship is unknown. Lesions with FeO enhancement volumes equal to or less than GBCA may be pathologically distinct or represent a different disease stage than those shown here. Longitudinal studies combining FeO and GBCA may reveal a causal relationship between expanded vascular space and BBB compromise throughout lesion evolution.

Grant Support

This work was supported by OHSU/Vertex SRA-05-07; Oregon Opportunity, DOD CDMRP-00486280; NIH: P51-RR00163-49; UL1-RR024140-S1; S10 OD018224 01.

References:

1. Popescu, *et al*, *Continuum* **19**:901-21 (2013). **2.** Ge, *et al*, *AJNR* **26**:1539:1547 (2005). **3.** Axthelm, *et al*, *Ann Neurol* **70**:362-73 (2011). **4.** Rooney, *et al*, *PISMRM* **13**:6973 (2005). **5.** Weinstein, *et al*, *J Cereb Blood Flow Metab* **30:**15-25 (2010). **6.** Njus, *et al*, *PISMRM* **17**:1480 (2009).

Lesion Distribution Probability in Japanese Macaque Encephalomyelitis: A Comparison to Human Demyelinating Diseases

Tagge, I. Kohama, S. Pollaro, J. Sherman, L. Bourdette, D. Woltjer, R. Wong, S. Rooney, W.

Proceedings of the International Society of Magnetic Resonance in Medicine 2016; **23**:0000 (Submitted)

Introduction

A spontaneous non-human primate demyelinating disease, Japanese Macaque Encephalomyelitis (JME), has recently been described.[99,100,164–166] JME bears marked clinical and pathological similarities to multiple sclerosis (MS), acute disseminated encephalomyelitis (ADEM), and neuromyelitis optica (NMO). To date, JME is the only known naturally-occurring MS-like disease in non-human primates. Here, we describe topography of gadolinium based contrast agent (GBCA) enhancing lesions typical in JME, presented in a lesion distribution probability map based on 21 cases of acute JME. This represents an important step in not only understanding this disease, but also in making meaningful comparisons to human demyelinating diseases.

Methods

Twenty-one animals experiencing an acute episode of JME were identified and selected for MRI examination. All MRI data were acquired on a whole-body

Siemens 3 Tesla (T) MRI instrument (Erlangen, Germany) using a quadrature radiofrequency (RF) coil with inner diameter of 15 cm. Animals were initially sedated with Telazol, intubated and maintained on 1% isoflurane in 100% O_2 and were continuously monitored by pulse oximetry, respiration, and end tidal CO_2 levels during the study. Quantitative R_1 ($\equiv 1/T_1$) mapping was performed with a multiple-inversion recovery experiment employing 3D T_1-weighted magnetic prepared rapid acquisition gradient echo (MPRAGE) sequence (TR: 2500 ms; TE: 3.49 ms; FA: 8°; FOV 130 mm x 97.5 mm x 96 mm, matrix: 192x144x96; TI: 200, 900, 2000ms, no inversion). R_1 maps were acquired before and 6 minutes after bolus injection of 0.2mmol (gadoteridol)/kg GBCA). Difference maps were created ($=R_{1post\text{-}CA} - R_{1pre\text{-}CA}$) and used to manually identify lesions. Only acute (defined as GBCA-enhancing) lesions were considered in this analysis. R_1 maps from 6 healthy Japanese macaques were nonlinearly coregistered and then averaged to create a common reference space for analysis. Lesion masks were created manually for each JME case based on the R_1 difference maps; R_1maps were coregistered to the reference image, and lesion masks were transformed accordingly. Binarized lesion masks in the reference space were then summed to create the final lesion distribution probability map shown in **Figure 1**.

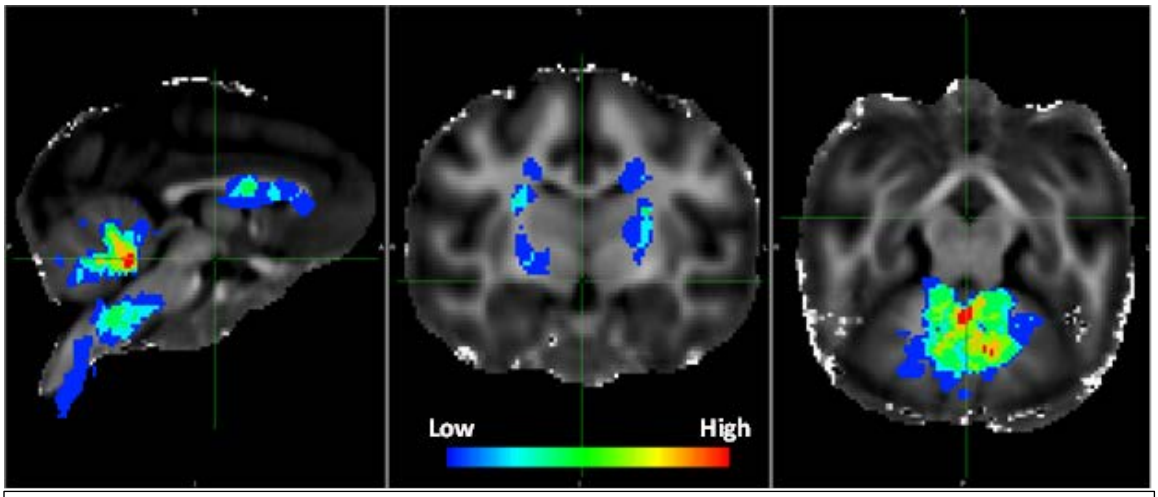

Figure 1. Lesion distribution probability map. Voxel-wise map of lesion occurrence probability shown in false-color (blue is low probability, red is high probability) overlaid on the average R_1 map created from six healthy control animals.

Results

A total of 100 GBCA-enhancing white matter lesions were identified in 21 Japanese macaques (median 4 lesions per animal, range 2-11) presenting with clinical symptoms typical of JME: ataxia, paresis, or optic involvement. The median age was 2 years [range 0.3-26 years] and 43% were female. Animals most commonly presented with lesions in the cerebellum (including peduncles, CBLL; n=18; 86% of animals), followed by the brainstem (n=11; 52%), internal capsule (IC; n=8; 38%), and upper cervical spinal cord (SC; n=5; 24%), as demonstrated in **Figure 2**. Overall lesion load across the population was greatest in the cerebellum (n=55 lesions), followed by the IC (n=14), brainstem (n=11), and SC (n=7). Lesions were also identified in the corpus callosum (CC), cerebral white matter (CWM), and periventricular white matter (PVWM). CBLL lesions were most frequent near the midline. Lesions were often observed bilaterally within cases, and demonstrated equal bilateral probability across all animals studied.

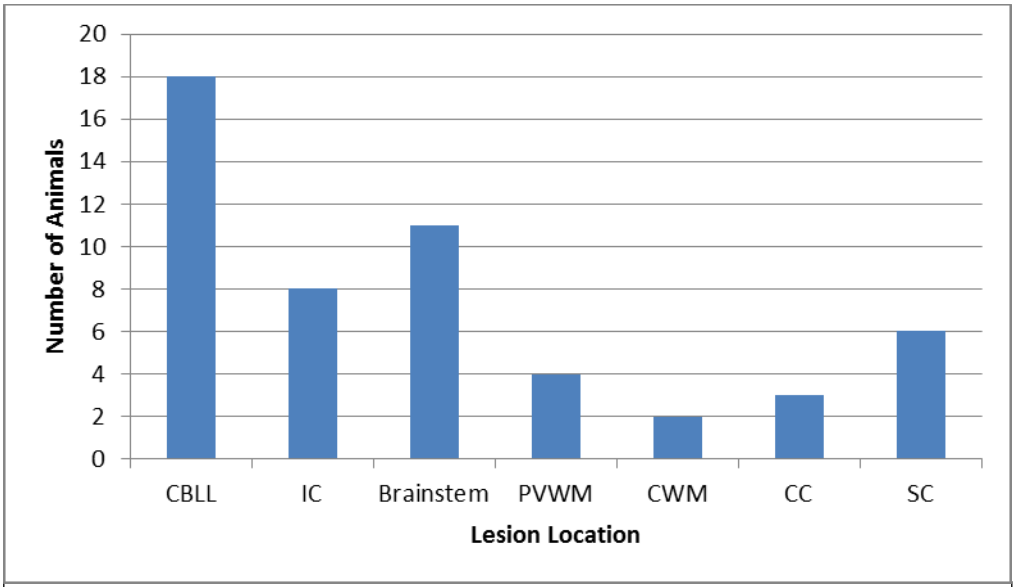

Figure 2. Overall lesion distribution. Number of animals presenting with a GBCA-enhancing lesion anywhere in the selected structures; CBLL – cerebellum, IC – internal capsule, PVWM – periventricular white matter, CWM – cerebral white matter, CC – corpus callosum, SC – spinal cord.

Discussion

Lesion morphology and distribution are important in obtaining correct differential diagnosis in demyelinating disease.[16] This work describes GBCA-enhancing lesion distribution typical of JME, a novel spontaneous demyelinating disease in non-human primates. Brainstem and SC lesions are found medially, suggesting a transverse myelitis as seen in ADEM and NMO, and laterally as seen in MS. CWM lesions are often sub- or juxtacortical; making distinctions between PVWM and CWM can be challenging due small brain size and close proximity of structures. Indeed, a juxtacortical WM lesion could be simultaneously classified as periventricular. However, these are both typical of MS, so the absolute distinction here may be of limited importance. Lack of optical tract involvement or longitudinally extensive transverse myelitis in this cohort suggests

dissimilarity to NMO.[21] Based on GBCA enhancing lesion distribution alone, JME appears most similar to MS or ADEM. Additionally, pediatric MS patients often have higher infratentorial lesion load and are more capable of completely resolving acute lesions compared to adult MS.[28] High infratentorial lesion load found in JME, and the ability for near complete acute lesion resolution in some cases[166] suggests JME may be more similar to pediatric than adult MS. JME commonly occurs in animals prior to sexual maturity (72% of this cohort). Image coregistration across the population was imperfect, so this map serves primarily for illustrative purposes rather than precise quantification. Additional characterization of disease natural history, T_2 lesion distribution, and CSF assays will be necessary before confident comparisons can be made with human disease. JME is a novel and promising non-human primate model of inflammatory and demyelinating disease with potential applications in understanding MS and MS-like diseases.

Grant Support

This work was supported by OHSU/Vertex SRA-05-07; Oregon Opportunity, DOD CDMRP-00486280; NIH: P51-RR00163-49; UL1-RR024140-S1; S10 OD018224 01; 1F31-NS089260; and the Portland chapter of the ARCS Foundation.

References

[See references for main document]

Appendix C – Related Manuscripts

Measurement science in the circulatory system.

Casey M Jones, Sandra M. Baker-Groberg, Flor A. Cianchetti, Jeremy J. Glynn, Laura D. Healy, Wai Yan Lam, Jonathan W. Neslon, Diana C. Parrish, Kevin G. Phillips, Devon E. Scott-Drechsel, Ian J. Tagge, Jaime E. Zelaya, Monica T. Hinds, and Owen J. T. McCarty.

Originally published in:

Cellular and Molecular Bioengineering, Vol. 7, No. 1, March 2015 (© 2013) pp 1-14.

DOI: 10.1007/s12195-013-0317-4

Ian Tagge created Figure 1 and wrote the *Measurement Tools* section in **Part I: Organ Physiology and Measurement Tools**.

Abstract

The dynamics of the cellular and molecular constituents of the circulatory system are regulated by the biophysical properties of the heart, vasculature and blood cells and proteins. In this review, we discuss measurement techniques that have been developed to characterize the physical and mechanical parameters of the circulatory system across length scales ranging from the tissue scale (centimeter) to the molecular scale (nanometer) and time scales of years to

milliseconds. We compare the utility of measurement techniques as a function of spatial resolution and penetration depth from both a diagnostic and research perspective. Together, this review provides an overview of the utility of measurement science techniques to study the spatial systems of the circulatory system in health and disease.

Introduction

Novel tools and measurement techniques with varying degrees of sensitivity and resolution have been extensively used to define the physical parameters of the circulatory system during homeostasis and in the pathological state. These tools have been implemented both *in vivo* and *ex vivo* with resolution ranging between nanometers and centimeters (Figure 1). In this review, we discuss the utilization of measurement science techniques to define the dynamical role of the cellular and molecular constituents of the circulatory system in regulating organ physiology. We divided the study of the circulatory system into three levels; organs, vessels, and cells. We start out by describing the physical and mechanical characteristics of the circulatory system in health, and where appropriate, how these parameters change in a pathological setting. We then discuss measurement tools that have been used to study each component of the circulatory system at various levels of resolution.

This review article was a collaborative effort by the members of the Cardiovascular Working Group at the Oregon Health & Science University. The tools and measurement techniques that were included were in part based on the

expertise of the members of the working group, are thus are not inclusive of all the techniques available to the field.

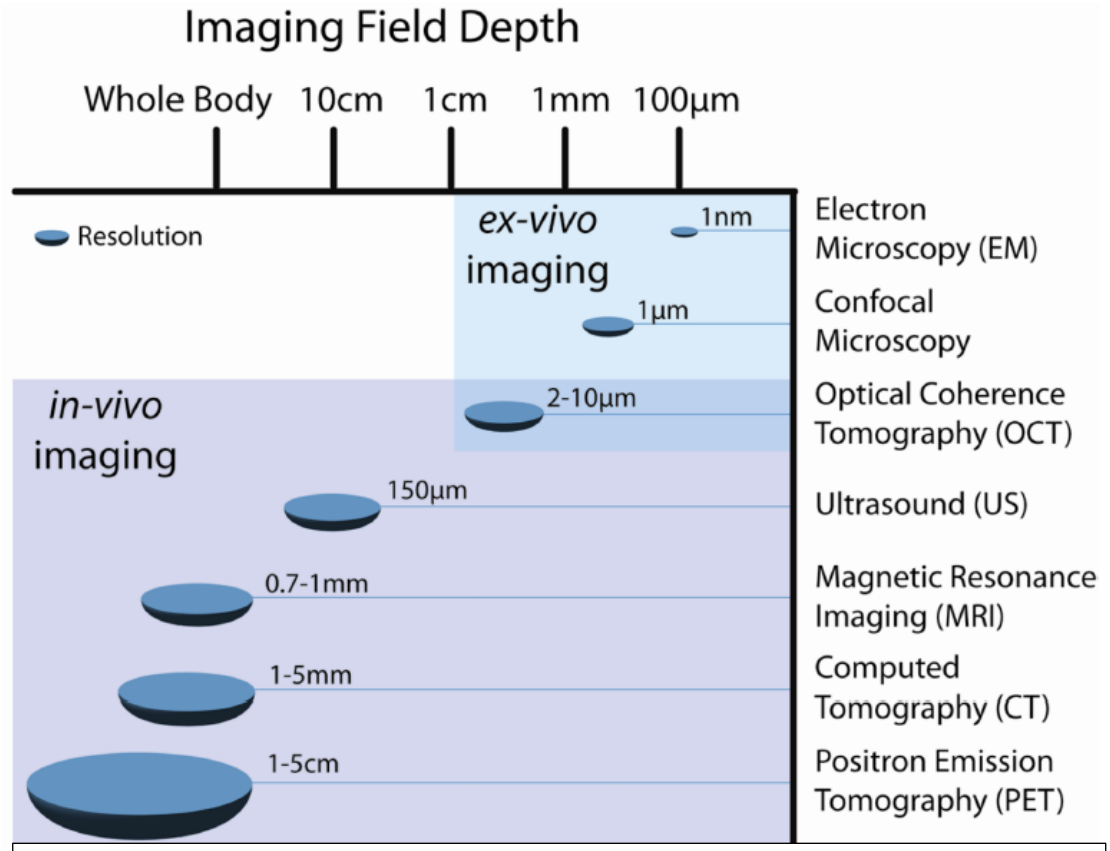

Figure 1. Resolution and imaging field depth (penetration) of several current imaging modalities are illustrated and compared. Note that resolution decreases as depth increases, rendering modalities such as CT and MRI suitable for imaging whole organs and systems *in vivo* whereas modalities with higher resolution are best suited for *ex vivo* and *in vitro* imaging of smaller structures on the cellular and sub-cellular level. Often two or more modalities are used in tandem to obtain a full understanding of a system or pathology.

Part I: Organ Physiology

1.1. Heart Function

The heart is the central organ of the cardiovascular system. Normal heart function is partially dependent on proper spatial and temporal electrical conduction. The heartbeat is initiated by the firing of Purkinje cells in the sino-atrial node (1). Electrical impulses are propagated through the Purkinje fibers to the atrio-ventricular node, which subsequently travel through the ventricles of the heart. Cardiac myocytes, which receive signals from both Purkinje fibers and adjacent myocytes, respond to depolarization by contracting in sequence to propel blood out of the atrium to the ventricle and into circulation. Heart rate, force of contraction, and speed of repolarization are modulated by neurotransmitter release from sympathetic and parasympathetic nerves that innervate the atria and ventricles (2). An electrocardiogram (ECG) measures heart rate and provides visualization of electrical impulse conduction through the heart. Normal adult human heart rates range from 60–100 beats per minute. Heart rates outside this range may be indicative of any number of pathological conditions, including but not limited to heart failure, myocardial infarction, sepsis, or peripheral vascular abnormalities (3).

Normal blood pressure in humans is considered to be between 100/60 and 120/80 (systolic/diastolic pressure). Blood pressures between 120/80 and 130/90 are categorized as prehypertensive, while blood pressures over 130/90 are categorized as hypertensive. Stroke volume, or the amount of blood pumped from the ventricle with each beat, varies considerably from person to person. Normal stroke volumes range between 55 and 100 mL, with men generally having higher stroke volumes than women. Stroke volumes below 55 mL are

indicative of heart failure, while stroke volumes over 100 mL may be indicative of intense and prolonged exercise training (4). A myocardial infarction (MI) occurs when an artery that supplies blood to the heart muscle becomes occluded, either by a blood clot or an arterial plaque. Following a myocardial infarction, the myocardium undergoes significant remodeling, often with pathological consequences, regardless of whether or not the occluded vessel is reperfused. Post-MI remodeling can include fibrosis of heart tissue, infarct expansion, ventricular dilation and wall thinning, and dispersion of repolarization (5). All of these outcomes, alone or in combination, contribute to mortality following MI by increasing the chances of ventricular rupture, heart failure, fatal arrhythmias or sudden cardiac death.

1.2. Measurement Tools

Heart structure and function in both normal and pathological conditions are routinely examined using a variety of imaging modalities in both research and diagnostic settings (6). In this section of the review, we will discuss the following measurement tools: ECG, ultrasound (US) imaging, X-ray computed tomography (CT) imaging, positron emission tomography (PET) imaging, and magnetic resonance imaging (MRI).

1.2.1. Electrocardiography

ECG is perhaps the least expensive and simplest of the methods used to detect heart abnormalities associated with MI, pulmonary embolism, heart murmurs, dysrhythmias, seizures and syncope (7). Electrodes placed on the patient's body

measure the electrical signals produced by the heart during each cardiac cycle. While the placement and number of electrodes used may vary depending on application, generally 12 electrodes are used during an ECG exam. Additional electrodes may be added, thus increasing coverage of the heart and improving the ability to detect MI. The result is a graph (“lead”) that traces the cardiac cycle and allows for identification of electrical abnormalities. The trace of a single cycle is split into segments based on peaks and valleys. Irregularities in specific segments of the cardiac cycle correspond to injury in specific areas of the heart and can thus indicate the exact nature of the damage. For instance, ST-segment elevation is a hallmark irregularity indicative of MI (8). While indispensable as a first-look and early-diagnosis tool, ECG is not capable of monitoring blood flow or cardiac pumping ability, and thus injury to some regions of the heart can be missed. Further, ECG is a non-imaging modality, thus is of limited utility in assessment of structural abnormalities.

1.2.2. Ultrasound Imaging

Ultrasound is used as a noninvasive diagnostic tool to assess structure and function within the cardiovascular system. Echocardiography (commonly referred to as ‘echo’) uses ultrasound to characterize cardiac structure and function. This technique utilizes a transducer that is held against the skin and emits ultrasound waves that travel through blood and soft tissue. The ultrasound waves scatter and bounce back when they encounter dense tissue. The deflected ultrasound waves are collected by the transducer and digitized to a real-time image to reveal structural information. Denser tissues will deflect more ultrasound and will be

represented on the image with a brighter pixel. Echocardiography can be used to construct planar images of the heart, 3D volumes, and when used in conjunction with Doppler, measure flow patterns in the heart. Echocardiography is often used to measure cardiac volumes, monitor wall motion, evaluate valve and intracardiac masses, and identify structural defects (9). These measurements use ultrasound frequency ranges between 2 and 18 MHz, with the standard 10 MHz instrument resulting in a longitudinal resolution of 150 μm at a frame rate between 15 and 40 frames per second, thus allowing for detection of movement. Higher frequencies result in increased spatial resolution; however, the depth of penetration decreases with higher frequencies. Doppler ultrasound is a type of ultrasound imaging that reveals information on the flow of blood within the chambers of the heart. During Doppler ultrasound imaging, ultrasound waves strike moving blood cells and are reflected back to the transducer. The frequency of the returning wave is modulated by the direction and velocity of blood flow according to the Doppler Effect. This information can be displayed graphically with spectral Doppler or, more commonly in medical applications, as a color image with a gradient color map corresponding to blood flow rate.

1.2.3. X-ray Computed Tomography and Positron Emission Tomography

CT imaging produces a 3D anatomical image using x-ray images and advanced computation (10). The temporal resolution of CT is between 100–300 ms; total scan times vary based on the use of contrast agent and the number of scans performed. The spatial resolution of CT is 1–5 mm (comparable to MRI, yet with slightly lower resolution); the spatial resolution of PET is between 1–5 cm. 3D

volumes are comprised of individual slices that are acquired in the axial plane; processing techniques often can re-slice volumes in a number of orientations depending on actual acquisition details. Computed tomography angiography specifically measures blood flow rate and is used to image coronary artery anatomy, often detecting non-obstructive atherosclerotic plaques even before a level of hemodynamic significance is reached.

PET is a nuclear medical imaging technique. A positron-emitting radionuclide tracer (generally administered intravenously or via inhalation) indirectly emits gamma rays that are subsequently detected in pairs to create a 3D image. The kinetic energy of the positron and the spatial resolution of each of the detectors limit the spatial resolution of PET imaging in humans to 1–2 mm. Because the tracer is attached to a biologically active molecule, PET images represent a biological (often metabolic) process within the body. In order to generate anatomical images, PET must be used in combination with MRI or CT because the tracer is the signal molecule. Most modern scanners acquire CT and PET images in the same session – PET for (metabolic) functional imaging and CT for anatomical and morphological imaging. PET data is then overlaid on the CT data to ascertain the functional significance via metabolic rate in the location of interest. While ^{18}F-fluorodeoxyglucose is the most prolific radiotracer in PET examinations, a wide variety of tracers have been developed to detect unstable atherosclerotic plaques and to measure myocardial perfusion and metabolism. Though not currently available commercially, development of PET-MRI scanners is an active and promising area of research (11).

PET is regarded as the gold standard technique for non-invasively quantifying myocardial blood flow and has been well validated in animal models of heart function following both reperfused and non-reperfused myocardial infarction (12), as well as in humans at rest and during hyperemia induced by bipyridamole stress (13). Quantification of myocardial blood flow and perfusion is essential in assessing myocardial infarction.

1.2.4. Magnetic Resonance Imaging

Cardiac MRI assesses both structural and functional features within a single examination. MRI is used to generate high-resolution 3D anatomical images to measure heart (and vessel) wall thickness in both healthy and diseased tissues. Single images can be acquired on the order of 20–200 ms. Acquisition of all desired images in a study generally requires ~30 mins. This non-invasive method can be used to measure wall thickening or atrophy due to disease as well as structure changes following treatment (6). Measurement of absolute tissue water-proton (^{1}H) longitudinal relaxation times (T_1, relaxation time in seconds) enables identification of acute myocardial infarction. Parametric maps produced by voxel-by-voxel fitting of T_1 (or R_1 ($\equiv 1/T_1$)) provides a tool to measure the extent and location of the infarct. Exogenous, non-irradiating contrast reagents provide a tool for physicians to study the structure and integrity of the vasculature based upon pharmacokinetic modeling of permeability (14). Contrast-enhanced MRI can detect more morphological details than standard MRI, with the expected detection limits around 0.3 cm^2 (2 × 2 pixels) and 0.5 cm^2 (3 × 4 pixels), respectively. Gadolinium-based contrast reagents administered intravenously are

known to transiently extravasate from the blood into the interstitium. Pharmacokinetic modeling of the extravasation rate quantitatively measures vessel permeability (15–18). Further, uptake of contrast reagents into tissue is indicative of deleterious processes such as scarring, infarct, or necrosis. Recent studies have shown that measuring MRI signal enhancement in the heart following cardiac infarct allows for prediction of tissue viability and overall capacity for recovery. Cine imaging, where ECG is utilized to trigger the collection of a series of segmented images, is widely used clinically to observe heart function throughout the entire cardiac cycle (19). Post-processing and advanced modeling techniques quantitatively measure such diagnostically relevant properties including flow, valve ejection rate, strain rates, and ventricular volume. Cardiac MRI has also shown promise as an alternative to PET for quantifying myocardial blood flow and perfusion, which is of both diagnostic and prognostic importance when treating myocardial infarction.

Part II: Vessel Physiology and Measurement Tools

2.1. Blood Vessel Physiology

The human vascular system facilitates the transfer of nutrients and metabolites throughout the entire body. A 70 kg man has approximately five liters of blood and a total vascular surface area of 30–70 m^2 depending on the subject's current activity level (20). Blood flow is driven by a pressure gradient which, in a healthy individual's systemic circulation, pulses between 80–120 mmHg in the arteries and is near zero in the right atrium. A large drop in pressure occurs in the

arterioles, vessels 20–80 μm in diameter, which are the next set of smaller blood vessels stemming from arteries, which are 0.1–3 cm in diameter. The diameter of an arteriole is largely dictated by the extent of arteriolar smooth muscle contraction, which is regulated by a number of local and circulating factors. Changes in arteriolar diameter regulates vessel resistance and the corresponding flow rate through the vessel (21). Although blood flow is typically unidirectional and laminar, vascular branching and atherosclerotic plaques can result in flow separation and recirculation.

2.1.1. Endothelial Cell Physiology

The luminal surface of blood vessels is lined with a confluent monolayer of endothelial cells (ECs). As the interface between the blood and other organs, ECs integrate multiple physical and biochemical cues to regulate platelet adhesion and activation, leukocyte adhesion and transmigration, vascular permeability, vascular tone, and angiogenesis (22, 23). ECs locally mediate these processes through both membrane-bound factors, such as tissue factor, thrombomodulin, and E-selectin, as well as secreted factors, such as nitric oxide and prostacyclin (24). A major determinant of the EC phenotype is the local hemodynamic environment. Wall shear stress resulting from blood flow through the vessel initiates EC cytoskeletal remodeling and causes cellular elongation and alignment in the direction of flow (25). ECs respond to unidirectional, laminar flow by producing numerous factors which inhibit blood platelet recruitment and activation, intimal proliferation and leukocyte adhesion. Conversely, disturbed flow conditions which yield a low average wall shear stress promote EC

dysfunction and facilitate the early stages of atherogenesis including leukocyte adhesion and transmigration into the sub-endothelial space (26). Tools that measure blood flow and characterize regions of disturbed flow can be used to identify vascular locations prone to atherosclerosis, as the connection between atherosclerotic plaque localization and regions of disturbed blood flow has been repeatedly demonstrated.

2.1.2. Atherosclerosis

As atherosclerosis progresses, fatty plaques develop that partially occlude the vessel immediately downstream of the lesion. This flow disturbance reduces the wall shear stress, inducing endothelium-dependent vascular remodeling consisting of intima-media thickening and reduced vessel diameter (27). The development of fatty plaques and intima-media thickening also alters the mechanical properties of blood vessels, resulting in increased cardiovascular morbidity and mortality risk. Additionally, plaques in regions of low wall shear stress progress to have more necrotic cores and fibrous tissue, suggesting an increased risk of plaque rupture (28). Measurement tools that enable the quantification of the physical properties of blood vessels and blood flow have been developed in order to provide information on the risk and progression of atherosclerosis.

2.2. Measurement Tools

Tools that measure the physical properties of blood vessels and blood flow have been employed to study and monitor the progression of vascular pathologies. In

addition, mathematical models have been developed to predict the physical parameters of the vasculature, such as wall shear stresses and micro pressures, which would otherwise be difficult to acquire experimentally *in vitro* or *in vivo* (29). When combined with powerful numerical techniques, such as finite element analysis (FEA), these mathematical models have been employed to improve, for instance, the assessment for the risk of rupture of an abdominal aortic aneurysm (AAA) (30). These tools and models will be reviewed in more depth below.

2.2.1. Angiography

Angiography of the blood vessels is routinely performed to identify areas of stenosis, narrowing or blockages of normal blood flow (31). This procedure relies on the insertion of a catheter into the femoral artery or vein for investigation of the arterial or venous system, respectively. The catheter is then used for delivery of a radio-opaque contrast agent that rapidly mixes with blood at the injection site. At the time of contrast injection, a series of X-rays of the relevant location is performed to capture both still frames and movies for the measurement of lumen diameter and blood flow through the vessels. In the peripheral cardiovascular system, digital subtraction angiography is often employed where a background X-ray of the bones and tissue at the injection site is subtracted from the total X-ray image, giving an image of the contrast alone (32). Digital subtraction angiography requires the acquisition of images at a rate of 2–3 frames per second for the quantification of blood flow through the vessels, and is limited to detection of the lumen of the vessels, albeit with good spatial resolution (0.3–0.4

mm); yet, angiography cannot provide information about vessel wall thickness or tissue structure.

2.2.2. Ultrasound Imaging

Diagnostic external ultrasound imaging is one of the non-invasive measurement tools for the investigation of blood vessel diameter and wall thickness. Doppler ultrasound allows for the measurement of the physical parameters of blood flow including blood flow rate, areas of disturbed flow, and valvular regurgitation (33). Intravascular ultrasound employs the same general technique as utilized by external ultrasound whereby a miniature transducer is located at the end of a catheter to produce images of vessel structure from within the cardiovascular system, eliminating scatter by other tissues and depth penetration issues. The spatial resolution of intravascular ultrasound (using a standard 20 to 40 MHz transducer) is 100 μm axially, and 200–250 μm laterally (34). Intravascular ultrasound provides information about vessel narrowing, plaque size and composition, as well as valve functionality (35).

2.2.3. Contrast Enhanced Ultrasound

The coupled use of microbubbles with ultrasound allows for non-invasive imaging of the cardiovascular system (36). Microbubbles consist of a shell composed of proteins, lipids, or polymers and a gas core consisting of air, nitrogen, or heavy gas such as perfluorocarbons. The microbubbles compress and oscillate when exposed to an ultrasound frequency field in a manner unique from the surrounding blood and tissue which allows for a strong signal in the vessel

lumen. Microbubbles are especially useful when investigating blood flow in small diameter vessels including capillary beds, and allows for the extension of Doppler-based techniques below the lower limit of blood flow (<1cm/sec). Additionally, microbubbles are being investigated for their therapeutic use in the molecular imaging of thrombus formation (37) and thrombolysis (38). Microbubbles can be targeted to a clot, where they can be burst by applying a short exposure to high-power ultrasound; the force of the bursting bubbles can break up the clot and help resume flow within the vessel (39).

2.2.4. Optical Coherence Tomography (OCT)

OCT is an echo-based imaging modality that measures light using low coherence interferometry (40). This imaging modality is a high resolution (2–20 μm), high speed (1ns to as fast as 30 fs for 10 μm resolution), non-invasive tomographic imaging technique that allows 3D imaging of the cardiovascular system in animal model systems with transparent tissue such as tadpoles, zebrafish, mouse and embryonic chick hearts (41). OCT allows the measurement of both blood flow and velocity, with exquisite spatial and temporal resolution, making it an ideal imaging modality for the study of heart development in embryonic hearts (42). OCT imaging of the human vasculature is limited to the utility of intravascular OCT, where an OCT core is located at the distal tip of a catheter. As red blood cells scatter the OCT signal, blood needs to be temporarily cleared by an injection of x-ray contrast medium throughout the duration of the OCT pullback to give information about the vessel wall microstructure with very fine resolution (~10 μm). Intravascular OCT can provide information about lumen size, wall

thickness, plaque size and composition with higher resolution than intravascular ultrasound.

2.2.5 Flow-sensitive 4D-Magnetic Resonance Imaging (4D-MRI

Also known as magnetic resonance velocimetry, flow-sensitive four-dimensional (4D)-MRI allows for analysis of blood flow parameters and measurement of structural blood vessel features, such as vessel diameters (43). Spatial resolution for these volumes are on the order 2 mm^3 with 40 ms scans, allowing for scans of large vessels on the order of 10–20 minutes for detailed flow and volume information. In 4D-MRI, there is no need for optical access, special flow markers, or exogenous contrast enhancing. Blood flow velocities can be measured along single lines, in planes, or in full 3D volumes (albeit with sub-millimeter resolution). Higher order flow patterns such as helical flow or vortex can also be imaged and analyzed. Data analysis is required for reduction of background noise, antialiasing, and eddy current correction. After analysis, vectorial wall shear stress and oscillatory shear index can be calculated.

2.2.6.1 Bright Field Microscopy

The use of optical microscopy is ubiquitous in the investigation of cellular organisms. One powerful tool available to vascular biologists that takes advantage of multiple microscopy techniques is *ex vivo* isolated vessel preparation (44).

In this technique, a vessel is dissected away from its resident tissue and cannulated in a bath chamber in order to study blood vessel dynamics. This

technique has been used to study vessels in many vascular beds including the brain (45), heart (46), and gut (47) with vessels ranging in size from 12 µm microvessels (47) to 200 µm arteries (45). In addition to having pharmacological access to the intra-luminal space of the blood vessel, there is also semi-restricted access to the extra-luminal space through the bath solution. While one of the strengths of this technique is that it allows the study of vascular reactivity within intact blood vessels, the cell-specific roles of blood vessels can also be teased apart through the selective removal of parts of the blood vessel such as the endothelial lining. Coupled to wide-field bright field microscopy, this technique allows for the non-invasive quantification of dynamic changes in blood vessel diameter with optical calipers in response to various stimuli including changes in pressure, flow, or chemotatic gradients.

2.2.6.2 Fluorescence Microscopy

Fluorescence microscopy is one of the most widely used research tools for modern cell biology. Through the use of highly specific fluorescent labeling techniques such as immunocytochemistry, *in situ* hybridization, or fluorescent protein tags, the spatial distribution and dynamics of proteins, subcellular structures or genomic sequences of interest can be analyzed in chemically fixed or living samples. Furthermore, the advent of fluorescent calcium indicators (48) and membrane potential dyes (49) has made it possible to utilize fluorescent microscopy techniques to study questions that once were only measureable though electrophysiology. Moreover, these fluorescent indicators are less invasive than electrophysiology techniques and allow for greater spatial

resolution. Paired with genetically engineered animals that have tissue-specific fluorescent reporters, co-localization analysis can provide cell-specific identification of labeling events (50).

2.2.7. Mathematical Modeling and Abdominal Aortic Aneurysms

Mathematical modeling is an effectual, cost-effective tool that provides investigators with opportunities to: i) explore novel avenues for addressing a research question; ii) build a fundamental understanding of the problem being studied; and iii) narrow knowledge gaps. When applied with numerical methods, such as finite element analysis (FEA), mathematical models provide important insight about a design's competency and stability. In the case of AAAs, for example, FEA and mathematical models are used to compute vascular wall stresses (forces per unit area). The stresses are subsequently employed to assess the risks of rupture of AAAs (30).

To model and solve an AAA biomechanical problem, a patient's AAA geometry must first be acquired from medical images, such as CT and MRI. This is achieved by using image segmentation algorithms that extract the outer wall and lumen contours from the cross-sectional images. Computationally, the contours are stacked to reconstruct the aneurismal geometry in the form of a mesh, which is subsequently imported to a finite element program. To properly simulate the physical structure and environment of the aneurysm, knowledge of the aortic tissue's material mechanical properties (e.g. tensile and compressive strengths and measures of stiffness), vascular loads, and boundary conditions are

indispensable (51). Methods for the acquisition of material properties are discussed further in Section 2.2.8. The intraluminal loads applied to the model walls are the brachial systolic and diastolic blood pressures measured at the time of the initial CT scan is taken. The typical boundaries imposed on the model include fixing the ends of mesh to simulate the connection of the AAA to the surrounding aorta. Once pertinent information is inputted into FEA software, the finite element program numerically solves a complex set of partial differential equations over the intricate AAA continuum by: i) dividing the complex aneurysmal geometry into discrete, smaller domains; and ii) simplifying the partial differential equations into algebraic equations involving a finite number of parameters within the smaller domains. From these computations, important physical measures, such as the extent of a model's deformation in response to the applied loads and the wall stresses, are obtained. One limitation of mathematical models is their sensitivity to the input parameters and set-up. If minimal care is placed in choosing the appropriate boundary conditions, for example, the models will yield incorrect wall stress results or solutions may fail to converge.

2.2.8. Tissue Material Properties and Tensile Testing

Conventionally, the physical parameters used in the modeling of a patient's AAA are not patient-specific; rather, they are derived from tensile testing measurements performed on tissues obtained from a population of cadavers or patients undergoing elective repair (52). For uniaxial tensile testing of aortic tissue, the specimen is secured on brackets that move in opposite directions. As

the tissue is stretched, a tension load cell placed on one end of the brackets converts the imposed load into an analog electrical signal. An analog-to-digital device subsequently digitizes the signal. The tension forces and the change in specimen length are recorded throughout the experiment. The tissue is stretched until failure to also acquire the failure tension, which is a good indicator of a tissue's vulnerability. Because the specimen in uniaxial tensile testing is extended in one dimension, knowledge gained about the failure tensions is limited to the tested direction. In contrast, biaxial tensile testing, which measures an AAA tissue's tension forces in the circumferential and longitudinal directions, may provide a more complete assessment of a tissue's wall mechanics and an opportunity for modeling AAA tissue more accurately (53).

2.2.9. Tissue Elasticity Imaging

Employing tensile testing measurements for the acquisition of patient-specific aneurismal material properties is not feasible due to its invasive protocol. Tissue elasticity imaging has been employed to non-invasively determine these material properties for the liver, kidney and heart, but its potential use for the characterization of patient-specific AAA material properties needs further assessment. In static elastography, a more common form of elastographic imaging, a tissue is externally compressed with a transducer and the pre- and post-compression imaging line pair data are subsequently acquired. A cross-correlation analysis is performed on the compression line pair data in order to compute a strain field. The applied stress is assumed to be a function of the ratio of the circular compressor radius and the axial distance between the compressor

and the point of interest within the tissue (54). Using the strain and stress, the tissue elastic modulus, a measure of stiffness, can be calculated. One limitation of elastography is its sensitivity to small motions, which can affect the cross-correlation analysis resulting in a probable erroneous strain field. Addressing the limitations in system stability can aid in improving elastography as a medical application. If elastography can be employed to assess AAA patient-specific properties, the acquired information may be instrumental in not only evaluating the strength of a patient's AAA but also in improving the accuracy of wall stress computations and the assessment of aneurismal rupture risk.

3. Blood Cell Physiology and Measurement Tools

3.1. Introduction and Background

Blood is an essential constituent of the circulatory system and is responsible for body temperature control, coagulation, pH regulation, oxygen and nutrient distribution to tissues, and removal of waste products from tissues. Blood is primarily composed of blood cells suspended in an aqueous solution of plasma. The three main types of blood cells are red blood cells (RBCs), white blood cells and platelets. Plasma is composed of water, plasma proteins, dissolved nutrients, and waste products. The average adult blood volume is about 5 L and has an average density of 1060 kg/m^3 (55).

3.1.1. Red Blood Cells

As the most abundant cell type in the blood, red blood cells (RBCs), or erythrocytes, compose approximately 99% of all blood cells at a concentration of

4.7 to 6.1 million cells/µL in humans (56). They are produced daily at a rate of 2.56×10^9 cells/kg, and have a life span of about 120 days in the circulation. RBCs play a critical role transporting oxygen from the lungs to other tissues in the body via the circulatory system. RBCs utilize hemoglobin to fix and transport oxygen and carbon dioxide in the blood. An individual molecule of hemoglobin can bind up to four molecules of oxygen and effectively transport 97% of the available oxygen to tissues (57). Hemoglobin is also responsible for the red color of erythrocytes, yielding light absorption peaks at the 275nm and 417nm wavelengths (58).

Human RBCs are anucleated cells that possess a biconcave disk shape with a diameter of 5.5 to 8.8 µm and a thickness of 2 µm at the periphery and 1 µm at the narrowest point (center). Their surface area is approximately 120 μm^2 and their volume is approximately 85 to 90 μm^3. They have a cytoskeletal structure formed by spectrin, a flexible rod-like molecule that maintains its shape, and a membrane that is composed of 40% lipid bilayer, 52% proteins, and 8% carbohydrates. Some of the most important physical features of RBCs are their high elasticity and deformability. The elastic shear modulus for RBCs at 25°C is approximately 6.8 µN/m, as measured by micropipette aspiration, while the membrane shear modulus is approximately 20 µN/m, and the area compressibility modulus is approximately 7.5 ± 2.5 µN/m. The physical parameters of RBCs allow them to circulate through the reticuloendothelial system through capillaries as small as 3 µm in diameter.

Several pathological disorders are associated with alterations in the physical parameters of RBCs. In the case of sickle cell anemia, mutations in hemoglobin result in the polymerization of hemoglobin S and subsquent distortion of the RBC morphology, including increasing the effective shear modulus of RBCs by two to three fold (59). Other hemoglobinopathies include hemoglobin C disease, hemoglobin S-C disease, and various types of thalassemia (60).

3.1.2. White Blood Cells

White blood cells, or leukocytes, which make about 1% of total blood cells, are cells of the immune system that combat infection and defend the body against foreign materials. They are grouped into three major types: granulocytes, monocytes, and lymphocytes. Granulocytes contain densely staining granules in their cytoplasm and are classified into three types: neutrophils, which make up about 5×10^9cells/L (61), eosinophils, which comprise about 4×10^7 cells/L (62), and basophils, which make up about 4×10^7 cells/L of human blood (63). Human neutrophils, at a diameter of 10–12 μm, are the most common type of granulocytes, and are produced at a rate of 2×10^{11} cells per day. They transit in the blood for approximately 5 to 7 days, during which time they constantly survey for microorganisms such as bacteria. Neutrophils target and destroy pathogens by a process termed phagocytosis, whereby bacteria are engulfed and trafficked to intracellular vesicles, where they are destroyed using degradative enzymes stored in cytoplasmic granules. As a result, neutrophils play a key role in the host innate immunity against bacterial infection. Basophils, which are 12–15 μm in diameter and eosinophils, which are 10–12 μm in diameter, are both involved in

allergic inflammatory reactions. Basophils secrete histamine to help mediate inflammatory reactions, while eosinophils destroy parasites and modulate allergic inflammatory responses (64). Monocytes, which are 7–9 μm in diameter and present in the blood at a concentration of 4×10^8 cells/L (65), mature into macrophages upon leaving the bloodstream, and share the responsibility with neutrophils of being the main phagocytic members in the body (66). In addition, during their 25 hr transit in the blood, monocytes also replenish the body's supply of dendritic cells, which specialize in presenting antigens to lymphocytes to trigger an adaptive immune response. Lymphocytes, which transit in blood for approximately 200 days, are divided into two classes that are both involved in immune responses: B-cells, which are primarily responsible for making antibodies, and T-cells, which kill virus-infected cells and regulate other leukocyte activities. B-cells circulate at a level of 2×10^9 cell/L of blood and are 7–8 μm in diameter, while T-cells circulate at a concentration of 1×10^9 cells/L of blood and are 12–15 μm in diameter (67).

Several pathologies are associated with perturbations in the physical parameters of these white blood cell populations. For instance, a reduction in the number of white blood cells, in particular neutrophils, results in leukopenia and renders individuals at higher risk for infection. In contrast, in leukemia, an abnormal increase in immature white blood cells is associated with cancer of the blood or bone marrow (24). Other diseases that develop due to aberrant quantities of leukocytes include lymphoma, which results from an overproduction of B and T

lymphocytes, and myeloma, which results from an abnormal accumulation of plasma B cells in the bone marrow (68).

3.1.3. Platelets

Platelets, or thrombocytes, are the smallest cells in the blood, with a diameter of 2 to 4 μm, a thickness of 70 to 90 Å, and a density of 1.04 to 1.08 g/mL. With a lifespan of about 5 to 9 days in humans, these cells are present in the blood at a concentration of 150 to 350 billion cells/L, and are produced by megakaryocytes at a rate of 10^{11} platelets per day (69). Platelets play a critical role in maintaining hemostasis by adhering to the lining of blood vessels upon endothelial cell injury to initiate thrombus formation (70, 71).

Platelets are anuclear, yet possess other common cellular structures such as microtubules, alpha and dense granules, mitochondria, Golgi, and lysosomes. Platelets exhibit an open canalicular system, which is a dense tubular system that plays an essential role in the rapid transport of agonists and platelet releasate to and from the cell, respectively (72). The outer glycocalyx membrane of platelets is key for the assembly of different enzyme complexes that culminate in coagulation, while the interior membrane is covered by cross-linked actin (73). Platelets are refractile, and their elastic moduli ranges from 1 and 50 kPa (74). When spread, platelet stiffness has been measured as between 1.5 to 4 kPa in the pseudonucleus, 4 kPa in the inner web, and 10 to 40 kPa in the outer web.

Several severe pathological conditions are associated with changes in the physical parameters of platelets (75). For instance, conditions such as

thrombocytopenia are associated with a dramatic drop in platelet count below 50,000cells/µL, which results in an impaired ability of patients to maintain hemostasis (76). Other conditions that are associated with altered platelet function are disseminated intravascular coagulation, myelodysplasia, Scott's Syndrome, Storage Pool disorder, Bernard Soulier Syndrome, Glanzmann's Thrombaesthenia, hemolytic anemia, hypersplendis, thrombocytosis, chronicmyelogenous leukemia, and polycythemia vera (77).

3.1.3. Plasma

Blood plasma is a light yellow, semi-transparent, aqueous solution in which blood cells are suspended. Plasma constitutes approximately 55% of the blood volume, with blood cells constituting the remaining 45%. The main components of plasma are water (90%), protein (8%), inorganic salts (0.9%), and organic substances (1.1%) (78). Proteins in the plasma such as prothrombin, fibrinogen and other coagulation factors are essential to facilitate the coagulation cascade (79), while proteins such as albumin are critical in maintaining the osmotic pressure of blood (80).

A number of clinical disorders are associated with deficiencies in blood plasma components, and can be treated following infusion of missing coagulation factors. For instance, infusion of the plasma protein Factor VIII or IX is the main treatment for FVIII- or FIX-deficient patients (hemophilia A or B), respectively (81). Other treatments using plasma include immunoglobulin treatment for patients with antibody deficiencies or antithrombin concentrates used for patients

with antithrombin deficiencies. Albumin has also been used to treat acute hypolemia (e.g. surgical blood loss, trauma, hemorrhage) as well as chronic liver disease (82).

3.2. Measurement Tools

Numerous measurement systems have been developed to analyze properties of blood cells, plasma, and blood disorders and disease. A few common techniques to measure the physical parameters of blood cells and components include atomic force microscopy (AFM), flow cytometry, microfluidics, micropipette aspiration, optical microscopy, optical tweezers, and electron microscopy (83).

3.2.1. Atomic Force Microscopy (AFM

AFM is a useful method to measure the mechanical properties of living cells, and has been widely utilized to characterize the physical properties of blood cells (84). Invented in 1986, contact AFM uses a soft cantilever probe that applies a known force or stress to a cell, and measures the deformation in order to determine the cell elastic properties (e.g., spring constant and Young's modulus) (85). The contact AFM probe typically depresses the cell surface at a constant velocity, resulting in the application of an increasing force. Contact AFM is capable of measuring forces down to 5–10 pN with a spatial resolution on the nanometer scale. Scanning AFM, which emerged a few years after contact AFM, uses a single frequency to excite the probe while being scanned across a sample to generate a three-dimensional topographical surface profile to investigate cell biophysical parameters (e.g., thickness, width, surface area, and volume).

Multifrequency AFM is a new and promising technique that improves the spatial and time resolution of traditional AFM and can measure subsurface properties through the use of multiple frequencies of the probe's oscillation (86)

3.2.2. Flow Cytometry

Flow cytometry is a non-destructive tool useful for quantifying phenotypes and sorting sizes of blood cell samples (e.g., cells, microorganisms, chromosomes and cell organelles). Flow cytometry accomplishes sorting by passing a flow stream of suspended particles single-file through a measurement station where they are illuminated by a light source. The light is scattered when it hits a particle, and analysis of the angle of scattering can reveal sample parameters (e.g., size, shape, viability, volume and density) (87). These measurements rely on the fact that a linear response in light scattering to diameter is observed over a wide range of particle sizes. Moreover, light scattering can also strongly depend on particle structure (e.g., absorbency of material, surface texture, and internal granularity), allowing for the characterization of the internal structure of cells or quantification of cell-cell interactions (88). Furthermore, flow cytometry can be used to detect fluorescent signals for the characterization of biological samples (88). Fluorescent labeling of cell surface or intracellular molecules allows for both the detection and selection of cell populations for cell sorting.

Fluorescence-activated cell sorting is a specialized flow cytometry technique that sorts heterogeneous mixtures of cells according to subtype or epitope expression based on light scattering and fluorescent characteristics. Flow cytometry-based

analysis has been extensively employed to characterize the physical parameters of RBCs, white blood cells, and platelets (89).

3.2.3. Microfluidics

The study of thrombus formation *ex vivo* can occur in closed or open systems, with or without flow (90). Microfluidic devices, which constrain fluids to a small (typically submillimeter) scale, facilitate characterization of platelet function, coagulation biology, cellular biorheology, adhesion dynamics, and pharmacology, under physiologically relevant shear flow conditions. Microfluidic devices have been developed to separate particles through the use of microelectrodes or asymmetric obstacles. The advantages of microfluidics include lower cost and complexity than flow cytometry and the ability to measure hydrodynamic cell size. Researchers and clinicians have used microfluidic devices to fractionate blood and separate white blood cells, red blood cells and plasma based on geometric parameters. Microfluidics devices are ideal for multicolor imaging of platelets, fibrin, and phosphatidylserine (91), and provide a human blood analog to mouse injury models (92). Overall, microfluidic advances offer many opportunities for research, drug testing under relevant hemodynamic conditions, and clinical diagnostics.

3.2.4. Micropipette Aspiration

Micropipette aspiration (micropipette suction) is a measurement tool capable of characterizing the mechanical properties of blood cells. With this technique, the surface of a cell is aspirated into a pipette with a known suction pressure and the

extension of the edge of the cell into the pipette or the movement of the cell away from an attachment point is measured (93). Subsequent modeling and interpretation of these measurements can be used to determine the elastic and viscous properties of cells. Capable of pressures in the range of 0.1 pN/μm^2 to atmospheric pressure, and forces from 10 pN to 10^4 nN, micropipette experiments have been utilized to characterize the mechanical properties of both soft cells (e.g., red blood cells and neutrophils) and rigid cells (e.g., endothelial cells and chondrocytes).

3.2.5. Optical Microscopy

Optical (light) microscopy has been the key tool used by researchers for visualizing and studying blood cells, blood disorders and disease. Classical optical microscopy involves passing transmitted or reflected light from a sample through a lens or series of lenses to magnify the sample for visualization (94). However, many biological samples are thin or have high reflectivity, which results in poor contrast or reduced visibility. This shortcoming has lead to development of imaging modalities (e.g., polarized light, differential interference contrast, fluorescence illumination, phase contrast imaging, and darkfield illumination) that increase contrast or color variations to improve sample visualization (95). Further, the combination of ultraviolet microscopy and microspectroscopy has been used to quantify hemoglobin concentration in red blood cells through analysis of light absorption at different wavelengths (96). Other studies have used phase retrieval methods applied to phase contrast microscopy to investigate volume, mass and density of RBCs (97) and platelet aggregates

(98, 99). Diffraction phase microscopy is another technique that utilizes principles of optical interferometric imaging combined with mathematical modeling to obtain cell mechanical parameters (e.g., spring constant, bending modulus and area modulus) (100). Diffraction phase microscopy has previously been applied to quantify thermal fluctuations of red blood cell membranes and to identify mechanical changes of red blood cells as they transform from a healthy shape to an abnormal, unhealthy shape.

3.2.6. Optical Tweezers

Mechanical properties of blood cells can also be studied using optical tweezers (laser tweezers). Optical tweezers use the intrinsic property of light to exert forces on matter to trap a bead within a beam of light. This small bead suspended in the optical trap can be adhered to a cell surface. Movement of the cell away from the bead will result in the pulling of the cell membrane. The force of extension of the cell membrane can be measured using the deflection of the bead in the optical trap perpendicular to the optical axis. Effects of Brownian motion and thermal forces cannot be avoided with optical tweezers, however, resulting in a force measurement limit of about 50 pN depending on the system. Optical tweezers represent a powerful tool for studying blood cell rheology and receptor-binding kinetics (101).

3.2.7 Electron Microscopy

Transmission electron microscopy (TEM) is achieved by passing a beam of electrons through the sample. Transmitted electrons are focused onto a high-

resolution photographic plate to create a two-dimensional image. Scanning electron microscopy (SEM), the reflection mode analog to TEM, uses backscattered electrons to reveal surface details of the sample. TEM enables imaging of samples with a magnification up to 50 million times and a resolution of 0.5 angstroms, while SEM is capable of a magnification of 2 million times and a resolution of 0.4 nm. TEM and SEM have been instrumental in visualizing the cellular constituents of blood in healthy and disease states (102). The combination of immunolabeling with TEM and/or SEM provides insight into the interaction of biomolecules within and on the surface of blood cells in normal or pathological states (103).

Three-dimensional EM imaging of blood cells has only recently been possible through the use of focused ion beam (FIB) ablation in conjunction with SEM. In FIB-SEM, a sample plane is first imaged with SEM and then that plane is removed through FIB ablation to reveal a deeper surface in the specimen. FIB-SEM has an axial resolution of 4.5 nm and a transverse resolution of 0.8 nm and currently requires tens of hours to complete image acquisition. This technology has been applied to the investigation of myosin IIA mediated organelle distribution in megakaryocytes and platelets (104). Although currently expensive and time consuming, the guiding technological principles behind FIB-SEM promise to enhance our knowledge of blood cell ultrastructure and ultimately guide our future multi-scale understanding of blood cell function.

Concluding Remarks

The development of measurement tools with resolution from the nanometer to centimeter length scales has allowed for the study of the physical parameters of the circulatory system. Together, these techniques provide a platform for the development of novel biomedical approaches for the detection, diagnosis and treatment of cardiovascular diseases.

Acknowledgments

We are grateful to Juliana Porter for technical assistance. This work was supported by the National Institutes of Health (NIH) grants U54CA143906 and R01HL101972 to O.J.T.M, R01HL095474 and R01HL103728 to M.T.H., R01HL101972-S1 to F.A.C, T32HL094294 to J.W.N., 5T32HL094294 to C.M.J., TL1TR000129 to J.Z., and the National Science Foundation (NSF) grants DGE-0925180 to J.J.G. D.C.P. is supported by an OHSU Graduate Research Fellowship and NIH grant HL093056. W.Y.L. is supported by NIH grant R01NS071116. J.Z. is supported by NSF grant DBI-1052688. S.M.B. is a Whitaker International Fellow. O.J.T.M. is an American Heart Association Established Investigator (13EIA12630000). W.Y.L. and J.J.G are ARCS Scholars.

Abbreviations

AAA	abdominal aortic aneurysm
AFM	atomic force microscopy
CT	computed tomography
EC	endothelial cell
ECG	electrocardiogram
FEA	finite element analysis
MI	myocardial infarction
MRI	magnetic resonance imaging
OCT	optical coherence tomography

PET positron emission tomography
RBC red blood cell
SEM scanning electron microscopy
TEM transmission electron microscopy
US ultrasound

References

1. Gittenberger-de Groot AC, Winter EM, Bartelings MM, Goumans MJ, DeRuiter MC, Poelmann RE. The arterial and cardiac epicardium in development, disease and repair. Differentiation. 2012 Jul; 84(1):41–53. [PubMed: 22652098]

2. Kimura K, Ieda M, Fukuda K. Development, maturation, and transdifferentiation of cardiac sympathetic nerves. Circ Res. 2012 Jan 20; 110(2):325–336. [PubMed: 22267838]

3. Simon MA. Assessment and treatment of right ventricular failure. Nat Rev Cardiol. 2013 Apr; 10(4):204–218. [PubMed: 23399974]

4. Rodeheffer RJ, Gerstenblith G, Becker LC, Fleg JL, Weisfeldt ML, Lakatta EG. Exercise cardiac output is maintained with advancing age in healthy human subjects: cardiac dilatation and increased stroke volume compensate for a diminished heart rate. Circulation. 1984 Feb; 69(2):203–213. [PubMed: 6690093]

5. Fraccarollo D, Galuppo P, Bauersachs J. Novel therapeutic approaches to post-infarction remodelling. Cardiovasc Res. 2012 May 1; 94(2):293–303. [PubMed: 22387461]

6. Motwani M, Jogiya R, Kozerke S, Greenwood JP, Plein S. Advanced cardiovascular magnetic resonance myocardial perfusion imaging: high-spatial resolution versus 3-dimensional whole-heart coverage. Circ Cardiovasc Imaging. 2013 Mar 1; 6(2):339–348. [PubMed: 23512780]

7. Drew BJ, Califf RM, Funk M, Kaufman ES, Krucoff MW, Laks MM, et al. Practice standards for electrocardiographic monitoring in hospital settings: an American Heart Association scientific statement from the Councils on Cardiovascular Nursing, Clinical Cardiology, and Cardiovascular Disease in the Young: endorsed by the International Society of Computerized Electrocardiology and the American Association of Critical-Care Nurses. Circulation. 2004 Oct 26; 110(17):2721–2746. [PubMed: 15505110]

8. Windecker S, Bax JJ, Myat A, Stone GW, Marber MS. Future treatment strategies in ST-segment elevation myocardial infarction. Lancet. 2013 Aug 17; 382(9892):644–657. [PubMed: 23953388]

9. Daniel WG, Mugge A. Transesophageal echocardiography. N Engl J Med. 1995 May 11; 332(19): 1268–1279. [PubMed: 7708072]

10. Schuleri KH, George RT, Lardo AC. Applications of cardiac multidetector CT beyond coronary angiography. Nat Rev Cardiol. 2009 Nov; 6(11):699–710. [PubMed: 19851349]

11. Catana C, Guimaraes AR, Rosen BR. PET and MR imaging: the odd couple or a match made in heaven? J Nucl Med. 2013 May; 54(5):815–824. [PubMed: 23492887]

12. Greco A, Fiumara G, Gargiulo S, Gramanzini M, Brunetti A, Cuocolo A. High-resolution positron emission tomography/computed tomography imaging of the mouse heart. Exp Physiol. 2013 Mar; 98(3):645–651. [PubMed: 23118016]

13. Johnson SG, Peters S. Advances in pharmacologic stress agents: focus on regadenoson. J Nucl Med Technol. 2010 Sep; 38(3):163–171. [PubMed: 20724531]

14. Lamb HJ, van der Meer RW, de Roos A, Bax JJ. Cardiovascular molecular MR imaging. Eur J Nucl Med Mol Imaging. 2007 Jun; 34(Suppl 1):S99–S104. [PubMed: 17505824]

15. Li X, Rooney WD, Springer CS Jr. A unified magnetic resonance imaging pharmacokinetic theory: intravascular and extracellular contrast reagents. Magn Reson Med. 2005 Dec; 54(6):1351–1359. [PubMed: 16247739]

16. Li X, Springer CS Jr, Jerosch-Herold M. First-pass dynamic contrast-enhanced MRI with extravasating contrast reagent: evidence for human myocardial capillary recruitment in adenosineinduced hyperemia. NMR Biomed. 2009 Feb; 22(2):148–157. [PubMed: 18727151]

17. Tofts PS. Modeling tracer kinetics in dynamic Gd-DTPA MR imaging. J Magn Reson Imaging. 1997 Jan-Feb;7(1):91–101. [PubMed: 9039598]

18. Tofts PS, Brix G, Buckley DL, Evelhoch JL, Henderson E, Knopp MV, et al. Estimating kinetic parameters from dynamic contrast-enhanced T(1)-weighted MRI of a diffusable tracer: standardized quantities and symbols. J Magn Reson Imaging. 1999 Sep; 10(3):223–332. [PubMed: 10508281]

19. Nacif MS, Zavodni A, Kawel N, Choi EY, Lima JA, Bluemke DA. Cardiac magnetic resonance imaging and its electrocardiographs (ECG): tips and tricks. Int J Cardiovasc Imaging. 2012 Aug; 28(6):1465–1475. [PubMed: 22033762]

20. Sumpio BE, Riley JT, Dardik A. Cells in focus: endothelial cell. Int J Biochem Cell Biol. 2002 Dec; 34(12):1508–1512. [PubMed: 12379270]

21. Busse R, Fleming I. Vascular endothelium and blood flow. Handb Exp Pharmacol. 2006; (176 Pt 2):43–78. [PubMed: 16999224]

22. Vartanian KB, Berny MA, McCarty OJ, Hanson SR, Hinds MT. Cytoskeletal structure regulates endothelial cell immunogenicity independent of fluid shear stress. Am J Physiol Cell Physiol. 2010 Feb; 298(2):C333–C341. [PubMed: 19923423]

23. Vartanian KB, Kirkpatrick SJ, McCarty OJ, Vu TQ, Hanson SR, Hinds MT. Distinct extracellular matrix microenvironments of progenitor and carotid endothelial cells. J Biomed Mater Res A. 2009 Nov; 91(2):528–539. [PubMed: 18985765]

24. Cines DB, Pollak ES, Buck CA, Loscalzo J, Zimmerman GA, McEver RP, et al. Endothelial cells in physiology and in the pathophysiology of vascular disorders. Blood. 1998 May 15; 91(10): 3527–3561. [PubMed: 9572988]

25. Anderson DE, Hinds MT. Extracellular matrix production and regulation in micropatterned endothelial cells. Biochem Biophys Res Commun. 2012 Oct 12; 427(1):159–164. [PubMed: 22995321]

26. Zilversmit DB. Atherogenesis: a postprandial phenomenon. Circulation. 1979 Sep; 60(3):473–485. [PubMed: 222498]

27. Berliner JA, Navab M, Fogelman AM, Frank JS, Demer LL, Edwards PA, et al. Atherosclerosis: basic mechanisms. Oxidation, inflammation, and genetics. Circulation. 1995 May 1; 91(9):2488– 2496. [PubMed: 7729036]

28. van der Wal AC, Becker AE, van der Loos CM, Das PK. Site of intimal rupture or erosion of thrombosed coronary atherosclerotic plaques is characterized by an inflammatory process irrespective of the dominant plaque morphology. Circulation. 1994 Jan; 89(1):36–44. [PubMed: 8281670]

29. Gijsen F, van der Giessen A, van der Steen A, Wentzel J. Shear stress and advanced atherosclerosis in human coronary arteries. J Biomech. 2013 Jan 18; 46(2):240–247. [PubMed: 23261245]

30. Venkatasubramaniam AK, Fagan MJ, Mehta T, Mylankal KJ, Ray B, Kuhan G, et al. A

comparative study of aortic wall stress using finite element analysis for ruptured and non-ruptured abdominal aortic aneurysms. Eur J Vasc Endovasc Surg. 2004 Aug; 28(2):168–176. [PubMed: 15234698]

31. Berger SA, Jou LD. Flows in Stenotic Vessels. Annual Review of Fluid Mechanics. 2000; 32(1): 347–382.

32. Lu L, Zhang LJ, Poon CS, Wu SY, Zhou CS, Luo S, et al. Digital subtraction CT angiography for detection of intracranial aneurysms: comparison with

three-dimensional digital subtraction angiography. Radiology. 2012 Feb; 262(2):605–612. [PubMed: 22143927]

33. Otto CM, Pearlman AS, Comess KA, Reamer RP, Janko CL, Huntsman LL. Determination of the stenotic aortic valve area in adults using Doppler echocardiography. J Am Coll Cardiol. 1986 Mar; 7(3):509–517. [PubMed: 3950230]

34. Mintz GS, Nissen SE, Anderson WD, Bailey SR, Erbel R, Fitzgerald PJ, et al. American College of Cardiology Clinical Expert Consensus Document on Standards for Acquisition, Measurement and Reporting of Intravascular Ultrasound Studies (IVUS). A report of the American College of Cardiology Task Force on Clinical Expert Consensus Documents. J Am Coll Cardiol. 2001 Apr; 37(5):1478–1492. [PubMed: 11300468]

35. Park SJ, Ahn JM, Kang SJ. Unprotected left main percutaneous coronary intervention: integrated use of fractional flow reserve and intravascular ultrasound. J Am Heart Assoc. 2012 Dec. 1(6):e004556. [PubMed: 23316329]

36. Wrenn SP, Dicker SM, Small EF, Dan NR, Mleczko M, Schmitz G, et al. Bursting bubbles and bilayers. Theranostics. 2012; 2(12):1140–1159. [PubMed: 23382772]

37. McCarty OJ, Conley RB, Shentu W, Tormoen GW, Zha D, Xie A, et al. Molecular imaging of activated von Willebrand factor to detect high-risk atherosclerotic phenotype. JACC Cardiovasc Imaging. 2010 Sep; 3(9):947–955. [PubMed: 20846630]

38. Kiessling F, Fokong S, Koczera P, Lederle W, Lammers T. Ultrasound microbubbles for molecular diagnosis, therapy, and theranostics. J Nucl Med. 2012 Mar; 53(3):345–348. [PubMed: 22393225]

39. Lindner JR, Sinusas A. Molecular imaging in cardiovascular disease: Which methods, which diseases? J Nucl Cardiol. 2013 Oct 4.

40. Subhash HM, Xie H, Smith JW, McCarty OJ. Optical detection of indocyanine green encapsulated biocompatible poly (lactic-co-glycolic) acid nanoparticles with photothermal optical coherence tomography. Opt Lett. 2012 Mar 1; 37(5):981–983. [PubMed: 22378459]

41. Yelin R, Yelin D, Oh WY, Yun SH, Boudoux C, Vakoc BJ, et al. Multimodality optical imaging of embryonic heart microstructure. J Biomed Opt. 2007 Nov-Dec;12(6):064021. [PubMed: 18163837]

42. Shi L, Goenezen S, Haller S, Hinds MT, Thornburg KL, Rugonyi S. Alterations in pulse wave propagation reflect the degree of outflow tract banding in HH18 chicken embryos. Am J Physiol Heart Circ Physiol. 2013 Aug 1; 305(3):H386–H396. [PubMed: 23709601]

43. Markl M, Kilner PJ, Ebbers T. Comprehensive 4D velocity mapping of the heart and great vessels by cardiovascular magnetic resonance. J Cardiovasc Magn Reson. 2011; 13:7. [PubMed: 21235751]

44. Halpern W, Kelley M. In vitro methodology for resistance arteries. Blood Vessels. 1991; 28(1–3): 245–251. [PubMed: 1825797]

45. Golding EM, Robertson CS, Bryan RM Jr. Comparison of the myogenic response in rat cerebral arteries of different calibers. Brain Res. 1998 Mar 2; 785(2):293–298. [PubMed: 9518656]

46. Kuo L, Davis MJ, Chilian WM. Myogenic activity in isolated subepicardial and subendocardial coronary arterioles. Am J Physiol. 1988 Dec; 255(6 Pt 2):H1558–H1562. [PubMed: 2462367]

47. Duling BR, Gore RW, Dacey RG Jr, Damon DN. Methods for isolation, cannulation, and in vitro study of single microvessels. Am J Physiol. 1981 Jul; 241(1):H108–H116. [PubMed: 7195654]

48. Adams SR. How calcium indicators work. Cold Spring Harb Protoc. 2010 Mar.2010(3) pdb top70.

49. Adams DS, Levin M. General principles for measuring resting membrane potential and ion concentration using fluorescent bioelectricity reporters. Cold Spring Harb Protoc. 2012 Apr; 2012(4):385–397. [PubMed: 22474653]

50. Homma R, Baker BJ, Jin L, Garaschuk O, Konnerth A, Cohen LB, et al. Wide-field and twophoton imaging of brain activity with voltage- and calcium-sensitive dyes. Methods Mol Biol. 2009; 489:43–79. [PubMed: 18839087]

51. Vorp DA. Biomechanics of abdominal aortic aneurysm. J Biomech. 2007; 40(9):1887–1902. [PubMed: 17254589]

52. Henebiens M, Vahl A, Koelemay MJ. Elective surgery of abdominal aortic aneurysms in octogenarians: a systematic review. J Vasc Surg. 2008 Mar; 47(3):676–681. [PubMed: 18207352]

53. Volokh KY. Comparison of biomechanical failure criteria for abdominal aortic aneurysm. J Biomech. 2010 Jul 20; 43(10):2032–2034. [PubMed: 20381050]

54. Ophir J, Moriya T, Yazdi Y. A single transducer transaxial compression technique for the estimation of sound speed in biological tissues. Ultrason Imaging. 1991 Jul; 13(3):269–279. [PubMed: 1957424]

55. Wagner DD, Frenette PS. The vessel wall and its interactions. Blood. 2008 Jun 1; 111(11):5271–5281. [PubMed: 18502843]

56. Dzierzak E, Philipsen S. Erythropoiesis: development and differentiation. Cold Spring Harb Perspect Med. 2013 Apr.3(4):a011601. [PubMed: 23545573]

57. Marks PA, Kovach JS. Development of mammalian erythroid cells. Curr Top Dev Biol. 1966; 1:213–252. [PubMed: 4944303]

58. Rubinstein DL, Ravikovich HM. Absorption spectrum of haemoglobin in red cells. Nature. 1946 Dec 28.158(4026):952. [PubMed: 20277889]

59. Poillon WN, Kim BC, Castro O. Intracellular hemoglobin S polymerization and the clinical severity of sickle cell anemia. Blood. 1998 Mar 1; 91(5):1777–1783. [PubMed: 9473246]

60. Thom CS, Dickson CF, Gell DA, Weiss MJ. Hemoglobin variants: biochemical properties and clinical correlates. Cold Spring Harb Perspect Med. 2013 Mar.3(3):a011858. [PubMed: 23388674]

61. Mocsai A. Diverse novel functions of neutrophils in immunity, inflammation, and beyond. J Exp Med. 2013 Jul 1; 210(7):1283–1299. [PubMed: 23825232]

62. Fulkerson PC, Rothenberg ME. Targeting eosinophils in allergy, inflammation and beyond. Nat Rev Drug Discov. 2013 Feb; 12(2):117–129. [PubMed: 23334207]

63. Voehringer D. Protective and pathological roles of mast cells and basophils. Nat Rev Immunol. 2013 May; 13(5):362–375. [PubMed: 23558889]

64. McCarty OJ, Tien N, Bochner BS, Konstantopoulos K. Exogenous eosinophil activation converts PSGL-1-dependent binding to CD18-dependent stable adhesion to platelets in shear flow. Am J Physiol Cell Physiol. 2003 May; 284(5):C1223–C1234. [PubMed: 12529243]

65. Ahn KC, Jun AJ, Pawar P, Jadhav S, Napier S, McCarty OJ, et al. Preferential binding of platelets to monocytes over neutrophils under flow. Biochem Biophys Res Commun. 2005 Apr 1; 329(1): 345–355. [PubMed: 15721313]

66. Pardali E, Waltenberger J. Monocyte function and trafficking in cardiovascular disease. Thromb Haemost. 2012 Nov; 108(5):804–811. [PubMed: 22918193]

67. Litman GW, Rast JP, Fugmann SD. The origins of vertebrate adaptive immunity. Nat Rev Immunol. 2010 Aug; 10(8):543–553. [PubMed: 20651744]

68. Younes A. Beyond chemotherapy: new agents for targeted treatment of lymphoma. Nat Rev Clin Oncol. 2011 Feb; 8(2):85–96. [PubMed: 21151205]

69. Machlus KR, Italiano JE Jr. The incredible journey: From megakaryocyte development to platelet formation. J Cell Biol. 2013 Jun 10; 201(6):785–796. [PubMed: 23751492]

70. Aslan JE, Itakura A, Gertz JM, McCarty OJ. Platelet shape change and spreading. Methods Mol Biol. 2012; 788:91–100. [PubMed: 22130702]

71. Watson SP, Auger JM, McCarty OJ, Pearce AC. GPVI and integrin alphaIIbbeta3 signaling in platelets. J Thromb Haemost. 2005 Aug; 3(8):1752–1762. [PubMed: 16102042]

72. Fox JE. Cytoskeletal proteins and platelet signaling. Thromb Haemost. 2001 Jul; 86(1):198–213. [PubMed: 11487008]

73. Aslan JE, McCarty OJ. Rho GTPases in platelet function. J Thromb Haemost. 2013 Jan; 11(1):35–46. [PubMed: 23121917]

74. Carr ME Jr. Development of platelet contractile force as a research and clinical measure of platelet function. Cell Biochem Biophys. 2003; 38(1):55–78. [PubMed: 12663942]

75. Heemskerk JW, Bevers EM, Lindhout T. Platelet activation and blood coagulation. Thromb Haemost. 2002 Aug; 88(2):186–193. [PubMed: 12195687]

76. Tucker EI, Marzec UM, Berny MA, Hurst S, Bunting S, McCarty OJ, et al. Safety and antithrombotic efficacy of moderate platelet count reduction by thrombopoietin inhibition in primates. Sci Transl Med. 2010 Jun 23.2(37):37ra45.

77. Hayward CP, Moffat KA, Liu Y. Laboratory investigations for bleeding disorders. Semin Thromb Hemost. 2012 Oct; 38(7):742–752. [PubMed: 23011792]

78. Tullis JL, Pennell RB. Transfusion of specific plasma components. Annu Rev Med. 1968; 19:233–246. [PubMed: 4172726]

79. Berny MA, Munnix IC, Auger JM, Schols SE, Cosemans JM, Panizzi P, et al. Spatial distribution of factor, Xa thrombin, and fibrin(ogen) on thrombi at venous shear. PLoS One. 2010; 5(4):e10415. [PubMed: 20454680]

80. Kolev K, Machovich R. Molecular and cellular modulation of fibrinolysis. Thromb Haemost. 2003 Apr; 89(4):610–621. [PubMed: 12669114]

81. Hedner U, Ezban M. Tissue factor and factor VIIa as therapeutic targets in disorders of hemostasis. Annu Rev Med. 2008; 59:29–41. [PubMed: 17845136]

82. Dellinger RP, Levy MM, Rhodes A, Annane D, Gerlach H, Opal SM, et al. Surviving sepsis campaign: international guidelines for management of

severe sepsis and septic shock-2012. Crit Care Med. 2013 Feb; 41(2):580–637. [PubMed: 23353941]

83. Stewart MP, Toyoda Y, Hyman AA, Muller DJ. Tracking mechanics and volume of globular cells with atomic force microscopy using a constant-height clamp. Nat Protoc. 2012 Jan; 7(1):143–154. [PubMed: 22222789]

84. Hanley W, McCarty O, Jadhav S, Tseng Y, Wirtz D, Konstantopoulos K. Single molecule characterization of P-selectin/ligand binding. J Biol Chem. 2003 Mar 21; 278(12):10556–10561. [PubMed: 12522146]

85. Binnig G, Quate CF, Gerber C. Atomic force microscope. Physical review letters. 1986; 56(9):930. [PubMed: 10033323]

86. Garcia R, Herruzo ET. The emergence of multifrequency force microscopy. Nat Nanotechnol. 2012 Apr; 7(4):217–226. [PubMed: 22466857]

87. Nicoletti I, Migliorati G, Pagliacci MC, Grignani F, Riccardi C. A rapid and simple method for measuring thymocyte apoptosis by propidium iodide staining and flow cytometry. J Immunol Methods. 1991 Jun 3; 139(2):271–279. [PubMed: 1710634]

88. McCarty OJ, Jadhav S, Burdick MM, Bell WR, Konstantopoulos K. Fluid shear regulates the kinetics and molecular mechanisms of activation-dependent platelet binding to colon carcinoma cells. Biophys J. 2002 Aug; 83(2):836–848. [PubMed: 12124268]

89. Burdick MM, McCarty OJ, Jadhav S, Konstantopoulos K. Cell-cell interactions in inflammation and cancer metastasis. IEEE Eng Med Biol Mag. 2001 May-Jun;20(3):86–91. [PubMed:11446216]

90. Colace TV, Tormoen GW, McCarty OJ, Diamond SL. Microfluidics and coagulation biology. Annu Rev Biomed Eng. 2013 Jul 11.15:283–303. [PubMed: 23642241]

91. White-Adams TC, Berny MA, Patel IA, Tucker EI, Gailani D, Gruber A, et al. Laminin promotes coagulation and thrombus formation in a factor XII-dependent manner. J Thromb Haemost. 2010 Jun; 8(6):1295–1301. [PubMed: 20796202]

92. Gutierrez E, Petrich BG, Shattil SJ, Ginsberg MH, Groisman A, Kasirer-Friede A. Microfluidic devices for studies of shear-dependent platelet adhesion. Lab Chip. 2008 Sep; 8(9):1486–1495. [PubMed: 18818803]

93. Hochmuth RM. Micropipette aspiration of living cells. J Biomech. 2000 Jan; 33(1):15–22. [PubMed: 10609514]

94. Betzig E, Trautman JK, Harris TD, Weiner JS, Kostelak RL. Breaking the diffraction barrier: optical microscopy on a nanometric scale. Science. 1991 Mar 22; 251(5000):1468–1470. [PubMed: 17779440]

95. Dawe GS, Schantz J-T, Abramowitz M, Davidson MW, Hutmacher DW. Light microscopy. Techniques in Microscopy for Biomedical Applications. 2006; 2:9.

96. Lakowicz, JR. Principles of fluorescence spectroscopy: Springer. 2009.

97. Phillips KG, Jacques SL, McCarty OJ. Measurement of single cell refractive index, dry mass, volume, and density using a transillumination microscope. Phys Rev Lett. 2012 Sep 14.109(11):118105. [PubMed: 23005682]

98. Baker SM, Phillips KG, McCarty OJ. Development of a label-free imaging technique for the quantification of thrombus formation. Cell Mol Bioeng. 2012 Dec; 5(4):488–492. [PubMed:23585817]

99. Baker-Groberg SM, Phillips KG, McCarty OJ. Quantification of volume, mass, and density of thrombus formation using brightfield and differential interference contrast microscopy. J Biomed Opt. 2013 Jan.18(1):16014. [PubMed: 23348747]

100. Popescu G, Park Y, Choi W, Dasari RR, Feld MS, Badizadegan K. Imaging red blood cell dynamics by quantitative phase microscopy. Blood Cells Mol Dis. 2008 Jul-Aug;41(1):10–16. [PubMed: 18387320]

101. Sleep J, Wilson D, Simmons R, Gratzer W. Elasticity of the red cell membrane and its relation to hemolytic disorders: an optical tweezers study. Biophys J. 1999 Dec; 77(6):3085–3095. [PubMed: 10585930]

102. Clauser S, Cramer-Borde E. Role of platelet electron microscopy in the diagnosis of platelet disorders. Semin Thromb Hemost. 2009 Mar; 35(2):213–223. [PubMed: 19408194]

103. Sjollema KA, Schnell U, Kuipers J, Kalicharan R, Giepmans BN. Correlated light microscopy and electron microscopy. Methods Cell Biol. 2012; 111:157–173. [PubMed: 22857928]

104. Pertuy F, Eckly A, Weber J, Proamer F, Rinckel JY, Lanza F, et al. Myosin IIA is critical for organelle distribution and F-actin organization in megakaryocytes and platelets. Blood. 2013 Nov 15.

Immunopathology of Japanese macaque encephalomyelitis is similar to multiple sclerosis

Tiffany C. Blair, Minsha Manoharan, Stephanie D. Rawlings-Rhea, Ian J. Tagge, Steven G. Kohama, Julie Hollister-Smith, Betsy Ferguson, Randall L. Woltjer, Meredith C. Frederick, James Pollaro, William d. Rooney, Larry S. Sherman, Dennis N. Bourdette, Scott W. Wong

Originally published in:

Journal of Neuroimmunology, (IN PRESS)

DOI:10.1016/j.jneuroim.2015.11.026

Ian Tagge acquired, processed, and analyzed MRI data, created Figure 1, and contributed to editing the manuscript before submission.

Abstract

Japanese macaque encephalomyelitis (JME) is an inflammatory demyelinating disease that occurs spontaneously in a colony of Japanese macaques (JM) at the Oregon National Primate Research Center. Animals with JME display clinical signs resembling multiple sclerosis (MS), and magnetic resonance imaging reveals multiple T_2-weighted hyperintensities and gadolinium-enhancing lesions in the central nervous system (CNS). Here we undertook studies to

determine if JME possesses features of an immune-mediated disease in the CNS. Comparable to MS, the CNS of animals with JME contain active lesions positive for IL-17, CD4 + T cells with Th1 and Th17 phenotypes, CD8 + T cells, and positive CSF findings.

1. Introduction

Multiple sclerosis (MS) is widely believed to be an immune-mediated disease that leads to multifocal destruction of the myelin and to a lesser extent axonal degeneration. It is proposed that MS pathogenesis is driven by auto-reactive T cells that aberrantly gain access to the central nervous system (CNS). Upon entry to the CNS, these T cells become reactivated when they recognize components of myelin, setting in motion a cascade of inflammatory events that ultimately lead to demyelination and axonal injury (Goverman, 2009). The mechanisms that trigger these T cells to become pathogenic are poorly understood, but genetic and environmental triggers are thought to play an important role (International Multiple Sclerosis Genetics et al., 2011). T cells expressing the cytokines IL-17 or IFN-γ appear to be key players in disease development, as studies have shown that these populations are present in MS lesions (Kebir et al., 2009, Kebir et al., 2007 and Tzartos et al., 2008). This highlights a central role for helper T cells (Th) in MS progression, and emphasizes the need to understand the function of these T cellsubsets in order to further unravel the etiology of the disease (Waisman et al., 2015). Active MS lesions also contain CD8 + T cells, macrophages filled with myelin debris andreactive astrocytes (Popescu and Lucchinetti, 2012). Beyond the CNS,

groups have reported an increased prevalence of auto-reactive myelin-specific T cells in the peripheral blood of MS patients (Kerlero De Rosbo et al., 1993 and Hedegaard et al., 2008). However, conflicting results have been published showing that both healthy controls (HC) and MS patients have similar frequencies of these T cells in the periphery (Hellings et al., 2001 and Hellings et al., 2002). These data hint at the role of defective regulation in controlling these potentially pathogenic T cells in MS patients as compared to HC.

B cells and plasma cells also play a significant role in MS immunopathogenesis, as their products are frequently detected in MS lesions and cerebrospinal fluid (CSF) (Berer et al., 2011, Probstel et al., 2015 and Serafini et al., 2004). Importantly, the detection ofintrathecally synthesized oligoclonal IgG bands (OCBs) in the CSF is a commonly used paraclinical measure to diagnose MS when utilized in conjunction with MRI and clinical history (Petzold, 2013 and Bonnan, 2015). Further substantiating the role of B cells in MS are clinical trials with the anti-CD20 monoclonal antibodies, rituximab and ocrelizumab, a treatment that resulted in reduced inflammatory brain lesions as detected by MRI and decreased clinical relapses in subjects with relapsing MS (Hauser et al., 2008).

Animal models that mimic the immune-mediated aspects of MS are valuable in elucidating mechanisms associated with disease pathogenesis. The most widely utilized animal model to study MS is experimental autoimmune encephalomyelitis (EAE). EAE can be induced in a variety of species, including mice, rats and nonhuman primates (NHP). EAE induction involves immunizing

animals with myelin proteins or peptides in Freund's complete adjuvant and results in T cell responses to myelin, focal inflammatory lesions within the CNS and ultimately leads to paralysis. EAE recapitulates the T cell-mediated aspects of MS, as studies find Th1 and Th17 cells are necessary for the induction of EAE (Jager et al., 2009). However, while EAE studies have yielded useful insight into several facets of MS pathogenesis, this model has well recognized limitations. First, immunizing animals with myelin proteins or peptides artificially induces the disease EAE, while MS occurs as a spontaneous disease. Second, EAE is studied in inbred mouse strains and this is in large contrast to MS, which occurs, in a heterogeneous population with highly variable genetic diversity. Third, the relatively small size of mice constrains the imaging that can be performed using MRI, whereas an array of sophisticated MRI techniques are available to study MS. An animal model that overcomes these limitations would be of considerable use in advancing our understanding of MS.

In 2011, we described a spontaneous inflammatory CNS demyelinating disease, called Japanese macaque encephalomyelitis (JME), that occurs in 1% to 3% of the animals in our colony of Japanese macaques (JM, *Macaca fuscata*) at the Oregon National Primate Research Center (ONPRC) (Axthelm et al., 2011). We proposed that JME was a spontaneous NHP model for MS based on the appearance of brain lesions as detectable with MRI and the presence of multifocal demyelinating lesions as observed usinghistology. Here, we present evidence that JME shares many immunopathological similarities with MS. Specifically, we demonstrate that JME lesions possess similar

immunohistopathological features as MS lesions, including active demyelination and significant T- and B-cell germinal areas surrounding perivascular and periventricular spaces. Importantly, immunofluorescence analysis revealed that within demyelinating lesions, both astrocytes and oligodendrocytes stain positively for interleukin 17 (IL-17). Moreover, multicolor flow cytometry analysis of infiltrating T cells revealed both $CD4^+$ and $CD8^+$ T cells that expressed IL-17 or IFN-γ, and in some instances both cytokines, similar to what has been shown in MS. Finally, we show that animals with JME have positive CSF findings that include an elevated IgG index and 2 or more oligoclonal bands, a common finding in MS (Polman et al., 2011). Collectively, these data support JME as a unique NHP model for a MS-like disease, which can be utilized to offer new insights into the pathogenesis of MS.

2. Materials and methods

2.1. Animals and animal procedures

All animal protocols and procedures were reviewed and approved by the ONPRC Institutional Animal Care and Use Committee. The ONPRC is an Association for Assessment and Accreditation of Laboratory Animal Care (AAALAC) International accredited research facility and conforms to National Institutes of Health guidelines on the ethical use of animals in research. JM exhibiting neurological dysfunction and symptoms associated with JME were brought in for physical examination and provided supportive care, and then scanned by MRI on a 3 T Siemens TIM Trio MR instrument as previously described

(Axthelm et al., 2011). Animals with progressive disease were humanely euthanized via exsanguination, with blood and CSF collection. The blood was immediately processed for plasma collection and peripheral blood mononuclear cell(PBMC) isolation. The CSF and serum were archived at –80 °C, while PBMCs were cryopreserved. Animals were subsequently perfused with sterile PBS through carotidcannulation, the brain was removed and immersed fixed in 4% buffered paraformaldehyde solution. For some necropsies, lesion areas that were detected by MRI were collected from affected areas after the PBS perfusion step in order to obtain fresh brain tissue for lymphocyte analysis. A portion of each lesion was placed in RPMI media supplemented with 10% fetal bovine serum and processed as described to isolate CNS-infiltrating mononuclear cells (CNS-MNCs) (Jager et al., 2009). In these cases the remainder of the brain was also immersed fixed in 4% neutral buffered paraformaldehyde solution for histopathological analysis. For comparisons to JME cases, blood and cisternal cerebrospinal fluid (CSF) samples were also collected from healthy controls (HC) after sedation with Telazol during routine physical examinations, and then processed as above. Each HC was subsequently given Carprofen (4 mg/kg) subcutaneously to minimize discomfort.

2.2. Histopathological examination

Fixed tissue was processed for paraffin embedding and subsequent histology. Fixed sections (0.5 mM) from the CNS were prepared and stained with Luxol fast blue (LFB) and hematoxylin and eosin (H&E) to visualize demyelinating regions and infiltrating inflammatory cells. Sections containing lesions were treated

essentially as described previously (Axthelm et al., 2011). For antigen detection analysis, the sections were deparaffinized, blocked with 10% goat serum and 5% bovine serum albumin, andendogenous peroxidase was quenched by standard techniques. Slides were treated with primary antibodies overnight at 4 °C and then processed for color detection orimmunofluorescence. Commercially available primary antibodies were used to detect the following cellular antigens and cell types: myelin basic protein (MBP, mouse anti-MBP, clone SMI 99; Covance, Princeton, NJ, 1:500), glial fibrillary acidic protein (GFAP, rabbit polyclonal anti-GFAP, RPCA-GFAP, EnCor Biotechnology, Gainsville, FL, 1:500),oligodendrocytes (rabbit anti-olig-2, AB9610, Millipore, Billerica, MA, 1:200), activatedmicroglia (rabbit anti-IBA-1, 019–19,741, Wako, Richmond, VA, 1:300), macrophages(mouse anti-human CD163, clone EDHu-1, AbD Serotec, Hercules, CA, 1:100), T cells(rabbit anti-human CD3, Dako, Carpinteria, CA, 1:200), B cells (mouse anti-CD20, clone L26, Dako, 1:200), activated complement C3d (rabbit polyclonal anti-3Cd, AB15981, Abcam, Cambridge, MA, 1:400) and IL-17 (mouse anti-IL17 F, clone 4H1629.1 Rockland, MD, 1:100).

For immunohistochemistry, detection of biotinylated secondary antibodies was performed with peroxidase ABC (Elite kit, Vector Laboratories, San Carlos, CA) and visualization with DAB (Dako) for CD163 and activated complement 3Cd, and Vector SG for MBP (Vector Laboratories). For immunofluorescence detection, secondary biotinylated goat anti-mouse (Vector Laboratories) or goat anti-rabbit IgG (H + L) (Vector Laboratories) were used, followed by Elite ABC kit and further stained with streptavidin Alexa 488 (Molecular Probes, Eugene, OR)

and streptavidin Alexa 594 (Molecular Probes), respectively, to visualize the antigens of interest. The sections were counterstained with 4,6′-diamino-2-phenylindole dihydrochloride (DAPI) (1:5000) and covered with Prolong gold anti-fade medium (Invitrogen, Carlsbad, CA) or Omnimount (National Diagnostics, Atlanta, Georgia). Sections were examined using a Zeiss Axio Imager M1 microscope (Carl Zeiss, Thornwood, NY) using Plan NeoFluar objective lenses (2.5 ×/0.5 NA and 40 ×/0.75 NA). Optical images were obtained with standard conditions of illumination and exposure on a Zeiss Axiocam camera (Carl Zeiss). Sections were routinely stained with isotype control monoclonal antibodies and the appropriate secondary antibodies, or secondary antibodies alone as negative controls. Normal JM CNS tissue was also stained to ensure specificity of the primary antibodies. An experienced neuropathologist examined the stained sections.

2.3. CNS-MNC stimulation and flow cytometry analysis

Freshly purified CNS-MNCs were promptly stimulated with a cocktail of phorbol-12-myristate-13 acetate (PMA) and Ionomycin that included BrefeldinA (Leukocyte Activation Cocktail with BD GolgiPlug, BD Biosciences, San Jose, CA) for 6 h (Slywester et al., 2014). After stimulation CNS-MNCs were stained with CD4 (RPA-T4, eBioscience, San Diego, CA), CD8β (2ST8.5H7, Beckman Coulter, Brea, CA) and in some instances CD3 (SP34-2, BD Biosciences). Cells were subsequently fixed and permeabilized using fixation buffer and permeabilization buffer (Biolegend, San Diego, CA). Intracellularcytokine staining was performed using IL-17A (eBio64CAP17, eBioscience) and IFN-γ (B27, BD

Biosciences). All flow cytometry data were acquired on LSR II (BD Biosciences) and analyzed using FlowJo (Tree Star, Ashland, OR).

2.4. Intrathecal IgG analysis

Quantification of IgG and albumin in paired CSF and plasma samples were performed at least twice in duplicate using a human IgG enzyme-linked immunosorbent assay (ELISA)alkaline phosphatase (ALP) kit (Mabtech, Cincinnati, OH) and a QuantiChrom BCG Albumin Assay Kit (BioAssay Systems, Hayward, CA), respectively. The CSF IgG index was calculated for all animals using the following formula (CSF IgG/CSF albumin)/(serum IgG/serum albumin) (Link and Tibbling, 1977). We defined a high CSF IgG index value as ≥ 1.0, which was derived by adding two standard deviations (SD) to the HC mean. For OCBs analysis, paired unconcentrated CSF and diluted plasma samples were resolved by isoelectric focusing (IEF) and proteins were transferred and immunoblotted to identify IgG bands (Fortini et al., 2003). Three separate scientists evaluated the blots in a blinded fashion.

2.5. Statistical analysis

CSF data from JME and HC were analyzed for statistical analysis using GraphPad Prizm (GraphPad Software, La Jolla, CA), and significant differences in the means were determined by an unpaired *t* test, with *p* values of ≤ 0.05 considered significant.

3. Results

3.1. JME lesions possess histopathological features resembling MS

We previously reported that JME lesions contain significant T cell and macrophageinfiltrates (Axthelm et al., 2011). To determine if these lesions displayed immunological signatures correlating with an immune-mediated disease, we evaluated a cohort of 11 Japanese macaques (JM) that presented with clinical signs of JME (Table 1). MRI scanswere performed on all 11 animals and 2 cases are shown in Fig. 1. A MRI of the brain and upper cord was performed on JM 22019 1 day after presentation with acute signs of JME. The T_2-weighted axial image in Fig. 1A showed both diffuse and hyperintense areas in the cerebellum. The post-gadolinium T_1-weighted image revealed a single area of focal contrast enhancement in the white matter (WM) of the cerebellum when compared to the pre-gadolinium image (Fig. 1B). JM 30760 underwent an MRI 1 day after presentation of acute JME signs and the T_2-weighted image in Fig. 1C showed a hyperintense area in the internal capsule. Post-gadolinium T_1-weighted image revealed a single area of focal contrast enhancement corresponding to the same area identified by the T_2-weighted image (Fig. 1D). Similar MRI abnormalities were observed in the other 9 cases of JME, with the cerebellum being the most common area of the brain affected (8/11 cases), followed by the cervical spinal cord (5/11 cases).

To characterize the neuropathology associated with JME, CNS tissues were collected from all of the animals and regions exhibiting demyelination were identified by histopathological examination using luxol fast blue (LFB) and hematoxylin-eosin (H&E) stain. Shown in Fig. 2A, B and C are low magnification

images of the cerebellar lesionisolated from JM 22019, and internal capsule lesions from JMs 30,760 and 30,773, respectively. Each lesion reveals areas of myelin loss as noted by minimal to no LFB positive staining. A large pronounced perivascular lymphocytic cuff is seen adjacent to the demyelinated lesion isolated from JM 22019 (Fig. 2A), and the internal capsule lesion of JM 30760 revealed a vascularized area with focal concentrations of lymphocytesforming perivascular cuffs (Fig. 2B). Similar findings were

Table 1. Animal history and condition

Animal ID	JME[a]/gadolinium+ MRI lesions	Age (years/days)	Gender	Histopathology (CD163/MBP)	IL-17+ staining
13221[b]	JME/pons and peduncule/cerebellum/ spinal cord	26y/50d	F	$CD163^+/MBP^+$	$CD3^+/Olig2^+$
19615	JME/cerebellum/brain stem/Cerebral white matter/spinal cord	14y/103d	M	$CD163^+/MBP^+$	CD3+/Olig2+
22019	JME/cerebellum/brain stem/ spinal cord	13y/186d	F	$CD163^+/MBP^+$	$CD3^+/Olig2^+$
27624	JME/corpus callosum /cerebellum/internal capsule	6y/12d	F	CD163+/MBP-	$CD3^+$
31522	JME/pons and peduncule/cerebellum/ cerebral white matter	2y/293d	F	$CD163^+/MBP^+$	Olig2+
26174[b]	JME/cerebellum/brain stem/spinal cord	2y/229d	M	$CD163^+/MBP^+$	$CD3^+/Olig2^+/GFAP^+$
31852	JME/midbrain to subcortical/spinal cord	1y/287d	F	$CD163^+/MBP^+$	$Olig2^+$
30493	JME/internal capsule	1y/282d	M	$CD163^+/MBP^+$	Not detected
30773	JME/cerebellum/ cerebral white matter	1y/074d	M	$CD163^+/MBP^+$	CD3+/Olig2+/ GFAP+
31509	JME/bilateral cerebellum	1y/126d	M	$CD163^+/MBP^-$	$CD3^+$
30760	JME/internal capsule	1y/105d	F	$CD163^+/MBP^+$	$CD3^+/Olig2^+/GFAP^+$

[a]JME was reported previously (Axthelm et al., 2011). Clinical signs included ataxia, paralysis or paresis of one or more limbs, and ocular abnormalities.

[b]MRI from these animals' CNS were previously reported (Axthelm et al., 2011).

observed in the internal capsule lesion of JM 30773 which affected the optic tract/lateral geniculate nucleus and revealed prominent immune cell aggregates in the periventricular space (Fig. 2C). These findings are consistent with our earlier characterization of JME lesions.

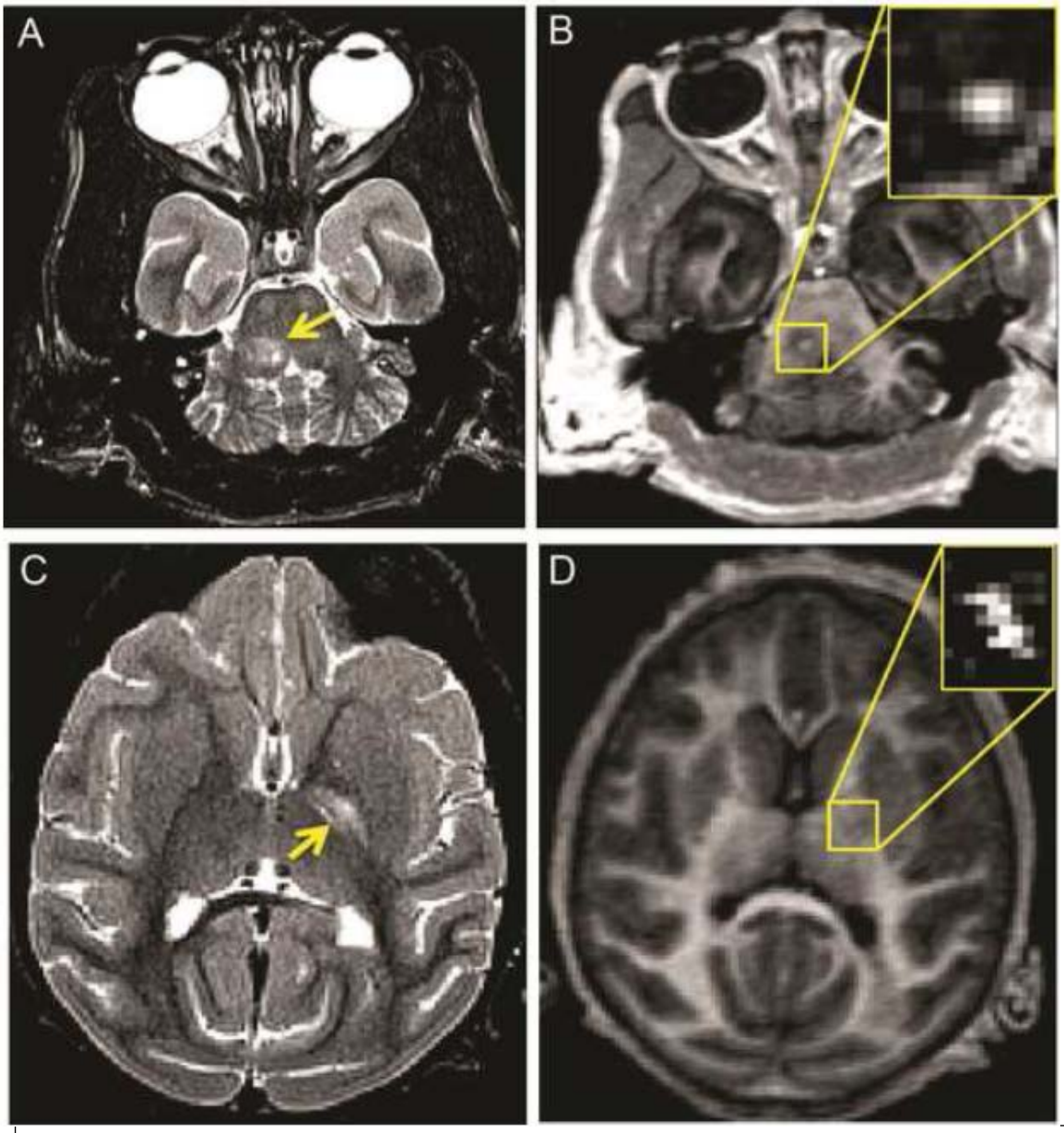

Fig. 1. MRI from animals with JME. Axial 3 T MRI from JM 22019 (A and B) and JM 30760 (C and D) 1 day after presentation with clinical signs of JME. **A.** Axial T_2-weighted image of cerebellum from JM 22019 shows hyperintense signal identified by arrow. B. Axial T_1-weighted MPRAGE image acquired 40 min post-0.2 mmol/kg gadoteridol administration shows an enhancing lesion in cerebellum; more readily visualized in the inset which represents a difference image T_1-weighted (pre-gadoteridol) subtracted from T_1-weighted (post-gadoteridol). C. Axial T_2-weighted image of JM 30760 shows hyperintense signal in the internal capsule region of the cerebral cortex (arrow). D. Axial post-gadoteridol T_1-weighted image shows enhancing lesion in the internal capsule; expanded in the inset showing difference image as in panel B**.**The lesion enhances on a T_1- weighted MPRAGE image acquired 6 min after the administration of gadoteridol. MPRAGE = *m*agnetization *pr*epared *r*apid *a*cquisition *g*radient *e*cho.

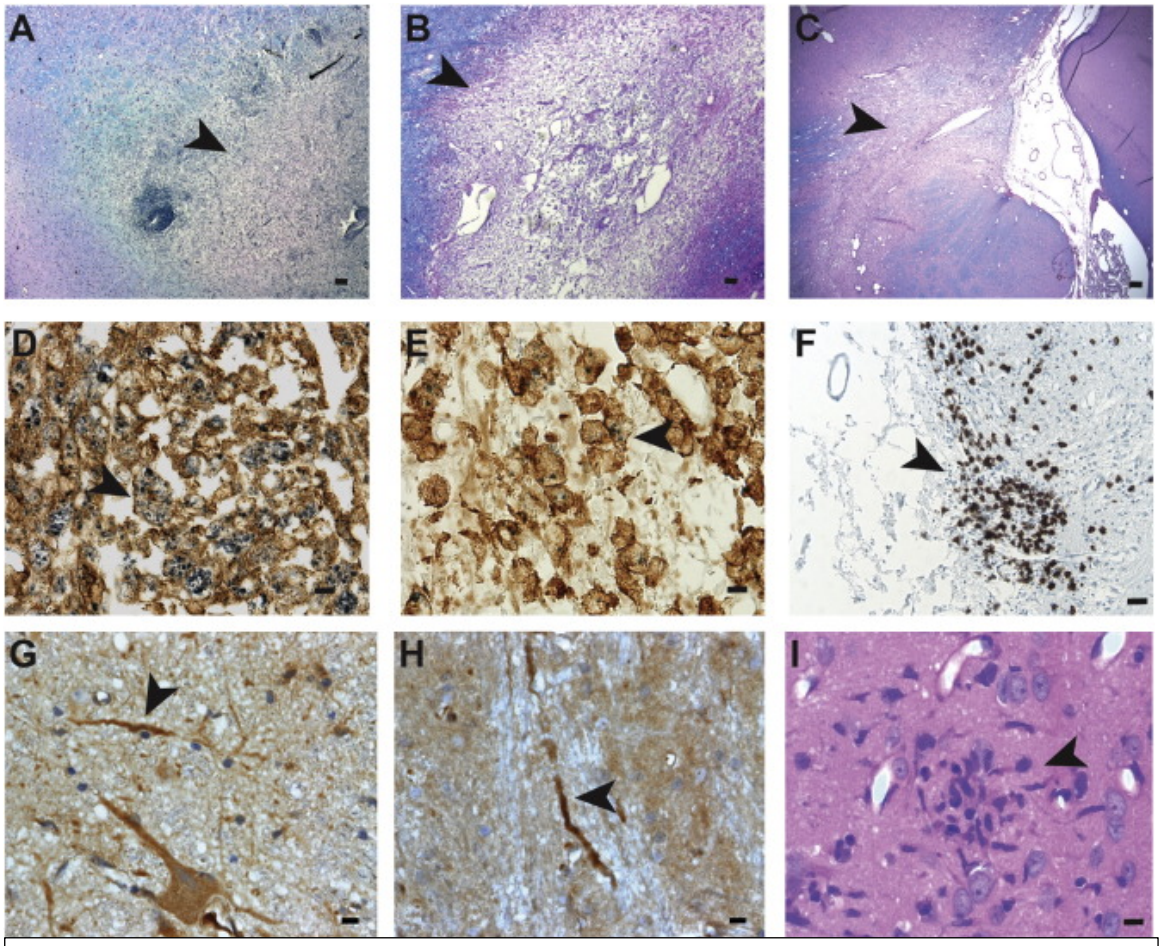

Fig. 2. Histopathology and immunostained images of gadolinium-enhancing CNS lesions acquired from JME animals. A**.** Low magnification (2.5 ×) image of luxol fast blue (LFB) and hematoxylin-eosin (H&E) stain of cerebellar lesion from JM 22019 shows demyelinated region adjacent to perivascular cuff surrounding the blood vessel. Arrowhead points to the demyelinated region. B and C. Low magnification (2.5 ×) images of LFB/H&E stain of internal capsule lesions from JM 30760 and JM 30773, respectively. Arrowheads point to the demyelinated regions. Scale bars for A, B and C = 100 μM. D. High magnification (40 ×) of immunostained cerebellar lesion from JM 22019 showing numerous CD163 + macrophage/activated microglia (brown) immunoreactive for myelin basic protein (MBP, gray). Arrowheads point to a representative macrophage/activated microglia immunoreactive for MBP. E. High magnification (40 ×) image of immunostained internal capsule lesion from JM 30760 showing fewer CD163 + macrophage/activated microglia (brown) immunoreactive for MBP (gray). Arrowhead points to a macrophage/activated microglia immunoreactive for MBP. F. High magnification (40 ×) of immunostained periventricular surface of inflammatory cell aggregates with arrowhead showing accumulation of CD20 + B cells. Scale bars for D, E and F = 10uM. G and H. Immunostains demonstrating activated complement 3Cd deposition on axons and neurons of demyelinating lesions from JM 22019 and JM 30760. Arrowheads points to activated complement 3Cd deposition on axons. **I.** Microglial nodule in normal appearing white matter surrounding hippocampus of JM 30773. Scale bars for G, H and I = 10 μM.

Each demyelinating lesion was subsequently analyzed by immunostaining to visualize macrophages containing myelin proteins and is the same method used to assess MS plaques for active demyelination (Frischer et al., 2015). Evidence of CD163 + macrophage/activated microglia immunoreactive for myelin basic protein (MBP) was detected in the lesions isolated from 9 JME animals, whereas 2 animals (JMs 27624 and 31509) possessed numerous CD163 + cells that were not immunoreactive for MBP. Representative immunostains from the cerebellar lesion isolated from JM 22019 and the internal capsule lesion of JM 30760 are shown (Fig. 2D and E). The internal capsule lesion from JM 30760 had notably fewer and sparsely located CD163 + macrophage/activated microglia immunoreactive for MBP. To identify the inflammatory cells in the aggregates on the periventricular surface of JM 30773 we immunostained the section with CD68, CD3 and CD20 and found a significant cluster of CD20 + B cells (Fig. 2F) with very few CD3 + T cells within the aggregate and parenchyma (data not shown). Prominent B cell clusters were observed in multiple JME animals. Sections exhibiting CD163 + macrophage/activated microglia immunoreactive for MBP macrophages were also found to stain positively for activated complement 3Cd along axons and neurons (Fig. 2G and H). Interestingly, we found numerous microglial nodules in the normal appearing white matter surrounding the hippocampus near the periventricular lesion of JM 30773 (Fig. 2I). These additional histopathological findings are consistent with pathological findings observed within MS lesions (Barnett et al., 2009, Breij et al., 2008 and Singh et al., 2013).

3.2. JME lesions are positive for the pro-inflammatory cytokine IL-17

The CNS lesions from the 11 JME animals were subsequently immunostained for the presence of IL-17, a pro-inflammatory cytokine expressed in active MS lesions (Tzartos et al., 2008). Nine of the 11 lesions revealed prominent IL-17 positive staining. We used double immunofluorescence to identify the cell types positive for IL-17 and found that CD3 + T cells, olig2 + oligodendrocytes, and GFAP + activated astrocytes were positive for IL-17, respectively (Fig. 3C, F, I). IL-17 positive staining was not uniform amongst the 9 lesions, as we observed dual staining for IL-17 in CD3 + T cell in 8 lesions, olig2 +/IL-17 + staining in 8 lesions, and GFAP +/IL-17 + staining in 3 lesions. Only lesions from 3 JME animals (JMs 26174, 30760 and 30,773) were positive for IL-17 in these 3 cell types and no IL-17 + staining was observed in CD163 + cells from any of the other lesions analyzed (data not shown). We did not detect IL-17 + staining in 1 animal's lesion, JM 30493.

3.3. JME lesions harbor infiltrating IL-17 and IFN-γ-producing T cells

To investigate the phenotype of infiltrating T cells, we isolated mononuclear cells (MNCs) from gadolinium-enhancing lesions of 5 JME animals and used flow cytometry to characterize these populations. Our analysis showed 50% to 80% of infiltrating lymphocytes were either $CD4^+$ or $CD8^+$ T cells (Fig. 4A). The $CD4^+$ to $CD8^+$ T cell ratio varied amongst the 5 animals. Lesions from 3 animals (JMs 22019, 27624 and 31522) had almost twice as many $CD4^+$ T cells as $CD8^+$ T

cells, while lesions from 2 animals (JMs 31509 and 31852) had almost 3 times as many $CD8^+$ T cells as $CD4^+$ T cells.

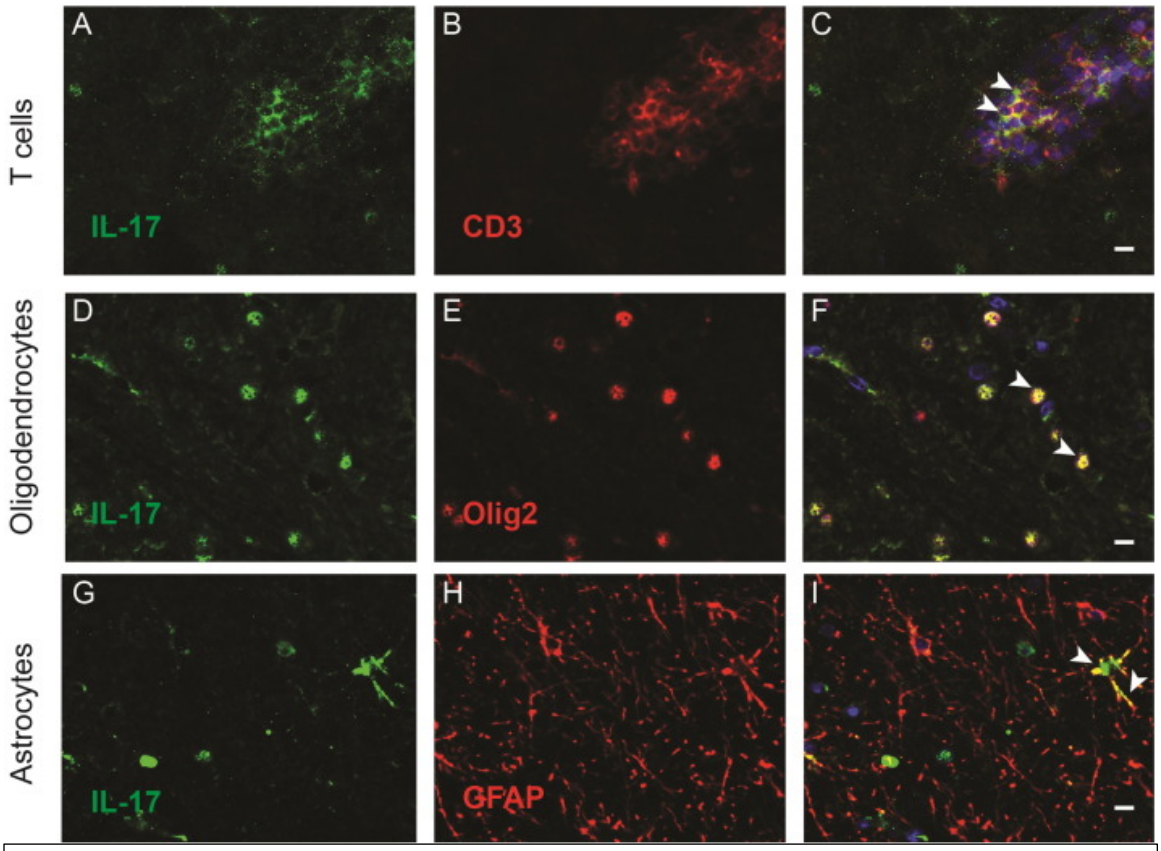

Fig. 3. IL-17 positive staining in the active cerebellar lesion of animal JM 26174 with JME. High magnification (40 ×) images of double immunofluorescence staining for IL-17 (A, D, and G; green), $CD3^+$ T cells (B, red), olig2 + oligodendrocytes (E, red), and GFAP + activated astrocytes (H, red) taken from the demyelinating cerebellar lesion in JM 26174. The overlay demonstrates IL-17 positive staining in CD3 + T cells (C, arrowheads), oligodendrocytes (F, arrowheads), and in astrocytes (I, arrowheads). Scale bars = 10 μM. (For interpretation of the references to color in this figure legend, the reader is referred to the web version of this article.)

Next we wanted to determine if lesions from JME animals harbored infiltrating IL-17 or IFN-γ producing T cells. These cells are hypothesized to play an important role in MS development and are highly enriched in CNS lesions from MS patients

(Tzartos et al., 2008 and Montes et al., 2009). Purified MNCs collected from the lesions of JMs 27,624, 31,522 and 31,852 were stimulated with PMA and ionomycin, followed by intracellular cytokine staining for IL-17 and IFN-γ. Each animal exhibited different patterns of cytokine expression within their T cell compartments (Fig. 4B). The lesion from JM 27624 contained a large percentage of cytokine-producing cells, which were IFN-γ^+($CD4^+$, 27.8%; $CD8^+$, 66.7%), IL-17^+ ($CD4^+$, 13.7%; $CD8^+$, 3.45%) or IFN-γ^+/IL-17^+ ($CD4^+$, 14.2%; $CD8^+$, 18.2%) expressing T cells. JM 31852 had fewer cytokine-producing T cells overall and these cells primarily expressed IFN-γ ($CD4^+$, 19.9%; $CD8^+$, 37.5%). A small percentage of the infiltrates were Th17 cells (8.96%) and hardly any double producers were present ($CD4^+$, 0.58%; $CD8^+$, 0.68%). T cell infiltrates from JM 31522 displayed a similar expression profile to JM 27624, albeit with a lower percentage of cytokine-producing cells [IFN-γ^+ ($CD4^+$, 12.1%; $CD8^+$, 44.3%), IL-17^+ ($CD4^+$, 12.6%; $CD8^+$, 5.48%)]. Unlike JM 27624, the lesion from JM 31522 had limited accumulations of IFN-γ^+/IL-17^+ double-positive cells in either T cell compartment ($CD4^+$, 2.24%; and $CD8^+$, 3.41%). These data indicate active lesions in the CNS of JME animals harbor infiltrating T cells that exhibit Th1 and Th17 phenotypes.

3.4. B cell processes occur in JME

The presence of CD20 + cell clusters in the CNS of JME suggests that B cells may be contributing to disease pathogenesis. To further evaluate the role of B cell processes in JME, we analyzed CSF and blood samples from 9 JME animals and 11 age- and gender-matched healthy controls (HC) and performed a

comparative IgG analysis. First, we determined the concentration of IgG and albumin in both the CSF and plasma for each animal. Notably, we found that the mean CSF IgG concentration for JME animals was 13.3 times higher than that of HC animals [4.39 mg/dL ± 1.45, standard error of the mean (SEM) for JME versus 0.31 mg/dL ± 0.05 SEM)] (Fig. 5A). The differences observed between the CSF IgG concentrations were statistically significant ($p < 0.006$, unpaired t test), whereas the plasma IgG concentrations were not. Additionally, we found that the CSF albumin concentrations were statistically higher ($p < 0.004$, unpaired t test) in the JME animals (57.1 ± 8.63 SEM) than the HC (30.27 ± 2.47 SEM), which could be explained by a leaky blood brain barrier (BBB) in JME animals, as these animals had gadolinium-enhanced lesions (data not shown).

Although elevated CSF IgG concentrations are an indicator of abnormal B cell processes occurring in the CNS, calculating the CSF IgG index is considered more reliable as it corrects for IgG appearing in CSF because of increased BBB permeability (Freedman et al., 2005, Polman et al., 2011, Tumani et al., 2011 and Link and Tibbling, 1977). The CSF IgG index was calculated for each animal and we found that JME animals have an elevated mean CSF IgG index of 1.23 ± 0.26 SEM, compared to HC (mean CSF IgG index of 0.36 ± 0.1 SEM), which was statistically significant ($p < 0.003$, unpaired t test) (Fig. 5B).

Lastly, we evaluated the CSF from JME and HC animals for the presence of 2 or more OCBs, as this sensitive qualitative assay is an indicator of the intrathecal IgG synthesis. Paired unconcentrated CSF and diluted plasma from animals with JME and HC were run on IEF agarose gels and then transferred to a

nitrocellulose membrane and immunostained for IgG. We found 2 or more OCBs in the CSF of 7/9 JME animals, whereas the age- and gender-matched HCs showed no evidence of OCBs (Fig. 5C). By these 2 CSF analyses, all 9 JME animals had positive CSF findings (Table 2).

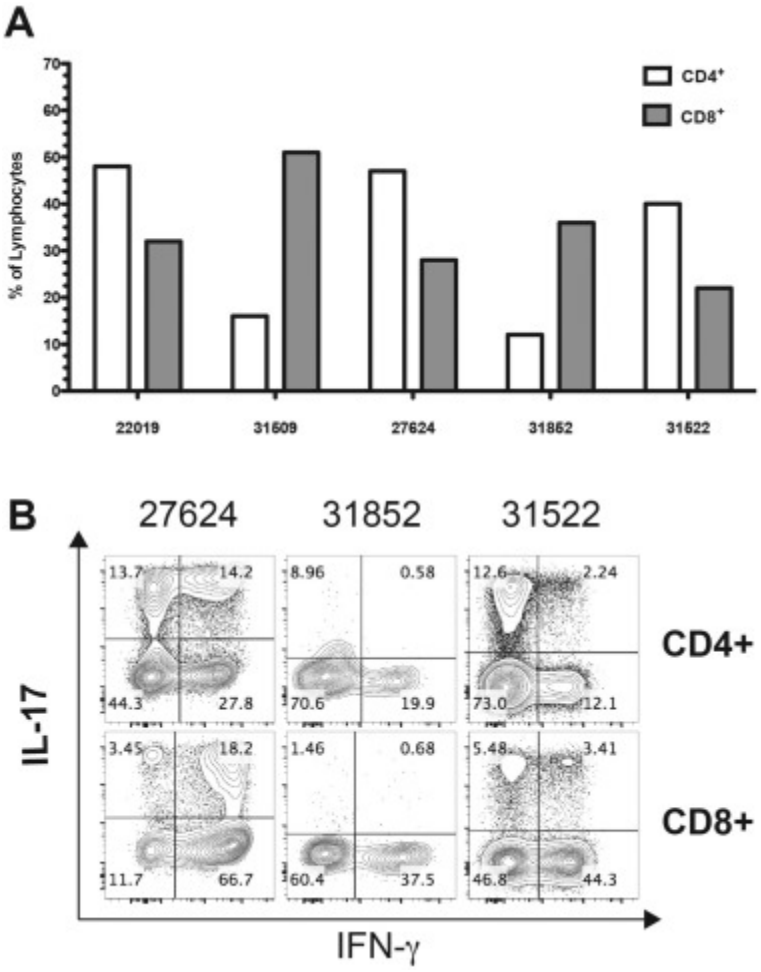

Fig. 4. Analysis of CNS mononuclear cell infiltrates in active CNS lesions of JME animals. A. Flow cytometry was used to analyze T cell populations infiltrating CNS lesions isolated from five JME animals (JMs 22019, 31509, 27624, 31852 and 31522). Mononuclear cells (MNCs) were stained with anti-CD4 and anti-CD8. Bars represent the percentage of lymphocytes expressing $CD4^+$ (white) or $CD8^+$ (gray). B. Infiltrating MNCs were stimulated for 6 h with PMA and ionomycin in the presence of Brefeldin A followed by intracellular cytokine staining for IL-17 and IFN-γ. Plots show the percentage of IL-17 and IFN-γ expressing cells within $CD4^+$ or $CD8^+$ T cell populations gated on $CD3^+$.

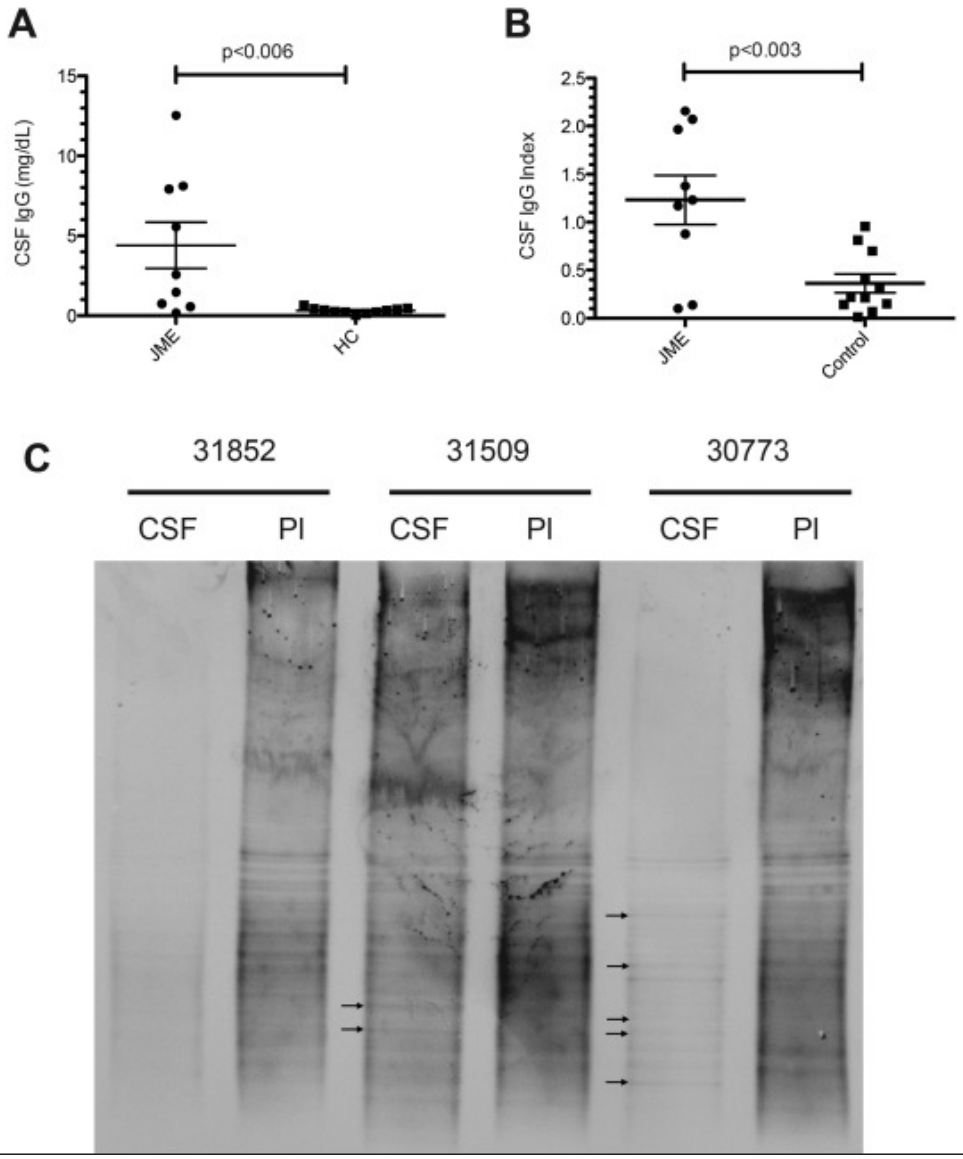

Fig. 5. Cerebrospinal fluid analysis of samples obtained from animals with JME and age- and gender-matched healthy controls. A. ELISA results of IgG concentration (milligrams per deciliter) in the cerebrospinal fluid (CSF) of animals with JME compared to age- and gender-matched healthy control (HC) animals. Each point represents CSF from an individual animal. The horizontal line indicates the mean and the error bars correspond to the standard error of the mean. IgG concentrations were significantly higher in the CSF of JME animals than in HC. Statistical significance was calculated using an unpaired t test. B. The CSF IgG index for each JME and HC animal is shown. The horizontal line indicates the mean CSF IgG index for each group and the error bars correspond to the standard error. An unpaired t test was utilized to determine that the difference between the two groups was statistically significant. C. Oligoclonal band (OCB) profiles of animals with JME. Matched CSF and diluted plasma from three representative animals with JME were resolved by isoelectric focusing (IEF), transferred to nitrocellulose and IgG detected by immunoblotting with a horseradish peroxidase conjugated mouse anti-human IgG (clone G18-145). The arrows indicate OCBs in the CSF for animals 31509 and 30773, which had 2 and 5 OCBs, respectively. No OCBs were detected in the CSF of animal 31852. Samples were run at least twice and representative blots are

Table 2.
CSF and plasma analysis of JME and HC animals.

Animal ID	CSF IgG (mg/dL)	Plasma IgG (mg/dL)	CSF albumin (mg/dL)	Plasma albumin (mg/dL)	CSF IgG Index	Oligoclonal bands
18276[a]	0.17	103.68	28	2364	0.138	Y
19615[a]	5.55	372.16	60	4705	1.169	N
22019[a]	1.45	186.12	38	4285	0.879	Y
27624[a]	7.90	511.92	58	4625	1.231	Y
31852[a]	0.74	47.16	39	4885	1.965	N
30493[a]	0.56	283.23	80	4055	0.100	Y
30773[a]	2.56	311.85	29	4860	1.376	Y
31509[a]	8.11	172.92	81	3725	2.157	Y
30760[a]	12.53	299.57	101	4995	2.069	Y
	4.397 ± 1.45	254.3 ± 47.6	57.1 ± 8.63	4278 ± 277.5	1.23 ± 0.26	
19616[b]	0.39	152.85	30	4770	0.406	N
19895[b]	0.46	80.63	31	4425	0.814	N
20471[b]	0.25	81.12	25	5675	0.700	N
24636[b]	0.64	239.88	53	6040	0.304	N
25473[b]	0.43	421.68	25	3685	0.150	N
25457[b]	0.22	40.68	29	5120	0.955	N
29202[b]	0.32	280.02	25	4690	0.214	N
29734[b]	0.22	382.00	25	6210	0.143	N
29759[b]	0.14	391.70	25	4865	0.070	N
30761[b]	0.03	284.52	31	4045	0.014	N
30765[b]	0.34	214.37	34	4710	0.220	N
	0.31 ± 0.05	233.6 ± 40.2	30.27 ± 2.47	4930 ± 237.1	0.36 ± 0.10	
	$p < 0.006$	$p < 0.74$	$p < 0.004$		$p < 0.003$	

a Animals with JME.

b Healthly controls.

4. Discussion

Based upon our earlier publication, JME is most similar to 2 human diseases, MS and acute disseminated encephalomyelitis (ADEM). Given that JME can follow a relapsing course, clinically it is most similar to MS. Whereas the acuity of onset and relatively high mortality rate appears to resemble ADEM (Steiner, 2011).

Here, we undertook an immunological based study within this colony of JMs to determine whether JME resembles MS, ADEM or a distinct demyelinating disease. First, we utilized immunopathological techniques that are commonly used in MS neuropathology to further characterize JME lesions. We found that a majority of the demyelinating lesions harbored macrophage/activated microglia cells that were immunoreactive for MBP. We considered these active lesions, as this is the accepted classification in MS. One caveat regarding this characterization is that we did not investigate whether macrophages/activated microglia were immunoreactive for any other myelin components such as myelin oligodendrocytes glycoprotein, myelin-associated glycoprotein, or cyclic nucleotide phosphodiesterase. Had we performed this analysis the 2 JME animals that did not exhibit active demyelination (CD163 +/MBP +) might have been immunoreactive for these myelin components. Future cases will include these targets to define if JME lesions can be characterized as early active lesion or late active lesions (Frischer et al., 2015).

Second, utilizing double immunofluorescence techniques we detected IL-17 positive staining within JME lesions. This recapitulates data from EAE and MS where IL-17 has been shown to be an important cytokine in disease pathogenesis (Pierson et al., 2012 and Baeten and Kuchroo, 2013). Notably, IL-17 is not central to ADEM development or progression (Ishizu et al., 2006). Our data closely parallels findings reported for MS as we detected production of IL-17 in CD3 + T cells, and IL-17 positive staining in oligodendrocytes and astrocytes in the lesioned tissue (Tzartos et al., 2008). Importantly, the finding that isolated

infiltrating MNCs from lesions in the CNS are comprised largely of CD4 + and CD8 + T cells further substantiated our discoveries. This observation correlates with published reports from MS lesions using immunohistochemistry, T cell receptor (TCR) repertoire usage defined by PCR amplification, and flow cytometry (Babbe et al., 2000, Montes et al., 2009, Axthelm et al., 2011 and Tzartos et al., 2008). More importantly, the infiltrating CD4 + T cells possessed both Th1 and Th17 phenotypes, which are widely accepted to play a relevant role in MS immunopathogenesis (Lovett-Racke et al., 2011, Montes et al., 2009, Tzartos et al., 2008, Jadidi-Niaragh and Mirshafiey, 2011 and Wingerchuk and Lucchinetti, 2007). We noted some variability in the composition of CNS infiltrating cells amongst animals and we suspect that this is most likely the manifestation of each animal presenting at varying disease stages prior to sample collection. Additional studies will be essential to determine if this diversity is consistent with animals and stages of disease.

Finally, our histopathological and CSF analyses demonstrate that B cells play a role in neuropathogenesis in JME animals, as these animals have significant B cell clusters in periventricular spaces. Importantly, we found that JME lesions were also positive for activated complement C3d deposition, which although not specifically indicative of MS, indicates that intrathecal antibodies may play a role in pathogenesis of JME (Barnett et al., 2009). Additionally, JME animals evaluated had positive CSF findings, paralleling data shown in MS (Serafini et al., 2004 and Magliozzi et al., 2010). In the clinical setting positive CSF findings are frequently used to help diagnose MS and to help differentiate between MS

and ADEM (Link and Huang, 2006, Polman et al., 2011 and Steiner and Kennedy, 2015).

Here we further define a spontaneous NHP model of inflammatory demyelination, JME that bears striking resemblance to MS. Animals presenting with JME possess MRI detectable lesions in the periventricular region, cerebellum, brain stem and spinal cord, which are regions commonly found to harbor lesions in MS patients (Trip and Miller, 2005). Additionally, these animals possess immunological signatures that are more akin to immunopathogenesis of MS than those of ADEM (Parrish and Yeh, 2012, Wingerchuk and Lucchinetti, 2007 and Steiner and Kennedy, 2015). Importantly, animals that develop JME are from distinct matrilines of the original JM troop, suggesting that host genetic factors contribute to risk of disease. We also believe an infectious etiology may be associated with JME, as animals were PCR positive for Japanese macaque rhadinovirus (JMRV) infection, a simian gamma-herpesvirus we reported earlier to be present in JME lesions (Axthelm et al., 2011 and Estep et al., 2013). Genetic susceptibility and an infectious etiology are two factors that are postulated to be associated with the induction of MS. Other environmental factor(s), such as vitamin D are also considered to be integral. In summary, this model has the potential to provide insight into a disease that has proven incredibly difficult to study, as the existing experimentally induced animal models do not recapitulate all aspects of MS (Procaccini et al., 2015). One of the major roadblocks in studying MS directly has been the inability to characterize CNS infiltrating immune cells directly ex vivo. This has severely limited our

understanding of these potentially pathogenic cells and the extent of their involvement in disease pathogenesis. Future studies will be aimed at investigating the triggers that lead to disease development, as well as further characterization of the immunological processes associated with JME. Ultimately findings from these studies will lead to the discovery of mechanisms driving MS.

5. Conclusions

We found that JME cases encompass several key signatures that are associated with MS, including comparable MRI results, IL-17 production within CNS lesions, and positive CSF findings. In addition, analysis using flow cytometry showed that CNS-infiltrating T cells from JME cases exhibited Th1 and Th17 phenotypes that are thought to be associated with MS immunopathogenesis. We conclude that the JME animal model will provide researchers with access to types of studies that are not otherwise feasible in MS patients and have exciting implications for identifying and targeting pathways that can be used to treat MS.

Abbreviations

ADEM	acute demyelinating encephalomyelitis
AAALAC	Association for Assessment and Accreditation of Laboratory Animal Care International
CNS	central nervous system
CSF	cerebrospinal fluid
dL	deciliter
ELISA	enzyme-linked immunosorbent assay
HC	healthy controls
H&E	hematoxylin and eosin
IL-17	interleukin 17
IEF	isoelectric focusing
IgG	gamma-immunoglobulin
JM	Japanese macaque
JME	Japanese macaque encephalomyelitis

LFB	luxol fast blue
Mg	milligram
MNC	mononuclear cells
MBP	myelin basic protein
MOG	myelin oligodendrocytes glycoprotein
MPRAGE	magnetization prepared rapid acquisition gradient echo
MRI	magnetic resonance imaging
MS	multiple sclerosis
OCBs	oligoclonal bands
ONPRC	Oregon National Primate Research Center
PBS	phosphate buffered saline
PLP	proteolipid protein
PMA	phorbol myristate acetate
SD	standard deviation
SEM	standard error of the mean
TCR	T cell receptor
Th1	T helper cell type 1

Competing interests: TCB, MM, SDR, IT, JP, SGK, JHS and BF have no competing interests. WDR received grants from Vertex Pharmaceuticals. MCF, LSS, DNB and SWW each received research support from the National Multiple Sclerosis Society (NMSS).

Authors' contributions: TCB participated in the design of the study, collected and processed the biological material, including blood and CSF, and infiltrating CNS MNC. She also performed the T cell analysis on infiltrating MNC, and participated in the writing of the manuscript. MM participated in the design of the study and performed immunohistopathological and immunofluorescence analysis on the CNS lesions and performed ELISA tests to quantify IgG, and assisted in the preparation of the manuscript. SDR participated in the design of the study, performed the ELISA tests to quantify IgG and albumin, performed the IEF and immunoblot assays to detect IgG OCBs, and assisted in the preparation of the manuscript. IT and JP performed the MR imaging on the Siemens TIM Trio 3 T

instrument, and IT analyzed the imaging data. SGK performed histological dissection of the CNS tissue for histopathological examination, assisted in the analysis of the MRI scans and participated in the preparation of the manuscript. JHS and BG provided JM parentage data to identify animals from affected matrilines. RLW and MCF performed the pathological analysis on JME cases and participated in the preparation of the manuscript. WDR developed the MR scanning protocol and analyzed the MRI scans. LSS provided immunohistopathological analysis, analyzed the OCB immunoblots and participated in the preparation of the manuscript. DNB participated in the study design and preparation of the manuscript. SWW participated in the study design, the analysis of the data, and prepared the manuscript. All authors read and approved the final manuscript.

Author declarations: All of the authors declare that this manuscript contains original work and that it has not been published or submitted for publication elsewhere.

Acknowledgments: The authors thank the dedicated animal care staff at the ONPRC for the humane treatment of the animals exhibiting JME, and Ms. Kristin Fitzpatrick and Ms. Lori Boshears for proof reading. This research was supported by a United States Department of Defense grant (W81XWH-09-1-0276) (LSS, BF, SGK, WDR, and SWW), a National Institutes of Health grant (P51OD011092-54) (BF, SGK, LSS and SWW), a Sylvia Lawry Fellowship from the National MS Society (MCF), and support from the Laura Fund for Multiple Sclerosis Research (DNB and SWW).

References

AXTHELM, M. K., BOURDETTE, D. N., MARRACCI, G. H., SU, W., MULLANEY, E. T., MANOHARAN, M., KOHAMA, S. G., POLLARO, J., WITKOWSKI, E., WANG, P., ROONEY, W. D., SHERMAN, L. S. & WONG, S. W. 2011. Japanese macaque encephalomyelitis: A spontaneous multiple sclerosis–like disease in a nonhuman primate. Ann of Neurol, 70, 362-373.

BABBE, H., ROERS, A., WAISMAN, A., LASSMANN, H., GOEBELS, N., HOHLFELD, R., FRIESE, M., SCHRODER, R., DECKERT, M., SCHMIDT, S., RAVID, R. & RAJEWSKY, K. 2000. Clonal expansions of CD8(+) T cells dominate the T cell infiltrate in active multiple sclerosis lesions as shown by micromanipulation and single cell polymerase chain reaction. J Exp Med, 192, 393-404.

BAETEN, D. L. & KUCHROO, V. K. 2013. How Cytokine networks fuel inflammation: Interleukin-17 and a tale of two autoimmune diseases. Nat Med, 19, 824-825.

BERER, K., WEKERLE, H. & KRISHNAMOORTHY, G. 2011. B cells in spontaneous autoimmune diseases of the central nervous system. Mol Immunol, 48, 1332-7.

BONNAN, M. 2015. Intrathecal IgG synthesis: a resistant and valuable target for future multiple sclerosis treatments. Mult Scler Int, 2015, 296184.

CHOI, S. R., HOWELL, O. W., CARASSITI, D., MAGLIOZZI, R., GVERIC, D., MURARO, P. A., NICHOLAS, R., RONCAROLI, F. & REYNOLDS, R. 2012. Meningeal inflammation plays a role in the pathology of primary progressive multiple sclerosis. Brain, 135, 2925-37.

FORTINI, A. S., SANDERS, E. L., WEINSHENKER, B. G. & KATZMANN, J. A. 2003. Cerebrospinal fluid oligoclonal bands in the diagnosis of multiple sclerosis. Isoelectric focusing with IgG immunoblotting compared with high-resolution agarose gel electrophoresis and cerebrospinal fluid IgG index. Am J Clin Pathol, 120, 672-5.

FREEDMAN, M. S., THOMPSON, E. J., DEISENHAMMER, F., GIOVANNONI, G., GRIMSLEY, G., KEIR, G., OHMAN, S., RACKE, M. K., SHARIEF, M., SINDIC, C. J., SELLEBJERG, ACCEPTED MANUSCRIPT ACCEPTED MANUSCRIPT F. & TOURTELLOTTE, W. W. 2005. Recommended standard of cerebrospinal fluid analysis in the diagnosis of multiple sclerosis: a consensus statement. Arch Neurol, 62, 865-70.

FRISCHER, J. M., WEIGAND, S. D., GUO, Y., KALE, N., PARISI, J. E., PIRKO, I., MANDREKAR, J., BRAMOW, S., METZ, I., BRUCK, W., LASSMANN, H. & LUCCHINETTI, C. F. 2015. Clinical and pathological insights into the

dynamic nature of the white matter multiple sclerosis plaque. Ann Neurol. doi:10.1002/ana.24497 (epub ahead of print).

GOVERMAN, J. 2009. Autoimmune T cell responses in the central nervous system. Nat Rev Immunol, 9, 393-407.

HAUSER, S. L., WAUBANT, E., ARNOLD, D. L., VOLLMER, T., ANTEL, J., FOX, R. J., BAROR, A., PANZARA, M., SARKAR, N., AGARWAL, S., LANGER-GOULD, A., SMITH, C. H. & GROUP, H. T. 2008. B-cell depletion with rituximab in relapsing-remitting multiple sclerosis. N Engl J Med, 358, 676-88.

HEDEGAARD, C. J., KRAKAUER, M., BENDTZEN, K., LUND, H., SELLEBJERG, F. & NIELSEN, C. H. 2008. T helper cell type 1 (Th1), Th2 and Th17 responses to myelin basic protein and disease activity in multiple sclerosis. Immunology, 125, 161-9.

HELLINGS, N., BAREE, M., VERHOEVEN, C., D'HOOGHE M, B., MEDAER, R., BERNARD, C. C., RAUS, J. & STINISSEN, P. 2001. T-cell reactivity to multiple myelin antigens in multiple sclerosis patients and healthy controls. J Neurosci Res, 63, 290-302.

HELLINGS, N., GELIN, G., MEDAER, R., BRUCKERS, L., PALMERS, Y., RAUS, J. & STINISSEN, P. 2002. Longitudinal study of antimyelin T-cell reactivity in relapsingremitting multiple sclerosis: association with clinical and MRI activity. J Neuroimmunol, 126, 143-60.

HOWELL, O. W., REEVES, C. A., NICHOLAS, R., CARASSITI, D., RADOTRA, B., GENTLEMAN, S. M., SERAFINI, B., ALOISI, F., RONCAROLI, F., MAGLIOZZI, R. & ACCEPTED MANUSCRIPT ACCEPTED MANUSCRIPT REYNOLDS, R. 2011. Meningeal inflammation is widespread and linked to cortical pathology in multiple sclerosis. Brain, 134, 2755-71.

INTERNATIONAL MULTIPLE SCLEROSIS GENETICS, C., WELLCOME TRUST CASE CONTROL, C., SAWCER, S., HELLENTHAL, G., PIRINEN, M., SPENCER, C. C., PATSOPOULOS, N. A., MOUTSIANAS, L., DILTHEY, A., SU, Z., FREEMAN, C., HUNT, S. E., EDKINS, S., GRAY, E., BOOTH, D. R., POTTER, S. C., GORIS, A., BAND, G., OTURAI, A. B., STRANGE, A., SAARELA, J., BELLENGUEZ, C., FONTAINE, B., GILLMAN, M., HEMMER, B., GWILLIAM, R., ZIPP, F., JAYAKUMAR, A., MARTIN, R., LESLIE, S., HAWKINS, S., GIANNOULATOU, E., D'ALFONSO, S., BLACKBURN, H., MARTINELLI BONESCHI, F., LIDDLE, J., HARBO, H. F., PEREZ, M. L., SPURKLAND, A., WALLER, M. J., MYCKO, M. P., RICKETTS, M., COMABELLA, M., HAMMOND, N., KOCKUM, I., MCCANN, O. T., BAN, M., WHITTAKER, P., KEMPPINEN, A., WESTON, P., HAWKINS, C., WIDAA, S., ZAJICEK, J., DRONOV, S., ROBERTSON, N., BUMPSTEAD, S. J., BARCELLOS, L.

F., RAVINDRARAJAH, R., ABRAHAM, R., ALFREDSSON, L., ARDLIE, K., AUBIN, C., BAKER, A., BAKER, K., BARANZINI, S. E., BERGAMASCHI, L., BERGAMASCHI, R., BERNSTEIN, A., BERTHELE, A., BOGGILD, M., BRADFIELD, J. P., BRASSAT, D., BROADLEY, S. A., BUCK, D., BUTZKUEVEN, H., CAPRA, R., CARROLL, W. M., CAVALLA, P., CELIUS, E. G., CEPOK, S., CHIAVACCI, R., CLERGET-DARPOUX, F., CLYSTERS, K., COMI, G., COSSBURN, M., COURNU-REBEIX, I., COX, M. B., COZEN, W., CREE, B. A., CROSS, A. H., CUSI, D., DALY, M. J., DAVIS, E., DE BAKKER, P. I., DEBOUVERIE, M., D'HOOGHE M, B., DIXON, K., DOBOSI, R., DUBOIS, B., ELLINGHAUS, D., et al. 2011. Genetic risk and a primary role for cell-mediated immune mechanisms in multiple sclerosis. Nature, 476, 214-9.

ISHIZU, T., MINOHARA, M., ICHIYAMA, T., KIRA, R., TANAKA, M., OSOEGAWA, M., HARA, T., FURUKAWA, S. & KIRA, J.-I. 2006. CSF cytokine and chemokine profiles in acute disseminated encephalomyelitis. J Neuroimmunol, 175, 52-58.

JADIDI-NIARAGH, F. & MIRSHAFIEY, A. 2011. Th17 cell, the new player of neuroinflammatory process in multiple sclerosis. Scand J Immunol, 74, 1-13.

JAGER, A., DARDALHON, V., SOBEL, R. A., BETTELLI, E. & KUCHROO, V. K. 2009. Th1, Th17, and Th9 effector cells induce experimental autoimmune encephalomyelitis with different pathological phenotypes. J Immunol, 183, 7169-77.

KEBIR, H., IFERGAN, I., ALVAREZ, J. I., BERNARD, M., POIRIER, J., ARBOUR, N., DUQUETTE, P. & PRAT, A. 2009. Preferential recruitment of interferon-gammaexpressing TH17 cells in multiple sclerosis. Ann Neurol, 66, 390-402.

KEBIR, H., KREYMBORG, K., IFERGAN, I., DODELET-DEVILLERS, A., CAYROL, R., BERNARD, M., GIULIANI, F., ARBOUR, N., BECHER, B. & PRAT, A. 2007. Human TH17 lymphocytes promote blood-brain barrier disruption and central nervous system inflammation. Nat Med, 13, 1173-5.

KERLERO DE ROSBO, N., MILO, R., LEES, M. B., BURGER, D., BERNARD, C. C. & BENNUN, A. 1993. Reactivity to myelin antigens in multiple sclerosis. Peripheral blood lymphocytes respond predominantly to myelin oligodendrocyte glycoprotein. J Clin Invest, 92, 2602-8.

LASSMANN, H., VAN HORSSEN, J. & MAHAD, D. 2012. Progressive multiple sclerosis: pathology and pathogenesis. Nat Rev Neurol, 8, 647-56.

LINK, H. & HUANG, Y. M. 2006. Oligoclonal bands in multiple sclerosis cerebrospinal fluid: an update on methodology and clinical usefulness. J Neuroimmunol, 180, 17-28.

LINK, H. & TIBBLING, G. 1977. Principles of albumin and IgG analyses in neurological disorders. II. Relation of the concentration of the proteins in serum and cerebrospinal fluid. Scand J Clin Lab Invest, 37, 391-6.

LOVETT-RACKE, A. E., YANG, Y. & RACKE, M. K. 2011. Th1 versus Th17: are T cell cytokines relevant in multiple sclerosis? Biochim Biophys Acta, 1812, 246-51.

MAGLIOZZI, R., HOWELL, O. W., REEVES, C., RONCAROLI, F., NICHOLAS, R., SERAFINI, B., ALOISI, F. & REYNOLDS, R. 2010. A Gradient of neuronal loss and meningeal inflammation in multiple sclerosis. Ann Neurol, 68, 477-93.

MONTES, M., ZHANG, X., BERTHELOT, L., LAPLAUD, D. A., BROUARD, S., JIN, J., ROGAN, S., ARMAO, D., JEWELLS, V., SOULILLOU, J. P. & MARKOVIC-PLESE, S. 2009. Oligoclonal myelin-reactive T-cell infiltrates derived from multiple sclerosis lesions are enriched in Th17 cells. Clin Immunol, 130, 133-44.

PARRISH, J. B. & YEH, E. A. 2012. Acuted disseminated encephalomyelitis. Adv Exp Med Biol, 724, 1-14. PETZOLD, A. 2013. Intrathecal oligoclonal IgG synthesis in multiple sclerosis. J Neuroimmunol, 262, 1-10.

PIERSON, E., SIMMONS, S. B., CASTELLI, L. & GOVERMAN, J. M. 2012. Mechanisms regulating regional localization of inflammation during CNS autoimmunity. Immunol Rev, 248, 205-15.

POLMAN, C. H., REINGOLD, S. C., BANWELL, B., CLANET, M., COHEN, J. A., FILIPPI, M., FUJIHARA, K., HAVRDOVA, E., HUTCHINSON, M., KAPPOS, L., LUBLIN, F. D., MONTALBAN, X., O'CONNOR, P., SANDBERG-WOLLHEIM, M., THOMPSON, A. J., WAUBANT, E., WEINSHENKER, B. & WOLINSKY, J. S. 2011. Diagnostic criteria for multiple sclerosis: 2010 revisions to the McDonald criteria. Ann Neurol, 69, 292-302. POPESCU, B. F. & LUCCHINETTI, C. F. 2012. Pathology of demyelinating diseases. Annu Rev Pathol, 7, 185-217.

PROBSTEL, A. K., SANDERSON, N. S. & DERFUSS, T. 2015. B Cells and Autoantibodies in Multiple Sclerosis. Int J Mol Sci, 16, 16576-92.

PROCACCINI, C., DE ROSA, V., PUCINO, V., FORMISANO, L. & MATARESE, G. 2015. Animal models of Multiple Sclerosis. Eur J Pharmacol, 759, 182-91.

SERAFINI, B., ROSICARELLI, B., MAGLIOZZI, R., STIGLIANO, E. & ALOISI, F. 2004. Detection of ectopic B-cell follicles with germinal centers in the meninges of patients with secondary progressive multiple sclerosis. Brain Pathol, 14, 164-74.

SLYWESTER, A. W., HANSEN, S.G., PICKER, L.J. 2014. Quantitation of T cell antigen-specific memory responses in rhesus macaques, using cytokine flow cytometry (CFC, also known as ICS and ICCS): from assay set-up to data acquisition. Bio-Protocol.org. April 20, 2014 ed.

STEINER, I. 2011. On human disease and animal models. Ann Neurol, 70, 343-344.

STEINER, I. & KENNEDY, P. G. 2015. Acute disseminated encephalomyelitis: current knowledge and open questions. J Neurovirol.

TUMANI, H., DEISENHAMMER, F., GIOVANNONI, G., GOLD, R., HARTUNG, H. P., HEMMER, B., HOHLFELD, R., OTTO, M., STANGEL, M., WILDEMANN, B. & ZETTL, U. K. 2011. Revised McDonald criteria: the persisting importance of cerebrospinal fluid analysis. Ann Neurol, 70, 520; author reply 521.

TZARTOS, J. S., FRIESE, M. A., CRANER, M. J., PALACE, J., NEWCOMBE, J., ESIRI, M. M. & FUGGER, L. 2008. Interleukin-17 Production in Central Nervous System-Infiltrating T Cells and Glial Cells Is Associated with Active Disease in Multiple Sclerosis. Amer J Pathol, 172, 146-155.

WAISMAN, A., HAUPTMANN, J. & REGEN, T. 2015. The role of IL-17 in CNS diseases. Acta Neuropathol, 129, 625-37. WINGERCHUK, D. M. & LUCCHINETTI, C. F. 2007. Comparative immunopathogenesis of acute disseminated encephalomyelitis, neuromyelitis optica, and multiple sclerosis. Curr Opin Neurol, 20, 343-50.

Corresponding author at: Vaccine and Gene Therapy Institute, 505 N.W. 185th Avenue, Beaverton, OR 97006, United States.